INVESTIGATING SELF-ASSEMBLING NANOMATERIALS (SANs) WITHIN A BIOLOGICAL ENVIRONMENT

GENNARO ANTONIO DICHELLO

A Thesis Submitted in partial fulfillment for the degree of Doctor of Philosophy

November 2017

The University of Brighton
School of Pharmacy & Biomolecular Sciences

ABSTRACT

Nanomaterials are defined as structures possessing one or more dimensions below 100 nanometres in size. They display unique properties that arise as a result of quantum behaviours, owing to their high surface area to volume ratios. Self-assembling nanomaterials (SANs), where individual components referred to as “building blocks” spontaneously organise into complex structural arrangements, is a prominent field that offers technological innovation within medicine and beyond. To effectively exploit this approach in healthcare however, a high-level of behavioural understanding within biological systems is required, which has yet to be ascertained.

Accordingly, work undertaken in this thesis aimed to investigate how gold nanoparticles self-assemble and interact within a biological environment. Molecular recognition and electrostatic attraction, two different underpinning mechanisms of self-assembly were studied. Based on findings within this thesis, the latter approach was chosen for further development. Corresponding functional gold nanoparticles were incorporated into PEGylated liposomes using a novel method and extensively characterised. Comparative cytotoxicity evaluation was carried out *in vitro* on a male Chinese hamster lung fibroblast cell line (V79), employing MTT and LDH assays. Investigations focused on identifying any differences in biological response after treatment with individually dispersed gold nanoparticles and as they underwent *in situ* self-assembly. Cellular uptake and any ensuing self-assembly was investigated using a combination of electron microscopy and elemental analysis on thin-sectioned specimens.

Results presented in this thesis reveal that both electrostatic interactions and molecular recognition facilitate self-assembly under aqueous conditions. Within a biologically relevant medium however, considerable nanoparticle-biomolecule complex formation occurs and only particles exploiting electrostatic interactions persist to self-assemble. Gold nanoparticles were capable of being encapsulated within liposomes by exploiting electrostatic

attractions between oppositely charged lipids and ligands on particle surfaces. The novel method resulted in variable internalised gold to lipid ratios, hypothesised to result from differing magnitudes of electrostatic attraction during preparation. At clinically relevant concentrations, gold nanoparticles functionalised with cationic or anionic ligands did not display significant cytotoxicity. A significant difference in cytotoxicity was displayed as they underwent *in situ* assembly however. Cellular internalisation of gold was evidenced, with nanoparticles seen to accumulate and reside within cellular vacuoles, but no confirmation of self-assembly was obtained.

In conclusion, the current work provides further knowledge regarding the feasibility, risk and current limitations associated with utilising and evaluating nanomaterials for *in-situ* self-assembly within biological environments. Extensive interactions shown to occur between initial building blocks and biological components can hinder self-assembly activity, highlighting the importance of rational design when manufacturing SANs. Individual nanoparticles were encapsulated within surface-modified liposomes, demonstrating a possible strategy towards implementing further control over SANs. Cellular studies identified a difference in toxicity between individual building blocks and their assembled suprastructures, demonstrating that unique biological responses could arise from the self-assembly of SANs. Evaluation of intracellular self-assembly and the ability to differentiate between individual building blocks, assembled suprastructures and cellular components is inherently difficult. Current techniques and approaches require further development to enable routine and reliable assessment of analogous in situ self-assembling nanosystems.

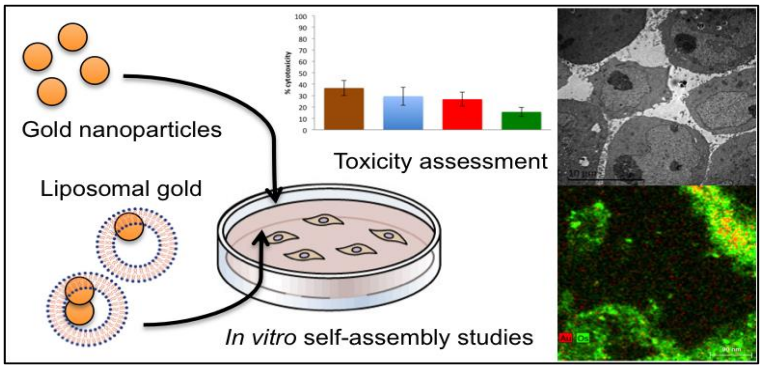

CONTENTS

Publications and presentations relevant to this thesis:

Dichello, G. A., Fukuda, T., Maekawa, T., Whitby, R. L., Mikhalovsky, S. V., Alavijeh, M., & Sarker, D. K. (2017). Preparation of liposomes containing small gold nanoparticles using electrostatic interactions. *European Journal of Pharmaceutical Sciences*,*105*, 55-63. (DOI: 10.1016/j.ejps.2017.05.001).

Dichello, G. A., Sarker, D. K. (2017). Encapsulation of lethal, functional and therapeutic medicinal nanoparticles and quantum dots for the improved diagnosis and treatment of infection. *Nanostructures for Antimicrobial Therapy*. 1st edition, 597-622. Elsevier. (DOI: 10.1016/B978-0-323-46152-8.00027-5).

Kothur, R. R., Fucassi, F., Dichello, G. A., Doudet, L., Abdalaziz, W., Patel, B. A., & Cragg, P. J. (2016). Synthesis and applications of copillar[5]arene dithiols. *Supramolecular Chemistry*,*28*(5-6), 436-443. (DOI:10.1080/10610278.2015.1111375).

Whitby, R. L., Korobeinyk, A. V., Gun'ko, V. M., Wright, D. B., Dichello, G A., Smith, L. C., & Mikhalovsky, S. V. (2013). Single-layer graphenes functionalized with polyurea: architectural control and biomolecule reactivity. *The Journal of Physical Chemistry C*, *117*(22), 11829-11836. (DOI:10.1021/jp4022213).

Whitby, R. L., Smith, L. C., Dichello, G. A., Fukuda, T., Maekawa, T., & Mikhalovsky, S. V. (2014). Cationic ring-opening polymerization of lactones onto chemically modified single layer graphene oxide. *Materials Express*, *4*(3), 242-246. (DOI: 10.1166/mex.2014.1165).

APS PharmSci 2016, 5th-7th September at the Technology and Innovation Centre, University of Stratchclyde, Glasgow. G.A. Dichello, R.D. Whitby, D.K. Sarker, S.V. Mikhalovsky, M. Alavijeh, A. Pannala "Exploiting Electrostatic Interactions for the Entrapment of Gold nanoparticles in liposomes."

LIST OF FIGURES

ACKNOWLEDGEMENTS

To my family; Mum, Dad and three younger brothers: I owe you an unreserved thank you!

Through the high times and the low times. You kept me motivated and offered invaluable support, even when my scientific ramblings were unappreciated. I am entirely grateful to my grandparents, past and present, who have helped guide me through life and provided endless inspiration. To my multinational friends who I travelled the Ph.D. journey with, it has been a pleasure and I will keep the memories we have made forever. Not to forget my friends away from the scientific community, who have undoubtedly felt a sense of abandonment in recent years, yet always remained supportive.

I would like to acknowledge the generosity of the Medical Research Council (MRC) and my industrial partner, Pharmidex, whom made this project possible. I would like to extend my appreciation to everyone at the University of Brighton, whilst I cannot name everyone, so many of you contributed in so many ways. Particular thanks go to my supervisors, Prof. Sergey Mikhalovsky, Dr. Dipak Sarker, Dr. Raymond Whitby and Dr. Mohammad Alavijeh. Not only have you provided me with incredible opportunities, you offered inspiring scientific knowledge and infectious enthusiasm. Special thanks go to my supervisor Dr. Ananth Pannala, for the hard work, never ending encouragement and friendly advice. You have been a great help and your reassurances are undeniably the reason why I was able to fulfil this project to the best of my ability.

I would also like to thank my friends and colleagues at Toyo University (Japan), The University of Sussex, (UK) and The University of Manchester, (UK), who provided me with vital opportunities and knowledge at various stages of this project.

AUTHORS DECLARATION

I declare that the research contained in this thesis, unless otherwise formally indicated within the text, is the original work of the author. The thesis has not been previously submitted to this or any other university for a degree and does not incorporate any material already submitted for a degree.

Signed

Dated

ABBREVIATIONS

CTAB	Cetyltrimethylammonium bromide
DMEM	Dulbecco's Modified Eagle's Medium
DMET	2-(Dimethylamino)ethanethiol
DNA	Deoxyribose nucleic acid
DSA	Dynamic self-assembly
EDL	Electrical double layer
EDS	Energy dispersive X-ray spectroscopy
ESA	Equilibrium self-assembly
FBS	Fetal bovine serum
GNP	Gold nanoparticle
LDH	Lactate dehydrogenase assay
MES	2-mercaptoethanesulfonate
MP-AES	Microwave-plasma assisted atomic emission spectroscopy
MTT	(3-(4,5-dimethylthiazol-2-yl)-2,5-diphenyltetrozolium bromide)
NCL	Negatively charged liposome
NCL-PCG	Negatively charged liposome: positively charged gold nanoparticle
NCG	Negatively charged gold nanoparticles
NP	Nanoparticle
PBS	Phosphate buffered saline
PCL	Positively charged liposome
PCL-NCG	Positively charged liposome: negatively charged gold nanoparticle
PCG	Positively charged gold nanoparticles
SAMs	Self-assembled monolayers
SANs	Self-assembling nanomaterials
SEM	Scanning electron microscopy
TEM	Transmission electron microscopy

1 Introduction

Nanotechnology is a multidisciplinary scientific field that has seen unparalleled curiosity and progress in recent years. Originally devised in 1986, the term nanotechnology was applied to describe the ambitions of precisely manipulating atoms and molecules to facilitate fabrication of materials and complex structures[1]. Today, terminology associated with nanotechnology is applied to describe techniques, materials and the design and manufacture of structures, systems and devices by manipulating molecular, atomic and supramolecular arrangements on the nanoscale[2]. As countless subdivisions of nanotechnology continue to emerge, this multi-encompassing field is being applied throughout in chemistry, biology, physics, environmental, engineering, biomedical and materials sciences. Owing to this level of ongoing development, nanotechnology is likely to be ever further impacting and fundamental to the future advancement of science and technology throughout the 21st century.

With an increasing ability to manufacture new nanomaterials and control their functionality, using the innovative tools and techniques provided by nanotechnology, a new frontier in the fields of medicine has emerged. This can be described as the integration of technology and biological systems at a subcellular and molecular scale, reaching magnitudes of precision and understanding not previously attainable[3]. Within medicine, nanomaterials are increasingly being utilised in the development of drug delivery systems[4], diagnostics[5], pharmaceutics[6], functional medical devices[7] and potentially medical nano-robotics in the future[8]. The generalised aim across these disciplines can be described as working towards the design of “smart” multifunctional nanosystems that interact, respond and provide treatment for medical conditions. As our understanding of human physiology and nanotechnology furthers, the ultimate goal is to enhance efficacy and safety of treatments, benefiting human health and reducing the ever-increasing financial burden on health services.

Self-assembly is broadly described as a process where individual components spontaneously assemble into larger functional units *via* a range of interactions. Described as a "*bottom-up*" approach towards manufacturing materials, this strategy is being utilised to provide variable spatial arrangements and temporal assembly of individual nanomaterials. Accordingly, self-assembly is regarded as a promising route to fabricate increasingly complex, multifunctional nanosystems, with recent examples including advanced drug delivery systems[9] and enhanced treatments for cancer[10]. However, at present, the majority of investigations have concentrated on utilising self-assembly as a method of nanomaterial fabrication under pre-defined, controlled laboratory conditions[11,12]. In other words, a finalised product is obtained for a specific application before introduction into a biological system. Alternatively, self-assembly activity could potentially be utilised *in situ*, with a notion of fabricating nanostructures from individual components *in vivo*; which underpins the basis of the current work. For this purpose, subsequent focus remains predominantly on the mechanisms and performance of self-assembling nanomaterials and how this activity can potentially be controlled and evaluated within biological systems. Accordingly, investigations within the presented thesis are directed towards furthering our understanding of how nanomaterials functionalised to display self-assembling activity perform under biological conditions and how their activity can be reliably assessed.

1.1 Nanomaterials, properties and application towards self-assembling systems

Nanomaterials are defined by the International Organisation of Standards (ISO) as individual entities that display at least one-dimension with a diameter of between 1 and 100 nm[13]. Putting the nanoscale into perspective (Figure 1.1), a red blood cell has a diameter of approximately 8,000 nm (8 μm), whilst an individual haemoglobin protein molecule is below 10 nm in size[14]. Nanomaterials can be engineered or naturally occurring, taking any structural form including particles, plates, fibres and tubes[15,16], which can be compact, hollow, porous[17] or comprise a composite or coating[18]. Described as intermediates between atoms and bulk materials, nanomaterials often display unique and intriguing physicochemical properties, which are detailed in section 1.1.1.1. These phenomena arise because of a change from classical to quantum physics, predominantly occurring because of their larger surface area to volume ratios[19]. This is often explained by the increasing contribution of surface atoms compared to bulk atoms for these materials, which frequently gives rise to size-dependent properties[20]. In addition to their small size, other physical attributes have been demonstrated to contribute towards the observed performance of nanomaterials, which include[21]:

i) Shape
ii) Structure and crystallinity
iii) Chemical composition
iv) Porosity
v) Surface topography
vi) Ionicity
vii) Solubility and state of dispersion

The fabrication and resulting behaviour of dissimilar nanomaterials has consequently attracted considerable scientific interest, with them having been manipulated and exploited to provide novel characteristics including catalytic, optical, magnetic, electrical, thermal and tensile strength[22]. Individual nanomaterials can also be linked together to prepare structures that display overall dimensions beyond the nanoscale, whilst retaining their nano-

associated properties[23]. Resultant characteristics typically depend on the underpinning structural arrangements. If a collection of nanomaterials interact non-covalently and remain as discrete structural components, their native properties could be expected to prevail. However, if individual nanomaterials strongly interact or fuse together, effectively reducing overall surface area to volume ratios, resultant properties could be inherently different. These distinguishing structural arrangements are described in current EU nomenclature[13,23]:

"Agglomerate: A collection, cluster or mixture of weakly bound particles where the resulting external surface area is similar to the sum of the surface area of the individual components.

Aggregate: A particle comprised of strongly bonded or fused particles where the resulting external surface area may be significantly less than the sum of surface areas of the individual components."

These definitions are important when considering the assembly of nanomaterials into larger associated structures and their resultant properties. Consequently, the types of interactions utilised to facilitate self-assembly and ensuing structural arrangements are considered to potentially be fundamental design parameters (see sections 1.1.2 and 1.2.1).

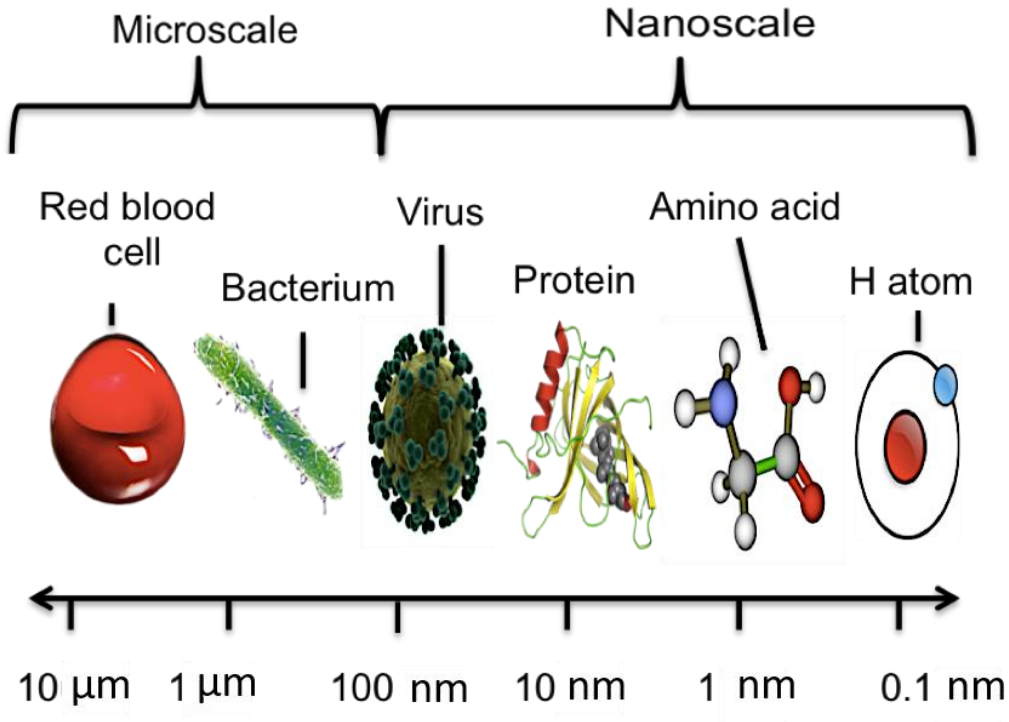

Figure 1.1: Graphical representation of the confinements of the nanoscale. (*Original image*.)

1.1.1 Gold nanoparticles

Nanoparticles (NPs), which are utilised in the current work to investigate *in situ* self-assembly, are described as entities that behave as a whole unit, with respect to their properties and transport[24]. There are numerous different types of NPs that have been developed and categorised; namely noble metals[25], semiconductors[26], magnetic metals[27] and carbon-based structures[7]. Gold nanoparticles (GNPs) in particular have been subject to intense study for a diverse range of applications in biology and medicine[28]. However, when NPs are dispersed in a solvent (colloidal suspension), which can often reflect their intended application, they display a tendency to aggregate because of van der Waal's attractions, particularly in the presence of high salt concentrations and biological molecules such as proteins[29]. Consequently, methods of stabilising GNPs to achieve colloidal homogeneity have been extensively studied[30]. Usually, nanoparticle stability in suspension is achieved either electrostatically or sterically[30]. The former approach exploits electrostatic double-layer (EDL) forces to implement repulsion between NPs, as a result of their surfaces being

modified to display equivalent charges[31,32]. However, notably the presence of electrolytes can cause “charge screening” effects, diminishing particle-particle separation, resulting in colloidal destabilisation[30]. In contrast, steric stabilisation is typically achieved using long-chain macromolecules such as polyethylene glycol (PEG) that extend away from particle surfaces into the surrounding environment, effectively separating NPs and overcoming van der Waal’s attractions[31,33]. Whilst charge-shielding effects do not usually influence steric protection, utilised ligands can sometimes display parameter-dependent conformational changes (temperature, pH, light), which can reduce particle-particle separation, triggering colloidal destabilisation if uncontrolled[31,34]. Whilst these two approaches are effective strategies that can provide colloidal stability under simple aqueous conditions, further considerations must be taken when NPs are utilised within biological environments (see section 1.3).

1.1.1.1 Nano-specific properties of GNPs and their application in medicine

Aside from the advantage of gold being a relatively inert and robust material[35], methods of synthesising nanoparticle derivatives of various sizes and shapes, as well as functional modification of their surfaces are well established[36,37]. In addition to the fact that even minor differences in size and shape can have profound effects on GNP properties[38], the ability to introduce an extensive range of functional surfaces to these particles has provided broad opportunities within medicine; leading to the opinion that GNPs could eventually be utilised at all stages of healthcare including, diagnosis, treatment, prevention and hygiene[39]. At present, GNPs are under investigation for a range of therapeutic applications encompassing fields of genomics, biosensorics, immunoanalysis, clinical chemistry, detection and photothermolysis of cancer and microorganisms, controlled and targeted drug delivery and monitoring of tissues and cells[39]. For example, numerous studies have demonstrated that drug molecules, proteins, peptides and genes can be attached to GNP surfaces for effective treatment of disease[40,41]; with a notion of enhancing therapeutic efficacy and safety by providing superior control over pharmacokinetic properties that govern biocompatibility, biodistribution and *in*

vivo elimination[41,42]. Similarly, GNPs have been modified with "*targeting ligands*" that enable effective transport through stringent biological defence mechanisms such as the blood-brain-barrier[43] or enable exclusive delivery to specific organs, tissues and cells, in an effort towards reducing systemic-associated side effects[44]. Much of the attention concerning the use of GNPs in medicine though, can be related directly to their display of nano-specific properties, which are governed by quantum effects; most renowned being local surface plasmon resonance (LSPR), which was first described by Mie *et al*[45]. LSPR is a phenomenon attributed to free electrons of metallic NP surfaces collectively oscillating with respect to their lattice, occurring at specific wavelengths of the electromagnetic spectrum in a particle-size dependant manner[46-48] (Figure 1.2). This electronic oscillation is described as photons confined to the small size of the nanostructure (quantum confinement), constituting an intense and localised electronic field around the particles[49]. As these surface plasmon oscillations undergo radiative decay, they facilitate enhanced spectral absorption and scattering properties[50] referred to as LSPR bands (Figure 1.2 A).

Accordingly, LSPR properties of GNPs have been developed for microscopy-based bioimaging techniques with work by El-Sayed *et al* providing one of the first practical demonstrations of this concept. This was achieved by attaching monoclonal anti-epidermal growth factor receptor to the surface of GNPs to selectively label and image two epithelial cancer cell models (HOC 313 and HSC 3) when co-cultured with a non-malignant cell line (HaCaT)[51]. Consequently, it was suggested that this approach could be utilised for *in vitro* and *in vivo* diagnostics and biosensing[51]. Differences in LSPR band intensity and spectral shift underpin the majority of sensing strategies involving GNPs, which can be highly sensitive to changes in the local dielectric environment[28]. This gives rise to unique localised-sensing properties that exist at nanoparticle-medium interfaces, where a nanoscale volume around a particle is effectively probed[28].

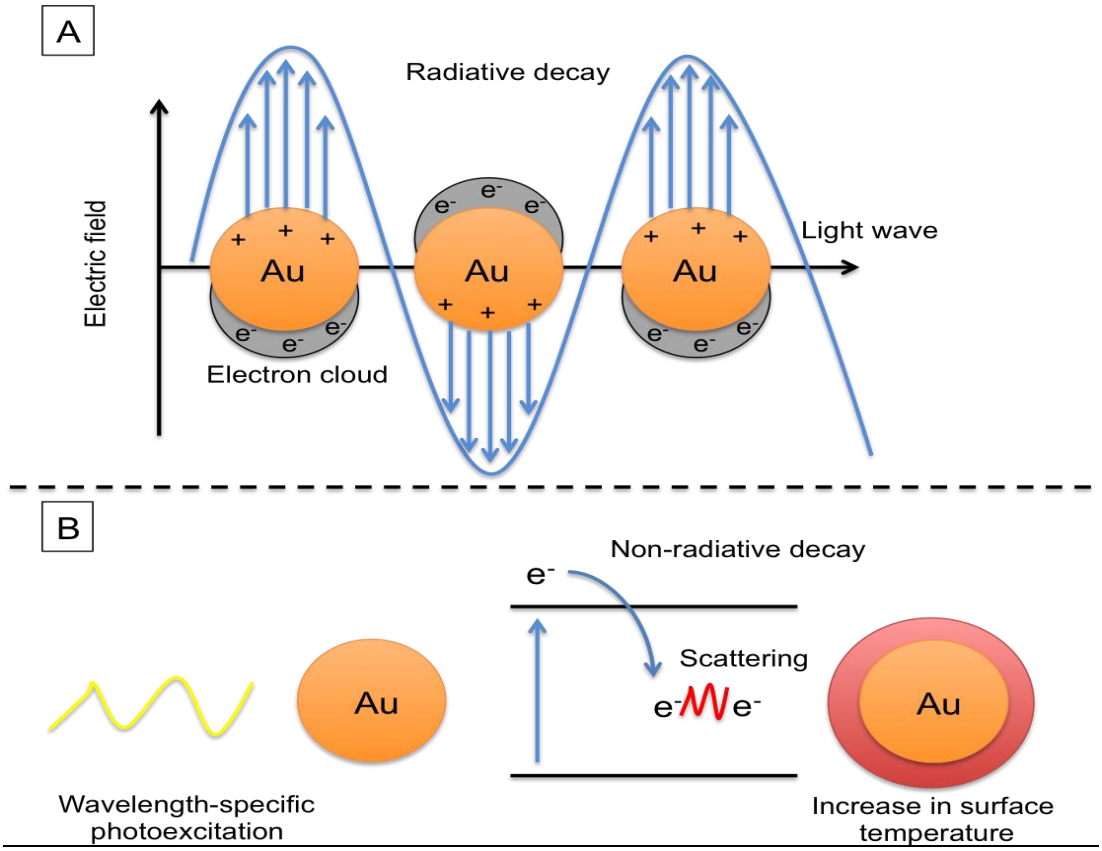

Figure 1.2 Schematic model of localised surface plasmon resonance (LSPR) of gold nanoparticles due to collective oscillations of surface electrons with wavelength-specific incident light. (A): Radiative decay resulting in enhanced light adsorption and scattering properties, (B): Non-radiative decay resulting in light to heat conversion. (*Original image*.)

LSPR related behaviour has consequently been investigated as a method of providing NPs with single-molecule detection capabilities and has attracted considerable interest[52], providing innovative techniques such as indirect-surface-enhanced Raman spectroscopic-bioimaging[53]. Additionally, LSPR can give rise to non-radiative decay, where absorbed light is converted and emitted as localised heat, as a result of electron-electron scattering and electron-phonon coupling[48,50,54] (Figure 1.2 B). This attribute provides wavelength specific optical and photothermal properties which for gold, silver and copper occurs upon exposure to visible and near-IR frequencies[50], within the optical range for effective biological penetration[55]. Accordingly, techniques involving photothermolysis, otherwise termed plasmonic photothermal therapy (PPTT), where metallic NPs are irradiated with non-ionising lasers to produce localised thermal treatment of cancer, are receiving considerable attention and being continuously developed[56,57]. In an effort towards designing

multifunctional nanosystems, GNPs with PPTT capabilities are also increasingly being combined with supplementary techniques, with recent examples including photothermal-chemotherapy[58] and photothermal-drug delivery-MRI enhancement systems[59].

1.1.2 Nanoparticles as components for self-assembly

In context of the current work, individual NPs are termed “building blocks”, which can be assembled into larger “suprastructures”. GNPs are appealing candidates as components for this purpose, for similar reasons why they are attractive therapeutic materials. Gold is relatively inert and robust displays valuable nano-properties for practical application and methods are widely available for the precise modification of surfaces to acquire the required functionality to facilitate self-assembly[60]. Within the broader field of self-assembling nanomaterials (SANs), it is well recognised that both significant challenges and opportunities exist; if uncontrolled aggregation can be avoided and architecture precisely controlled, self-assembly and resultant structures could be utilised for a host of advanced applications[61]. Currently there are three major routes being developed towards achieving predictable activity of SANs:

Substrate assembly – building blocks are assembled onto solid substrates that provide support for organising and aligning components into two and three-dimensional suprastructures.

Interfacial assembly – A liquid-air or liquid-liquid interface is utilised for structural support, with an induced reduction in interfacial-energy facilitating the organisation of building blocks into two-dimensional arrays.

Template-assisted assembly – Functionalised surfaces or template materials are used to provide specific, non-covalent interactions between building blocks for direct self-assembly into two and three-dimensional arrangements.

Whilst substrate and interfacial assembly approaches have been applied for the fabrication of suprastructures under controlled conditions[62,63], derivatives of template-assisted assembly “in solution” appears to be the predominant approach currently under investigation when *in situ* self-assembly or dynamic states of particle-dispersion are required for application[64,65]. In principle, any nanomaterial or building block could be functionalised to direct self-assembly *via* the template-assisted approach. This can include a “*core*” structure that acts as a foundation for the networking of smaller ‘*satellite*’ building blocks; an approach employed by Ou *et al* using 1-pyrenemethylamine as a linker-molecule between carbon nanotubes and GNPs to achieve high density, non-covalent attachment[66]. Alternatively, NPs can be directly functionalised to dictate subsequent assembly and organisation of building blocks; as demonstrated by Nykypanchuk *et al* and Park *et al*, using GNPs with surface-attached DNA of variable length and flexibility to provide basic architectural control, fabricating suprastructures with body-centred or face-centred cubic morphologies[67,68]. Additionally, it has been demonstrated that NPs can be functionalised with ligands to enable *in situ* triggered or “responsive” self-assembly. Cheng *et al*, exploited acetylcholinesterase-catalysed hydrolysis to provide enzyme-specific mediated self-assembly of GNPs in an *in vitro* system for the ultrasensitive colorimetric detection and monitoring of biomarkers for hepatitis C virus[69]. A similar example provided by Hu *et al* utilised metalloproteinase-2, an enzyme that is overexpressed during metastasis of tumours, to trigger *in vivo* self-assembly of GNPs within cancer sites, providing enhanced retention of NPs for subsequent use as PPTT reagents[70].

At present self-assembly of dissimilar nano-building blocks has primarily focused on manipulating their collective properties, for the design of multifunctional materials and devices, with a notion of performing multiple tasks simultaneously or in sequence. However, as proposed in the current work, self-assembly could potentially serve as an on-demand method of fabrication *in situ* and eventually *in vivo*, which could prove useful for advanced biological applications. At present, several strategies that provide different underpinning mechanisms of facilitating self-assembly have been developed, which could also be investigated for this purpose (See section

1.2). However, reflecting on the complex environments that will be encountered within a biological system, the utilised mechanism towards bio-*in situ* self-assembly is potentially a critical design parameter that will need to be further understood before predictable nanosystems can be attained for medical applications. Equally important are the suprastructure morphologies that display different structural arrangements, which have been demonstrated to display various properties that are frequently dependent on the retention of nanoscopic characteristics. Consequently, a resultant suprastructure morphology should also be potentially considered as a critical design parameter, that must eventually be predefined and rigorously controlled (see subsequent section 1.1.2.1 for further detail).

1.1.2.1 Classification of self-assembled suprastructures

Relating to current definitions of agglomerates and aggregates, self-assembled suprastructures can in principle take either form, although how they are classified appears to be an area of ongoing debate, owing to conflicting characterisation and interpretation[71]. For example, Shim *et al* demonstrated reversible self-assembly of GNPs utilising a disulphide-modified polypeptide (poly(L-glutamic acid)) as a surface-bound ligand that underwent pH-dependent structural changes between pH 4.5 and 5.5, which ultimately determined whether particles were assembled or dispersed[72]. However, resultant suprastructures were described as aggregates despite being revealed to display a discrete nanoparticle morphology and an ability to dissociate back into individual GNP building blocks[72]. Furthermore, whilst the ensuing properties of the assembled structures were different from the original NPs, they were still specific to the nanoscale, namely the LSPR effect[72]. To clarify in this instance, individual GNPs were assembled using non-covalent reversible interactions, with overall surface area of the suprastructures reflecting the sum of the individual components, characteristic of agglomeration. In contrast to another study, Wen *et al* used controlled destabilisation of individual GNPs to form three-dimensional porous nanostructures appropriately described as aggregates[73]. The resultant

suprastructures were found to be comprised of networks of nanowires, which were initially formed from the fusion of individual GNPs to fabricate chain-like particles[73]. Elucidating in this situation, the “atomic cores” of individual GNPs were initially amalgamated to produce new chain-like particles, where a reduction in overall surface area could be expected, which is characteristic of aggregation.

The methodology used in the current work is represented in Figure1.3, which differentiates between self-assembled aggregates and agglomerates. This theory agrees with current EU considerations and models proposed by Walter *et al*[71]. In summary, self-assembled agglomerates are dynamic structures formed when individual building blocks are linked together through weak interactions, with structural aggregates representing covalent bonding between individual building blocks to produce entirely new particles[71].

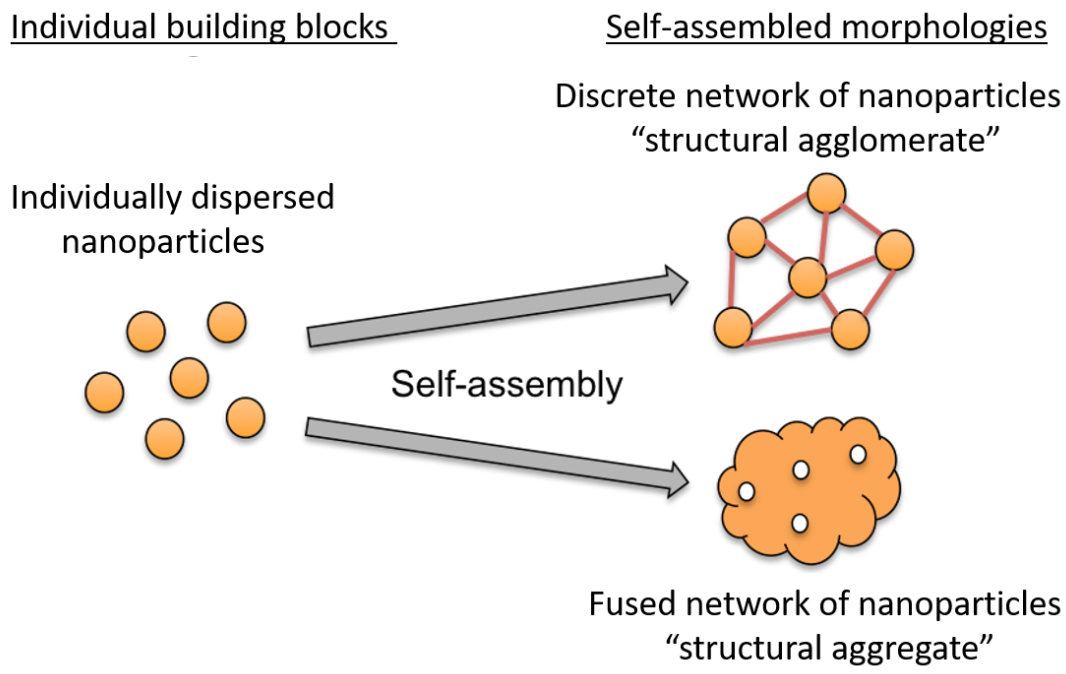

Figure 1.3: Simplified illustration of the underpinning difference between a self-assembled agglomerate and aggregate. Structural-agglomerates are comprised of discrete nano-building blocks that are non-covalently linked together whilst structural-aggregates represent newly formed particles, lacking discrete building-block morphologies. (*Original image*.)

1.1.2.2 Properties and applications of self-assembled suprastructures

Assemblage and networking of nanomaterials has been shown to result in both the display of new collective properties and a combination of properties displayed by the individual components[64]. Whilst the combination of unrelated properties, such as LSPR and magnetism for example, can be directly associated with the inclusion of dissimilar building blocks that exhibit these native characteristics, hybrid nano-properties have also been demonstrated[64]. Hybrid properties are considered to originate from the near-field coupling of localised properties, occurring when NPs are sufficiently close to each other (approximately between 2 and 10 nm)[64]. Coupling effects that have been evidenced include the transfer of electromagnetic energy, transfer of electrons and interactions of magnetic dipoles between neighbouring particles[64,74-76]. These coupling phenomena have been attributed to deviations in LSPR band intensity, spectral shift and broadness[74,77] and photoluminescence emission[78] for assemblies of metallic NPs, with complex disordered magnetic spin-states (magnetic glass behaviour)[79] for assemblies of magnetic NPs. Numerous investigations focus on combining or manipulating these hybrid properties by varying parameters such as building block size, shape and composition, interparticle spacing (distances between building blocks) and their arrangement within a suprastructure[64,74-77]. For example, reducing or increasing interparticle spacing between self-assembled GNPs has been exploited to provide nanosystems with either lower energy (red-shift) or higher energy (blue shift) LSPR bands, an approach that is utilised to fine tune optical properties of suprastructures[64]. On this basis, substrate-induced changes in interparticle spacing of SANs and their resultant optical profiles have also been studied for a range of biosensor-colorimetric applications[77,80]. Work by Schopf *et al* further supports the concept that self-assembly of dissimilar SANs can be used a strategy to combine or enhance properties within suprastructures via coupling phenomena. This group concluded from theoretical and experimental observations that when GNPs of different sizes were assembled with controlled stoichiometry (monomer, dimer and trimer configurations), using a di-rhenium thio-isocyanide complex, they displayed LSPR-related optical properties that were a combination of those displayed by

the individual particles[81]. Crucially, Schopf *et al* also rationally described how controlled self-assembly of building blocks into suprastructures with well-defined and predictable spatial arrangements would be a fundamental requirement before such properties could be reliably harnessed[81]. This requirement is further highlighted by the work of Ghosh *et al*, who demonstrated that optical properties of GNPs are influenced amongst other factors by their local environment, which for assembled suprastructures includes neighbouring particles each with their own intrinsic properties[74]. Demonstrating how multiple SANs can be incorporated into a nanosystem, with a notion of implementing multifunctionality, Paterson *et al* recently reported the co-assembly of a variety of different sized GNPs onto dextran-coated superparamagnetic iron oxide NPs to fabricate suprastructures[82]. It was concluded in this study that the agglomerated-arrangement of building blocks resulted in several key characteristics arising: (a) spatial organisation of GNPs permitted enhanced heating capacity that could be exploited for photothermal purposes, (b) a combined LSPR effect corresponding to the inclusion of different sized NPs provided enhanced optical properties for a range of potential applications and (c) the inclusion of superparamagnetic iron oxide offered additional magnetic capabilities enabling functions such as externally directed bio-accumulation[82].

Although self-assembly of building blocks into suprastructures can provide valuable properties for a range of potential applications, predictable and reliable behaviour depends on an ability to precisely control interactions and spatial geometry between SANs[64]. At present, the ability to consistently fabricate highly ordered suprastructures from building blocks has seldom been achieved, even under pre-defined laboratory conditions, with key factors that determine assembly quality, reproducibility and yield yet to be fully understood[83]. Accordingly, development of simple strategies to facilitate *in situ* self-assembly for the fabrication of basic suprastructures under biological conditions is a fundamental step that must be investigated before desired properties or applications can be considered.

1.2 Strategies towards self-assembly of nanomaterials

Self-assembly is portrayed as the "*autonomous organisation of components into patterns or structures without human intervention*"[84]. Originally devised to describe spontaneous association of molecules into stable, well-defined macromolecular arrangements, the same criteria is considered to apply to nanomaterials but on a larger scale[85,86]. Although at present, application of SANs is mostly limited to fabrication of structures under pre-defined laboratory conditions. The same underpinning principles are considered to pertain within complex environments, such as those potentially encountered *in vitro* and *in vivo*[86]:

I. Individual components must be interlinked by localised, short-range and weak interactions.
II. Interactions between individual building blocks must be more favourable than the interactions with the surrounding matrix.
III. Networking between building blocks must overcome external forces and entropic limitations.

Spontaneous activity of SANs can arise from both non-specific and specific interactions, taking place either directly between adjacent building blocks (direct self-assembly) or because of external forces (externally directed self-assembly)[64,89]. Direct self-assembly, which is the focus of the current work (section 1.2.1) typically applies to nanomaterials with functional surfaces to provide attractive forces between individual building blocks. In contrast, externally directed self-assembly typically utilises a magnetic[87] or electric field[88] to provide a driving-force towards organising individual building blocks. An additional distinction is also described between equilibrium self-assembly (ESA) and dynamic self-assembly (DSA)[89]. The former process is considered to represent the evolution of individual components into stable structures, as a result of minimising Gibb's free energy potential to achieve a state of thermodynamic equilibrium[89]. Consequently, ESA activity fundamentally depends on favourable thermodynamic parameters (temperature, pressure

and number of components), which are governed by the local environment[89]. The main applications of ESA within the fields of SANs include the fabrication of organic[90] and inorganic crystals[91], block-copolymer[92] and lipid structures[93] and supramolecular arrangements[94]. In contrast, DSA represents the fabrication of ordered non-equilibrium structures *via* a supply of energy (favourable interactions)[89]. Avoiding thermodynamic limitations, complex spatial and temporal organisation of individual building blocks can be achieved using a range of direct and externally directed forces, which underpins the basis of systematic design and control of resultant suprastructures prepared via DSA[89].

1.2.1 Direct self-assembly

The basis of utilising direct interactions between nanomaterials to facilitate self-assembly relies predominantly on the rationale use of surface chemistry; including the application of molecular, biomolecular, supramolecular, polymer and nano-chemistry[95-98]. Accordingly, potential approaches towards providing direct interactions for suprastructure fabrication are diverse, encompassing derivatives of both template-assisted and substrate self-assembly, via physical, chemical and biological template approaches[95]. Whilst physical features of SANs such as size, shape and surface topography can assist the organisation of individual building blocks within a suprastructure, additional interactions between components are still required to provide mechanisms towards overcoming entropic and external forces[86]. Electrostatic interactions and molecular recognition, approaches utilised in the current work to facilitate self-assembly, were identified from literature as promising strategies, having been recently reported for a range of nanofabrication techniques and relevant applications[99,100].

1.2.1.1 Electrostatic interactions

Intermolecular electrostatic interactions are considered non-covalent, non-specific long or short-range forces between ionic molecules[101], arising from

ion-dipole and ion-ion interactions. Ionic molecules are typically attached to metallic nanoparticles (gold, silver, platinum, palladium, copper and nickel) via thiol (SH), amide (NR_2) and carbonyl (OCR_2) terminal functional groups[101], providing particles with surface-associated, self-assembled monolayers (SAMs) that display electrostatic potentials[102]. When nanomaterials that display oppositely charged SAMs are combined within solution, they can spontaneously self-assemble into suprastructures. In contrast, when nanomaterials display identical surface charges, repulsive electrostatic forces can arise between nanomaterials because of an overlap of electrical double layers (EDL) surrounding particles[101]. Resultantly, electrostatic interactions can be utilised to both direct the assembly of individual building blocks and reinforce (stabilise) the resultant suprastructures[103]. Self-organisation of individual building blocks via electrostatic interactions is generally perceived as an equilibrium process (ESA), although as S. Whitelam explains, resulting suprastructures are often non-equilibrium, kinetically trapped arrangements[104] as depicted in Figure 1.4. Kinetic traps are thought to arise when nanomaterials initially assemble into non-equilibrium arrangements, with their subsequent reorganisation towards a state of equilibrium occurring on extremely long timescales[104]. There are two main methods towards introducing further control within electrostatic self-assembling systems: (a) modifying the EDL of individual building blocks and (b) the use of variable SAMs on nanomaterial surfaces[101]. The former approach relies on a change in thickness of the EDL, which determines the extent and range of electrostatic interactions within a solution. In principle this can be easily achieved by introducing solvents with different dielectric constants or by changing the pH and availability and concentration of electrolytes within the surrounding environment, although within biological systems these parameters are predetermined. In contrast, building blocks functionalised with SAMs can be designed and optimised prior to application; with a range of specific, charged functional groups (COO^-, SO_3^-, PO_3^-, $N(CH_3)_3^+$) and neutral “charge diluting” molecules having being investigated for the preparation of SAMs with different magnitudes of surface charge density[102,105].

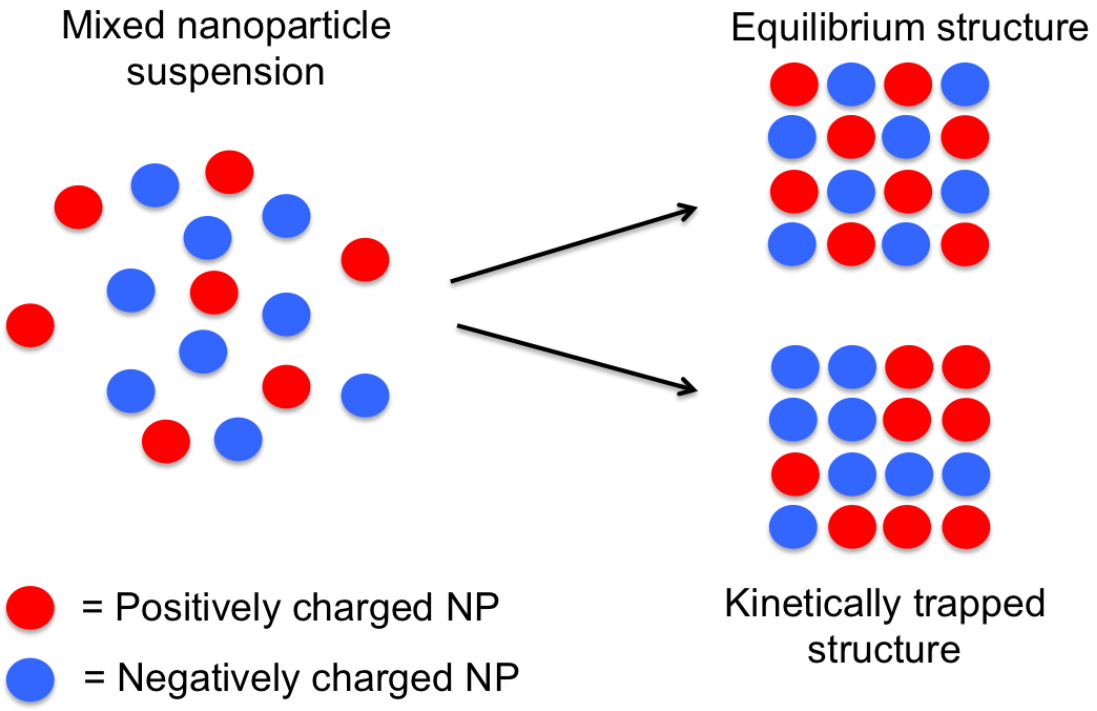

Figure 1.4: Simplified representation portraying the theoretical self-assembly of oppositely charged nanoparticles into suprastructures with equilibrium and kinetically trapped building block arrangements. In theory, electrostatic self-assembly should progress towards a state of equilibrium but in practice the timescale for this evolution can be exceptionally long and kinetically trapped arrangements often prevail. (*Original image*.)

Exemplifying the use of electrostatic interactions as a suitable mechanism towards self-assembly of individual building blocks, numerous studies have reported the fabrication of assembled suprastructures with different compositions and morphologies. At a rudimentary level, simply combining complementary charged spherical nanoparticles in solution results in spontaneous self-assembly into irregular suprastructures, as demonstrated by Kalsin *et al* using gold and silver NPs functionalised to display oppositely charged SAMs[106]. Under highly optimised conditions however, further control over resulting suprastructures can be achieved. This is shown by Gschneidtner *et al*[107] who functionalised spherical, cubic and polyhedron shaped gold, silver and palladium NPs with either negatively (2-mercaptoethanesulfonate) or positively (cetyltrimethylammonium) charged ligands[107]. Experimental conditions were then derived to restrict the electrostatic self-assembly of these different shaped nanoparticles into specific NP-dimer formations[107]. Describing these optimised conditions as a

"stability zone", assembled NP-dimers were provided with an electrostatic repulsion potential, avoiding further self-assembly into larger structures[107]. Whilst conditions within biological systems are fixed and cannot be optimised, it should be possible to design building blocks according to their encountered environment to acquire a desired performance. Won *et al* evidences this approach, also providing evidence that electrostatic self-assembly could potentially persist within biological systems. A ligand was synthesised to include a hydrolysis-susceptible citraconic amide functionality, enabling SAMs on the surface of GNPs to "switch on" both positive and negative charges. Self-assembly resultantly occurs under mild acidic conditions encountered within cancerous cells[108], with the larger size of the suprastructures blocking the cells ability to remove them *via* exocytosis[108]. Furthermore, Won *et al* also show that highly-ordered suprastructures are not necessarily required within biological systems for practical application, having exploited the collective properties of the unsystematically assembled GNPs (as described in section 1.1.2.1) for effective infra-red photoexcitation and subsequent PPTT application[108]. In addition to this study, Yang *et al* evidenced intracellular self-assembly of NPs using a relatively straightforward electrostatic approach[109]. GNPs were initially modified with either citrate or branched polyethylenimine to provide them with positive and negative SAMs. Building blocks were then exposed to human breast carcinoma cells (MDA-MB-231) consecutively (positive and negative GNPs added at different times), which resulted in intracellular GNP clusters, which was not seen when either positive or negative GNPs were added alone[109].

1.2.1.2 Molecular recognition

Methods that utilise specific intermolecular interactions to facilitate self-assembly of individual building blocks are often referred to collectively as "*molecular recognition*" strategies. In principle, any non-covalent interaction or their combination can be exploited for this purpose, including van der Wall's forces, pi-pi interactions, hydrogen bonding and hydrophobic effects[89]. Nanomaterials are typically modified with a variety SAMs, with a proportion of

surface molecules functioning as specific “active sites” or “recognition sequences”[89]. Individual building blocks are designed accordingly so that their recognition motifs display complementarity as depicted in Figure 1.5. Specific interactions between complementary recognition sites can then be used to subsequently direct and restrict the self-assembly of distinct building blocks, potentially permitting the fabrication of highly ordered, non-equilibrium suprastructures[103,110]. Numerous examples have been reported that attain molecular recognition for the fabrication of self-assembled structures via the application of surface attached polymers, biomolecules and macromolecules. Although notably a lot of studies until more recently have focused on using derivatives of DNA[103,110-112].

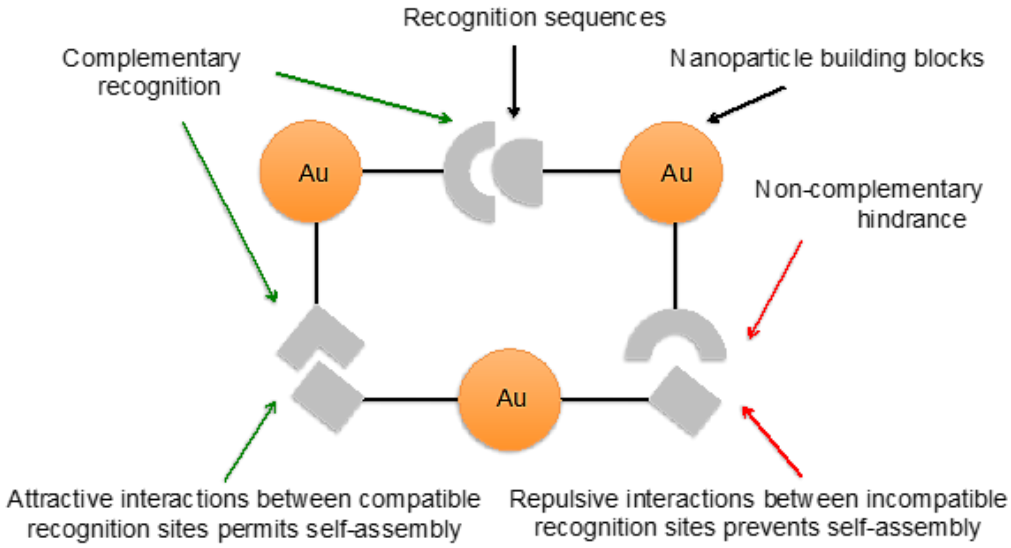

Figure 1.5 Simplified schematic representing individual GNP building blocks functionalised with recognition sequences. In theory, complementary sequences (green arrows) facilitate self-assembly whilst non-complementary sequences (red arrow) prevent self-assembly, enabling specific arrangements to form. (*Original image*.)

Oligonucleotides, which are short strands of synthetic DNA, provide an infinite range of specific recognition sequences that can be designed to network individual nanomaterials. Their ability to form Watson-Crick hydrogen bonding between adenine (A) and thymine (T) and cytosine (C) and Guanine (G)[103,113], the four major nucleobases that can be encoded into DNA, enables single strands of complementary sequences to hybridise (parallel bonding) to form linear double stranded complexes[113]. When complementary single strands of oligonucleotides are attached to the surface of individual nanomaterials,

hybridisation can result in spontaneous self-assembly into two and three-dimensional structures[113]. Methods of attaching oligonucleotides to metallic nanoparticles are also well established, which utilise a thiohexyl functional group (C_6SH) end-grafted onto the phosphate backbone that underpins the nucleobase recognition sequence[114]. Additionally, as oligonucleotide recognition sequences can be synthesised with a variable number of nucleobases, with complementary sequences acting as "linkers" between building blocks, interparticle distances and bonding strength can be easily controlled to optimise associated properties[113]. In an attempt to provide further structural complexity, several groups have also synthesised non-linear oligonucleotides, with branched and junction motifs used to direct SANs into ordered assemblies such as GNP trimer and tetramer configurations[111,115]. With the intention of designing further complex self-assembling systems for the fabrication of multifunctional platforms. Kim *et al* recently proposed attaching multiple distinct DNA recognition sequences at different locations on discrete building blocks. In agreement with the views of the current work, Kim *et al* also recognised that physiochemical and structural properties of nanomaterials as well as the design of suitable recognition sequences need to be further investigated and understood before further complex systems are fabricated, considering them to be critical design parameters[110]. Despite these challenges, there has been considerable ongoing development of DNA-based self-assembling nanosystems, which primarily involve two respective strategies: (a) attachment of complementary oligonucleotides directly onto nanomaterial surfaces[116] or (b) attachment of oligonucleotides which are partially complementary towards a third "template" oligonucleotide that acts as a freestanding scaffold between nanomaterials[117]. Utilising these strategies, oligonucleotides have since been applied to fabricate a range of finite-number of regularly spaced and extended two and three-dimensional ordered suprastructures for a range of potential applications[118].

Relating to the current work which focuses on *in situ* self-assembly, Yunqi *et al* described one of the first reports of stimuli-triggered and reversible self-assembly in 2012, using oligonucleotides on the surface of GNPs that had been modified to incorporate a photo-sensitive azobenzene functional

group[119]. This approach was underpinned by the ability of azobenzene to respond to UV-light exposure, undergoing cis-trans isomerisation that in turn destabilised the hybridised oligonucleotides used to network individual building blocks[119]. An alternative approach reported by Seela *et al* demonstrated pH-dependent reversible self-assembly of GNPs, utilising a modified cytosine nucleobase (2-deoxycytidine) incorporated within hybridised oligonucleotides, attached to the surface of discrete nanoparticles[120]. Double-stranded oligonucleotides containing this modification on the surface of GNPs were rendered complementary to an additional set of double-stranded oligonucleotides attached to GNPs only under acidic conditions, inducing a DNA "i-motiff" configuration and subsequent self-assembly[120]. A DNA i-motif is described as two parallel double-strands of DNA held together in an anti-parallel orientation by intercalated cytosine-cytosine^{+} base pairing[121].

Despite the advances of DNA-based molecular recognition for self-assembly, there are very few studies that attempt to translate this technology *in vitro* or *in vivo*. Whilst a lack of progression towards bio-*in situ* self-assembly using DNA could potentially be hindered by several conceivable issues, such as degradation or fouling of recognition sequences *via* the activity or adsorption of biomolecules to the surface of nanomaterials. A recent study by Tang *et al* appears to offer optimism where two dissimilar GNPs functionalised with oligonucleotides were used as "core" and "satellite" building blocks for fabrication of suprastructures prior to PEGylation. Stability studies of these building blocks in serum showed that these constructs remained intact and were entirely resistant to enzymatic degradation[122]. Additionally, when suprastructures were further modified with a targeting ligand (N-acetylation chitosan), they were seen to accumulate in the kidneys of mice, still intact, with suggestions that this technology could be further developed for *in vivo* imaging purposes[122]. Whilst this investigation only utilised self-assembly prior to application *in vivo*, resultant stability of PEG-modified oligonucleotide-GNP suprastructures indicates that with suitable preservation, it could potentially be possible to preserve sensitive recognition sequences, either through surface modification or alternative strategies such as encapsulation within therapeutic delivery systems (discussed in section 1.3.3).

1.3 Biological considerations relating to nanomaterials

Application of nanotechnology within medicine has offered unparalleled opportunities to improve the way we currently diagnose, monitor and treat numerous diseases. Besides the advantage that nanomaterials are inherently small, display useful properties for practical applications and can be easily modified to optimise their functionality and performance, they can also potentially be engineered to interact with specific biological components, down to a subcellular scale[44]. Whilst understanding interactions between nanomaterials and biological systems is critical for the rational design of therapeutic nanosystems, safety is a fundamental concern that must also be given due consideration. As the application of nanomaterials within medicine and biology has increased, so has the attention towards the outcomes of human exposure and the potential for adverse effects on normal physiology. Since nanomaterials display unique physicochemical properties, predicting their performance and consequences on human health can be challenging[123]. Furthermore, with an increasing desire to functionalise different nanomaterials and provide them with ever complex capabilities, additional parameters may arise which could further influence biological consequences. With evidence suggesting that a biological response to a nanomaterial is likely to be dependent on their functionality and application[124], no individual material should be considered inherently hazardous or particularly safe[123,125,126]. Accordingly, novel nanomaterials and complexes, including individual building blocks and their self-assembled structures, which are intended for biomedical purposes should be assessed on a case-by-case basis, at an early stage, with experimental designs reflecting their proposed application[124].

1.3.1 Biocompatibility of nanomaterials

Biocompatibility is a term typically applied to describe both beneficial and adverse effects and subsequent events that may arise because of a materials interaction within the human body. Defined by IUPAC, biocompatibility is regarded as the ability of a material to perform with an appropriate host-response within a specific situation. This in turn reflects how a material will

interact within a biological system and ultimately how these interactions will determine clinical success[127]. There are several key factors that must be considered when determining biocompatibility using *in vitro* or *in vivo* testing. Firstly, nanomaterial biocompatibility is highly dependent not only on inherent physicochemical properties, but also on the biological components encountered. For instance, Sohaebuddin *et al* extensively investigated nanomaterial toxicity by quantifying the generation of reactive oxygen species (ROS), intracellular vacuolic destabilisation (lysosomes) and mitochondrial permeability on three dissimilar cell models (fibroblasts (3T3), macrophages (RAW 264.6) and epithelial cells (hTERT-CBECs))[128]. Conclusions of this study show that cellular responses can be both nanomaterial and cell-type dependent, resulting in unique alterations of cellular functions that ultimately determine the extent of toxicity and cellular fate[128]. Secondly, whilst morphological, topographical and chemical characteristics of a nanomaterial are considered contributing parameters[129-131], inherent properties alone will not appropriately determine a materials biocompatibility. Highlighting the complex nanomaterial-biological responses that can occur, Zhang *et al* investigated the size-dependent toxicity of GNPs surface modified with PEG-SAMs, administered to mice over 28 days. Results showed that exposure to 10nm NPs induced an immune response, which increased white blood cell counts, whilst 5nm and 30nm NPs resulted in a reduction in both white and red blood cell counts, potentially owing to interference with the hematopoietic system[132]. Furthermore, in the same study heightened levels of alanine transaminase and aspartate transaminase, biochemical markers that indicate damage to the liver[132], were detected after systematic exposure to 10nm and 60nm GNPs. In contrast, 5nm and 60nm NPs did not appear to induce any noticeable liver damage[132], indicating that there was no size-dependent toxicity trend for the PEG modified GNPs utilised in this particular *in vivo* study. Thirdly, length of nanomaterial exposure time within a biological system can have a significant influence on biocompatibility, as shown by Lin *et al.* This group investigated the effects of exposure time to 15 nm silica nanoparticles (SiO_2) on a human lung cancer cell model after a period 24 and 72 hours; by monitoring indicators of oxidative stress (ROS and glutathione), lipid peroxidation (malondialdehyde) and cell membrane damage (lactate

dehydrogenase). A significant increase in cytotoxicity was seen after 72 hours compared to 24 hours[133]. Lastly, owing to the potential for numerous contributing factors, including severity of a particular disease or condition, a nanomaterials biocompatibility should be considered as situation-dependent, reflecting a risk-to-benefit ratio[134]. Accordingly, risk assessments need to be made for each type of nanomaterial being considered for a specific medical application or purpose, to determine the likelihood of achieving a predictable, safe and suitable outcome.

1.3.2 Toxicity at the nanoscale

Preliminary *in vitro* assessment of nanomaterial-associated toxicity is an essential step before *in vivo* models and clinical trials can be considered; for safety and ethical reasons[135,136]. Toxicity is generally described as a measure of harm a substance produces to a living organism and any substructures such as cells and organelles (cytotoxicity), which could arise from processes such as cellular uptake, bioaccumulation, disruption to cell signalling, production of reactive by-products, immunogenicity or carcinogenicity[137,138]. Significant attention has been given to the potential for nanomaterials to produce toxic effects, since it was realised that inert bulk materials such as gold, frequently appear increasingly bioactive when they display nanoscale dimensions[139]. This situation is further complicated by the fact that different nanomaterials and applications appear to result in variable biological responses[140]. In addition to physical and chemical attributes both potentially contributing to toxicity displayed by nanomaterials, their small sizes often also permit enhanced mobility within biological systems[140]. This has led to considerable concern regarding unregulated access to unintentional locations within whole organisms and at a sub-cellular level[140,141]. Whilst underpinning mechanisms of toxicity are not yet fully understood and are conceivably different for each dissimilar type of nanomaterial, several trends have started to emerge[142]. For example, a wide range of metallic NPs, including gold, have been shown to trigger the production of free radicals and reactive oxygen species (ROS) when internalised within cells, contributing to oxidative stress

and localised inflammation resulting in membrane, protein or DNA disruption and damage[143]. Such mechanisms can often be related to high surface areas displayed by these nanomaterials, which can result in enhanced reactivity, a characteristic that has been widely shown to promote interactions with cellular processes and contribute to cytotoxicity[144].Similar to how NP surfaces are coated with SAMs to achieve a desired functionality, ligands can also be utilised to modify resultant surface properties of nanomaterials to improve biocompatibility and reduce toxicity by providing favourable pharmacokinetic properties[145-148]. On the contrary, surface molecules used to acquire functionality can also contribute towards toxicity displayed by nanomaterials. For example, it has been shown that GNPs functionalised with cetyltrimethylammonium bromide (CTAB), a ligand widely used during synthesis to achieve colloidal stability and induce shape-control, are significantly toxic, yet CTAB alone in solution at the same concentration is relatively well tolerated[149,150]. Considering the diverse range of molecules that can be attached to nanomaterials to alter their chemistry and the fact that their impact on biological systems is still not fully understood[151], it should be assumed that there is a potential to either increase or decrease associated toxicity, necessitating comprehensive nanomaterial characterisation as well as standardised toxicity assessment[152].

Whilst at present there are no studies that have specifically investigated toxicity arising from activity of *in situ* self-assembly or SANs within biological systems, current understanding of the influence of particle dispersion and agglomeration of nanomaterials on resultant toxicity offers some insight. Owing to this gap in knowledge regarding the potential influence of *in situ* self-assembly of nanomaterials within biological systems, experimental designs will need to reflect the need to evaluate both individual building blocks and suprastructures, as depicted in Figure 1.6.

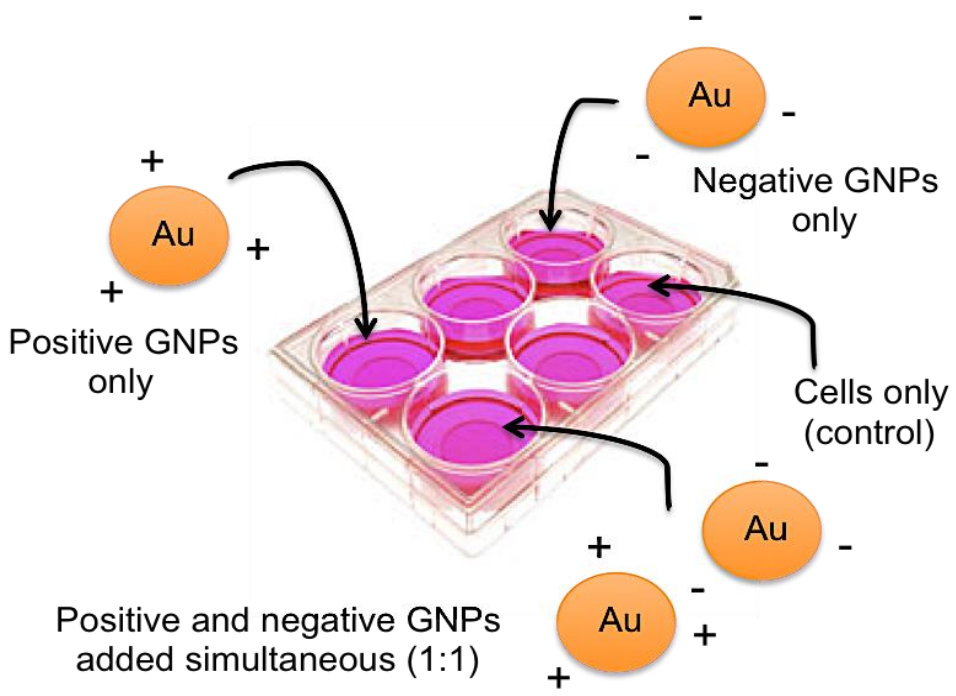

Figure 1.6 Proposed *in vitro* experimental design to evaluate the potential toxicity of individual GNP building blocks and as they undergo *in situ* self-assembly to form suprastructures. (*Original image*.)

When individual nanomaterials, analogous to building blocks, are dispersed in biological mediums they can interact or adsorb a range of biomolecules such as proteins, electrolytes and lipids to form a "biological corona"[154,155], effectively increasing their size and modifying surface characteristics[153]. Accordingly, different biological environments can result in variable surface modifications to nanomaterials, an effect that has been evidenced to produce differing toxic manifestations for the same NPs when dispersed in different biological mediums[155]. To explain this behaviour, Lesniak *et al* exposed silica NPs with an absence or presence of pre-formed protein coronas to human lung epithelial carcinoma cells (A549), in serum-supplemented (10%) and serum-free culture medium. It was subsequently shown that formation of protein coronas, in addition to the composition of available biomolecules within the local environment can significantly influence NP uptake, internalisation and subsequent intracellular distribution[156]. The situation appears to be equally complex for NPs that undergo agglomeration or aggregation in biological mediums, which could potentially reflect self-assembling suprastructures. Albanese *et al* prepared individually dispersed and aggregated GNPs modified with transferrin-SAMs, exposing them to three

dissimilar cell lines (an immortalised human cervical carcinoma (HeLa), lung epithelia carcinoma (A549) and a human breast carcinoma (MDA-MB 435))[157]. It was concluded from this study that whilst GNP aggregates did not produce a unique toxic response, cellular uptake was markedly different with a 25% reduction in cellular uptake compared to individual GNPs in HeLa and A549 cell models[157]. Conflictingly however, a 2-fold increase in uptake was shown for aggregates in the MDA-MB 435 cell line[157]. In another study, Gosens *et al* prepared 50 and 250 nm GNPs in a dispersed and agglomerated state and administered them directly into the lungs of rats at a concentration of 1.6 mg/kg body weight, before extracting bronchoalveolar lavage fluid and blood at 3 and 24 hours post-exposure[158]. Assessments of pulmonary inflammation, cell damage and cytotoxicity subsequently showed there was no significant difference in biological response *in vivo* either locally (lungs) or systemically, which is in contradiction to results obtained by Albanese *et al* under *in vitro* conditions[158]. These studies emphasise our limited understanding of how different NP dispersions and arrangements can influence toxicity within various biological scenarios, highlighting a necessity in the current work to rationally design comprehensive experiments that evaluate both individual building blocks and *in situ* self-assembling suprastructures (Figure 1.6.)

1.3.3 Multifunctional nanosystems for therapeutic delivery

Analogous to the delivery of traditional drug entities, targeted and “smart” delivery strategies for effective application of nanomaterials are of considerable current interest[159-161]. Within the field of therapeutic delivery, traditional approaches and nanotechnology have merged with a focus towards designing multifunctional platforms that not only effectively deliver therapeutic drugs and nanomaterials but also perform a range of tasks as and when required[162,163]. Putting multifunctional nanosystems into context (Figure 1.7) multiple features could be designed into a single construct. This could provide an inert “carrier” system that enables targeting capabilities to reach a specific site of disease, subsequently releasing therapeutic agents and permitting *in vivo* imaging and sensing capabilities in a responsive manner[164]. At present a

diverse range of nanoscale delivery strategies are under development, which include technologies based on lipid (liposomes)[165], polymer (polymersomes)[166] and carbon (fullerenes) systems[167] amongst numerous others[168]. Liposomes, which feature in the current study, represent one of the most clinically established nanoscale lipid-systems[169], having been first reported in the 1960s by A.D. Bangham and R.W. Horne[170] and successfully reaching market for the first time in 1995 with the development of the PEGylated liposomal formulation Doxil®[171]. Liposomes, which are essentially closed-lipid bilayers that constitute a vesicular structure with an internalised aqueous compartment, have been extensively investigated for the targeting of drugs and therapeutics to a specific site of action *in vivo*, often in an attempt to improve efficacy and safety[172].

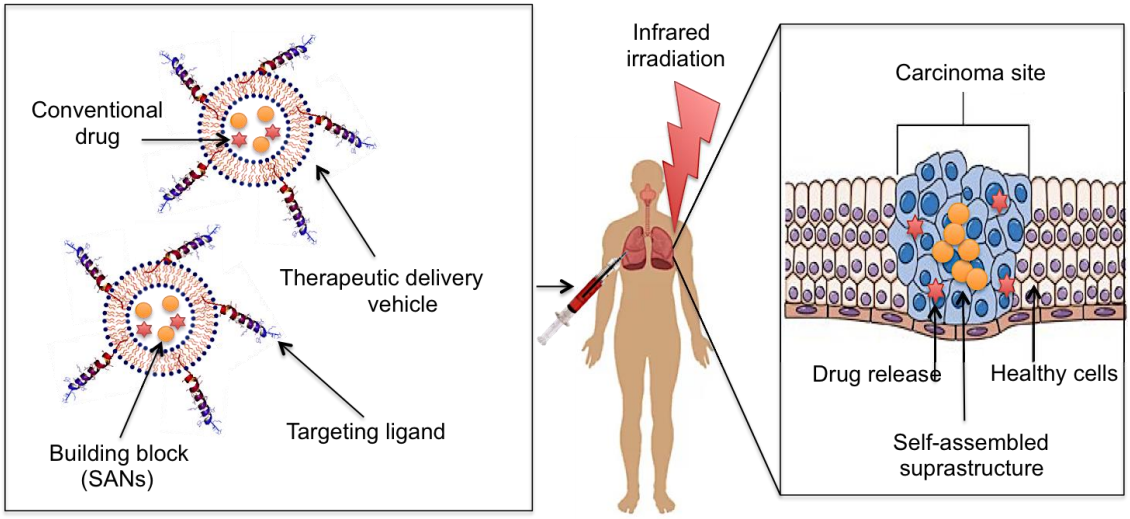

Figure 1.7 Representation of a multifunctional nanosystem with incorporated building blocks for targeted delivery of conventional drugs and SANs to a carcinoma, with subsequent self-assembly enabling infrared activated photothermal therapy specifically at the site of disease. (*Original image*).

Liposomes, like nanoparticles, can be surface modified to obtain a range of desirable properties, including the attachment of active targeting ligands (antibodies, peptides) and biologically inert molecules such as PEG to increase blood-circulation times by reducing uptake *via* the mononuclear phagocyte system (immune response)[173]. Additionally, liposomes can be designed to incorporate controlled-release mechanisms, either by utilising changes in the local environment of the target site (pH, enzyme upregulation) or by external stimuli (light, heat, ultrasound)[174]. Considering that lipids utilised

to formulate liposomes have specific melting properties and GNPs can convert light to localised heat, it was not unexpected that these technologies have been combined. Guohui *et al* provides demonstration of this principle, having incorporated GNPs into a liposomal formulation to enable remote-controlled drug release upon irradiation with infrared light[175]. Underpinning this work, it was proposed that rapid increases in GNP temperature triggered destabilisation of the liposomes, with drug release occurring within a timeframe of just a few seconds[175]. Looking towards implementing multifunctionality, Rengan *et al* investigated liposome-GNP constructs for infrared activated PPTT treatment, evidencing highly effective cancer obliteration on breast carcinoma cells (MDA-MB-231) whilst also enabling direct imaging capabilities[176]. Interestingly, it was also recently shown that GNPs can be confined within liposomes to induce plasmonic coupling properties (as described in section 1.1.2.2); Chen *et al* encapsulated GNPs modified with oligonucleotide-SAMs within liposomes, with a change in pH from 8 to 4 triggering hybridisation between adjacent GNPs and a change in plasmonic properties, suggesting that this responsive behaviour could have implications for biochemical sensing and *in vivo* imaging techniques[177]. Furthermore, the fact that individual oligonucleotides on the surface of GNPs could hybridise within these liposomes, indicates that such a strategy could potentially be used to isolate and preserve the surface of sensitive nanomaterials, such as those used to facilitate molecular recognition self-assembly (as discussed previously in section 1.2.1.2).

Currently there does not appear to be any reports of utilising liposomes or similar technologies for either delivery or control of self-assembling nanomaterials. Whilst individual functional GNPs that have been evidenced as effective building blocks for self-assembly have been encapsulated separately within PEGylated liposomes as a proof-of-concept[165], future work is required to determine whether this concept could be utilised to trigger self-assembly or prevent self-assembly until required.

1.4 Aims and objectives of the thesis

The work presented in this thesis was inspired by the late Nobel physicist Richard P. Feynman, who introduced the vision of nanotechnology “there’s plenty of room at the bottom”, promising the inevitable realisation of atomic scale machines[178].

GAP IN KNOWLEDGE:
Before SANs and associated mechanisms can predictably and safely be applied towards effective *in situ* self-assembly within biological systems, a fundamental understanding of the basic principles and experimental framework is required. The current study aims to fulfil this gap in knowledge by establishing rudimentary strategies towards self-assembly of GNPs as models for SANs. Subsequent investigations will then be designed to ascertain potential toxicity concerns and assess how *in situ* performance translates from pre-defined aqueous conditions into biological fluid and *in vitro* cell models.

RESEARCH QUESTIONS:
Addressing the identified gap in knowledge, research questions emerge regarding the application, behaviour and fate of SANs within biological systems and how experimental framework can be designed to enable reliable evaluation.

I. Can suitable SANs for investigating mechanisms of self-assembly be easily prepared using currently available methods? If so, do different mechanisms towards self-assembly result in the fabrication of dissimilar suprastructures; are they representative of either structural agglomerates or aggregates?

II. Considering recent trends towards designing multifunctional nanosystems, which could incorporate SANs in the future, could established therapeutic delivery systems be utilised to encapsulate individual building blocks?

III. Is there a potential associated risk of toxicity related to the process of *in situ* self-assembly within biological systems? Do different toxic responses arise between individual building blocks and self-assembled suprastructures?

IV. Does the self-assembly activity of SANs facilitated by different mechanisms persist within biological conditions? Are currently established approaches of cellular evaluation sufficient to assess the activity of SANs *in vitro* and can they confidently differentiate between unassembled building blocks and self-assembled suprastructures intracellularly?

RESEARCH AIMS AND OBJECTIVES:

The aim of the current study is to prepare SANs for *in situ* activity within biological systems and evaluate the effectiveness of electrostatic interactions and molecular recognition as different mechanisms towards facilitating self-assembly. GNP building blocks and their self-assembled suprastructures will be prepared and characterised with subsequent *In vitro* studies designed towards furthering current understanding of how *in situ* self-assembly could influence biological outcomes. To address the primary aim, SANs will be studied under representative biological conditions, evaluating individual building blocks and their self-assembled counterparts., Investigations will then be undertaken to determine whether intracellular self-assembly can be reliably evaluated using currently established protocols, identifying limitations and providing experimental framework for future investigations.

To address research questions and fulfil the stated aims, the following objectives were proposed as key investigative milestones within the current work:

I. Prepare and characterise GNP building blocks functionalised to facilitate self-assembly either via electrostatic interactions or molecular

recognition with subsequent characterisation of self-assembled suprastructures.

Owing to a lack of consistency regarding the characterisation of self-assembled suprastructure morphology, microscopy will be used in Chapter 3 to accurately evaluate the size and morphology of individual building blocks and ensuing suprastructures. This will determine whether they are representative of structural agglomerates or aggregates, additionally verifying whether electrostatic interactions and molecular recognition are effective strategies towards self-assembly.

II. Ascertain a synthetic strategy for the formulation of a delivery system containing GNP building blocks, with subsequent characterisation and quantification of encapsulated SANs.

The current work will provide a proof-of concept using functional GNPs as model SANs to encapsulate within liposomes. In Chapter 4, established techniques of liposome preparation will be used whilst exploiting electrostatic interactions between oppositely charged lipids and GNP building blocks. Microscopy combined with elemental analysis will be used to precisely evaluate the distribution of gold within liposomes, with validated methods applied to quantify encapsulated gold and liposomal lipid concentrations.

III. Determine whether the process of *in situ* self-assembly and resultant suprastructure fabrication results in a different toxic response compared to the individual GNP building blocks.

Whilst these fundamental principles could possibly be related to current understanding of how nanoparticle agglomeration and aggregation influences toxicity, this has not yet been established. An *in vitro* study comprising a lung fibroblast model and biochemical assays (MTT & LDH) will be applied in Chapter 5 to identify potential differences in cytotoxicity. Experimental designs will reflect the recognised necessity to evaluate both individual building blocks and resultant *in situ* self-assembling suprastructures.

IV. Evaluate the efficacy of electrostatic attraction and molecular recognition as mechanisms towards facilitating self-assembly of GNP building blocks under biological conditions. Determine whether intracellular self-assembly can be reliably evaluated using current analytical approaches and identify limitations to provide scope for future investigations.

Identifying effective mechanisms of self-assembly and critically analysing analytical approaches is fundamental to the development of SANs for *in situ* biological applications. In Chapter 6, self-assembly of GNP building blocks will initially be tested within a biologically relevant medium. Resultant suprastructure morphology and hydrodynamic sizes will be evaluated and compared to self-assembly of GNP building blocks under aqueous buffer conditions. This will reveal any potential bio-complex formation and assert whether mechanisms established in the current work towards self-assembly of SANs could be effective within biological systems. Based on these results a mechanism will be chosen for *in vitro* studies on a carcinoma cell model. Cellular specimens exposed to individual building blocks and as they undergo *in situ* self-assembly will be preserved and thin-sectioned for subsequent microscopy and elemental analysis according to previously established protocols. Corresponding results will be used to evaluate any potential intracellular self-assembly and critically assess the capability of current techniques to reliably interpret whether individual SANs have persisted to self-assemble *in vitro*.

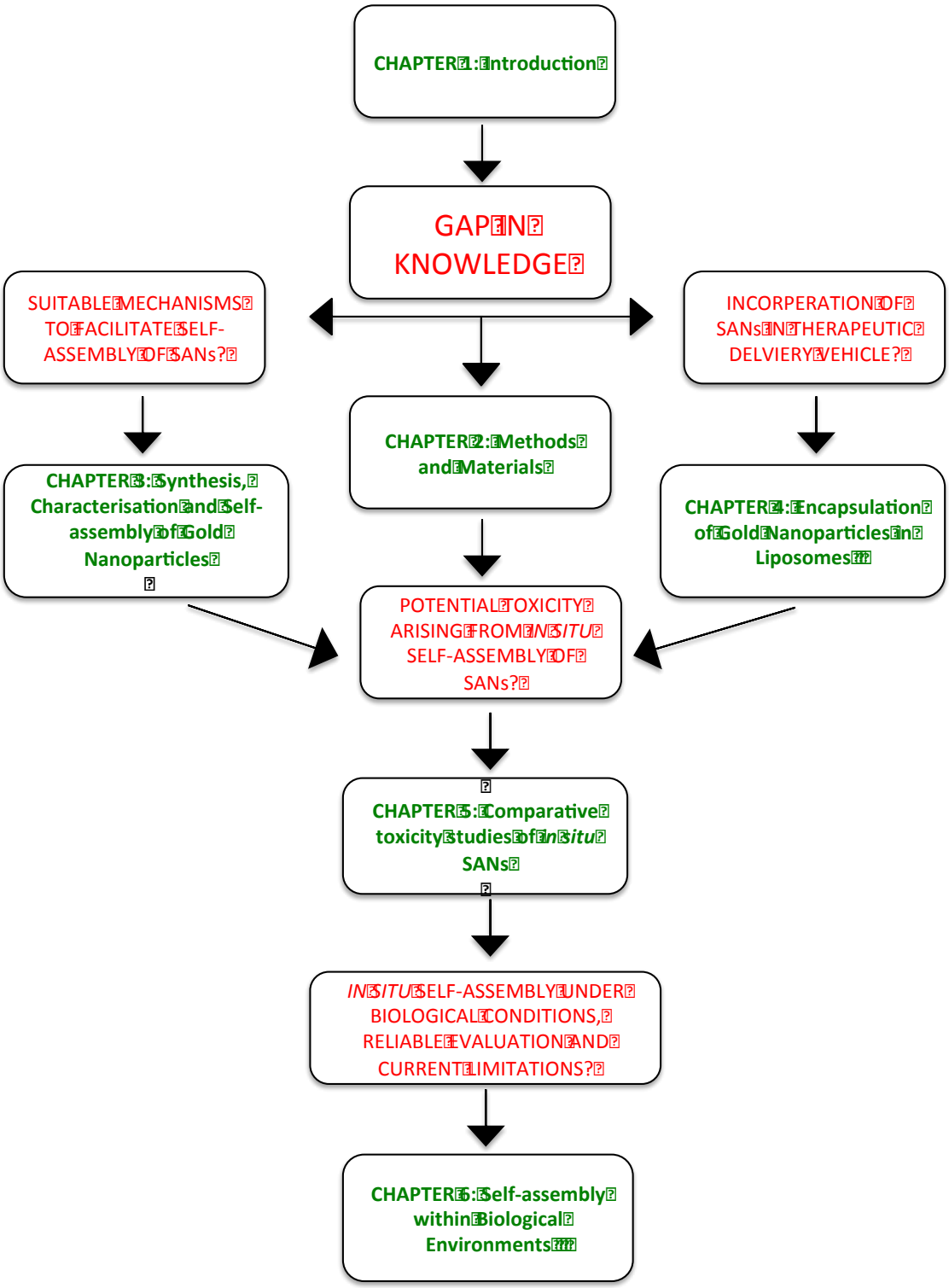
CHAPTER 1: Introduction
GAP IN KNOWLEDGE
SUITABLE MECHANISMS TO FACILITATE SELF-ASSEMBLY OF SANs?
INCORPERATION OF SANs IN THERAPEUTIC DELVIERY VEHICLE?
CHAPTER 2: Methods and Materials
CHAPTER 3: Synthesis, Characterisation and Self-assembly of Gold Nanoparticles
CHAPTER 4: Encapsulation of Gold Nanoparticles in Liposomes
POTENTIAL TOXICITY ARISING FROM *IN SITU* SELF-ASSEMBLY OF SANs?
CHAPTER 5: Comparative toxicity studies of *in situ* SANs
IN SITU SELF-ASSEMBLY UNDER BIOLOGICAL CONDITIONS, RELIABLE EVALUATION AND CURRENT LIMITATIONS?
CHAPTER 6: Self-assembly within Biological Environments

2 Materials and Methods

2.1 Materials

Unless otherwise stated in described methods all materials were used as purchased without prior modification. Details of reagents, consumables and suppliers are summarised below.

Reagents and consumables	Suppliers
AGAR 100 Resin Kit	Agar Scientific, UK.
Aluminium specimen stubs (12.5 mm)	Agar Scientific, UK.
Bromothymol blue (95%)	Sigma-Aldrich, UK
Carbon Formvar coated 200 mesh copper TEM specimen grids	Agar Scientific, UK.
Custom-made oligonucleotides with 5'-thiol modification	ATDBIO LTD, UK.
CytoTox 96® Non-radioactive cytotoxicity kit	Promega Corp. UK.
2-(dimethylamino)ethanethiol hydrochloride (95%)	Sigma-Aldrich, UK.
1,2-dipalmitoyl-*sn*-glycero-3-phosphocholine (99%)	Avanti Polar Lipids, USA
1,2-dipalmitoyl-*sn*-glycero-3-phosphoethanolamine-N-[methoxy(polyethylene glycol)-5000] (DPPE-PEG5000) (99%)	Avanti Polar Lipids, USA.
1,2-dipalmitoyl-*sn*-glycero-3-phospho-(1'-*rac*-glycerol) (99%)	Avanti Polar Lipids, USA
1,2-dipalmitoyl-3-trimethylammonium-propane (99%)	Avanti Polar Lipids, USA
Dulbecco's modified eagle medium, high glucose (4.5 g/L) without phenol-red	ThermoFisher, UK
DL-dithiothreitol (>99%)	Sigma-Aldrich, UK
Ethanol (anhydrous >99.5%)	Sigma-Aldrich,UK
Ethylene glycol (99.8%)	Sigma-Aldrich, UK
Eppendorf® Biopur® safe-lock (1.5 ml) microtubes	Sigma-Aldrich, UK
Fetal bovine serum, heat inactivated	GE Healthcare, UK
FisherBrand® 4 mL single use UV cuvette	ThermoFisher, UK
FisherBrand® microcentrifuge tubes (1.5 ml)	ThermoFisher, UK
Hydrochloric acid (37%)	Simga-Alrdich, UK
Hydrogen tetrachloroaurate trihydrate (99.9%)	Sigma-Aldrich, UK
Isopropanol (>99.7%)	Sigma-Aldrich, UK.
Nalgene™ OakRidge polycarbonate centrifuge tube (30 ml)	ThermoFisher, Germany
Nitric acid (70%)	Sigma-Aldrich, UK.

Nunc® CryoTube™ vials	ThermoFisher, UK.
Nunc™ delta surface treated 12-well multidishes	ThermoFisher, UK.
Nunc™ delta surface treated 96-well multidishes	ThermoFisher, UK.
Nunc™ delta surface treated T75 tissue culture flask	ThermoFisher, UK.
Osmium tetroxide (100 mg) in sealed ampules	Sigma-Aldrich, UK.
Phosphate buffer solution (0.1 M, pH 7.4)	Sigma-Aldrich, UK.
Platinum Blue dye (Pt4N8H6O24C20)	Nisshin EM Corp., Japan.
Polystyrene polymer spheres in suspension (21nm) NIST™ traceable size standard	Brookhaven Instruments Corporation, USA.
Prepacked NAP-25 columns – (DNA grade)	GE Healthcare, UK.
Propylene oxide – (ReagentPlus® 99%)	Sigma-Aldrich, UK.
Sephadex G100 gel media (superfine)	Sigma-Aldrich, UK.
Silicon polished wafer mounts (5× 5 mm)	Agar Scientific, UK.
Sodium borohydride (98%)	Sigma-Aldrich, UK.
Sodium 2-mercaptoethanesulfonate (>98%)	Sigma-Aldrich, UK.
Sodium cacodylate trihydrate (BioXtra >98%)	Sigma-Aldrich, UK.
Syringe filters, cellulose acetate (0.45 μm) Corning®	Sigma-Aldrich, UK.
Tetraoctylammonium bromide	Sigma-Aldrich, UK.
Thiazolyl blue tetrazolium bromide	Sigma-Aldrich, UK)
Triphenylphosphine (TPP) (>98.5%)	Sigma-Aldrich, UK.
Trisodium citrate dihydrate (>98%)	Sigma-Aldrich, UK.
Triton X-100™	Sigma-Aldrich, UK.
Water sterile-filtered suitable for cell culture Whatman®	Sigma-Aldrich, UK.
Nucelpore™ track-etched polycarbonate membranes (diameter 13 mm, pore size 0.2 μm)	Sigma-Aldrich, UK.
Zeta disposable capillary cell (DTS1070)	Malvern Instrument, UK.
Zeta potential transfer standard (68 mV)	Malvern Instrument, UK.

2.2 Methods

2.2.1 Nanoparticle synthesis

Preparation of spherical gold nanoparticles (GNPs) was achieved by direct wet chemical synthesis procedures employing the methods of Turkevich[179] and Brust[180]. Modification of nanoparticle surface-functionality was attained by post-preparative interfacial ligand exchange reactions with thiol (SH) containing compounds according to previous reports[181,182]. Gold nanoparticles displaying specific shaped morphologies were synthesised either by direct or seed-mediated approaches according to previously published methods[183-185].

2.2.1.1 Synthesis of GNPs surface functionalised with ionic ligands

Preparation of triphenylphosphine GNPs:

Gold nanoparticles surface-stabilised with phosphine anions (TPP-GNPs) were prepared by a modified Brust method[186]. Using glassware, hydrogen tetrachloroaurate trihydrate (0.25 g, 0.64 mmol) and tetraoctylammonium bromide (TOAB) (0.4 g, 0.73 mmol) were dissolved in nitrogen (N_2) sparged water-toluene (13 ml/17 ml) mixture. After approximately 20 minutes under vigorous stirring, the gold colour visually transferred from the aqueous into the organic phase (bottom) and triphenylphosphine (0.58 g, 2.2 mmol) was added. The reaction vessel was then purged with cycles of vacuum and flushing with nitrogen ($N_{2)}$ before sealing. A freshly prepared aqueous sodium borohydride solution was prepared by dissolving (0.35 g, 9.4 mmol) in 10 ml of distilled water. This solution was injected directly into the organic phase triggering a rapid colour change to dark purple and the mixture was stirred for a further 3 hours. The organic phase was isolated with a pipette, washed with distilled water (3×100 ml) and dried under vacuum to yield a black solid. The product was further washed with a series of hexane (2×40 ml) and (2:3) water-methanol solution (3×40 ml) to remove the TOAB phase-transfer catalyst. GNPs were then precipitated from chloroform by step-wise addition of pentane to remove any unreacted materials.

Ligand-exchange reactions:

Phosphine on the surface of GNPs was exchanged with the anionic 2-mercaptoethanesulfonate (MES) or cationic 2-(Dimethylamino)ethanethiol (DMET) ligands according to an established method[181]. Using a round-bottom flask, TPP-GNPs (20 mg) were suspended in dichloromethane (4 ml) and the reaction vessel was purged by cycles of vacuum and flushing with argon (Ar) before sealing. Aqueous solutions of either MES (10 mg / 2 ml) or DMET (40 mg / 3ml) were then added at once under vigorous magnetic stirring by injecting into the GNP suspension using a glass syringe. Reactions were then covered to protect from light and stirred for 4 hours at room temperature, at which point the brown colour had visually transferred from the organic into the aqueous phase (top). The coloured fraction was isolated with a pipette, washed with dichloromethane ($\times$ 3) and GNPs were recovered by ultracentrifugation (Thermo Scientific, Sorvall WX90, rotor: T865) at 200,000 $\times$ g for 30 minutes. The products were then suspended in ethanol and precipitated by step-wise addition of hexane, repeating centrifugation and washing procedures a further three more time to remove any unattached ligands. After drying under vacuum, GNP powders were dispersed in deionised water at a concentration of 1 mg / ml and stored at 4°C. For clarity, GNPs functionalised with DMET are subsequently referred to as “positively charged gold” (PCG) and those functionalised with MES “negatively charged gold” (NCG).

2.2.1.2 Synthesis of GNPs surface-functionalised with oligonucleotides

Preparation of citrate-stabilised GNPs:

A previously described modified Turkevich method was used to prepare ~20 nm citrate-stabilised GNPs[187]. Using glassware, hydrogen tetrachloroaurate trihydrate (20 mmol, 0.7876 g) was dissolved in distilled water (1 L) to provide a 2 mM stock solution. An aliquot (200 ml) was heated on a mantle to near boiling (~ 95°C) under vigorous magnetic stirring to prevent refluxing conditions. Trisodium citrate (1.6 mmol, 0.4705 g) was dissolved in a minimal amount of distilled water, heated on a mantle to approximately 70 °C and injected directly into the gold solution using a glass syringe. A colour change from yellow to red

was observed within 15 minutes at which point the mixture was cooled to room temperature. The product was washed with 2 mM aqueous sodium citrate solution and isolated by centrifugation at 4000 $\times$ g for 10 minutes, repeating centrifugation and washing procedures a further three more times. Recovered GNPs were suspended in further 2 mM sodium citrate solution and stored at 4 °C.

Commercially available ~5 nm citrate-stabilised spherical GNPs in suspension (Sigma-Aldrich, UK) were diluted in (2 mM) sodium citrate buffer (1:1 v/v) and stored at 4 °C before subsequent functionalisation with oligonucleotides

The approximate concentration of the prepared and commercially supplied citrate-GNP suspensions were determined spectrophotometrically (λ =522 nm) using estimated extinction coefficient values for GNPs of corresponding sizes according to a previous report[182]. See section 2.2.3.6 for a detailed explanation on ultraviolet-visible spectroscopy. Further dilutions were carried out as required with 0.5 mM aqueous sodium citrate solution to provide final concentrations of 5 nM. It should be noted that approximate concentrations are sufficient for this protocol because subsequent functionalisation of GNPs with oligonucleotides is carried out under excess conditions.

Preparation of oligonucleotides:

Two custom-made complementary single-strand oligonucleotides (ATDBio Ltd., UK) with a length of 20-units and possessing 5'-terminus thiohexyl (SH-$(CH_2)_6$-oligo) modifications were supplied as lyophilised powders (5'-TTTTTTTTCATGACGTCATG and 5'-TTTTTTTTGTACTGCAGTAC). To avoid oxidation and resultant dimer formation, the thiohexyl group was supplied protected with a disulphide linkage (R-S-S-$(CH_2)_6$-oligo). Working under aseptic conditions in a laminar airflow cabinet, according to manufacturer instructions, the contents of supplied vials were dissolved in distilled water to provide 200 µM stock solutions. Solutions were then accurately divided into 100 µl aliquots in sterile microtubes and snap-frozen by submerging in liquid nitrogen for 1 minute, before storing at -20 °C until required. Aliquots of oligonucleotide stock solution were thawed on the day of use in a water bath at 25 °C. To remove the

disulphide linkage 125 µl of a 100 mM dithiothreitol (DTT) solution in 50 mM sodium phosphate buffer (pH 8.5) was added to each aliquot and the mixtures stirred on an orbital shaker (Elmi Sky Line Analog Orbital Shaker, Cole-Parmer, UK) at 60 rpm for one hour. Oligonucleotides were then isolated by column chromatography on a Sephadex® G-25 gel column (illustrata NAP-25 prepacked columns, GE Healthcare Life Sciences, UK) with phosphate buffer (50 mM, pH 8.5) as eluent. Fractions (1 ml) were collected and combined if they contained oligonucleotide, as identified spectrophotomerically (λ = 260 nm). The Beer-Lambert equation was applied to determine the resultant concentration of the oligonucleotide using the manufactures stated molar extinction value (1.807×10^5 $M^{-1}cm^{-1}$).

Attachment of oligonucleotides to GNPs

To prepare GNPs with a dense surface coverage of oligonucleotide (oligo-GNPs) the reaction was carried out in excess according to a previous established protocol[182]. The minimum quantity of oligonucleotide required was calculated by multiplying its expected surface density by the average GNP surface area:

Equation 2.1. Quantity of oligonucleotide required

$$moles\ of\ oligonucleotide = (A_n \times C_n \times D_o \times V)$$

Where:

A_n = Average surface area of GNP ($4 \times \pi \times \text{particle radius}^2$)

C_n = GNP concentration (from section 2.2.1.3) in one litre

D_o = Expected oligonucleotide density per particle

V = Volume of GNP suspension in litres

The value of D_o is approximated to 35 pmol/cm^2 as previously reported[182], reflecting the experimentally observed density of short-chain oligonucleotides on GNP surfaces[188]. The final quantity of oligonucleotide used in the attachment was twice the minimum calculated value (2×.molar excess.)

Working in dedicated, sterilised ultracentrifuge tubes, 5 ml of synthesised (~20 nm) and commercially supplied (~5 nm) citrate-stabilised GNP suspensions (5

nM) were combined with an excess quantity of oligonucleotide (calculated in previous step). Protected from light, the mixtures were rotated on an orbital shaker at 60 rpm for 16 hours. Sodium chloride (1 M) and sodium phosphate buffer (0.1 M) were added (0.5 ml each) and the mixtures was further mixed for 24 hours. Resultant GNPs were isolated from excess oligonucleotide by ultracentrifugation at 60,000 $\times$ g for 1 hour and then washed in sodium chloride (0.1 M) / sodium phosphate (10 mM) buffer (1:1 v/v), repeating centrifugation and washing procedures a further three more times. The final products were suspended in 5 ml of buffer mixture with sodium azide (0.01%), protected from light and stored at 4°C.

2.2.1.3 Synthesis of rod-shaped GNPs

Gold nanorods (GNRs) were prepared according to a previously reported seed mediated growth method utilising a shape directing additive, cetyltrimethylammonium bromide (CTAB)[183]. Using glassware, 10 ml of aqueous hydrogen tetrachloroaurate trihydrate (1mg, 0.0030 mmol) was combined with CTAB (0.37g, 1 mmol) and 0.5 ml of freshly prepared ascorbic acid solution (8.8 mg, 0.05 mmol). Commercially available ~5 nm citrate-stabilised spherical GNPs in suspension (50 µl) (Sigma-Aldrich, UK) were injected into the aqueous mixture, triggering a colour change to reddish-brown within 5 minutes. The reaction mixture was then allowed to stand at room temperature for 1 hour, without any stirring. To isolate GNRs, the resultant suspension was centrifuged at 4,000 $\times$ g for 10 minutes. The supernatant was discarded and the pelleted product was resuspended in 50:50 water:methanol (5 ml). before isolating by centrifugation again to remove excess CTAB. The final product was then suspended in distilled water at a concentration of 0.4 mg/ml.

2.2.1.4 Synthesis of triangle-shaped GNPs

Gold nanotriangles (GNTs) were prepared according to a previous report which utilises a modification of the Turkevich method in the presence of potassium

chloride[184]. Using glassware, 90 ml of aqueous hydrogen tetrachloroaurate trihydrate (4 mg, 0.01 mmol) was combined with potassium chloride (0.8 mg, 0.01 mmol) and 10 ml of freshly prepared citric acid solution (19.2 mg, 0.0118 mmol). The reaction vessel was then protected from light and heated to 30ºC for 12 hours. To isolate GNTs, the resultant suspension was repeatedly ($\times$ 3) centrifuged at 4,000 $\times$ g for 10 minutes, with the solid pellet resuspended in distilled water by sonication. The final product was then suspended in aqueous citric acid solution (10 μM) at a concentration of 1 mg/ml.

2.2.1.5 Synthesis of star-shaped GNPs

Gold nanostars (GNSs) were prepared according to a previously reported approach that uses silver ions as a shape directing additive[185]. Using glassware, 100 μl of aqueous hydrogen tetrachloroaurate trihydrate(1mg, 0.0030 mmol) was combined with 100 μl of aqueous silver nitrate (17 μg, 0.1 μmol) and 4.8 ml of distilled water. The mixture was sonicated for 5 minutes to achieve homogeneity before proceeding. Whilst mixing vigorously, 100 μl of aqueous ascorbic acid (88 mg, 0.5 mmol) was added at once, triggering a colour change from yellow to blue. After 2 minutes stirring was stopped and the reaction mixture was allowed to stand at room temperature for one hour. To isolate GNSs, the resultant suspension was repeatedly ($\times$ 3) centrifuged at 4,000 $\times$ g for 10 minutes, with the solid pellet resuspended in distilled water by sonication. The final product was then suspended in aqueous ascorbic acid solution (5 μM) at a concentration of 0.5 mg/ml.

2.2.2 Liposome formulation

Multilamellar liposomes containing encapsulated GNPs (GNP-lipo) were prepared by a newly developed multistep strategy that exploits electrostatic interactions between the two components (Chapter 4). Employing previously reported methods with modifications, reverse-phase evaporation (REV)[189] was used to initially formulate crude GNP-lipos. Liposomes were subsequently

processed by size-extrusion[190] and post-formulation lipid-PEG modification[191]. Un-encapsulated GNPs and excess reagents were then removed by size-exclusion chromatography[192].

Lyophilised lipids comprising anionic lipid composition 1,2-dipalmitoyl-*sn*-glycero-3-phosphocholine (DPPC) and 1,2-dipalmitoyl-*sn*-glycero-3-phospho-(1'-*rac*-glycerol) ($DPPG^{(-)}$) (molar ratio 6.1:0.7) or cationic DPPC and 1,2-dipalmitoyl-3-trimethylammonium-propane ($DPTAP^{(+)}$) (molar ratio 6.1:0.8) were dissolved in 2 ml of chloroform:methanol (2:1), providing a 2.5 mg/ml total lipid content. Aqueous suspensions of NCG and PCG (0.5 mg/ml) were then combined with lipid solutions of opposing charge (1:1 v/v). Mixtures were sonicated for 5 minutes to afford a white/brown emulsion. The biphasic suspensions were transferred to a rotary evaporator for gradual removal of the organic phase (1 hour at 50 °C/200 mbar). Resultant aqueous suspensions were diluted in PBS (0.01 M, pH 7.4) to provide a total lipid content of 1 mg / ml. Aliquots (1 ml) were sonicated for 30 seconds before heating on a mantle to 45 °C, which is above the melting transition temperature of the main lipid component, DPPC (41 °C). Atop a heated stage, suspensions were then passed repeatedly ($\times$ 15) through porous (200 nm) filter membranes utilising an “Avanti mini extruder system” (Avanti Polar Lipids, USA.) Aliquots were then either set-aside for purification or added immediately to 0.2 ml of preheated (50 °C) aqueous 1,2-dipalmitoyl-*sn*-glycero-3-phosphoethanolamine-N-[methoxy(polyethylene glycol)-5000] (DPPE-PEG5000) solution (0.01%). The temperature was maintained for 30 minutes before allowing liposomal suspensions to reach room temperature.

To isolate GNP-lipos, size-exclusion chromatography was performed on Sephadex®-G50 gel with PBS (0.01 M, pH 7.4) as eluent. Fractions were collected (1 ml) and the first five fractions identified to contain phospholipids by spot staining with bromothymol blue (pH 6, 10% aqueous-ethanol solution), were combined (5 ml) and stored in glass vials at room temperature whilst protected from light. For clarity, GNP-lipos prepared using DDPG lipids and NCG are subsequently referred to as “positively charged liposomes-negatively charged gold” (PCL-NCG) and those prepared from DPTAP and PCG “negatively charged liposomes-positively charged gold” (PCL-NCG).

2.2.3 Characterisation and analytical techniques

2.2.3.1 Transmission electron microscopy

Transmission electron microscopy (TEM) was utilised to investigate the configuration and state of dispersion of GNPs in addition to prepared GNP-lipos and cellular specimens. A fundamental technique for characterisation and analysis, TEM provides detailed information about morphology (i.e. size and shape), stability and internal ultrastructure such as cellular organelles193. The use of higher operating voltages (80 – 400 KeV) compared to other microscopy techniques delivers superior resolution, approaching atomic-scale[194]. It operates by accelerating electrons that are subsequently condensed by magnetic lenses to produce a high-energy beam that is transmitted through an ultra-thin specimen (< 100 nm)[195]. Resulting electron-specimen interactions are detected to produce magnified two-dimensional micrographs. The types of interactions that occur can broadly be categorised as transmission (un-scattered) and diffraction (scattered), with each being detected to produce different types of images. For the purpose of this project differences in transmission of the electron beam were detected at 180° (below the specimen). Distinctions in transmission and resultant image contrast arise depending on material-electron interactions, which vary depending on specimen-thickness and atomic mass of elements present[194]. Materials such as lipids do not contain elements of high atomic number, have low electron-interaction and display low image contrast. Overcoming this, negative staining techniques are applied to enhance the difference between material and surrounding background[196]. Specimens that are too large (i.e. biological samples) are thin-sectioned to display electron transparency. In addition, such samples must also be preserved and stabilised to withstand the intense conditions under the electron beam[197] (see section 2.2.6.5).

Routine observations were achieved on a JEOL-JEM1400 microscope (JEOL Ltd., Japan) with an operating voltage of 120 KeV. High-resolution (HRTEM) imaging was performed on a JEOL-JEM2200FS microscope (JEOL Ltd., Japan)

at 200 KeV. Formvar carbon coated square 400 mesh copper specimen grids were used as supplied for analysis of GNP specimens and were hydrophilised by glow discharge using a JEOL HDT-400 hydrophilic treatment device (JEOL Ltd., Japan) to study GNP-lipos. Aqueous dispersions of representative samples were pipetted directly onto grids, excess solution was wick dried after 10 minutes and specimens were air-dried for a further 30 minutes prior to analysis. Negative staining of samples was carried out by pipetting 50 µl of a platinum-based dye (Pt4N8H6O24C20) directly onto specimens and wick drying excess solution after 10 minutes. Biological samples were studied on a FEI-TALOS F200X S/TEM microscope (FEI Company, USA) operating at 80 or 200 KeV. For details on preparation of tissue specimens see section 2.2.6.5.

2.2.3.2 Scanning electron microscopy

Scanning electron microscopy (SEM) enabled the study of topographical features and compositions of specimen surfaces providing pseudo three-dimensional micrographs. A narrowly focused electron beam is applied across the surface of a specimen in a rectangular raster fashion. Electrons interact with atoms at varying depths throughout the sample producing various detectable emission signals[198]. Secondary electron (SE) emission occurs at or just below the surface of the specimen and can be detected to produce high-resolution images of sample topography. Back-scattered electron detection results from beam-electrons that are reflected from greater depths within the specimen. In each case, allocating pixels to the position and intensity of the detected signals forms the displayed micrograph[199]. Specimens must be electrically conductive at least at the surface for sufficient signal detection as well as to prevent accumulation of electrostatic surface-charge and thermally induced damage. Samples that do not display such properties are coated with a layer of conductive material by physical vapour deposition (PVD)[200]. Similarly to TEM, the vacuum conditions of the microscope make hydrated specimens unsuitable for analysis. To study aqueous colloids such as the prepared GNP-lipos in this project, samples are dehydrated by freeze-drying approaches[201].

Observations were carried out on a ZEISS-Sigma-300 field emission gun scanning transmission electron microscope (FEG-STEM) in SEM mode (Carl Zeiss Ltd., UK). Analysis was routinely performed operating at an accelerating voltage of 5 KeV and using SE detection. Suspensions of GNP-lipos were pipetted onto silicon wafers mounted on aluminium specimen stubs, snap-frozen by submerging in liquid nitrogen and subsequently freeze-dried at 0.5 mbar, -80 °C for 30 minutes (Christ®-ALPHA 1-4). Specimens were then sputter coated with a 5 nm thickness of platinum (Quorum Q150T ES Turbo-Pumped coater device).

2.2.3.3 Energy Dispersive X-ray Spectroscopy

Energy dispersive X-ray spectroscopy (EDS) is a supplementary technique to electron microscopy that provides localised elemental analysis of a specimen. A fundamental tool for studying the composition of a sample, the technique exploits the principal that each element emits a unique and characteristic spectrum of X-rays under an electron beam. When energy is transferred from an incident electron (beam) to an electron from a discrete low-energy orbital in an atom it is ejected forming an “electron hole.” An electron from a higher energy orbital simultaneously fills the hole in the electron shell and the excess energy is emitted as characteristic X-rays. The energy (eV) and intensity (counts per second) of the X-ray emissions detected reveal the identity and extent of elements present in the specimen[202]. Similarly to SEM, the electron beam is applied in a raster fashion, with the number of X-ray emissions generated from each location recorded over a fixed time. Allocating emissions to pixels on a digital viewing screen generates elemental distribution “maps”.

Analysis of GNPs and GNP-lipos was performed alongside TEM studies on the JEOL-JEM2200FS microscope with an integrated JEOL-JED-2300 EDS detector (JEOL Ltd., Japan). The FEI-TALOS F200X S/TEM system with Super-X silicon drift EDS detectors (FEI Company, USA) was used to Study biological specimens. High-angle annular dark-field (HAADF) image acquisition was combined with EDS simultaneously on the TALOS system. Analysis was

performed in each case with an operating voltage of 80 KeV in scanning-transmission electron microscopy (STEM) mode. The same specimens studied using TEM were analysed without any further modification.

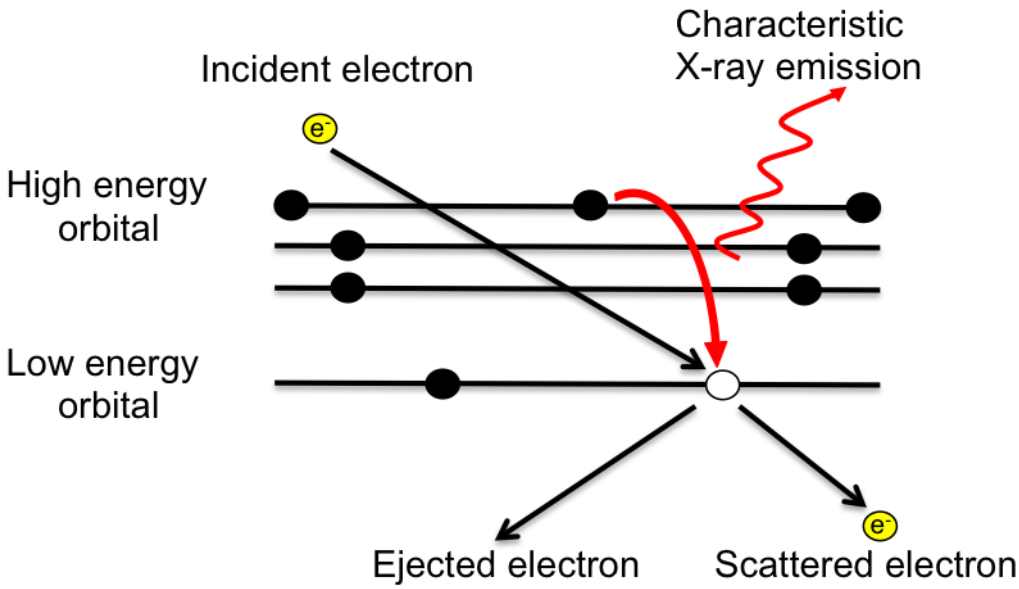

Figure 2.1: Schematic representation of X-ray emission during energy dispersive X-ray spectroscopy. (*Original image.*)

2.2.3.4 Dynamic Light Scattering

Dynamic light scattering (DLS) is a technique that can measure the dispersity and hydrodynamic size distribution of particles in suspension and was used to characterise GNP-lipos (Chapter 4) and self-assembled GNP suprastructures (Chapter 6). The method relies on the measure of Brownian motion of particle diffusion as they pass through a monochromatic laser. Backscattered light fluctuations that occur as particles move through the laser pathway are detected by a photo-multiplier at a 90° angle**.** The intensity of light detected is then recorded by a digital correlator and a computer algorithm known as the auto-correlation function is applied[203]. From this correlation, the equivalent hydrodynamic sizes (dH) of particles in the specimen are calculated from the Stokes-Einstein equation:

Equation 2.3: Stokes-Einstein Equation

$$d(H) = \frac{kT}{3\pi\eta D}$$

Where:

D = transitional diffusion coefficient

k = Boltzmann's constant

T = Absolute temperature

η = Viscosity of the surrounding medium

Particle size analysis was undertaken using a Malvern Zetasizer Nano ZS90 (Malvern Instruments Ltd., UK) operating at 25 °C with measurements recorded at a 90 ° detection angle. A single drop of NIST™ polystyrene latex particles (192 nm) was diluted in distilled water (1 ml) and was used to validate instrument calibration (control) before analysis (See appendix 2). Distilled water (0.45 µm filtered) was used to dilute unfiltered specimens to ensure an accurate size distribution. After dilution all specimens were capped in UV-grade cuvettes and rested for 10 minutes prior to analysis. For GNP-lipos, (PEGylated and non-PEGylated) 100 µl of a sample batch was diluted up to 1 ml. No dilution was carried out prior to analysis of individual GNPs and self-assembled suprastructure (5 µg/ml total gold).

2.2.3.5 Zeta Potential Analysis

Zeta potential (ζ) is a measurement of the electrostatic potential difference between medium (bulk fluid) and an associated ionic layer at the particle surface when dispersed. The technique provides insight into the magnitude of surface charge displayed by particles, signifying their degree of repulsion and potential colloidal stability[204]. In the current study zeta potential analysis was used to validate the attachment of ligands to GNP surfaces, to prepare building blocks for electrostatic self-assembly. It was also used to confirm modification of GNP-lipo surfaces with DPPE-PEG5000.

Based on the colloidal behaviour theory of Derjaguin and Landau, Verwey and Overbeek (DLVO)[205], two parallel ionic layers interfacing between particle

surfaces and bulk fluid are assumed, the *electrical double layer* (EDL). The inner stationary layer (Stern layer) is comprised of adsorbed ions on the particle surface. The outer dynamic layer (diffuse layer) is formed through the attraction of oppositely charged free ions in solution, otherwise known as the *Coulomb force.* The diffuse layer electrically shields the stern layer contributing towards electrostatic repulsion between particles. Under particle motion ions that constitute the diffuse layer can undergo exchange with other free ions under the influence of electric attraction and thermal motion. The position at which this exchange occurs is termed the *slipping plane* and the ionic potential at this location is where the zeta potential measurement is recorded[206] Applying laser Doppler micro-electrophoresis, measurements of particle electrophoretic mobility (∪E) in solution are recorded under the influence of an external electric field[207]. This is then used to calculate the zeta potential and its relative distribution by applying Henry's Equation:

Equation 2.4. Henry's Equation

$$UE = \frac{2\, e\, Z\, f(ka)}{3\, \eta}$$

Where:

z = zeta potential

e = dielectric constant

η = viscosity

f(ka) = Henry's Function

Henry's Function is the ratio of particle radius to double layer thickness (ka). For particles with large (ka) values in aqueous suspensions containing electrolytes, *Smoluchowski Approximation* value of 1.5 is applied[208]

Analysis was performed using a Malvern Zetasizer Nano ZS90 (Malvern Instruments Ltd., UK) operating in zeta potential mode at 25 °C. A -42 mV zeta potential transfer standard reference (control) was used to confirm instrument calibration before analysis. (See appendix 3). Distilled water (0.45 µm filtered) was used to dilute unfiltered samples to ensure measurements were inclusive of

any larger particles or aggregates. Specimens were capped and rested for 10 minutes before injecting into DTS1070 folded zeta capillary cells for analysis. GNPs suspensions were prepared at a total concentration of 5 µg/ml gold, whilst for GNP-lipos, (PEGylated and non-PEGylated) 100 µl of a sample batch was diluted up to 1 ml.

2.2.3.6 Ultraviolet-visible spectroscopy

Ultraviolet-visible spectroscopy (UV-Vis) was used to quantify oligonucleotide concentrations during synthesis of oligo-GNPs (as described in section 2.2.1.3) and characterise GNPs to determine if they had undergone self-assembly (Chapter 3). Additionally, UV-Vis was used to quantify the formation of a molecular complex in a colorimetric assay revealing the concentration of DPPC lipid in GNP-lipos (Chapter 4), see section 2.2.4.3 for further details.

A PerkinElmer LAMBDA-25 (PerkinElmer, USA) spectrophotometer system was routinely used in “scanning mode” between wavelengths (λ) of 500 and 3000 nm. Samples were diluted as required with appropriate medium (0.45 µm filtered), with the same solvent used as a blank reference. This step ensures spectral features arise only from the material of interest. No dilution was carried out prior to analysis of GNPs or their self-assembled suprastructures (5 µg/ml total gold) and measurements were recorded in “scanning mode” Colorimetric assays measurements were recorded in “wavelength mode” at specific wavelengths according to protocols, for sample preparation details see section 2.2.4.2. All Specimens including blank references were measured in quartz glass cuvettes with a standard 1 cm optical pathlength and a 3.5 ml chamber volume.

UV-visible Melting analysis

Studying the self-assembly and thermally induced dissociation of oligo-GNPs was achieved using temperature regulated UV-Vis according to a previously reported method[209]. Initial concentrations corresponding to an optical density of 0.5 A (λ = 260) were used, with complementary oligo-GNP suspensions combined (1 ml each) at a ratio of 1:1 (v/v) immediately before experiments.

Analysis was performed using a water bath coupled cuvette-holder with measurements recorded at 1 °C intervals as the temperature was increased from 30 to 70 °C at a rate of 1 °C / minute. Absorbance was measured in wavelength mode (λ = 260 nm) and scanning mode (λ = 240 – 700 nm) consecutively after samples had been shaken gently by hand to avoid any potential sedimentation and a 1-minute holding time.

2.2.4 Quantification and validation approaches

2.2.4.1 Gold Quantification using Atomic Emission Spectroscopy

Atomic emission spectroscopy (AES) enables the quantitative analysis of multiple elements of interest within a sample. The technique measures concentration dependent light emission from a material as it passes through a high intensity flame. The thermal energy provided breaks chemical bonds producing free atoms that are promoted to excited electronic states. As the atoms subsequently return to their ground state excess energy is emitted as light with resultant wavelengths being characteristic to specific elements. Various instrumental setups are available, throughout this project a microwave-assisted plasma flame system was used operating at approximately 5000°C. A nebuliser was used to generate an aerosol from a sample solution and emissions were detected by an *in situ* spectrometer.

An Agilent 4100 MP-AES system (Agilent Technologies, USA) was used to quantify the concentration of gold in GNP-lipo samples following a previously reported protocol with modifications[210] (Chapter 4). TPP-GNPs (10 mg) were digested in 1 ml of aqua regia ($HCl:HNO_3$ - 3:1) for 24 hours before diluting in distilled water to provide a 100 µg/ml stock solution. Applying the method of external standards, a series of gold solutions (0 - 20 µg/ml) for calibration were prepared in replicate (n=6) by serial dilution. GNP-liposome specimens (200 µl) were combined with chloroform (1 ml), sonicated for 2 minutes and the two phases separated by centrifugation at 300 ×g for 5 minutes. The chloroform layer was discarded and the specimens were evaporated to dryness under mild

heating. Aqua regia was added (200 µl) and samples were digested for 24 hours before diluting in distilled water (2 ml). Blank reference solutions were prepared by digesting 0.1 mmol of the appropriate ligand (TPP, DMET or MES) in aqua regia (200 µl) and diluting as required to achieve a fitting baseline. All samples were introduced to the nebuliser using the fast pump setting (80 rpm) with a 15 second stabilisation period before measurements were recorded (λ = 267.595 nm).

Validation of gold recovery:

The method of standard additions was applied to validate the protocol. Stock solutions of NCG and PCG at concentrations of 6.25 µg/ml and 25 µg/ml were prepared by digesting in aqua regia and diluting in distilled water. Aliquots (10 ml) of the 6.25 µg/ml digested GNP solutions were then serially spiked (0, 2, 4, 6, 8 ml) with the 25 µg/ml GNP stock and made up to 25 ml with distilled water. An identical approach of analysis for three individual experiments (n=3) was performed (see appendix 1) using the same blank reference solutions and instrument parameters as for GNP-lipo evaluation above.

2.2.4.2 Quantification of DPPC lipid using the Stewart Assay

Quantification of the main lipid component (DPPC) in GNPs- lipos was achieved by application of the Stewart assay[211], using the method of external standards (Chapter 4). The procedure relies on the stoichiometric formation of a phosphorous-ammonium complex between dissolved lipids and ammonium ferrothiocyanate. The resulting concentration of the complex is measured spectrophotometrically revealing the amount of phospholipid present in a specimen.

Ammonium ferrothiocyanate (AF) standard solution was prepared by dissolving iron(III) chloride hexahydrate (27.03 g, 0.1 mol) and ammonium thiocyanate (30.4 g, 0.4 mol) in distilled water (1 litre). A stock solution of DPPC in chloroform (100 µg/ml) was serially diluted to prepare a range of lipid standards (0 – 40 µg/ml) for calibration. An aliquot of each prepared standard (1 ml) was combined with AF (2

ml) to afford a biphasic mixture. For analysis of GNP- lipos, 100 µl of a sample was mixed with chloroform (2 ml) and sonicated for 5 minutes before the addition of the AF reagent (2 ml). All mixtures were then vortexed and allowed to rest for 1 minute (2 cycles) and subsequently centrifuged at 500 ×g for 5 minutes. The organic phase (bottom) containing the lipid-AF complex was then isolated and the volume was corrected with chloroform to account for any evaporation (2 ml total volume) before measuring absorbance by UV-vis spectroscopy (λ = 485 nm).

Validation of DPPC recovery:

For validation, the method of standard additions was applied. A lipid stock solution containing DPPC (200 µg/ml), DPPG (20 µg/ml) and DPTAP (20 µg/ml) was prepared by hydrating the lyophilised components in PBS and sonicating for 10 minutes. Portions of the lipid stock (10 ml) were then serially spiked (0, 1, 2, 3, 4 ml) with a solution of DPPC in PBS (200 µg/ml) and diluted with further buffer in 50 ml volumetric flasks. Aliquots of each standard (1 ml) were then treated in an identical manner to the preparation of GNP-lipo specimens before analysis.

2.2.5 Protocols towards investigating self-assembly of GNPs

Self-assembly of GNPs via the electrostatic and molecular recognition approaches was carried out within aqueous buffer conditions (PBS, pH 7.4) and simulated biological fluids (DMEM supplemented with 5% heat inactivated FBS). Stock solutions containing 10 µg/ml total gold in PBS were prepared and sterile filtered (0.45 µm) on the day of application. Stock suspensions were briefly vortexed before use and aliquots (1 ml) were set aside. Working in glass vials, entire aliquots of NCG and PCG or 5 and 20 nm oligo-GNPs were pipetted directly into 2 ml of either PBS or DMEM (5% FBS). Vials were then sealed and protected from light before agitating gently by hand for 1 minute. Test mixtures were then stored undisturbed at room temperature for one hour. For analysis, specimens were extracted from the medium by pipette, with subsequent sample preparation carried out according to the methods detailed in 2.2.3.1 for microscopy evaluation and 2.2.3.4 for hydrodynamic size analysis.

2.2.6 *In vitro* methods towards evaluating SANs

Biochemical assays were performed to determine the associated cytotoxicity of individual building blocks (NCG and PCG), their corresponding self-assembled suprastructures and GNP-lipos in parallel (Chapter 5). An established adherent lung fibroblastic cell line derived from a male Chinese hamster (V79) was selected as an *in vitro* model, employing the colorimetric MTT and LDH assays investigate cell viability and membrane integrity. Intracellular uptake and distribution of GNPs after exposure was investigated using TEM-EDS, with cell specimens preserved and thin-section according to established protocols.

2.2.6.1 Culture of V79 tissue monolayer

The adherent monolayer forming cell line V79, derived from male Chinese hamster lung fibroblast was used throughout tissue culture investigations. The cells display a fast growth rate, high plating efficiency and have been widely used to study reagent-induced toxicity with quantitative assays[212]. Cells were cultured in growth medium consisting of high glucose Dulbecco's modified eagle medium (DMEM, 4.5 µg/ml glucose) supplemented with (10% v/v) heat inactivated fetal bovine serum (FBS.) Cells were routinely cultured to a maximum of 25 passages, between total numbers 50 to 75.

2.2.6.2 Routine cell growth and subculture

Cells were maintained in exponential growth as monolayers using a minimum seeding density of 1.0×10^3 cells /cm^3 in sterile, surface-treated polystyrene culture flasks with an effective growth area of 75 cm^2. Cultures were incubated under normoxic conditions in an incubator (Sanyo-MCO715) at 37°C in a humidified, 5% CO_2 atmosphere. Growth medium was exchanged every 48 hours and cell populations were sub-cultured (passaged) after monolayers had proceeded to reach approximately 70-80% confluence.

Routine passage consisted of treating cells with 50 µl trypsin-EDTA (0.05% w/v) for approximately 5 minutes under standard incubation conditions until cells had visibly detached from the flask surface. Further growth medium (100 µl) was then added to neutralise the trypsin. Cells were isolated from flasks and pelleted under centrifugation at 500 ×*g* for 5 minutes. Recovered cells were then re-suspended in 10 ml of growth medium and counted using a light microscope and haemocytometer to determine the appropriate dilution required prior to seeding in new flasks.

2.2.6.3 Cryo-storage and thawing of V79 cell stocks

Cell stocks were prepared at a density of 1.0×10^7 cells/ml at passage number 50, in a solution consisting of 95% growth medium and 5% dimethyl sulfoxide (v/v) which acts as a cryoprotectant reagent. Aliquots (1 ml) were pipetted into cryo-tubes (Nunc®, Fisher scientific UK) and placed into freezing-pots containing an isolated isopropyl alcohol sleeve that acts to regulate the rate of temperature change upon freezing (~ 1°C / 1 minute.). Cryo-tubes were stored at -80°C for 24 hours and then transferred into liquid nitrogen for long-term storage.

Cells were thawed in the original cryo-tubes at 37°C in a water bath before removing the freezing solution and rinsing cells twice with growth medium. Cells were re-suspended in further medium and an entire aliquot (1.0×10^7 cells) seeded into culture flasks (Nunc™ T25, ThermoFisher Scientific, UK) with an effective growth area of $25cm^2$. After 24 hours of incubation medium was replaced and cells were cultured until 60-70% confluent before reverting to routine passaging.

2.2.6.4 Cell culture and treatment in multidishes

Cells were cultured in Nunclon™ Delta hydrophilic surface treated 96 and 12-well multidishes (Nunc® 96 / Nunc® 12 multidishes, ThermoFisher Scientific, UK) for

cytotoxicity and uptake experiments. Each well provides an effective growth area and working volume of 0.32 cm2 / 0.2 ml (96-wells) or 3.5 cm2 / 2 ml (24-wells). A seeding density of 4.5×103 (96-wells) or 5.3 x 104 (12-wells) cells/ cm2 was used to provide a 70% confluent monolayer after 24 hours of growth under standard incubation conditions. Outermost wells were not used for cell growth but were filled with growth medium alone to reduce the "edge effect" which predominantly arises from differences in evaporation resulting in higher assay variability[213]

2.2.6.5 Preparation of test materials in suspension for *in vitro* assessment

Preparation of GNP and GNP-lipo suspensions was performed on the day of application working under aseptic conditions in a laminar airflow cabinet throughout. Stock solutions containing equivalent concentrations of gold were prepared for each test material (10 µg/ml) and sterile filtered (0.45 µm). Stock suspensions were briefly vortex mixed and diluted with PBS (pH 7.4) to provide a range of gold concentrations (10, 2 and 0.2 µg/ml).

2.2.6.6 Treatment of cells and exposure to test materials

Growth medium was aspirated from culture plates and cells were washed twice with PBS before all investigations. For biochemical assays, wells of a 96-well plate were treated with 100 µl of test suspensions and 100 µl of DMEM culture medium containing heat inactivated FBS (5% v/v). To study the toxicity of *in situ* self-assembling GNPs, (NCG and PCG or 5 and 20 nm oligo-GNPs) test materials were co-administered at a concentration of 10 µg/ml, by directly adding 50 µl of the corresponding solutions (1:1 v/v) in 100 µl DMEM growth medium containing heat inactivated FBS (5% v/v) immediately prior to use. Negative controls consisted 200 µl of culture medium and vehicle controls contained 100 µl each of culture medium and PBS (pH 7.4). Cells were exposed to test materials for 24 hours under standard incubation conditions. Cell supernatant was then removed and collected in a new 96-well cell culture plate for subsequent use in

the LDH assay (see section 2.2.7.2). Each well was then further washed twice with PBS and the MTT assay was immediately applied (see section 2.2.7.1). For *in vitro* self-assembly studies, wells of a 12-multidish were treated with 1 ml of test suspension and 1 ml of DMEM culture medium containing 5% heat inactivated FBS. After 24 hours supernatant was discarded and cells were washed twice with PBS before TEM preparation (see section 2.2.6.7).

2.2.6.7 Preparation of cells for TEM analysis

After treatment with test materials cells were processed according to a previously reported protocol that encompasses tissue preservation (fixation), dehydration, resin embedment and cross-sectioning[214]. Each well was treated with trypsin-EDTA (0.05% w/v) and cells were pelleted under centrifugation at 500 ×*g* for 5 minutes in microtubes. Each microtube containing pelted cells was then treated with glutaraldehyde solution (2.5 %) in 0.1 M sodium cacodylate buffer (pH 7.4) for 2 hours and rinsed four times with further buffer. Cell pellets were then exposed to osmium tetroxide solution (1%) in buffer for 1 hour before thoroughly washing ($\times$ 10) with distilled water. Dehydration was achieved using a series (20 minutes each) of graded ethanol (25%, 50%, 75%, 100% v/v) and immersion in propylene oxide. Epoxide resin (AGAR 100 resin, Agar Scientific, UK) was prepared according to the manufacturer's instructions and added to each tube with fresh propylene oxide (1:1 v/v). Fresh resin was then added and exchanged every 12 hours over 2 days before polymerising at 60 °C for 24 hours. Thin-sectioning was achieved by ultramicrotomy on a Leica EM UCT device (Leica microsystems Ltd., UK) using a Pelco® Microstar 35-degree diamond-tipped knife with a cutting speed of 0.3 mm/s, providing sections with a thickness of 75 nm mounted on square 200 mesh gold TEM specimen grids (Agar Scientific, UK). The reverse side of the specimen grids (where no sample was mounted) was then coated with 5 nm of carbon using a Quorum Q150T ES Turbo-Pumped sputter coater.

2.2.7 Evaluation of cytotoxicity using biochemical assays

2.2.7.1 MTT assay for measurements of cell viability after exposure to test materials

Cell metabolic activity is measured by the reduction of the soluble yellow dye 3-(4,5-dimethylthiazol-2-yl)-2,5-diphenyltetrozolium bromide (MTT) to an insoluble purple product that precipitates[215]. The reduction correlates with the presence of nicotinamide adenine dinucleotide phosphate hydrogenase (NADP-H) dependent enzyme activity, occurring in metabolically active cell populations. The precipitated product is subsequently solubilised and concentration measured spectrophotometrically, with absorbance proportional to cell viability.

An MTT solution (1mg / ml) in DMEM culture medium (without FBS) was prepared, sterile filtered (0.45 µm) and heated to 37^{o}c in a water bath prior to use. To each well containing cells, 200 µl of MTT solution was added before cell culture plates were protected from light and incubated under standard conditions for 3 hours. Assay supernatant was then carefully aspirated using a pipette to avoid removing the precipitated products. Isopropanol (200 µl) was added to solubilise the purple dye and the absorbance (540 nm) was recorded using a Thermo Multiskan Ascent 354 multidish spectrophotometer (ThermoFisher Scientific, USA). A positive control was prepared by using a 1% (v/v) solution of Triton-X-100™, which induces cell lysis. Untreated cells in culture medium provided a negative control (average maximum cell viability) and isopropanol was used as a blank reference. The resultant (%) cell viability was calculated from absorbance values using the following equation:

Equation 2.5. Conversion of absorbance to (%) viability for MTT assay

$$(\%)\ cell\ viability = \left(\frac{As - Ab)}{An - Ab}\right) \times 100$$

Where:

As = treated cell absorbance

Ab = Average blank absorbance

An = Average negative control absorbance

Calculated values are relative to cell viability without treatment (negative control). Treatments. that induce greater than 50% cell mortality are considered to be a toxic condition (TC_{50}), significantly inhibiting biological activity. This criterion has previously been applied to assess nanoparticle toxicity and was considered analogous to a lethal dose that causes greater than 50% cell death in a given time period[216], conventionally applied to compare the toxicity of drugs *in vitro*[217].

2.2.7.2 LDH assay for evaluation of membrane integrity after exposure to test materials

Lactate dehydrogenase is an intracellular cytosolic enzyme found across numerous cell species, which catalyses the conversion of lactate to pyruvic acid through the reduction of NAD^+ to NADH[218]. Release of LDH into the extracellular matrix (culture supernatant) occurs upon cellular lysis, indicating a loss of membrane integrity and consequently, biological homeostasis. The assay selectivity measures the enzymatic activity of LDH by the reduction of NAD^+, with NADH participating in the stoichiometric conversion of a tetrazolium dye. The concentration of the produced violet coloured dye was then detected by measuring its absorbance spectrophotometrically.

The release of LDH was measured using the Promega CytoTox96® Non-Radioactive Cytotoxicity Assay Kit (Promega UK) and was prepared according to the manufacturer's instructions. Aliquots of culture supernatant (50 µl) extracted

after treatment with test materials were combined with an equal volume of LDH-substrate mixture in 96-well plate. The enzymatic-reaction was allowed to proceed for 30 minutes under ambient conditions whilst protected from light. A 1 M acetic acid solution (supplied in kit) was then added to each well (100 µl) terminating the reaction process. Negative controls consisted of untreated cells in culture medium only providing average background LDH release from healthy cell populations. A positive control was prepared by lysing untreated cells with 1% (v/v) Triton X-100™ solution, 1 hour before analysis. A mixture of assay culture medium and PBS (1:1 v/v) was used as a blank reference. The resultant absorbance of each well was measured at 492 nm using a UV-vis plate reader (Thermo Multiskan Ascent 354) and converted to (%) LDH release using the following equation:

Equation 2.6. Conversion of absorbance to (%) release for LDH assay

$$(\%)\ LDH\ release = \left(\frac{(As - Ab) - (An - Ab)}{(Ap - Ab) - (An - Ab)} \right) \times 100$$

Where:

As = treated cell absorbance
Ab = Average blank absorbance
An = Average negative control absorbance
Ap = Average positive control absorbance

Calculated results are relative to the maximum LDH release during complete cell lysis (positive control). Values greater than 50% were considered to represent a condition (TC_{50}) that exhibited cytotoxicity as a consequence of significant loss of cell membrane integrity.

2.2.8 Statistical analysis

The sizes of a population data set (n) with each value being the average of a number of replicates (r) are stated accordingly throughout this thesis. Values are reported as mean averages ± standard deviation (S.D.) unless otherwise stated.

2.2.8.1 Calibration and regression

Calibration and recovery (validation) plots were prepared by applying either the method of external standards or standard additions[219]. For the former approach, a range of standards of known analyte concentration were prepared and analysed. For the latter method, a series of standards were prepared by serially spiking a representative sample with known concentrations of analyte. The standards were analysed according to the described protocol to prepare a standard addition plot. Instrument response was then plotted against concentration to calculate the least-squares regression line using Microsoft® Excel 2011 (Microsoft Corporation, USA).

2.2.8.2 Student's t-test

To compare data sets for significant difference paired two-tail student's t-tests were applied, using GraphPad Prism version 5.01 for Windows (GraphPad Software, USA). Working at the 95% confidence level, values of $P < 0.05$ indicate that population means are significantly different. The degree of significance is indicated on figures where appropriate.

3 Synthesis, Characterisation and Self-assembly of Gold Nanoparticles

Pharmaceutically relevant gold nanoparticles[220] (GNPs) were synthesised according to the methods detailed in section 2.2.1. GNPs were subsequently characterised following established protocols, to determine their size, shape, surface chemistry and suitability as building blocks in the current investigation. Utilising complementary particle functionality, GNP building blocks were prepared to investigate electrostatic attraction and molecular recognition as two mechanisms of nanomaterial self-assembly. Two dissimilar NP sizes were utilised for the latter approach, to determine whether self-assembly altered the original plasmonic properties of these nanoparticles. The same self-assembly strategy was also further applied to demonstrate how self-assembly can be reversible and controlled under specific conditions, replicating findings of a previous study. Assembled suprastructures were analysed and compared to their monodispersed counterparts to determine the feasibility of each approach towards self-assembly of nanomaterials and provide a reference for subsequent investigations in this project.

3.1 Characterisation of synthesised GNPs

Morphology and physicochemical properties of GNPs were analysed after initial preparation and subsequent functionalisation, according to the methods described in section 2.2.3. Resultant TEM images and UV-visible spectra were studied to determine the particle size distribution, morphology and state of dispersion. Zeta potential analysis was utilised to confirm attachment of ionic ligands and determine relative particle surface charge whilst in an aqueous colloidal state.

3.1.1 Evaluation of functionalised spherical-shaped GNPs

3.1.1.1 Triphenylphosphine-stabilised precursor GNPs

Precursor particles stabilised with TPP were initially synthesised (section 2.2.1.1) for subsequent use in ligand-exchange reactions to prepare either negatively (NCG) or positively charged (PCG) GNPs. Acquired TEM micrographs of resultant structures and corresponding size distribution histograms, derived from direct microscopy measurements in multiple discrete locations within the specimen are displayed in Figure 3.1. Uniform, spherical and dispersed particles with a diameter of 2.7 ± 0.9 nm were observed (n=200, mean ± SD). At higher magnifications, repeating distinctions in image contrast were observed in a single direction within the confinements of particles (highlighted with white arrows in (Figure 3.1 B), characteristic of GNPs with a monocrystalline lattice[221].

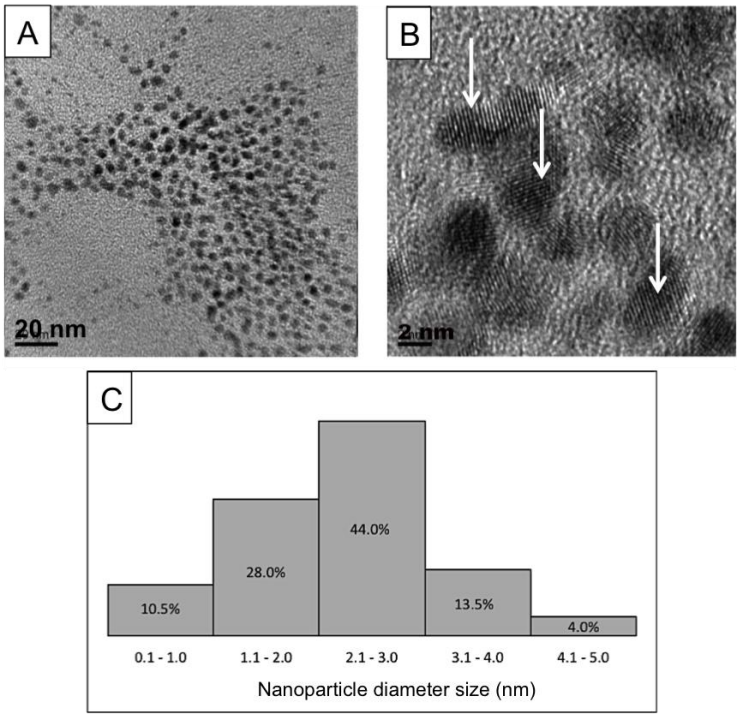

Figure 3.1 (A-B): TEM micrographs of individually dispersed triphenylphosphine stabilised precursor gold nanoparticles that display a spherical morphology and monocrystalline lattices (white arrows highlight uniform crystalline lattice of particles). (C): corresponding size distribution histogram of GNPs measured to have an average diameter of 2.7 ± 0.9 nm (n = 200, mean ± SD).

3.1.1.2 Analysis of DMET and MES functionalised GNPs

Triphenylphosphine was exchanged on GNP surfaces with either cationic DMET or anionic MES ligands to prepare the building blocks NCG and PCG, respectively (section 2.2.1.1). Resultant TEM micrographs of GNP structures are displayed in Figure 3.2 alongside their corresponding size distribution histograms, derived from direct microscopy measurements in multiple discrete locations within the specimen. Individual, monodispersed and spherical particles were again observed with diameters of 2.8 nm ± 1.2 nm for PCG and 2.6 nm ± 1.2 for NCG (n=200, mean ± SD). From UV-visible spectra (Figure 3.3), distinctive size-dependent LSPR peaks (plasmonic properties) were not observed for either NCG or PCG, characteristic of GNPs with diameters below 2 nm[222]. Verifying the successful attachment of either DMET or MES to GNP surfaces, values obtained from zeta potential measurements were compared for NCG and PCG (Figure 3.4) As expected, a positive zeta potential of +15.1 ± 1.2 mV was revealed for PCG, signifying

the attachment of the cationic ligand DMET to GNP surfaces. In contrast, a negative zeta potential value of -17.5 mV ± 1.4 mV was recorded for NCG, also confirming the effective attachment of the anionic ligand MES to particle surfaces.

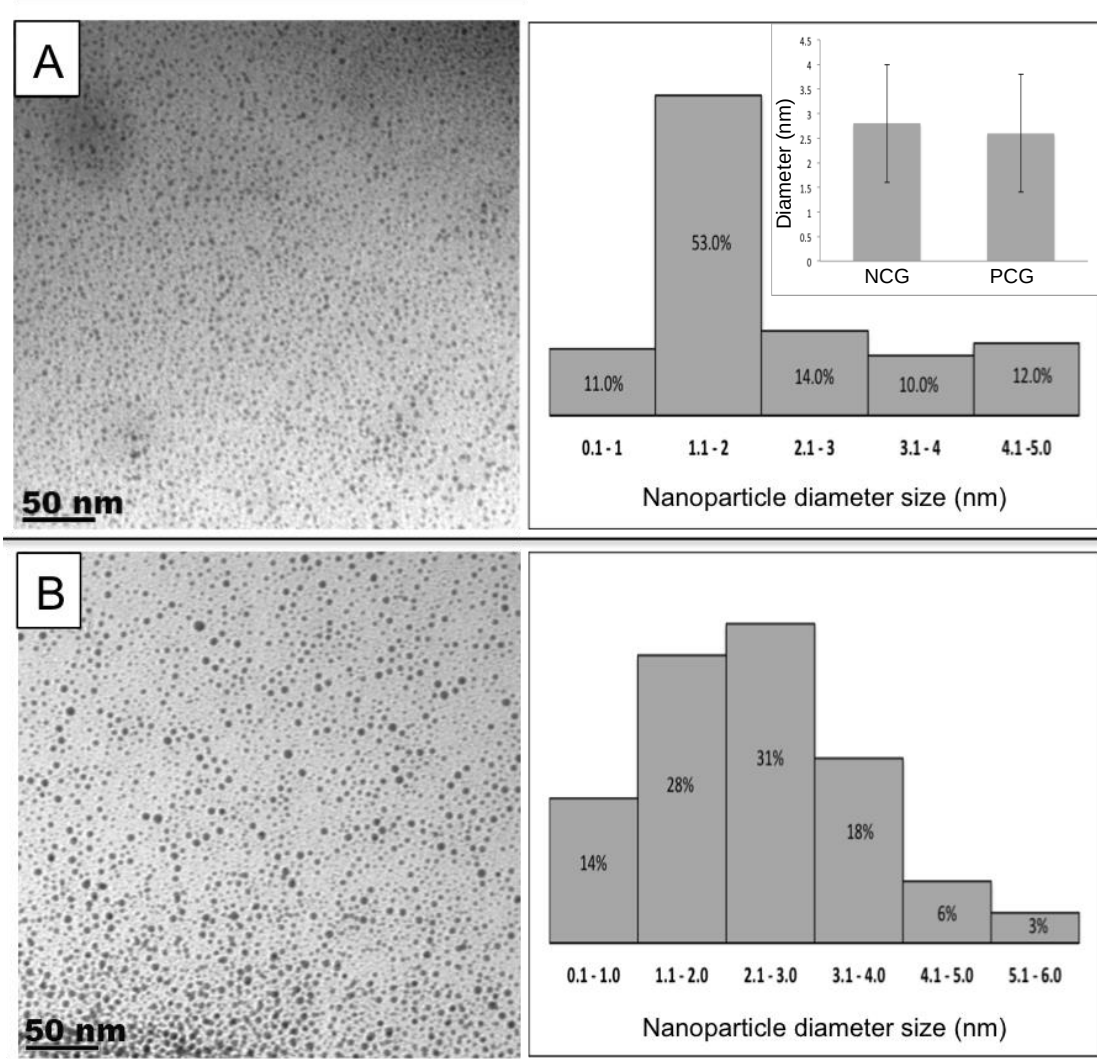

Figure 3.2. TEM micrographs with corresponding size distribution histograms, revealing a spherical morphology and average diameters of individual GNP building blocks (A): NCG (2.6 nm ± 1.2) and (B): PCG (2.8 nm ± 1.2 nm), at a concentration of 0.5 mg/ml in PBS (n = 200, mean ± SD). Insert :(A, top right): graph displaying average particle size for NCG and PCG with error bars displaying mean ± SD.

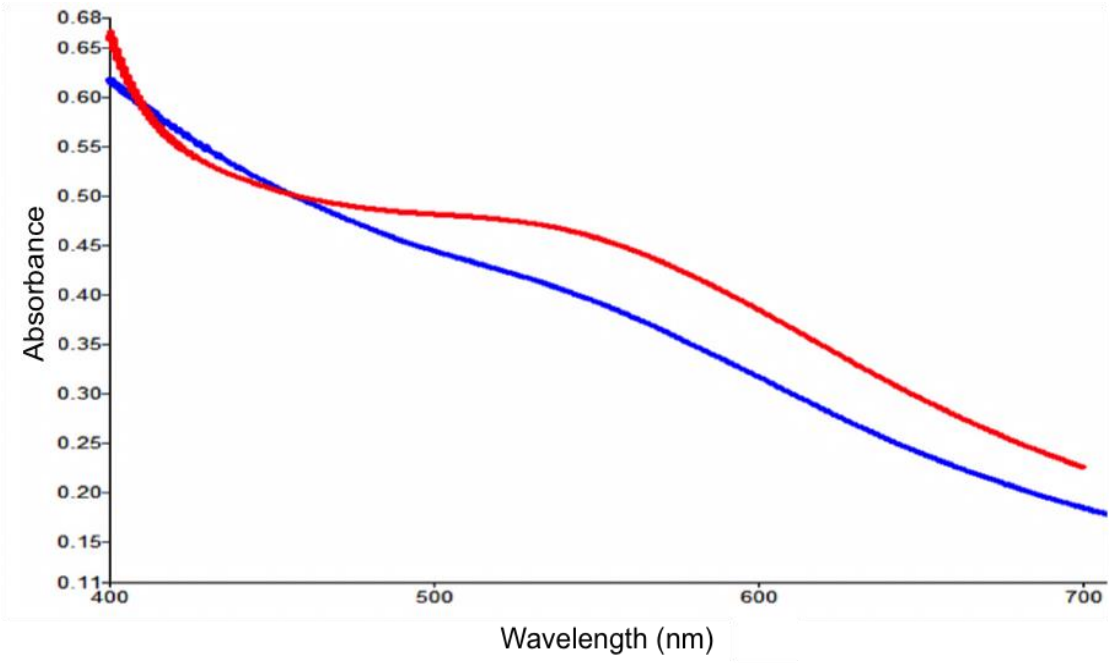

Figure 3.3 Ultraviolet-visible spectra obtained for GNP building blocks (red): NCG and (blue): PCG when dispersed in PBS (with PBS used as a blank reference). Broad optical adsorption peaks seen between 500 and 600 nm corresponds to a lack of LSPR properties, which is indicative of GNPs with diameter sizes below 2 nm[222].

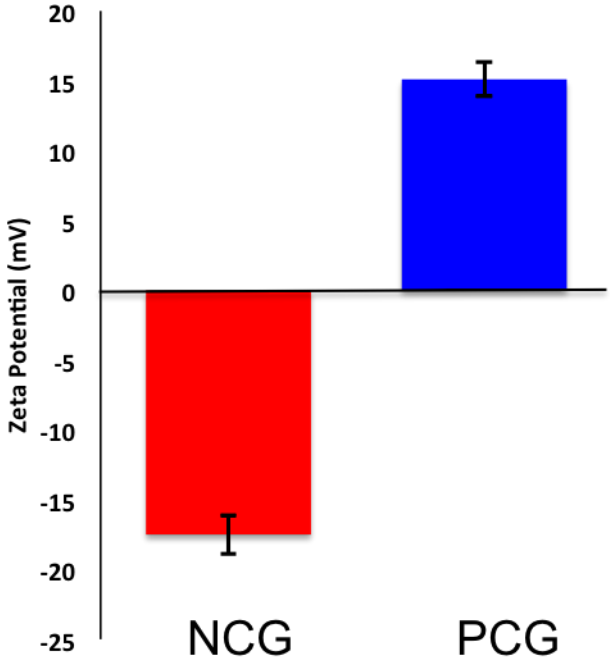

Figure 3.4. Comparison of zeta potential of (red): NCG and (blue): PCG nanoparticles when suspended in PBS at a concentration of 0.5 mg/ml. (n = 6, r = 10, with error bars displaying mean ± SD).

3.1.1.3 Analysis of oligonucleotide functionalised GNPs

Two dissimilar sized GNPs, functionalised with complementary oligonucleotides (5'-TTTTTTTTCATGACGTCATG and 5'-TTTTTTTTGTACTGCAGTAC) were prepared (section 2.2.1.2) from 5 nm (commercially supplied, Sigma Aldrich, UK) and 20 nm (synthesised, section 2.2.1.2) precursor GNPs stabilised with citrate (section 2.2.1.2). Resultant oligo-GNPs are revealed in TEM micrographs displayed in Figure 3.5 alongside their corresponding size distribution histograms, derived from direct microscopy measurements in multiple discrete locations within the specimen. Uniform and monodispersed GNPs were observed displaying a spherical morphology with average particle sizes of 4.9 ± 1.4 nm and 18.2 ± 2.0 nm (n=100, mean ± SD), respectively. In agreement, UV-visible spectroscopy (Figure 3.6) showed size-dependent SPR peaks for the two dissimilar sized GNPs with the larger particles displaying a minor increase in the maximum absorption wavelength (red-shift) (λ = 526 nm), compared to the smaller particles (λ=524 nm), consistent with previous reports[223]. The identification of size-dependent LSPR peaks also further confirms that GNPs are stable colloidal dispersions with no particle-particle agglomeration or aggregation. For clarity, these nanoparticles are hereafter referred to as "5 nm oligo-GNPs" and "20 nm oligo-GNPs".

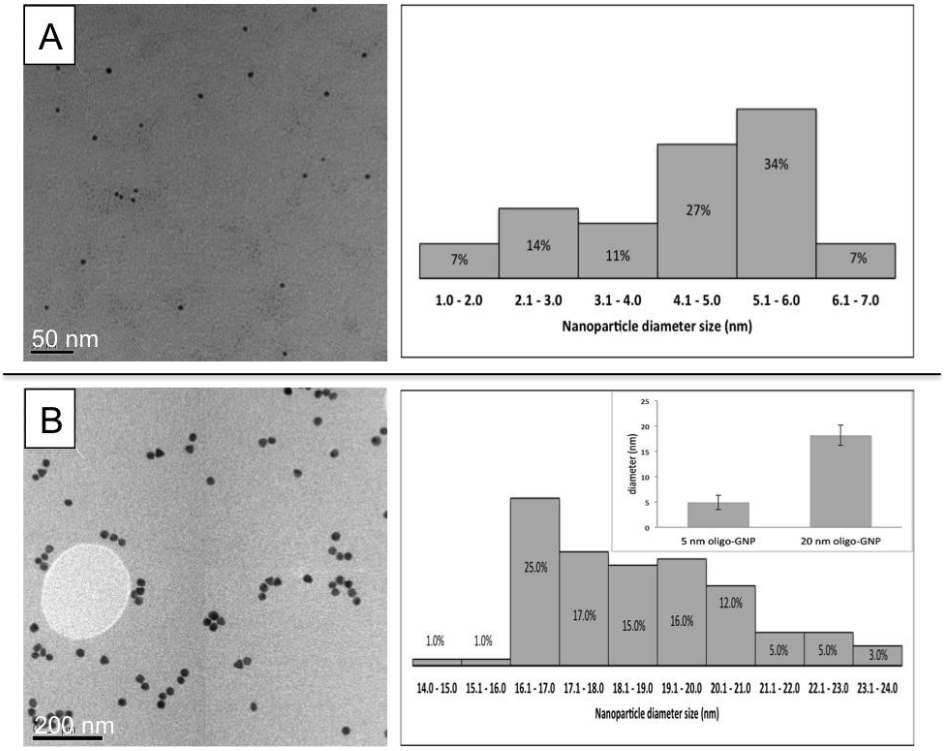

Figure.3.5 TEM micrographs with corresponding size distribution histograms for spherical oligo-GNPs with an approximate size of (A): 4.9 ± 1.4 nm and (B): 18.2 ± 2.0 nm, at a concentration equating to 0.1 O.D. (n = 100, mean ± SD).). Insert :(B, top right): graph displaying average particle size for 5 nm and 20 nm oligo-GNPs with error bars representing SD.

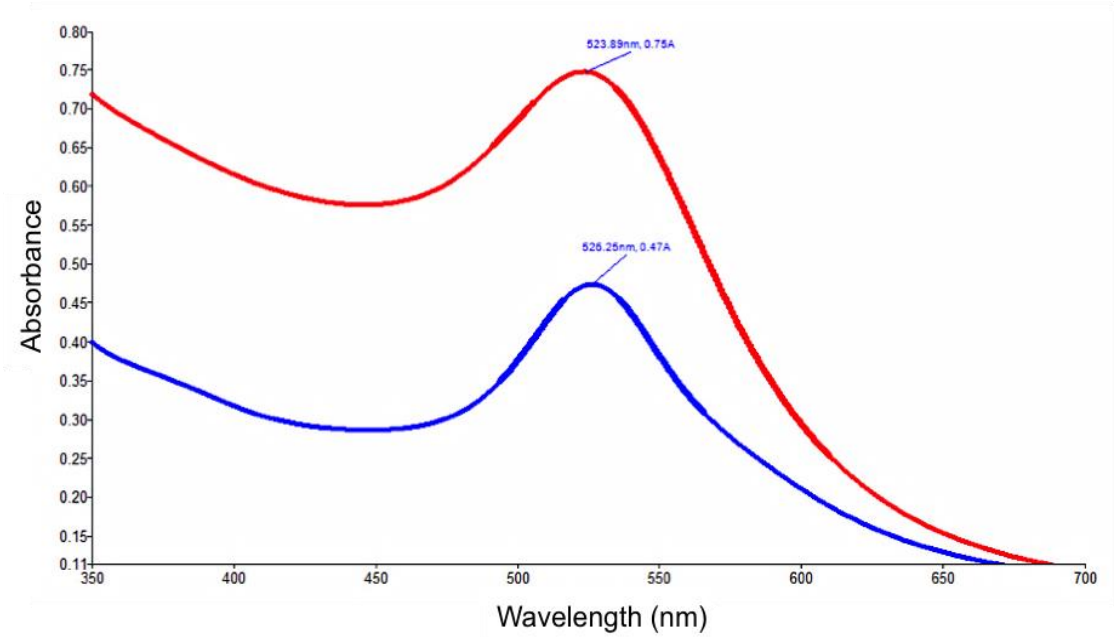

Figure 3.6 UV-visible spectra obtained for GNP building blocks (red): 5 nm and (blue): 20 nm oligo-GNPs when dispersed in PBS at a concentration of 0.5 mg/ml.

3.1.2 Evaluation of different shaped GNPs

3.1.2.1 Analysis of rod-shaped GNPs

GNRs were synthesised using spherical 5 nm GNPs stabilised with citrate (commercially supplied, Sigma Aldrich, UK) as precursors for seed mediated growth, with CTAB used as a shape directing additive (section 2.2.1.3). Synthesised particles seen in micrographs presented in Figure 3.7 predominantly display a cylindrical, elongated shape morphology and appear dispersed (Figure 3.7A). After repeated purification attempts, irregular spherical and cubic shaped particles could not be completely removed (Figure 3.7B). Measurements from four discrete locations within the specimen revealed average particle edge lengths of 25.5 ± 6.1 nm and widths of 14.4 ± 8.4 nm, with corresponding aspect ratios (ratio of width to length) of 2.1 ± 0.8 (n=50, mean ± SD).

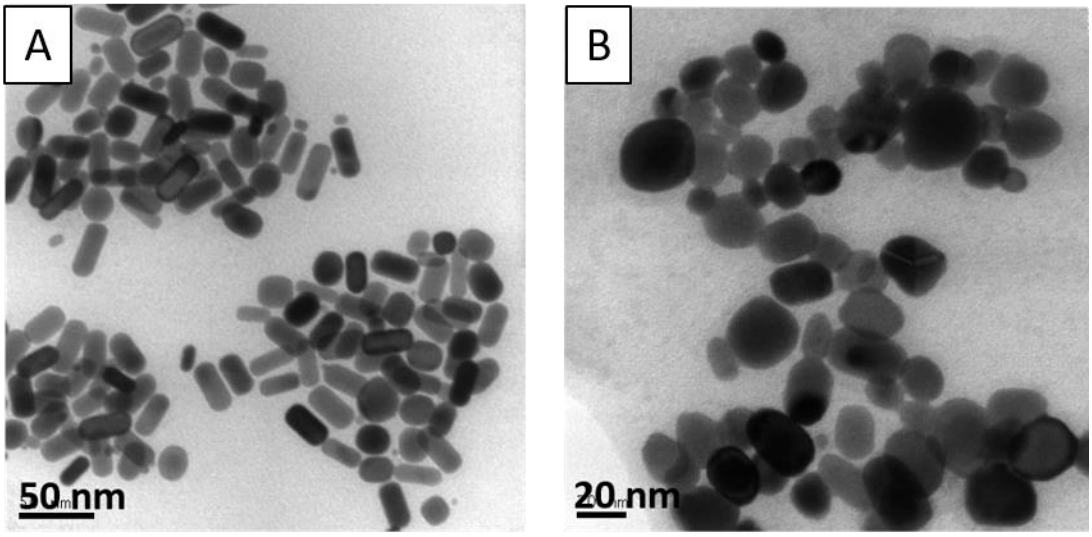

Figure 3.7 TEM micrographs of CTAB stabilised GNRs suspended in distilled water at a concentration of 0.4 mg/ml. Particles display variably elongated shape morphologies and corresponding average aspect ratios (ratio of length to width) of 2.1 ± 0.8 (n=50, mean ± SD).

3.1.2.2 Analysis of triangle-shaped GNPs

Attempts to synthesis GNTs using a direct approach employing a modified Turkevich method (section 2.2.1.4) were unsuccessful, as revealed in

micrographs shown in Figure 3.8. After multiple purification attempts resultant particles regularly displayed multifaceted spherical shape morphologies, representative of polyhedrons. Measuring from four discrete locations within the specimen, particle dimensions were revealed to be between 4 and 40 nm. Infrequently, GNPs were observed to display the desired triangular shape configuration, with average edge lengths measured to be 21.4 ± 7.7 (n=60, mean ± SD).

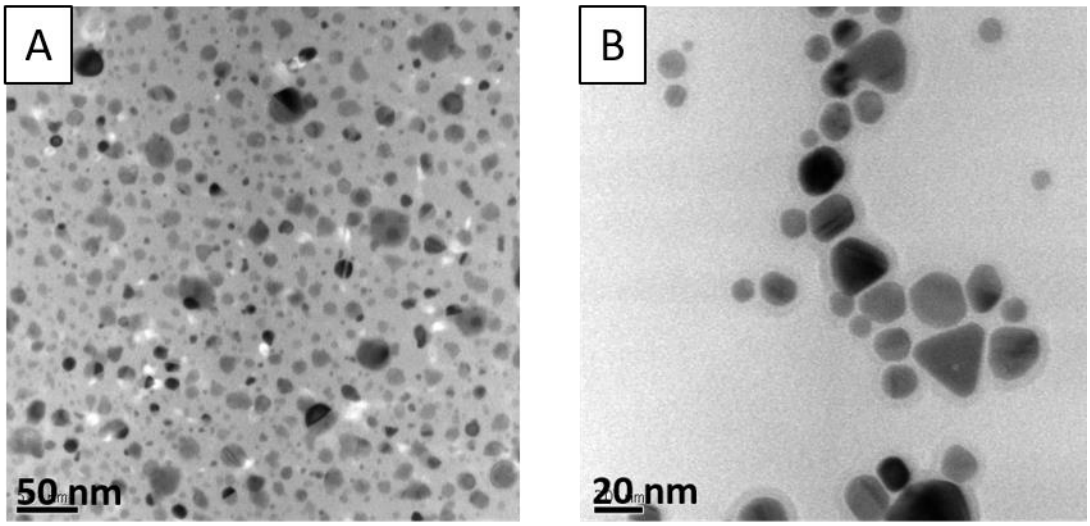

Figure 3.8 TEM micrographs of citric acid stabilised gold particles suspended in aqueous citric acid solution at a concentration of 1mg/ml. Irregular shape morphologies are seen with those displaying triangular morphologies having average edge lengths of 21.4 ± 7.7 nm (n=60, mean ±SD).

3.1.2.3 Analysis of star-shaped GNPs

GNSs were prepared using a direct approach that utilises silver ions as a shape directing additive (section 2.2.1.5). Synthesised particles seen in micrographs presented in Figure 3.9 appear uniform and display highly branched star-like shape morphologies. Particles appear to display dense cores, becoming increasingly porous towards the peripheries where individual well-defined branches can be seen. Measurements recorded from multiple discrete locations within the specimen revealed these particles to display a large size distribution, ranging from approximately 500 nm and exceeding beyond 1 µm in diameter (n=10).

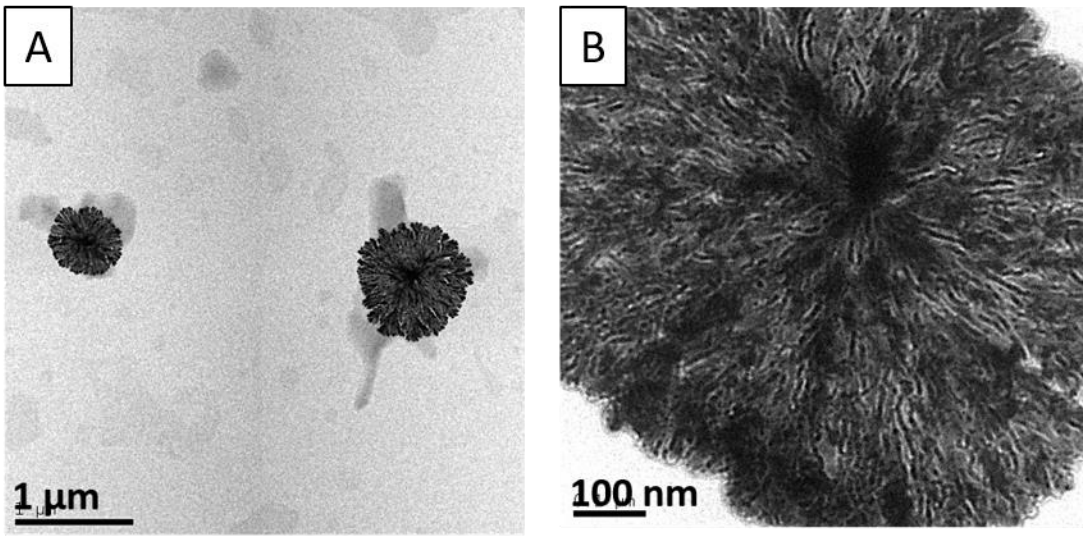

Figure 3.9 TEM micrographs of ascorbic acid stabilised GNSs suspended in aqueous ascorbic acid solution at a concentration of 0.5 mg/ml. Particles consistently display a highly branched morphology with a large size distribution ranging from approximately 500 nm and exceeding above 1 µm in diameter (n=10).

3.2 Investigating the self-assembly activity of GNPs

Self-assembly activity of GNPs facilitated either by electrostatic interactions or molecular recognition was investigated. Within aqueous conditions, oppositely charged NCG and PCG were utilised to investigate the former strategy and 5 nm and 20 nm oligo-GNPs to study the latter. Using the same approach as for characterisation, microscopy and UV-visible spectroscopy were employed to determine the state of particle dispersion and ensuing self-assembled suprastructure morphology and size.

3.2.1 Self-assembly of GNPs facilitated by electrostatic attraction

Functionalised GNP building blocks that displayed either negative (NCG) or positive (PCG) surfaces (section 3.1.2) were utilised to investigate electrostatic attraction as a mechanism of facilitating self-assembly. Upon combining colloidal suspensions of NCG and PCG in equal proportion (1:1 v/v), extensive nanoparticle assemblage was observed within one-hour (Figure 3.7) Resultant GNP suprastructures were seen to display variable and irregular morphologies, comprised of densely amassed particles with multiple interconnecting branch-like structures. Frequently, GNPs were also observed to be overlapping within planar micrographs, indicating that suprastructures could potentially be three-dimensional configurations. Overall sizes of GNP suprastructures were consistently measured in at least one dimension to exceed several microns (μm), multiple orders of magnitude larger in comparison to individual GNP building blocks (control) observed in section 3.1.1.2. At higher magnification (Figure 3.7 C) discrete GNPs were identified within assembled suprastructures with distances between neighbouring particles measured to be approximately 1 nm, characteristic of structural-agglomerates. Additionally, no evidence of larger particle formation or particle-particle aggregation was seen, indicating that the assembled GNPs had retained their original building block morphologies. Resultant plasmonic properties of assembled GNP structures determined by UV-visible

spectroscopy were also compared to NCG and PCG individually, presented in Figure 3.8. Minor differences in the optical profiles were noted between individual GNP building blocks of NCG and PCG, compared to their assembled counterparts, with an increase in absorption intensity at λ ~450 nm and a decrease in adsorption intensity between λ ~500 - 650 nm.

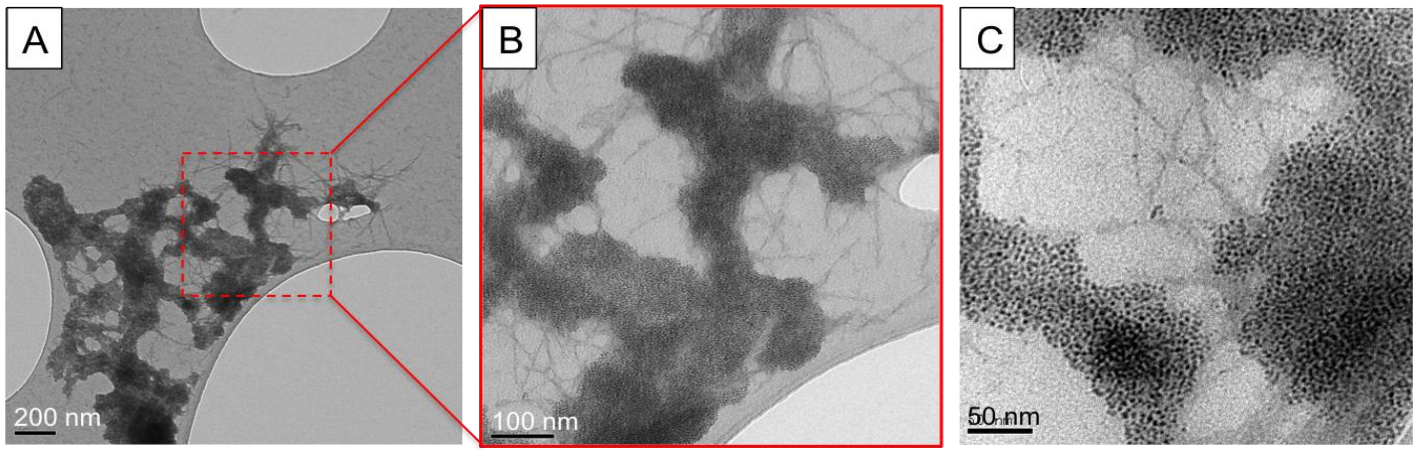

Figure 3.7 Series of TEM micrographs with increasing magnification revealing self-assembled GNP suprastructures, obtained one hour after combining colloidal suspensions of NCG and PCG at a concentration of 0.5 mg/ml (1:1 v/v). Dashed red boxes indicate areas where successive images were acquired at higher magnification with corresponding micrographs highlighted with red borders.

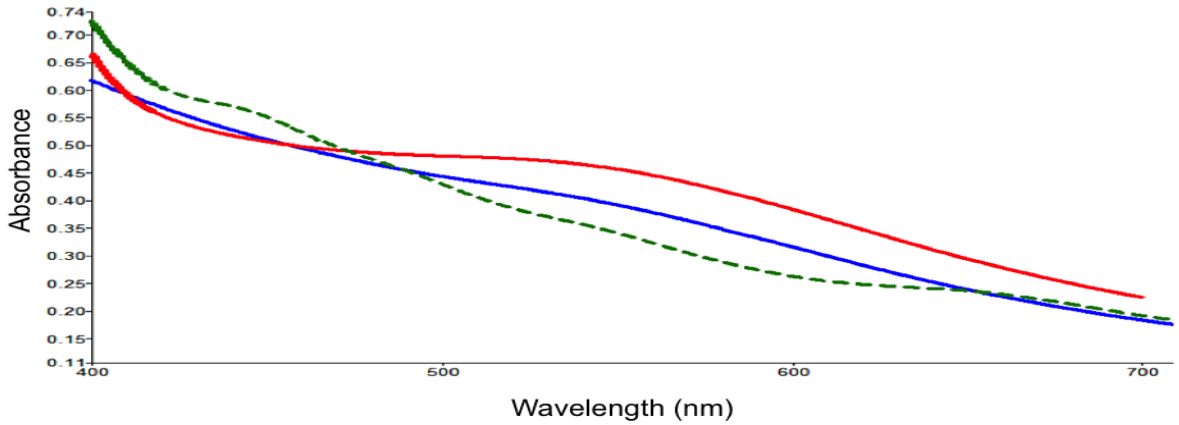

Figure 3.8 Comparison of UV-visible spectra obtained for individual building blocks (red: NCG, blue: PCG) and assembled suprastructures (green) when dispersed in PBS at a concentration of 0.5 mg/ml..

3.2.2 Self-assembly of GNPs facilitated by molecular recognition

Synthesised GNPs with approximate diameters of 5 and 20 nm (section 3.1.2), functionalised with complementary oligonucleotides, were utilised as building blocks to investigate molecular recognition as a mechanism of self-assembly. Comparable to observations after electrostatic self-assembly of GNPs, oligo-GNP suprastructures consistently formed within one hour of combining colloidal suspensions of 5 and 20 nm oligo-GNPs (Figure 3.9) in equal proportion (1:1 v/v). Interpretation of micrographs revealed these suprastructures to display variable and irregular morphologies comprising of tightly packed, discrete GNPs, representative of structural agglomerates. to the electrostatic derived suprastructures, GNPs frequently appeared to overlap within the planar micrographs, indicative of a three-dimensional configuration. It was further noted that oligo-GNPs appeared more compact and lacked distinctive branch-like features, which were seen after self-assembly of NCG and PCG. At higher magnification (Figure 3.9 C), inclusion of both 5 and 20 nm oligo-GNPs within assembled structures was also clearly evidenced. Overall suprastructure sizes were again revealed to exceed beyond several microns (μm) in at least one-dimension, multiple orders of magnitude larger than individual oligo-GNP building blocks (control) observed in section 3.1.1.3. In further support of this observation, obtained UV-visible spectra displayed in Figure 3.10 showed that the characteristic size-dependent LSPR peaks for both 5 and 20 nm oligo-GNPs had noticeably diminished. Plasmonic activity for assembled GNPs were instead markedly broader and had experienced red shift, with increased adsorption intensity between $\lambda \sim 600 - 700$ nm compared to the original dispersed GNP building blocks.

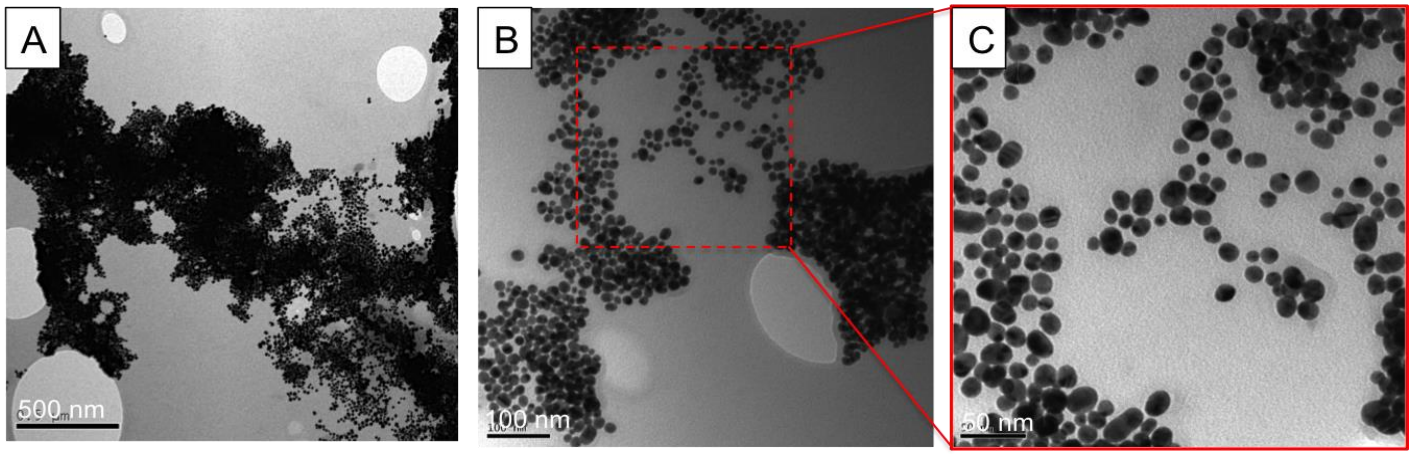

Figure 3.10: Series of TEM micrographs with increasing magnification revealing assembled GNP structures, obtained one hour after combining suspensions of 5 and 20 nm oligo-GNPs at a concentration of 0.5 mg/ml (1:1 v/v). Dashed red boxes indicate areas where successive images were acquired at higher magnification with corresponding micrographs highlighted with red boarders.

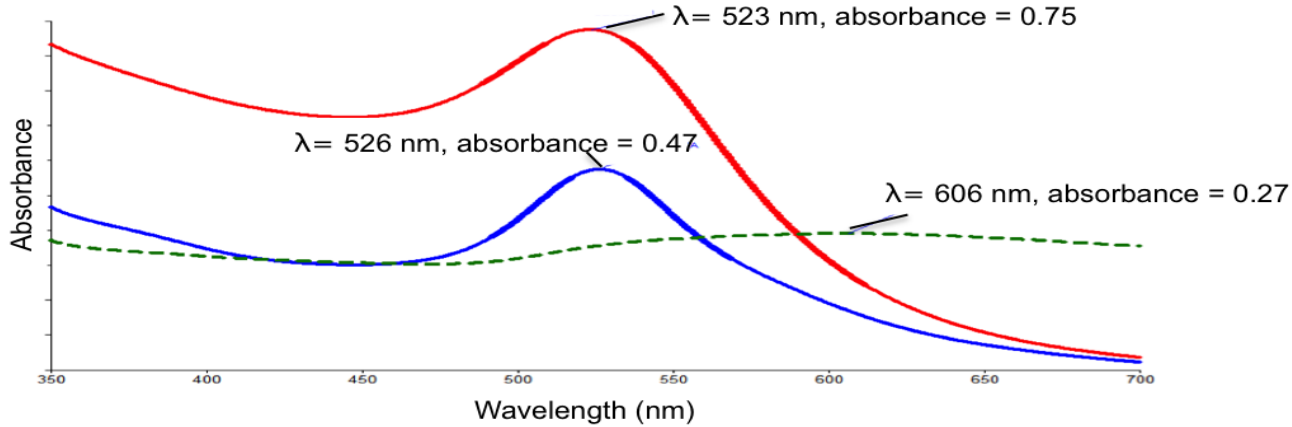

Figure 3.11: Comparison of UV-visible spectra obtained for individual building blocks (red: 5 nm, blue: 20 nm) and assembled suprastructures (green) when dispersed in PBS with an initial concentration corresponding to an optical density of 0.5 A (λ = 260).

3.2.3 Thermally triggered dissociation of self-assembled of GNPs

Thermal dissociation activity of self-assembled oligo-GNPs was analysed using a protocol that monitors absorbance as a function of temperature, as described in section 2.2.3.6, replicating a previously published study[224]. By monitoring absorbance over a range of temperatures it is possible to determine the "melting transition temperature" (T_m), which can be described as a critical point where hybridised oligonucleotides (double stranded) become thermodynamically unstable and dissociate (single stranded). Considering self-assembly of oligo-GNPs is thought to be entirely dependent on oligonucleotide hybridisation, above this critical temperature suprastructures were expected to also dissociate back into individual oligo-GNP building blocks. A thermal dissociation curve was plotted at 1°C intervals by measuring absorbance at λ=260 nm (Figure 3.11). When complementary oligonucleotides hybridise to form double strands, they are known to show a notable reduction in absorbance at this particular wavelength. Results revealed that oligonucleotides attached to GNP surfaces were in a hybridised state below 57°C. Above this temperature an increase in absorbance was recorded at 260 nm, signifying that oligonucleotides have dissociated back into individual sequences. To confirm that oligonucleotide dissociation resulted in the disassembly of oligo-GNPs, optical absorbance was monitored between λ= 240 – 700 nm (Figure 3.12). From obtained spectra it can be seen that below 57°C oligo-GNPs display broad plasmonic activity between λ = 600 – 700 nm, corresponding to results obtained in 3.2.2 for self-assembled oligo-GNP suprastructures. Above this melting transition temperature, a distinctive peak emerges at λ~ 525 nm, characteristic of individual 5 and 20 nm GNPs, as confirmed in section 3.1.3. It was concluded from these results that oligonucleotides dissociation, evidenced at 57°C, initiates the disassembly of oligo-GNP suprastructures back into individual building blocks. Furthermore, the experimentally derived T_m in this investigation corresponds to the manufacturers (ATDBio Ltd., UK) specified T_m for the utilised oligonucleotides (57°C), theoretically calculated using the method of nearest neighbour[226]. Retention of the manufacturers stated T_m for self-assembling GNPs suggests that attachment

of oligonucleotides to building surfaces does not influence their characteristic thermodynamic properties in this study.

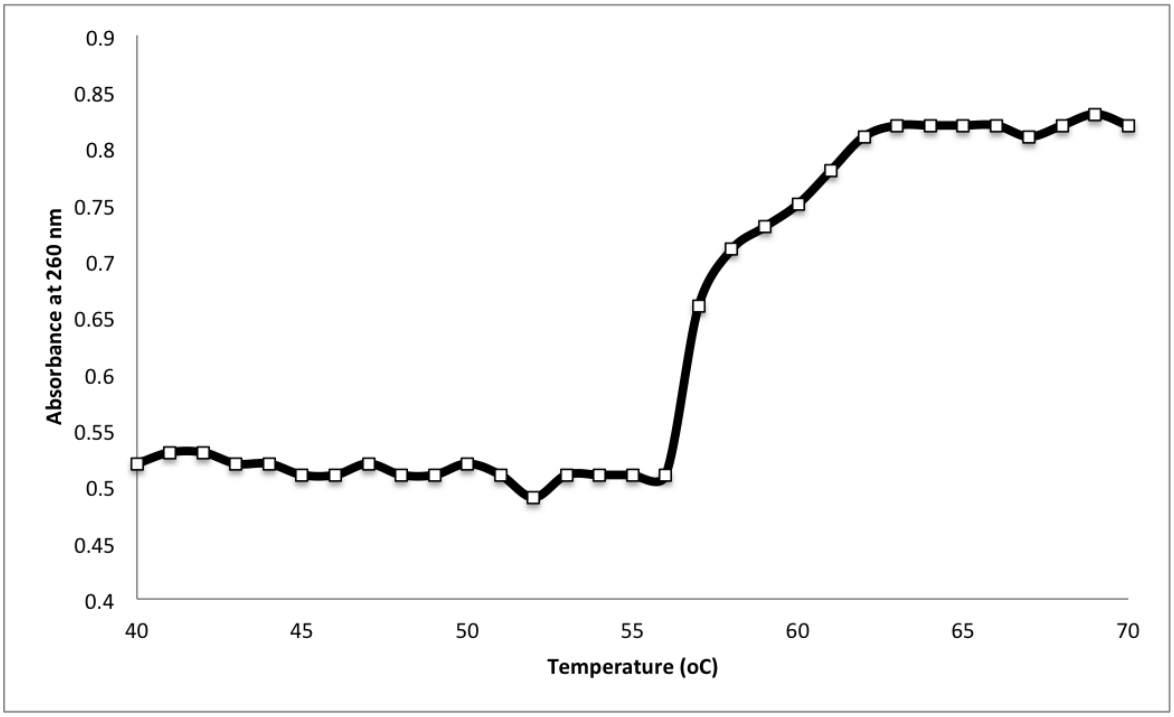

Figure 3.12: Thermal dissociation curve of assembled oligo-GNP suprastructures with a concentration corresponding to an initial optical density of 0.5 A (λ = 260). obtained my monitoring absorbance (λ= 260 nm) as a function of temperature (1°C increments), revealing the melting transition temperature of hybridised oligonucleotides to be 57°C.

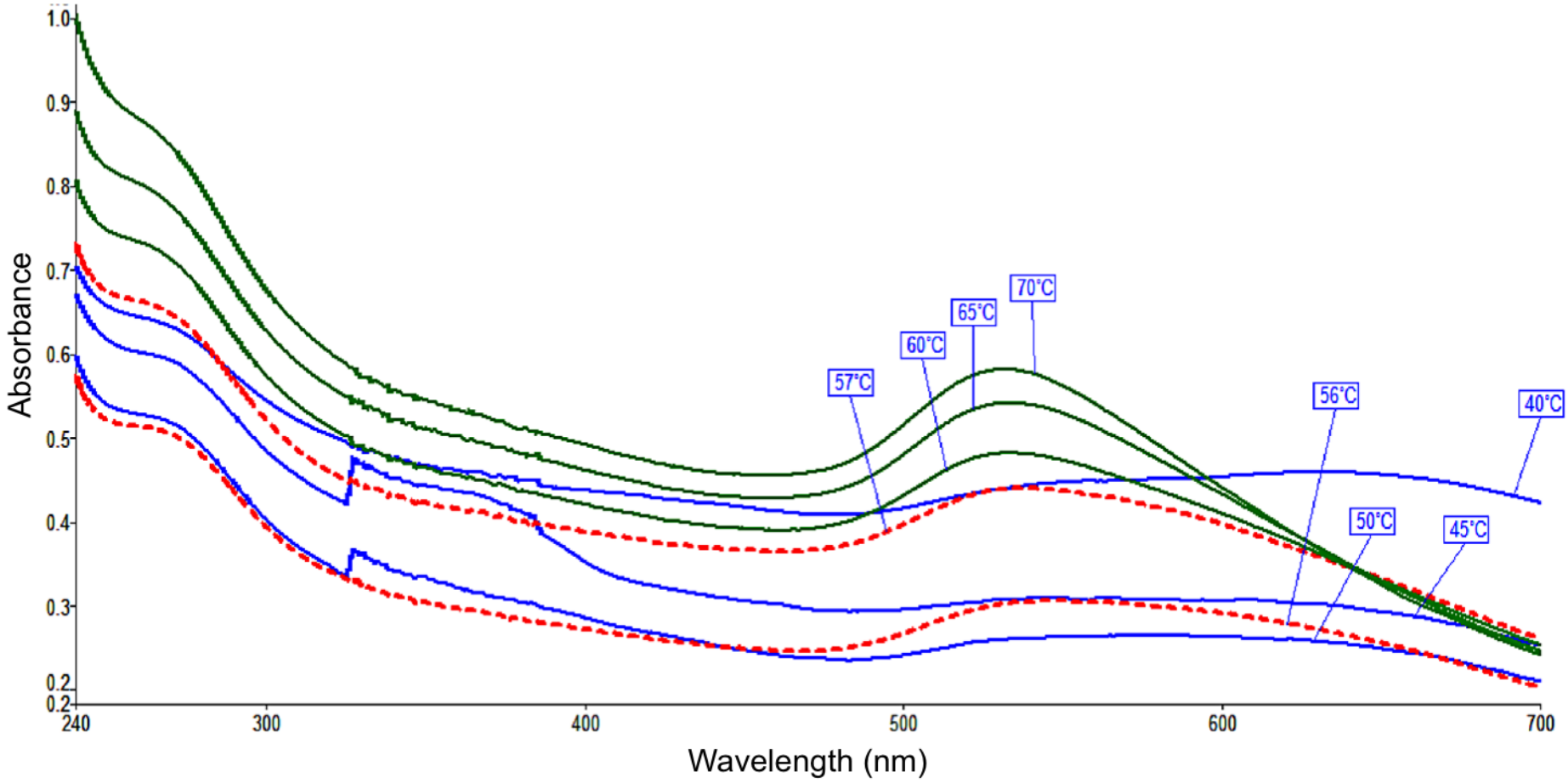

Figure 3.13: UV-visible spectra indicating the dissociation of hybridised oligonucleotide and resultant state of oligo-GNP dispersion, with a concentration corresponding to an initial optical density of 0.5 A (λ = 260). Data obtained by thermally regulated UV-visible spectroscopy analysis with curves in blue representing self-assembled oligo-GNP suprastructures (below 57°C) and curves in green represent dispersed oligo-GNP building blocks (above 57°C) and curves in red highlight the melting transition temperature where noticeable changes in LSPR properties occur.

3.3 Discussion

Self-assembly of individual building blocks into organised structures is a strategy currently being applied for the bottom-up fabrication of nanosystems[226], with examples including self-assembled monolayers (SAMs) and multi-layered nanostructures[227,228]. *In situ* self-assembly with respect to application, however, is a more recent development that could be utilised to provide further functionality and novel manufacturing opportunities[229,230]. This approach is envisaged as being advantageous within the fields of biology and medicine by potentially enabling non-invasive, responsive medical procedures[231].

In view of the intentions of the current work, which aims to provide further understanding of how SANs might perform within biological systems, rudimentary approaches towards self-assembly were initially established for subsequent investigations. Synthesised GNP building blocks and resultant suprastructures assembled using either the electrostatic attraction or molecular recognition approach are evaluated and compared.

3.3.1 Preparation and analysis of spherical GNPs as building blocks

Methods used to prepare precursor NPs, followed by post-preparative interfacial ligand exchange reactions with thiol containing compounds afforded surface functionalised spherical GNPs (section 3.1.1). Introducing complementary SAMs to GNP surfaces provided building blocks that self-assembled (section 3.2), providing suitable models for subsequent investigations. Synthetic routes were relatively quick and straightforward, utilised widely available reagents and produced sufficient yields for the current study. Adopting a two-step approach enabled easy control of NP size and shape with subsequent introduction of the desired surface functionality whilst ensuring retention of the original morphology, in agreement with earlier reports[232]. A decision to exclusively use thiol (SH) containing ligands was

based on previous findings that these functionalised NPs remain stable in the presence of electrolytes and pH ranges encountered within biological environments[233]. DMET and MES specifically were chosen as ligands to provide building blocks with either cationic or anionic SAMs because they are small monoionic molecules that provide a dense surface-coverage to GNPs, displaying the desired charge at neutral pH (pH 7.4)[181]. Oligonucleotides with 5'-terminal thiol modification (SH) were used to prepare building blocks for the intermolecular bonding approach, owing to widely reported success in literature[182]. Oligonucleotides were combined with GNPs in excess during synthesis (section 2.2.1.2), to ensure a consistent high ligand density on particle surfaces, according to previous reprots[182]. Whilst no attempts were made to control surface ligand or charge density, a range of synthesis strategies are under development[234,235] along with methods of quantification such as x-ray photon spectroscopy[236], which could be used in future enable further investigations into how these parameters influence self-assembly activity. Furthermore, separation techniques such as gel-electrophoresis have been used to isolate nanoparticles based on their corresponding charge density[237,238], which could be applied to obtain necessary control over critical design parameters. Regarding characterisation, TEM was an invaluable technique that enabled direct visualisation of GNPs and effectual evaluation of their size and morphology. Additionally, zeta potential measurements for NCG and PCG offered a suitable and reliable approach towards confirming ligand attachment whilst evidencing the desired building block surface functionality under aqueous buffer conditions. For oligo-GNPs, particle sizes calculated from TEM micrographs correlated with results of UV-visible spectroscopy, where size-dependent LSPR properties were revealed for both ~5 and ~20 nm particles. Attachment of oligonucleotides onto GNP surfaces was also conveniently verified using this approach, by detecting the resultant absorbance for these ligands at λ= 260nm. Although approaches used to confirm ligand attachment onto GNPs to form SAMs in this study did not directly confirm the formation of characteristic thiol-gold bonds (SH-Au), this could have been achieved using alternative techniques such as inductively coupled plasma–mass spectrometry[239]. However, considering that representative surface charges were observed for NCG and PCG (arising

from DMET and MES) and characteristic optical absorbance was detected for 5 nm and 20 nm oligo-GNPs at λ= 260nm (arising from oligonucleotides), this was considered as sufficient evidence to confirm ligand attachment. Furthermore, it was anticipated that subsequent self-assembly investigations would ultimately determine whether the prepared GNPs were effective building blocks as a result of successfully attaching the desired ligands.

3.3.2 Preparation and analysis of GNPs with specific shape morphologies

Direct and seed-mediated approaches described in section 2.2.1.3 to 2.2.1.5 to control the shape morphology of GNPs resulted in varied success (section 3.1.2). For instance, whilst rod-shaped GNP formation was observed, efforts to isolate these particles could not remove dissimilar shaped particles of a similar size (section 2.2.1.3). These results were supported by previous observations, which revealed that this approach produced rod-shaped particles mixed with spherical GNPs[183]. An average aspect ratio of 2.1 ± 0.8 nm was calculated for GNRs, compared to previous reports of 4.6 ± 1.2 nm using the same method[183]. This difference was attributed to the dissimilar precursor GNP size used in the seed-mediated synthesis, resulting in divergent width to length ratios for GNRs. Similarly for GNTs, particles displaying the desired morphology were mixed amongst a diverse range of multifaceted polyhedron-like spherical GNPs after purification attempts (section 2.2.1.4), in agreement with previous findings[184]. Extensive shape control was achieved however for star-shaped GNPs, in support of earlier reports[185]. Particles appeared highly uniform, exclusively displaying the desired branched morphology (section 2.2.1.5). Effective control of the resulting shape in this instance can be related to the highly anisotropic characteristics of these particles and high concentration of shape-directing additives used during synthesis[240].

Considering physiochemical and structural properties of nanomaterials have been identified as critical design parameters for self-assembly[110]; uniform GNP shape morphology was considered fundamentally important for

subsequent investigations. Additionally, introducing functional SAMs, required to facilitate self-assembly, whilst retaining specific shape morphology remains particularly challenging, particularly when ionic surfactants such as CTAB are utilised in the synthesis[241]. It was noted that, there is considerable interest towards the design of specifically shaped nanoparticles[242], although underpinning mechanisms that govern shape control are still not fully understood[242]. Nevertheless, empirical trends are being reported, which inevitably will result in further optimisation in future. Consequently, it was decided that at present, spherical GNPs would be most suited for further investigation as rudimentary building blocks for self-assembly under biological conditions. Furthermore, it is anticipated that experimental designs and approaches developed in the current work could be subsequently applied to different shaped nanoparticle building blocks in future.

3.3.3 Evaluation of electrostatic attraction as a mechanism of self-assembly

Electrostatic interactions between oppositely charged nanomaterials have previously been utilised as a mechanism to facilitate self-assembly for the fabrication of nano-clusters, solid thin-films and hybrid colloids, via direct mixing and sequential addition[243]. Whilst ionic interactions of this nature have been extensively studied in many fields of chemistry, influence on nanomaterial behaviour is arguably less understood and often does not compare to microscopic or bulk equivalents[244]. Nevertheless, there has been notable progress towards understanding how electrostatically regulated nanosystems behave and how their properties can be controlled, modified and utilised[245-247]. Highlighting this, in 2013 Liu *et al* reported the first *in situ* visualisation of electrostatically driven self-assembling GNPs in real-time, using a fluid-cell to contain and observe aqueous specimens within an electron microscope[248]. In the current study, GNPs surface functionalised with oppositely charged mono-ionic ligands were combined (1:1 v/v) within aqueous buffer solution (pH 7.4) for one hour (section 3.2.1). In agreement with previous reports, simple mixing of the two complementary GNP building

blocks was seen to trigger the extensive formation of three-dimensional assembled suprastructures, multiple orders of magnitude larger than the original NPs (section 3.2.1)[244,245]. Underpinning this behaviour, it has been proposed that oppositely charged nanoparticles in suspension self-organise into repeating core-shell formations[244], as depicted in Figure 3.13. Additionally, it has been suggested by Kalsin *et al* that repulsive forces between nanoparticles of the same charge are overcome in this structural arrangement as a consequence of electrostatic screening, resulting in tightly packed particle clusters[244], as observed in this study. Supporting this notion further, Gellner *et al* evidenced multiple negatively charged 20 nm "satellite" GNPs self-assembling onto the surface of individual positively charged 80 nm "core" GNPs[249]. In addition to structural characteristics, self-assembly of nanoparticles is also understood to directly influence corresponding plasmonic properties[245,249]. However, results of the current work showed that plasmonic properties for self-assembled suprastructures had remained relatively unchanged, with minimal activity displayed within optical and near infrared regions of the electromagnetic spectrum (λ = 400 -700 nm), comparable to individual GNP building blocks, NCG and PCG (Figure 3.8) This was not unexpected, considering that wavelength specific coupling of photons with electrons via LSPR is determined by the nanoscale dimensions of the GNPs[249], with plasmonic properties known to be almost entirely diminished when particle diameters are comparable in size to the Fermi wavelength of electrons, as with NCG and PCG[222,250]. Instead, it is thought that nanoparticles displaying such small dimensions behave similar to "molecular species" with discrete electron excitations, according to the free-electron model[250], rather than the classical electrodynamic model according to Mie theory, which describes plasmonic behaviour for larger nanoparticles[251]. In summary, negatively and positively charged GNP building blocks, NCG and PCG, effectively self-assembled under aqueous conditions and offered a straightforward electrostatically-driven system for subsequent investigations under biological conditions.

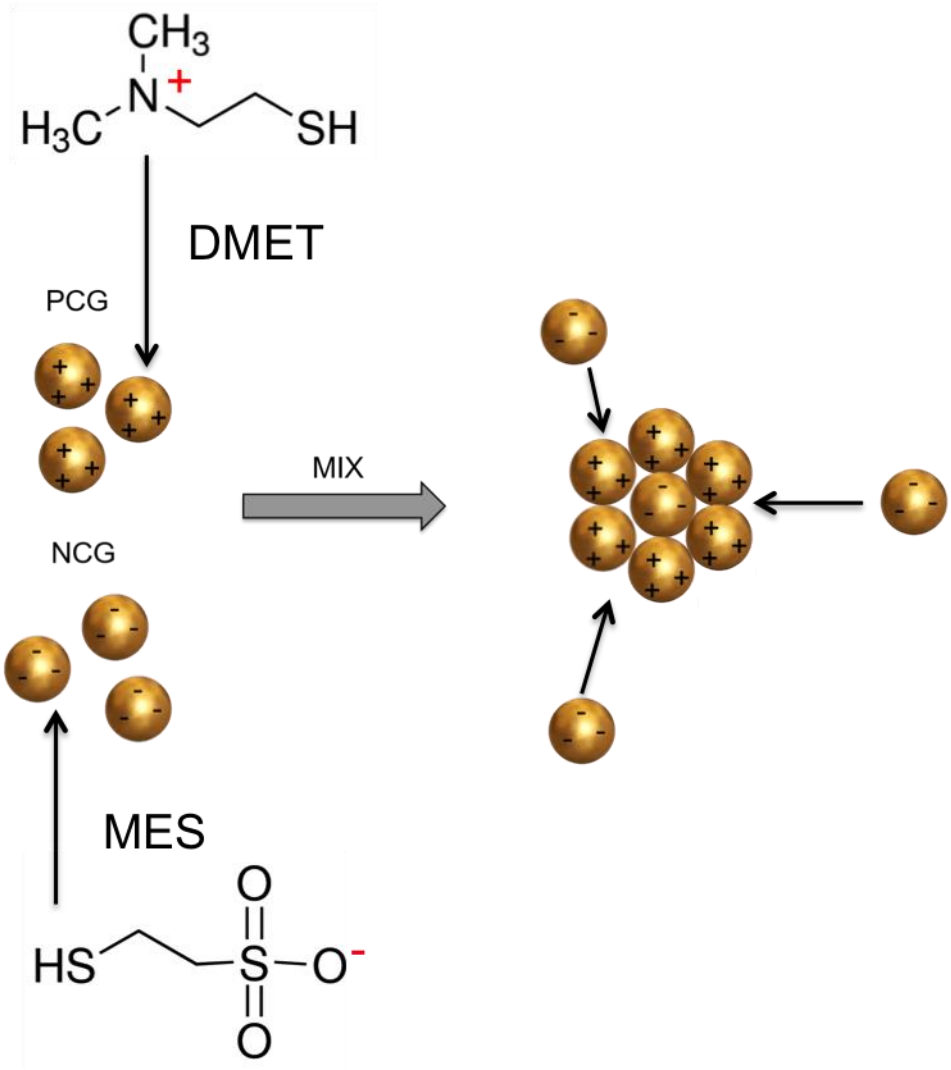

Figure 3.14 Schematic representation displaying the proposed self-organisation of oppositely charged GNPs as they self-assemble into larger nanostructures (black arrows indicate subsequent GNP interactions and assembly). Molecular structures of functional ligands DMET and MES on the surface of GNPs are provided with their relative complementary charges highlighted in red. (*Original image.*)

3.3.4 Evaluation of molecular recognition as a mechanism of self-assembly

Intermolecular bonding, broadly defined as attraction between neighbouring molecules, may arise as a result of any combination of van der Waals forces. More precisely, when specific interactions between complementary molecules are exploited, such as oligonucleotide hybridisation, the process is often referred to as "molecular recognition"[252]. This strategy, which has been utilised throughout macromolecular chemistry, has also previously been applied to prepare SANs[252,253.] Oligonucleotides in particular have attracted

considerable attention owing to the fact that they can be both naturally and synthetically obtained, providing an extensive range of sequence-specific molecules that can be used to implement programmed self-assembly and architectural control of nanomaterials[253]. In the current study, GNPs with diameters of either 5 or 20 nm were surface functionalised with complementary linear short-chain oligonucleotides to provide building blocks. To investigate their subsequent self-assembly, oligo-GNPs were simply mixed (1:1 v/v) under aqueous conditions (pH 7.4) for one hour (section 3.2.2). In agreement with previous findings[224], combining corresponding oligo-GNPs resulted in the formation of three-dimensional suprastructures, that displayed size dimensions in multiple orders of magnitude larger than when compared to the original GNP building blocks (section 3.2.2). Evaluation of TEM micrographs also confirmed the consistent inclusion of both 5 and 20 nm oligo-GNPs, supporting the notion that self-assembly was facilitated by oligonucleotide hybridisation between the dissimilar sized GNPs. In consideration of results of another study, further increasing the difference between particle sizes for complementary oligo-GNPs would have been advantageous with respect to structural characterisation via microscopy[249]. Regarding plasmonic properties, considerable distinctions were identified between the spectral profiles of individual oligo-GNPs compared to their assembled counterparts. Distinctive particle size-dependent SPR peaks at 524 nm (5 nm oligo-GNPs) and 526 nm (20 nm oligo-GNPs) were observed to entirely diminish, with plasmonic activity for suprastructures experiencing notable red shift and broadening between 500 – 700 nm, with a maximum absorbance at 605 nm. This behaviour, which is considered characteristic of GNP clustering, is known to arise as a result of interparticle plasmonic coupling[245,249] and is often described as a hybrid nano-property. Although there is still some debate regarding the underpinning mechanisms, models based on the work of Maxwell and Garnett are often applied to explain this phenomenon[254]. According to their theory, resultant optical profiles are determined both by the discrete individual building blocks and the collective properties of the assembled structures[255]. Furthermore, it has been demonstrated that when neighbouring GNPs which are sufficiently close to each other are irradiated with light, an

extremely intensified, localised electric field is produced around the NPs. Interactions between photons and surface atoms are typically amplified as a result, producing surface-enhanced optical phenomena[256]. This effect has been exploited most notably for SERS applications, although more recently biomolecular imaging techniques have also emerged[257-261].

Regarding the design of oligonucleotides used in this study, general structure and specific sequences are represented in Figure 3.14. A 5'-terminus modified thiohexyl functional group (1) was utilised to graft oligonucleotides to the surface of GNPs, following a well-established route of attachment[114]. The characteristic negatively charged phosphate backbone (2) is then followed by an 8-nucleobase poly-thymine "spacer" and the specific 12-nucleobase complementary sequences (3). The decision to incorporate a spacer region was based on suggestions by Hurst *et al* that moving the "recognition sequence" further away from the surface of nanoparticles can reduce steric crowding[262], which can obstruct subsequent oligonucleotide hybridisation, potentially reducing self-assembly activity. Additionally, nucleobases are known to interact with gold through van der Walls forces, which can result in oligonucleotides "laying down" on the surface of GNPs, reducing their overall surface density and potentially further increasing steric crowding[263]. According to numerous studies, this effect is least notable for thymine nucleobases, as a result of lower affinity displayed towards gold[262,264]. In summary, 5 and 20 nm oligo-GNP building blocks effectively self-assembled under aqueous conditions, providing a system facilitated by molecular recognition for subsequent investigations under biological conditions.

Figure 3.15 Graphical representation of modified oligonucleotides and specific "recognition sites" used to investigate self-assembly of GNPs via molecular recognition. Highlighted, (1) thiohexyl functional group, (2) phosphate backbone, (3) complementary oligonucleotide sequence with an 8-nucleobase poly-thymine spacer. (*Original image*.)

3.3.5 Thermally regulated dissociation of self-assembled oligo-GNPs

Replicating a previously published study[222], thermal dissociation of oligo-GNP superstructures was employed to demonstrate how self-assembly can be reversible and regulated (section 3.2.3). In principle, there are numerous ways that reversible self-assembly could be achieved, including the use of parameters such as pH and temperature as well as enzymatic activity, light-to-heat conversion and application of magnetic and electrical fields for example[247,265,266]. In the present study, nucleic acid thermodynamic melting properties were exploited to trigger the disassembly process. Hybridised oligonucleotide sequences, referred to as double strand complexes undergo a process of "melting transition" at a specific temperature (T_m), as briefly described in section 3.2.3. Above this temperature, hybridisation becomes unstable, dissociation ensues and single-stranded oligonucleotides are reformed. Conveniently, single-strand oligonucleotides absorb twice as much light compared to their double-stranded counterparts at a characteristic wavelength (λ=260 nm)[222]. Furthermore, as evidenced in section 3.2.2 individual monodispersed oligo-GNPs also display considerably different optical properties compared to their self-assembled counterparts. Correlating these two events, using a programmed heating regime in conjunction with UV-visible spectroscopy, enabled the state of oligo-GNP dispersion to be determined as a consequence of oligonucleotide conformation. As revealed, utilised oligonucleotides in this investigation displayed a definitive T_m at 57 °C

(Figure 3.11). Below this temperature, optical properties of oligo-GNPs remained unchanged (Figure 3.12), consistent with the plasmonic profile of self-assembled oligo-GNPs and indicative that superstructures remained intact. At 57 °C, a sudden shift in plasmonic properties were seen, with the reappearance of a definitive peak corresponding to the SPR of individual monodispersed oligo-GNPs above this temperature. These findings were considered conclusive evidence that self-assembly activity of oligo-GNP building blocks was dependent on oligonucleotide hybridisation and could be thermally regulated, as depicted in Figure 3.15. Significantly, the T_m of oligonucleotides, which determines the temperature at which SANs will either self-assemble or dissociate, can be tailored by changing the length of recognition sequence and content of nucleobases[267]. In theory, several dissimilar oligonucleotides could therefore, be attached to multiple building blocks, permitting temperature controlled, multi-stage programmed self-assembly and disassembly, although this does not appear to have been demonstrated at present.

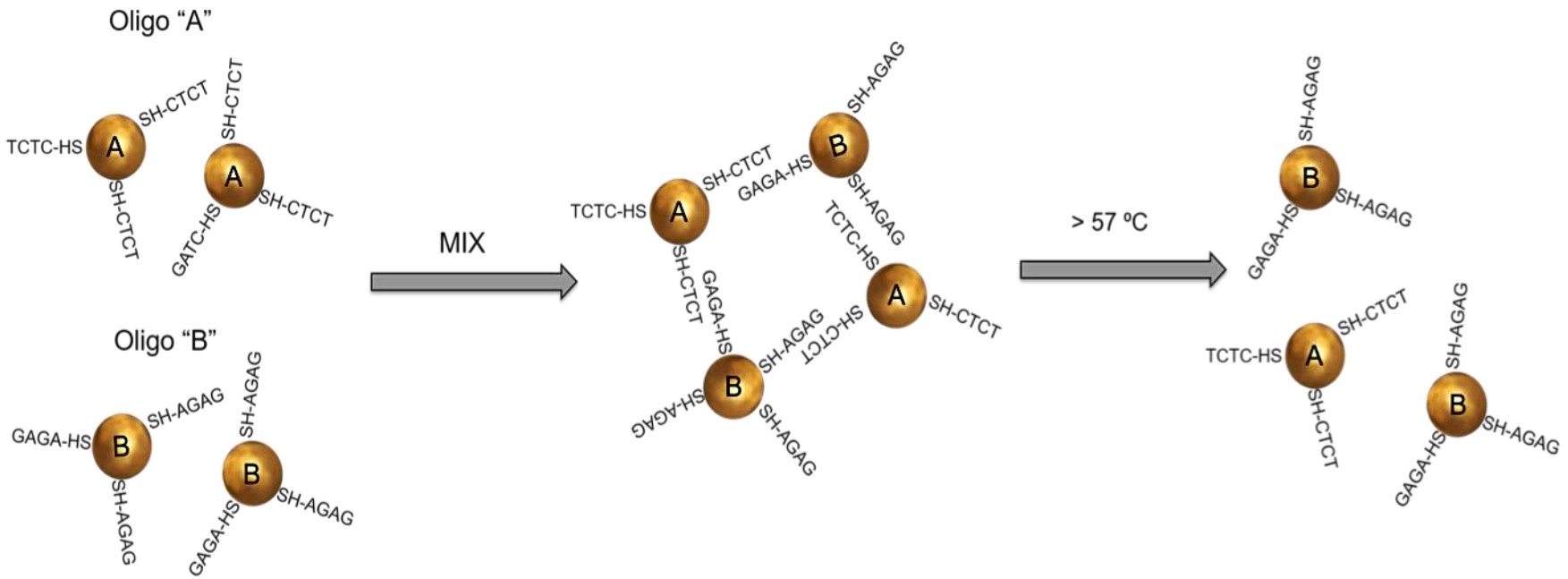

Figure 3.16 Schematic representation displaying the spontaneous self-assembly of GNPs functionalised with complementary oligonucleotides and thermally triggered disassembly and recovery of individual “building blocks” above (T_m) 57 °C (experimentally derived). (*Original image.*)

3.4 Conclusion

Two-step synthetic routes employed enabled preparation of uniform spherical GNPs with narrow size distributions and functional surfaces. Methods investigated for the synthesis of GNPs with specific shape morphologies were not suitable however, owing to a lack of shape uniformity. Consequently, spherical GNPs were selected for subsequent self-assembly investigations. Investigating the self-assembly of spherical GNPs under buffered aqueous conditions; both electrostatic attraction and molecular recognition were found to be effective mechanisms that facilitate the self-assembly of individual GNPs into suprastructures. It was concluded that modification of GNPs with functional SAMs is an effective method for the preparation of complementary “building blocks”. Furthermore, electrostatic interaction and molecular recognition are appropriate strategies for further investigation under biological conditions. Assembled suprastructures were revealed to be considerably larger in size than their individual GNP counterparts and were characteristic of structural agglomerates. The morphology and size of suprastructures was considered representative, providing a reference for evaluation of self-assembled structures formed under biological conditions in subsequent investigations. In agreement with previous studies, plasmonic properties of individually dispersed GNP building blocks with diameters of 5 and 20 nm were revealed to be different in comparison to their suprastructure counterparts. Although plasmonic properties were not utilised to implement further functionality in this study, extensive literature is available which describes how these properties could be applied within medicine and biology. Lastly, replicating the findings of a previously published study, thermal regulation was successfully applied to disassemble oligo-GNPs, demonstrating how individual building blocks can be designed to implement reversibility and further control over the processes of self-assembly activity.

4 Encapsulation of Gold Nanoparticles in Liposomes

Complementary building blocks NCG and PCG developed in chapter 3 were encapsulated in separate PEGylated liposome formulations (GNP-lipo) providing a proof-of-concept for the use of drug delivery vehicles to potentially control self-assembly activity. An alternative method of synthesis (section 2.2.2) based on "*lipofection*" technology[268] was investigated in an attempt to overcome current limitations associated with non-systematic encapsulation of hydrophilic nanoparticles that occurs using currently established methods. Lipid compositions of opposite charge relative to GNPs were employed with resultant electrostatic interactions between the two components exploited to facilitate their amalgamation. Physicochemical characterisation and morphological assessment of the prepared GNP-lipo systems was described to verify the successful inclusion of GNPs within these lipid vesicles with quantification of the lipid and internalised gold content attained using validated approaches. The loading content of each formulation was then derived from the measured ratio of gold to lipid to evaluate the influence of variable lipid and nanoparticle functionalities on the electrostatically driven encapsulation process.

4.1 Characterisation of GNP-liposomes

GNP-lipo systems were analysed using zeta potential, hydrodynamic particle size and microscopy studies as described in section 2.2.3, which follows the standard approach to liposome characterisation. Inclusion of the PEG moiety after post-formulation modification was evidenced and short-term (48 hour) colloidal stability was evaluated. SEM was utilised to evaluate the surface of liposomes and determine whether GNPs were present on the exterior of structures, with TEM applied to visualise internalised GNPs as a result of the electron density difference between gold and lipids. Specimens negatively stained with an electron-dense dye revealed whether vesicles were comprised of intact lipid bilayers with STEM-EDS mapping used to precisely locate the distribution of gold and identify additional elements within representative structures. This approach was also used to verify the successful removal of un-encapsulated GNPs.

4.1.1 Analysis of zeta potential displayed by liposomes

Table 4.1 summarises the zeta potential analysis of six independent batches of both NCL-PCG and PCL-NCG, respectively (n=6, mean ± S.D.). Measurements were performed before and after post-formulation modification with DPPE-PEG5000 (PEGylation). As depicted in Figure 4.1, NCL-PCG initially displayed a negative zeta potential of -20.1 ± 0.2 mV, which decreased in magnitude to -5.11 ± 0.59 mV after incorporation of the PEG-grafted lipid moiety. By contrast, PCL-NCG displayed a positive zeta potential of +2.9 ± 0.3 mV, which subsequently shifted to a negative value of -3.61 ± 0.32 mV after PEGylation. These observations reveal a characteristic charge-shielding effect taking place, consistent with previous reports for the insertion of PEG-grafter lipids into the exterior lamellar of liposomes[269]. Validating the accuracy of acquired measurements, analysis of a -42 mV zeta potential transfer standard gave a result of -38.8 mV, within the manufacturers specified variation limits (± 4.2 mV). (See appendix 3.)

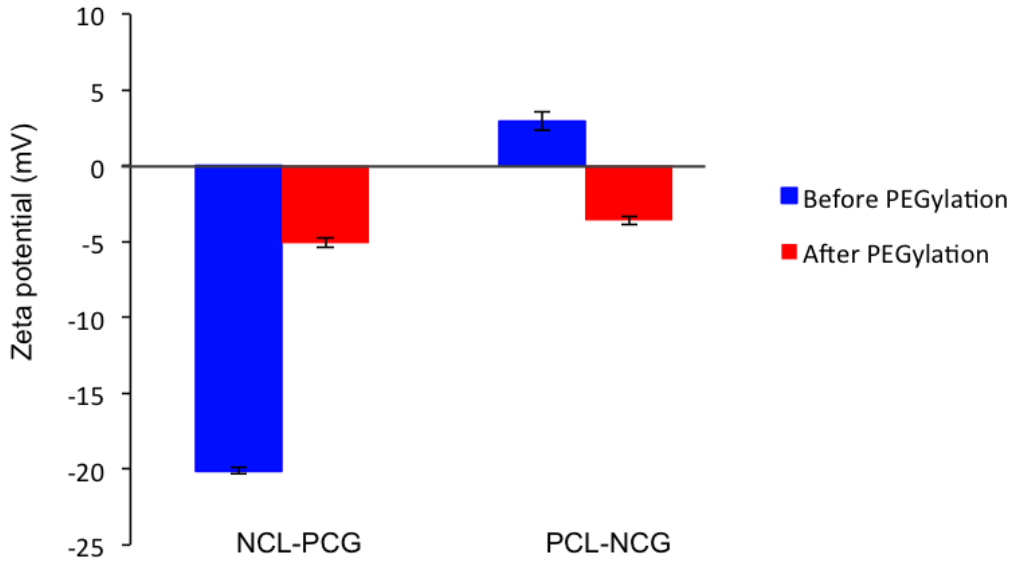

Figure 4.1: Comparison of zeta potential measurements recorded for NCL-PCG and PCL-NCG before and after (n=6, r=10) post-formulation modification with the PEG-grafted lipid, DPPE-PEG5000.

4.1.2 Analysis of liposomal hydrodynamic particle sizes

Table 4.1 summarises the intensity weighted (Z-average) hydrodynamic diameter of liposomes for the same six independent batches of NCL-PCG and PCL-NCG analysed in section 4.1.2 (n=6, mean ± S.D.). Size measurements for each GNP-lipo system were performed after initial preparation (T0) and after 48 hours of storage in glass vials at room temperature whilst protecting from light (T48). Observed in size distribution graphs (Figure 4.2), initial liposome hydrodynamic diameters were measured to be 183.0 ± 12.3 nm for NCL-PCG and 175.9 ± 8.1 nm for PCL-NCG with corresponding dispersity values of 0.08 ± 0.02 and 0.17 ± 0.06, respectively. By comparison, analysis of the same specimens after 48 hours revealed average liposome hydrodynamic diameters of 148 ± 2.3 nm for NCL-PCG and 147 ± 1.2 nm for PCL-NCG with dispersity values of 0.08 ± 0.02 and 0.08 ± 0.05, respectively. Statistical comparison using a paired two-tail student *t*-test shows the observed decreases in particle size for T48 to be significant from T0 for both NCL-PCG ($p < 0.01$) and PCL-NCG ($p < 0.001$). Dispersity values for T48 and T0, however, remain statistically identical ($p > 0.5$) for both GNP-lipo systems, indicating that the decreasing size of

colloidal particles is a universal trend. Validating the accuracy of acquired measurements, analysis of a polystyrene latex standard with a particle diameter of 192 nm gave a result of 200.7 nm, within the manufacturers specified variation limits (± 11 nm). (See appendix 2.)

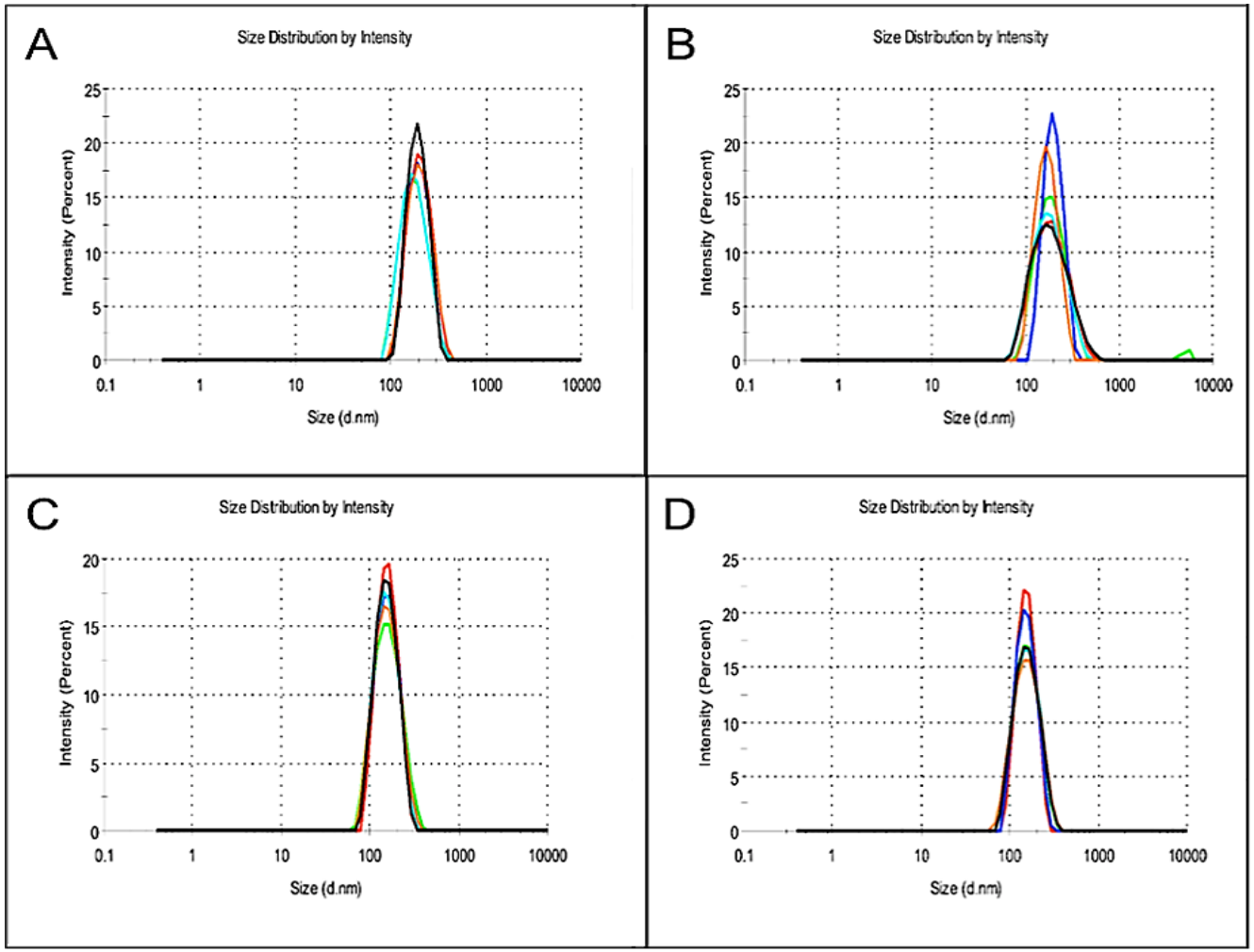

Figure 4.2. DLS hydrodynamic particle size distribution by intensity for six independent batches (n=6, r=20) of each GNP-liposome system (A): NCL-PCG, (B) PCL-NCG after preparation (T0) and (C): NCL-PCG, (D): PCL-NCG 48 hours after preparation (T48).

Table 4.1 Data obtained from the zeta potential evaluation of NCL-PCG and PCL-NCG before and after PEG-modification and hydrodynamic size analysis after initial preparation (T0) and after 48 hours of storage (T48). (n=6, mean ± S.D.).

	Initial DLS measurements (T0)		DLS measurements after 48 hours (T48)		Zeta potential measurements (mV)	
	Size (d.nm)	Dispersity	Size (d.nm)	Dispersity	Without PEGylation	After PEGylation
NCL-PCG	183 ± 12	0.08 ± 0.02	148 ± 2	0.08 ± 0.02	-20.1 ± 0.20	-5.11 ± 0.59
PCL-NCG	176 ± 8	0.13 ± 0.05	147 ± 1	0.08 ± 0.05	+2.94 ± 0.30	-3.61 ± 0.32

4.1.3 Microscopy studies and elemental analysis

Micrographs of SEM, TEM and corresponding EDS maps for NCL-PCG and PCL-NCG are presented in Figure 4.3 and Figure 4.4, respectively. From SEM images (Figure 4.3 A and Figure 4.4 A) spherical and well-dispersed structures were seen that display uniform, smooth surface morphologies with no features that can be ascribed to surface-exposed GNPs. Micrographs of negatively stained specimens (Figure 4.3 D, E and Figure 4.4 D, E) further reveal that these structures exhibit well-defined boundaries with the interior domain remaining unstained relative to the darkly contrasted background. Features characteristic of GNPs can be located within the confinements of these structures and appear as densely contrasted regions relative to the unstained background. To verify GNP encapsulation, a single representative structure for NCL-PCG and PCL-NCG were selected for elemental analysis. Resultant STEM micrographs and EDS elemental mappings of gold are presented in Figure 4.3 (B, C) and Figure 4.4 (B, C) with the corresponding interpreted EDS spectra displayed in Figure 4.5 Comparing STEM images with elemental maps confirmed features previously ascribed to GNPs correlated with the detection of gold, appearing confined within the boundaries of the selected vesicular structures with a clear distinction compared to the background. Other elements identified from EDS spectra include carbon, oxygen and phosphorus which can be assigned to the presence of lipids, sulphur which is indicative of ligands on GNP surfaces and copper from TEM specimen grids used in the analysis.

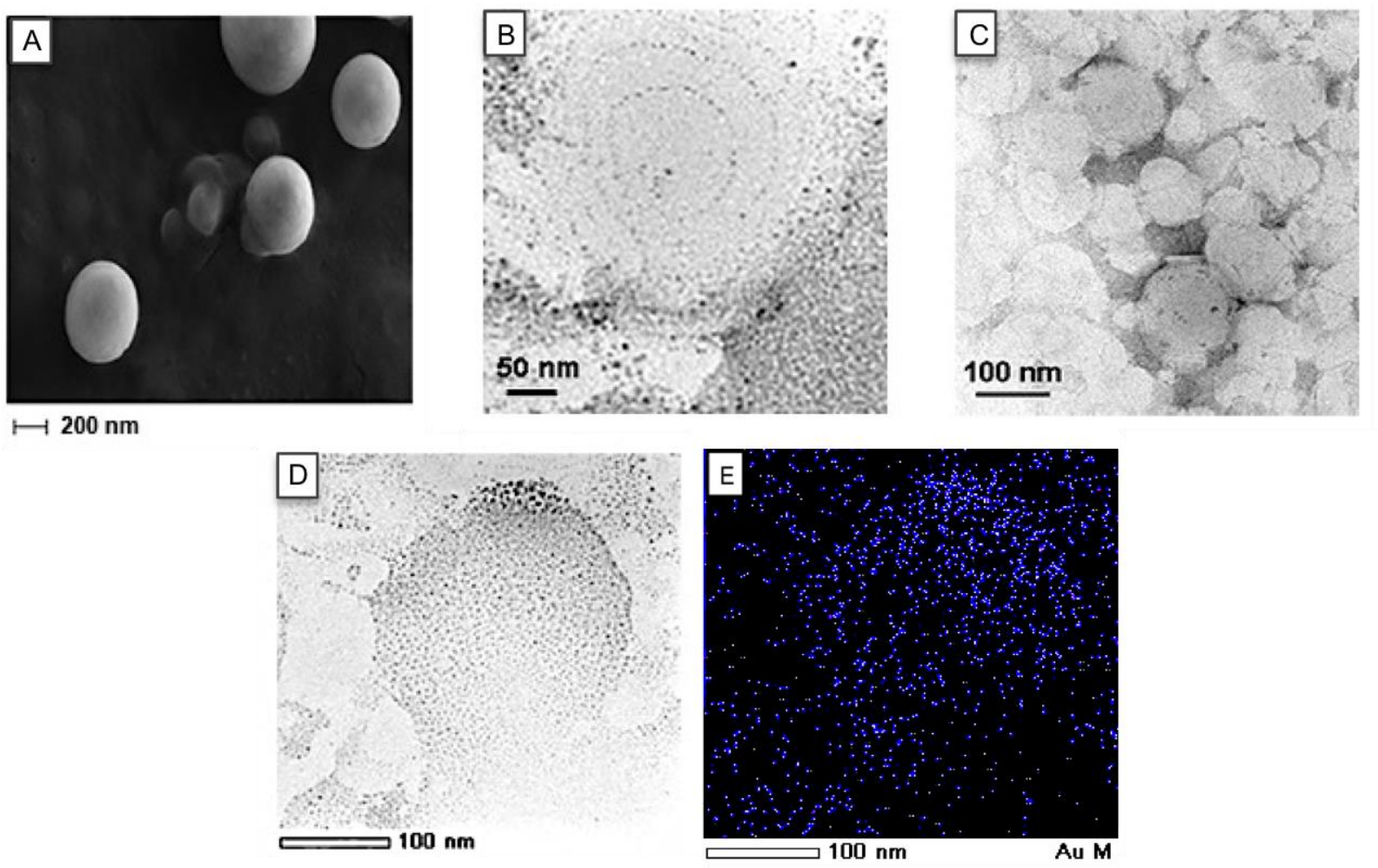

Figure 4.3.Representative images of NCL-PCG (A): SEM micrograph (B): STEM micrograph of an individual vesicular structure with (C): corresponding EDS map for gold. (D, E): TEM micrographs of negatively stained specimens.

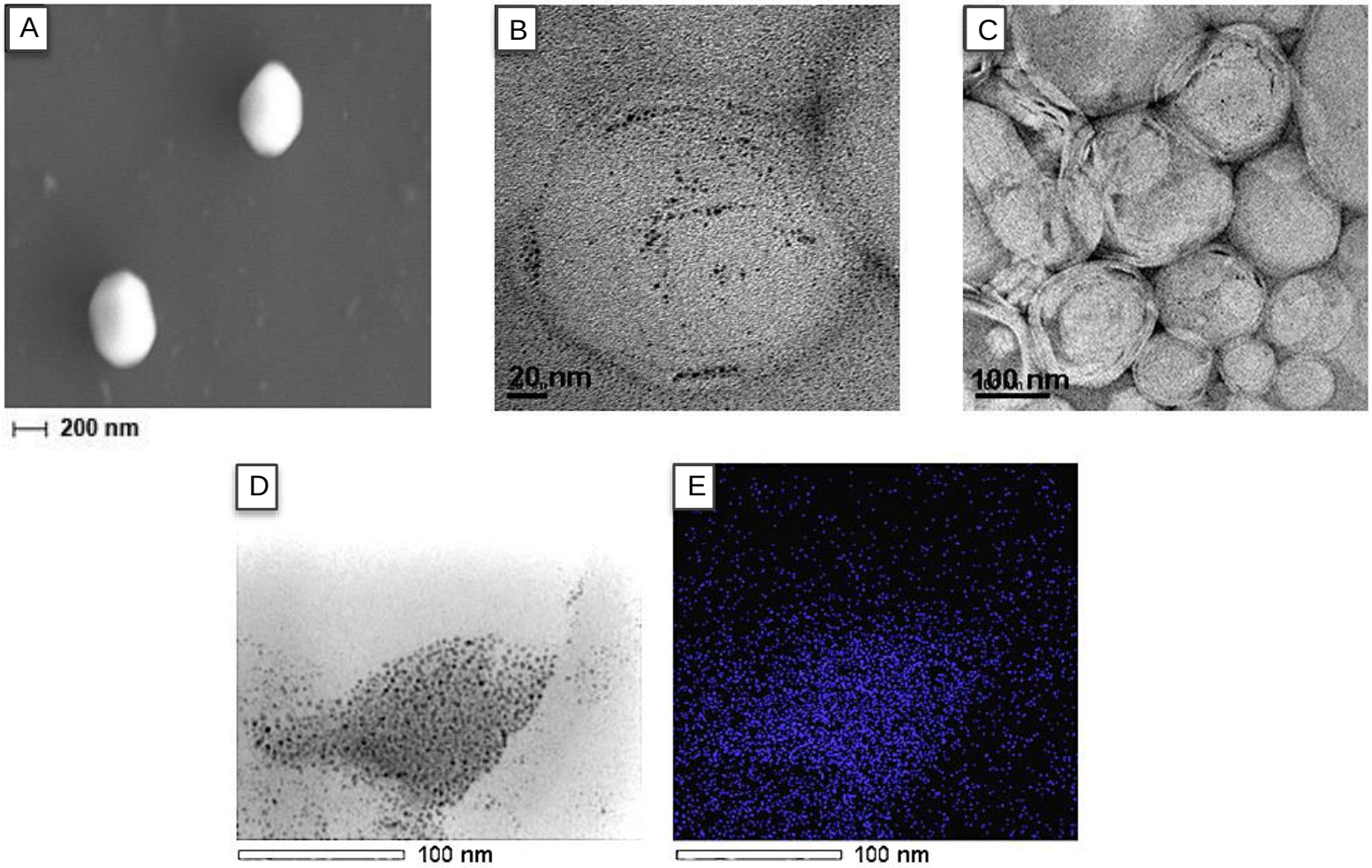

Figure 4.4. Representative images of PCL-NCG (A): SEM micrograph (B): STEM micrograph of an individual vesicular structure with (C): corresponding EDS map for gold. (D, E): TEM micrographs of negatively stained specimens.

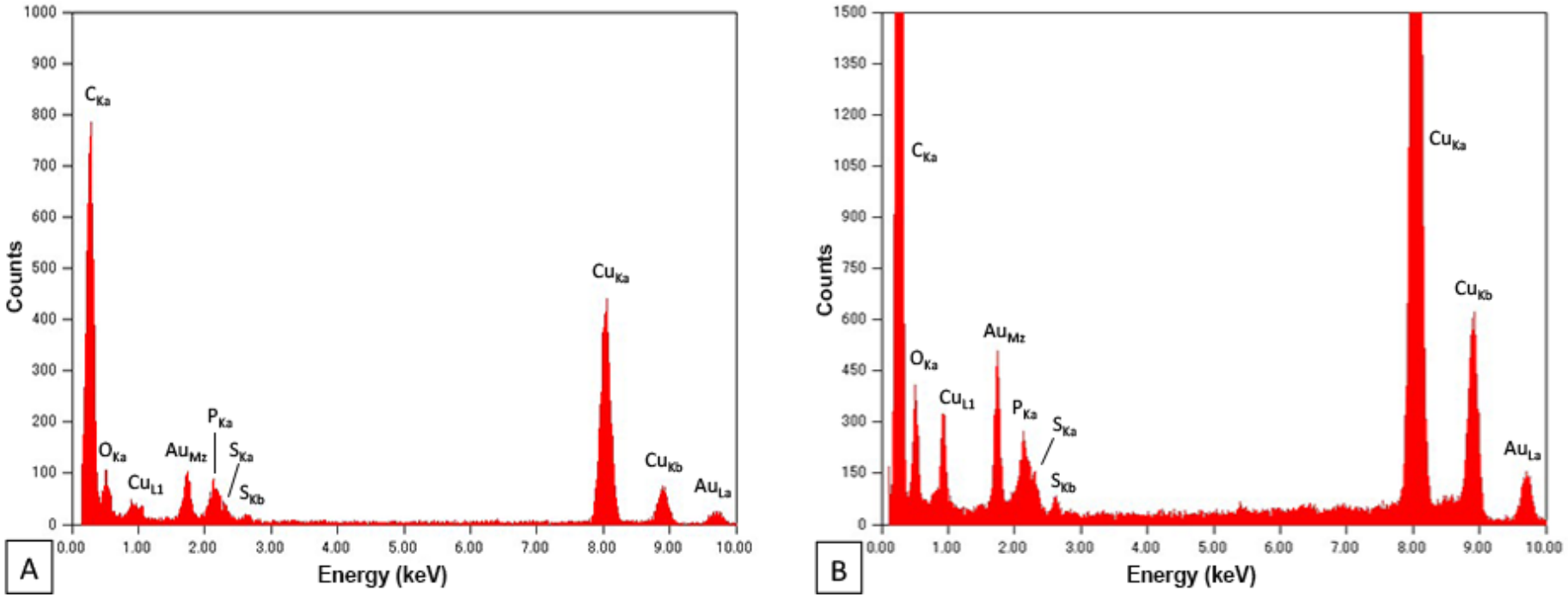

Figure 4.5**.** Interpreted EDS spectra corresponding to STEM images displayed in Figures 3B and 4B (A): NCL-PCG and (B): PCL-NCG. Identified elements include carbon, oxygen and phosphorus which can be ascribed to the presence of lipids, gold and sulphur attributed to gold nanoparticles with thiol-containing surface ligands and copper, which was present in the TEM specimen grid utilized in the analysis. Elements are labelled with the corresponding principal energy level (electron shell) from which the characteristic X-ray emission was detected (K*a*, L1, M*z*, K*b* and L*a*).

4.2 Evaluation of GNP encapsulation in liposomes

Evaluating GNP-lipo formulations, atomic emission spectroscopy (section 2.2.4.1) was used to quantify the encapsulation of gold and a colourimetric assay (section 2.2.4.2) was applied to measure the inclusion of the main lipid component (DPPC). A calibration curve was prepared for each approach by employing the method of external standards with percentage recovery determined in validation by adding known concentrations of analyte (spiking) to representative samples under identical experimental conditions. Corresponding concentrations of gold and lipid were calculated in parallel on the same samples for each independent batch of NCL-PCG and PCL-NCG, using the derived equations of the least squares regression lines obtained from calibrations. The resolved ratios of gold to lipid were then calculated to determine the corresponding loading content percentage of each formulation.

4.2.1 Quantification of gold in liposomal formulations

Concentrations of encapsulated gold calculated for each independent batch of NCL-PCG and PCL-NCG, as determined by AES are displayed in Table 4.2. A calibration curve was initially plotted from the analysis of prepared standards in replicate (n=5), ranging from 0 – 20 µg/ml of acid digested TPP-GNPs (Figure 4.6 A), from which the equation of least squares regression line was derived ($y= 8507.5x + 204.02$). Subsequent analysis of GNP-lipo specimens revealed NCL-PCG to contain an average of 14.9 ± 6.1 µg/ml of gold and PCL-NCG 6.2 ± 2.9 µg/ml (n=6, mean ± S.D.). To validate the procedure, average recovery of gold from samples containing known concentrations of either acid digested NCG or PCG in three separate experiments (n=3) was determined and calculated to be 93.6 ± 4.6% and 98.8 ± 7.4%, respectively. Figure 4.6 (B) shows statistical comparison using a paired two-tail student *t*-test and it was observed that there was no significant difference ($p>0.05$) in recovery and detection of gold from specimens containing either NCG or PCG, which were utilised in the preparation of GNP-lipo systems.

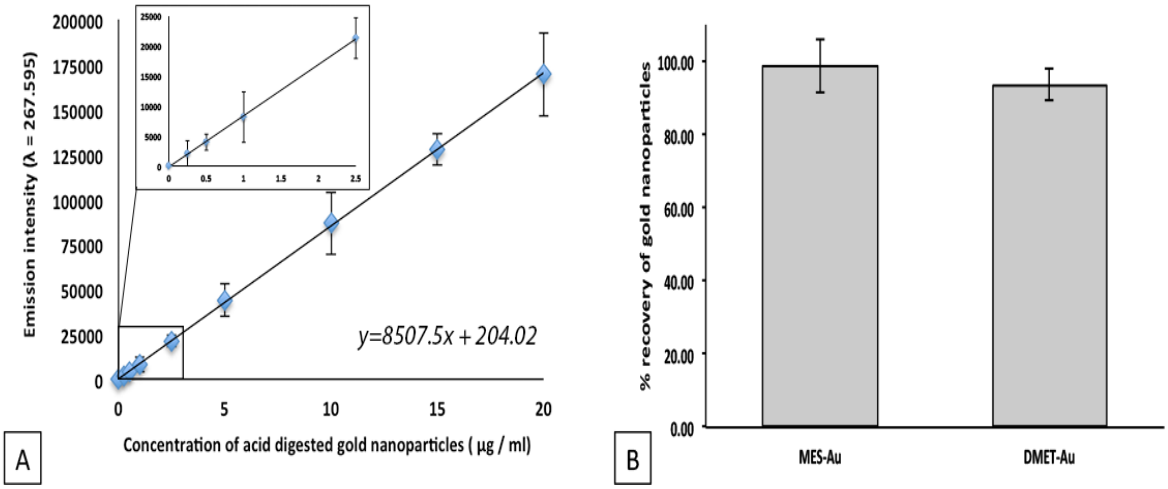

Figure 4.6 Quantification of gold encapsulation by AES (A): Calibration plot of digested TPP-GNPs with (insert) highlighting lower concentrations (n=6). (B): Bar graph comparing the relative (%) recovery of DMET-GNPs and MES-GNPs (n=3). Values are expressed as mean with error bars representing standard deviation.

4.2.2 Quantification of DPPC lipid in liposomal formulations

Concentrations of DPPC lipid calculated for each independent batch (n=6) of GNP-lipo systems as determined using the colorimetric Stewart assay are displayed in Table 4.2. A calibration curve was initially plotted from the analysis of prepared standards, ranging from 0 – 40 µg/ml of DPPC in chloroform to determine the assay response (Figure 4.7 A), from which the equation of least squares regression line was derived (y= 0.0103x + 0.0291). Specimens from the same batches of each GNP-lipo system used for gold quantification were then analysed, with NCL-PCG revealed to contain an average of 202.4 ± 39.7 µg/ml and PCL-NCG 148.0 ± 30.4 µg/ml of DPPC lipid (mean ± S.D.). To validate the procedure and confirm selectivity of the ammonium ferrothiocyanate reagent, average recovery and detection of DPPC from samples containing known concentrations of analyte in the presence of additional lipids included in formulations, PCL and NCL, (DPPG and DPTAP) in three separate experiments (n=3) was calculated to be 103.7 ± 7.3% (Figure 4.7 B).

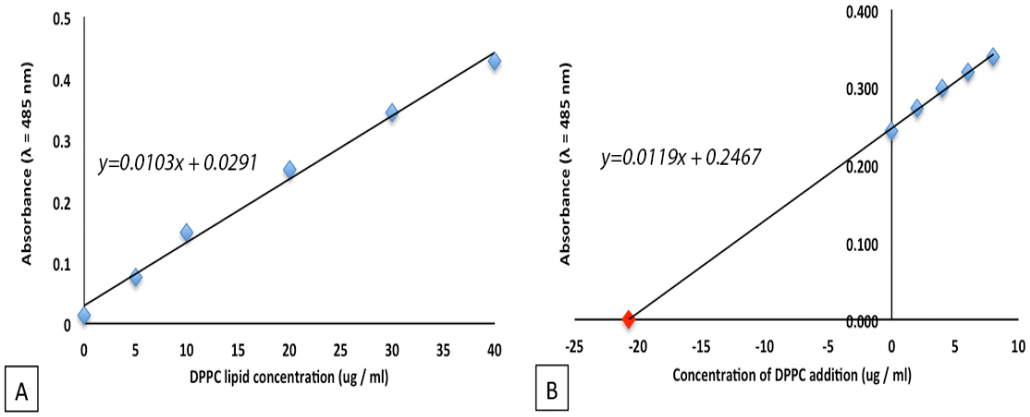

Figure 4.7 Quantification of DPPC lipid using the colorimetric Stewart Assay (A): Calibration plot for the detection of DPPC lipid (B): standard additions curve (validation, n=3) for DPPC recovery with (red marker) extrapolated value representing an average recovery of 103.7 ± 7.3% of the original concentration of DPPC (20 µg/ml) from the sample matrix

4.2.3 Loading content of encapsulated gold for GNP-liposomes

In an attempt towards standardising the evaluation of nanoparticle encapsulation, concentrations of gold and the main lipid component (DPPC) have been determined in parallel on the same samples. Applying the ratio of the two components, loading content percentage was calculated (Equation 4.1), providing assessable values for the concentration of encapsulated gold relative to lipid in each formulation. Derived loading content percentages for each independent batch (n=6) of NCL-PCG and PCL-NCG are displayed in Table 4.2.

Equation 4.1. Loading content percentage

$$\text{Loading content (\%)} = \frac{\text{Concentration of gold encapsulated}}{\text{concentration of DPPC lipid}} \times 100$$

From the measured concentrations of gold and DPPC in each batch, average loading content values were calculated to be 7.3 ± 2.6 % for NCL-PCG and 3.1 ± 1.5 % for PCL-NCG (mean ± S.D.). Statistical comparison using an unpaired student *t*-test revealed that the loading content for the two systems

was significantly different (p<0.05), indicating that the encapsulation of gold relative to the inclusion of DPPC lipid is dissimilar for the two GNP-lipo systems investigated.

Table 4.2. Values obtained from the quantification of gold and DPPC lipid for individual batches of NCL-PCG and PCL-NCG

	Batch number	Gold (μg/ml)	DPPC (μg/ml)	Loading content (%)
NCL-PCG	1	17.4	170.7	10.2
	2	17.2	240.6	7.2
	3	16.8	225.0	7.5
	4	7.8	213.4	3.7
	5	22.8	227.0	10.0
	6	7.2	137.7	5.2
	Mean ± S.D.	14.9 ± 6.1	202.4 ± 39.7	7.3 ± 2.6
	%RSD	41.2	19.6	35.3
PCL-NCG	1	5.3	159.0	3.3
	2	7.5	162.9	4.6
	3	7.1	151.3	4.7
	4	10.7	182.3	5.9
	5	2.6	139.6	1.8
	6	3.8	93.0	4.1
	Mean ± S.D.	6.2 ± 2.9	148.0 ± 30.4	4.1 ± 1.4
	%RSD	47.2	20.5	34.4

4.3 Discussion

Various strategies towards controlling the self-assembly of nanomaterials are currently under investigation[99], which could be utilised to regulate *in situ* performance. At present, these strategies typically utilise external stimuli, including light [266] and magnetic fields[86], or changes within the localised environment such as pH[72]. Alternatively, it might be possible to control self-assembly activity by physically separating complementary building blocks until activity is desired. Working towards providing a proof-of-concept, a synthetic strategy was developed to prepare liposomes and encapsulate NCG and PCG separately.

4.3.1 Synthesis of GNP-liposomes

Two distinct GNP-liposome systems were prepared using a developed synthesis strategy that exploits electrostatic interactions between functionalised GNPs and lipids of opposing charge, as detailed in section 2.2.2. The proposed configuration of the formulated GNP-lipo systems is illustrated in Figure 4.8, displaying a regular nanoparticle distribution at the aqueous-bilayer interface, located at the peripheral of the central aqueous core and in-between adjacent lamellae. It is conceived that the liposomal systems prepared in this study are dissimilar from the three general categories of metallic nanoparticle-liposome configurations previously reported: nanoparticles distributed amongst lipid tails that constitute bilayers[270], within the liposomal aqueous core[271,272] or physically absorbed onto the exterior surfaces of liposomes[273]. Additionally, it is hypothesised that the presented synthetic strategy overcomes current limitations identified from current methods of encapsulating nanoparticles in the aqueous core, which rely on a spontaneous process that results in low numbers of particles per liposome[272].

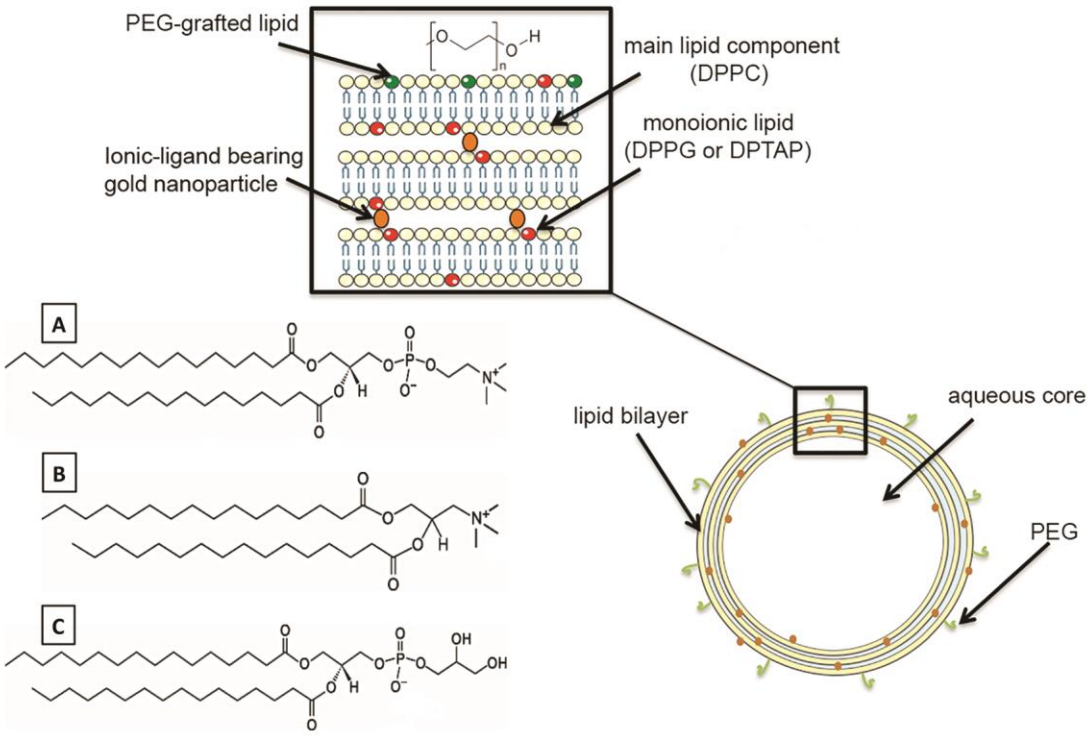

Figure 4.8 Proposed structure of a multilamellar liposome with encapsulated GNPs at the bilayer-aqueous interface, with lipid structures. Molecular structures of lipids utilised in the preparation of NCL-PCG and PCL-NCG are presented (A): DPPC, (B): DPTAP, (C): DPPG. (*Original image*.)

The multistep strategy presented in Figure 4.9 initially utilises the widely reported reverse-phase evaporation method (REV)[274] to formulate GNP-lipos whilst exploiting electrostatic interactions between lipid "headgroups" and ligands on GNP surfaces. The attraction between oppositely charged GNPs and lipids is proposed as a facilitating mechanism that brings the two components into close proximity at the interface of a biphasic mixture (white arrows, Figure 4.9 A, B). As the REV procedure progresses the organic solvent is gradually depleted, lipids progressively transfer into the aqueous phase triggering spontaneous self-organisation of the lipid molecules to form closed lipid-bilayers[275], entrapping associated GNPs throughout their liposomal structures. Crude GNP-lipos are then processed *via* "size extrusion", a technique that repeatedly forces the vesicles through 200 nm porous filter membranes to achieve a homogenous colloidal particle size distribution[276]. Starting extrusion at an elevated temperature and working towards room temperature was found to assist the process, avoiding fouling of the extrusion filter membrane. The resultant suspensions were then

immediately subjected to PEGylation, using the PEG grafted lipid DPPE-PEG-5000. This was performed whilst passing through the melting-transition temperature (T_m) of the main lipid component, DPPC (41°C), which supports insertion into the outermost lamella of liposomes[277]. The decision to incorporate PEG exclusively into the exterior surface of vesicles using a post-formulation approach was based on previous reports that it prevents reduction of the internal aqueous volume of liposomes compared to pre-formulation methods[277], which could potentially hinder the encapsulation of GNPs. Post-formulation methods also avoid the use of excessive quantities of PEG which is known to make size-extrusion processing challenging[269,278]. In the final stage, excess nanoparticles and reagents are separated from GNP-lipos by size-exclusion gel chromatography, which exploits the differing mobility of particles and molecules as they pass through a porous matrix, a technique previously employed to separate liposomes and excess nanomaterials[272]. Although visually a band of nanoparticles was seen to retain within the chromatography column, as a precautionary measure the recovery of liposomes was restricted to a total of five 1 ml aliquots. This step was taken to ensure that subsequent characterisation and quantification was representative of GNP-lipos and encapsulated gold exclusively.

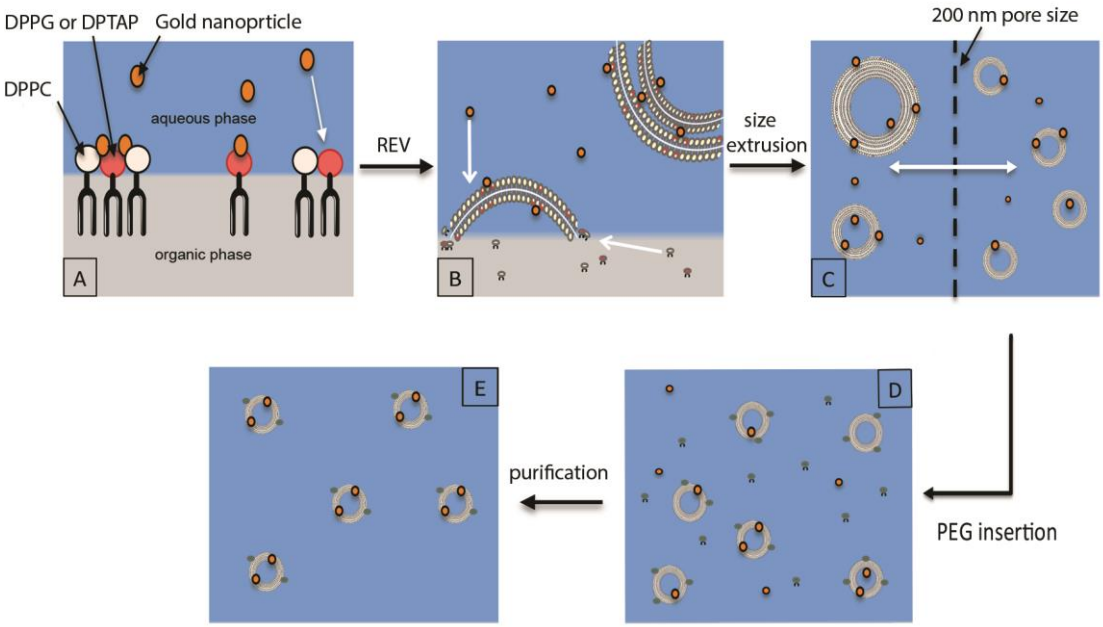

Figure 4.9: Simplified representation of the processes involved in the preparation of GNP-liposomes. (A) Lipid molecules interacting with GNPs (white arrow) at the aqueous-organic interface (B) GNP-liposome formation as the organic phase is depleted during reverse-phase evaporation, (C) size extrusion "resizes" crude liposomes to afford uniform colloidal particles, (D) post-formulation PEG insertion into the outer lamella of liposomes and (E) resultant PEG-grafted GNP-liposomes after removal of un-encapsulated GNPs and excess reagents *via* size exclusion chromatography. (*Original image*.)

4.3.2 Physicochemical properties of GNP-liposomes

Effective application of liposomes as delivery vehicles depends on their physicochemical characteristics, with parameters such as size, surface charge and composition having a profound influence on their stability and pharmacokinetic profile. In-turn, these properties dictate the ability of liposomes to retain encapsulated therapeutic reagents and also influence their behaviour within biological environments[279]. Consequently, when designing liposome-based technologies for medical applications, comprehensive evaluation reflecting the intended application is of paramount importance. Typically, this is achieved by using a range of complementary techniques, for instance, direct imaging by electron microscopy techniques provides qualitative information about the shape and internal architecture of liposomes but is not considered a reliable method to determine their size distribution. Instead, DLS is used to measure the hydrodynamic diameter of

liposomes whilst in a hydrated colloidal state, taking into account particle dispersion and the deposition of ions from solution that form the electrical double layer, appropriately replicating exposure conditions[272]. Additionally, this method provides insight into colloidal stability and homogeneity in a particular medium which can be monitored over time, which is not possible by microscopy[280].

Adopting this approach in the present study, colloidal particle size analysis of GNP-lipos via DLS (section 4.1.2) shows NCL-PCG and PCL-NCG to be well-dispersed suspensions consisting of vesicles that initially display narrow size distributions after preparation. Subsequent analysis on the same specimens after 48 hours however, reveals a statistically significant decrease in liposomal size for both systems, although dispersity values remain consistent indicating this to be a universal trend. In agreement with these observations, previous reports have demonstrated that interactions between ionic nanoparticles and phospholipid membranes can trigger lipid reorganisation, resulting in a decrease in vesicle size equivalent to approximately 20 % by volume[281]. This was suggested to occur as a consequence of the alteration of the tilt-angle of lipid head groups, facilitating an increase in lipid-tail density, characteristic of solid phase lipid bilayer fluidity[282]. Typically, solid phase behaviour results in increased order, tighter packing of lipids and a reduction in associated volume per molecule, contributing towards the overall liposomal size[283]. With regards to colloidal stability, liposomes must remain dispersed in solution at equilibrium to avoid well-known phenomena such as Ostwald ripening and flocculation, which can result in agglomeration, aggregation and phase separation. This can be achieved by introducing electrostatic properties to particle surfaces, or as in the present study, by steric stabilisation. The latter approach, attained in this investigation by insertion of a PEG-grafted lipid, was chosen based on previous observations that using PEG with the same average molecular weight (~5000 g/mol) provided liposomes with a 5 nm thick “coating” shielding the liposomal surface[284]. On this notion, it was hypothesised that PEG modification would provide a covering for GNPs bound to the exterior surface preventing them from subsequently “bridging” neighbouring

liposomes, demonstrated previously as a mechanism of colloidal destabilisation[285]. It was concluded from DLS observations that this approach had been effective, with no evidence of liposome-liposome interactions that would result in significantly larger size distribution profiles over time.

Further evidence of PEG inclusion into the exterior surface of liposomes was provided by Zeta potential analysis (section 4.1.1), with a reduction in the magnitude of surface charge displayed by NCL-PCG and a shift from a positive to a negative potential for PCL-NCG after PEGylation (section 4.1.1). These observations were considered to be characteristic of charge-shielding effects, where the ionic lipid headgroups are consequently positioned below a PEG stratum, effectively sheltering their contribution towards net surface charge, in-turn diminishing the electrical potential of the double-layer[269]. The low magnitude, negative zeta potential resultantly displayed by both GNP-lipo systems after insertion of DPPE-PEG5000 can be ascribed to the PEG structure itself[269]. Liposomal surface properties are known to significantly contribute towards toxicity and performance under biological conditions[286], with PEGylation typically associated with a range of technological and biological advantages including increased colloidal stability and biocompatibility[287]. Additionally, modification of liposomes with PEG is known to influence cellular uptake as a result of changes to long-range liposome-cell electrostatic interactions that determine the extent of cell membrane adhesion and internalisation[288]. Depending on cell type, it is suggested that liposomes with optimised PEG layer thickness and electrostatic properties could be designed to improve cell uptake and target specific cell populations[288], providing scope for future optimisation and development of analogous systems using the presented synthetic strategy.

4.3.3 Morphological assessment of GNP-liposomes

Electron microscopy techniques are routinely applied to visualise liposomes and study encapsulation of therapeutic agents, bilayer characteristics, structural integrity and surface topography[289]. Effective analysis is considered to be highly dependent on the use of appropriate sample

preparation methods so as to avoid undesired specimen changes that can produce unrepresentative artefacts making interpretation of results challenging[290]. For TEM analysis, carbon-coated specimen grids were chosen to ensure specimen stability under the electron beam, by providing an electron-transparent supporting substrate. Carbon support films however are typically hydrophobic which prevents uniform spreading and adhesion of the specimen, often referred to as drying effects. Overcoming this, a method of glow discharge was employed as described in section 2.2.3.1 to render the specimen grid hydrophilic before analysis, an approach that has been applied to optimise imaging of liposomes in previous studies[291]. Furthermore, as lipids are comprised of low mass elements that interact poorly with electrons, liposomes consequently display low contrast towards the electron beam and resulting micrographs. To enhance image contrast and the resolution of structural features for qualitative analysis, negative staining was attained utilising an electron-dense dye as detailed in section 2.2.3.1. By applying an electron-dense dye that is impenetrable to intact lipid bilayers, only the background becomes stained leaving the interior of liposome structures unchanged[292,293], as seen in micrographs presented in section 4.1.3. Similarly for SEM, sample preparation techniques were selected to preserve the physical characteristics of liposomes and optimise imaging (section 2.2.3.2) Snap-freezing and subsequent lyophilisation, a method widely used to preserve the structures of lipid-based vesicles and extend their shelf life was employed for this purpose[294,295]. Typically, a cryoprotectant agent such as trehalose or sucrose is added to colloidal suspensions before lyophilisation, binding to lipid headgroups to further preserve their structure and facilitate their reconstitution. The liposome systems investigated in this study however were not required for reconstitution and were also found to be sufficiently stable upon examination without addition of a cryoprotectant. Specimens were finally sputter coated before analysis to increase their conductivity, enhancing secondary electron detection and reducing beam penetration, which improves edge resolution required for topographical studies.

It was concluded from microscopy studies (section 4.1.3) that both NCL-PCG and PCL-NCG are representative of stable colloidal systems comprised of dispersed, spherical vesicular structures. Negative staining of the same specimens confirmed these structures to be intact with their internal aqueous domains remaining unstained relative to the background, as a result of their impermeable lipid bilayers[296]. The internal architecture of liposomes appears to be characteristic of multilamellar structures, with an "onion-like" appearance indicating the presence of concentric lipid bilayers that are separated by layers of water[297]. It is hypothesis that these separating layers of water between adjacent lipid headgroups are the primary location of GNP encapsulation, arising as a result of electrostatic interactions. However, it is noted that the distribution and extent of nanoparticle encapsulation appears to be variable between liposomes for both systems with occurrences of liposomes without any features that can be ascribed to GNPs. Smooth and uniform liposomal topography indicates the inclusion of a PEG-grafted lipid provides an additional coating to liposomal surfaces, effectively shielding otherwise exposed GNPs, in agreement with observations of DLS and zeta potential evaluation. Elemental analysis further confirms that the distribution of gold is primarily concentrated within the confinements of vesicle structures. A clear distinction in the detection of gold relative to the exterior of structures suggests the successful removal of excess GNPs *via* size exclusion chromatography, verifying subsequent quantification of gold to be exclusively from encapsulated nanoparticles. These observations indicate the developed synthetic strategy to be a promising route for the preparation of stable liposomes with internalised small (<4 nm) metallic nanoparticles.

4.3.4 Nanoparticle encapsulation efficacy

At present the evaluation of nanoparticle encapsulation within liposomes primarily involves qualitative and visual elucidation alone, which can be subjective[298]. Even instances investigating how the concentrations of nanoparticles in liposomal systems influence resultant performance provide no direct quantification in support[299]. As a matter of safety, it is of the opinion that newly developed nanosystems for therapeutic applications are prepared

with absolute precision. Further, as highlighted above, the encapsulation and distribution of nanoparticles in liposomes can influence resultant physical and chemical properties making the gold to lipid ratio a critical design parameter. In an attempt to standardise the evaluation of nanoparticle encapsulation in liposomes, the concentration of gold (section 4.2.1) and the main lipid component (DPPC) (section 4.2.2) were determined in parallel on the same samples and subsequently evaluated using conventional criteria (section 4.2.3). Established protocols utilised for quantification purposes in this study (section 2.2.4) were selected based on previous successful studies; with acid digestion and subsequent detection of gold *via* AES having been applied to measure GNP uptake in cellular studies[300] and the colorimetric Stewart assay to detect sub-micromolar concentrations of phosphatidylcholine lipids in the presence of phosphate buffers utilised in this investigation[301,302]. Whilst measuring only the main lipid component in the developed liposomal systems provides insight into the relationship between different lipid compositions and GNPs and what influence this has on nanoparticle encapsulation, it is noted that this approach is limited. Alternative techniques under investigation have been demonstrated to provide comprehensive analysis of the concentration of individual lipids in liposome formulations simultaneously, which may provide additional understanding in future investigations[303]. Validating method performance, the recovery of known quantities of analyte in representative matrices was calculated to be within 10% of the original concentration for both GNPs (NCG and PCG) and DPPC lipid (sections 4.2.1 and 4.2.2). Additionally, statistical comparison revealed no difference in the recovery and detection of gold from specimens of NCG and PCG, demonstrating that a single calibration can be used to quantify a range of functionalised GNPs, if their metal composition and nanoparticle core-sizes are not dissimilar (section 4.2.1). For the Stewart assay, which relies on the stoichiometric formation of a complex between the ammonium ferrothiocyanate reagent and phosphatidylcholine head group of lipids, the assay response is confirmed to be selective towards DPPC in the presence of supplementary lipids and phosphate buffer used in this investigation (section 4.2.2).

Assessing the efficacy of GNP encapsulation in liposomes for the two developed systems, loading content (%) was calculated to reveal the ratio of nanoparticles relative to lipid, providing a quantitative metric that can be compared, criterion previously applied to evaluate the encapsulation of drugs in nanosystems[304,305]. Considering the two developed GNP-lipo systems differ by inclusion of mono-ionic lipid (DPPG or DPTAP) and GNP functionality, it was hypothesised that ensuing variable electrostatic interactions thought to facilitate the entrapment process would result in different GNP entrapment capabilities. This notion is in agreement with experimental observations of this study with derived loading content values for NCL-PCG and PCL-NCG revealed to be significantly different (section 4.2.3). These results indicate that the selection of GNPs and lipids and their consequential interactions significantly influence the extent of nanoparticle encapsulation within liposomes. In view of earlier studies, parameters thought to be contributing towards this electrostatic process include the ligand density on GNP surfaces and the relative charge distribution of both the ligands and lipid structures[306,307] Comparably, electrostatic attractions have previously been recognised as an essential mechanism for the encapsulation of macromolecules in liposomes[308], including *lipofection* systems from which the presented synthetic strategy was based on[309]. Further studies have highlighted that the electrostatic attraction between lipids and macromolecules are the primary factor determining encapsulation potential[310], with experimental conditions that diminish the interaction significantly and reducing efficacy[311]. Additional parameters identified from these studies that have not been investigated in the current study but could be examined in future to provide optimal conditions to increase the loading content of analogous GNP-lipo systems including buffer composition, pH, ionic strength and liposomal size[310].

4.4 Conclusion

A novel synthetic strategy of encapsulating GNPs within multilamellar liposomes has been developed exploiting electrostatic interactions between ionic lipid compositions and particle surfaces. Evaluation of GNP-lipo morphology reveals particle distribution at the bilayer-aqueous interface, differing from previous reports of nanoparticles in bilayers or within the aqueous core of liposomes. The prepared GNP-lipo systems remain as well dispersed and uniform populations of colloidal particles for at least 48 hours but experience a universal reduction in particle size. Determining the ratio of gold to hydrated lipid and calculating corresponding loading content provides a quantitative metric that can be compared between different formulations, demonstrating a standardised approach of evaluating nanoparticle encapsulation efficacy. In the current work, a combination of variable lipid compositions and GNP functionalities was revealed to influence the encapsulation process and could be exploited for further control and optimisation. The reported strategy of utilising electrostatic interactions for the encapsulation of metallic nanoparticles is envisaged as a platform for the future development and study of analogous nanosystems.

5 Comparative toxicity studies of *in situ* SANs

GNP building blocks PCG and NCG (Chapter 3) and corresponding GNP-lipo systems NCL-PCG and PCL-NCG (Chapter 4) were tested using *in vitro* biochemical assays to determine whether they display any cytotoxic effects. Assessment was carried out on individual SANs and as they undergo *in situ* self-assembly to form suprastructures. Evaluation of individual and co-treatments with both GNP-lipo systems provides further information about the influence of liposomal surface coating on SANs, which could potentially prevent their self-assembly activity. It was anticipated that cytotoxicity could possibly be related to nanomaterial size[312], with different biological responses arising from *in situ* self-assembled suprastructures compared to their dispersed counterparts.

Evaluation of test material cytotoxicity was determined using MTT cell viability and LDH release assay following protocols described in section 2.2.7. An adherent, monolayer forming, male Chinese hamster lung fibroblast cell line (V79) was utilised in all experiments and routinely cultured to maintain exponential growth as detailed in section 2.2.6. Light microscopy was utilised to examine cell morphology and health after 24 hours of treatment time to supplement assay results.

5.1 MTT cell viability assay results

MTT assay results displayed in Figure 5.1 to Figure 5.3 show cell viability of male Chinese hamster lung fibroblast (V79) cell populations after 24 hours of exposure to a range of test material concentrations; 5, 1 and 0.1 µg/ml total gold with equivalent DPPC lipid concentrations of either 67.9, 13.6 and 1.4 (NCL-PCG) or 119.2, 23.8 and 2.4 µg/ml (PCL-NCG) respectively. Values are reported as % MTT metabolised relative to a healthy cell population (negative control), with less than 50% cell viability indicating a toxic treatment condition as defined by the TC_{50} criteria[313] Triton X-100™ (1%) induced cell lysis was applied as a positive control with PBS (pH 7.4) used as a vehicle control.

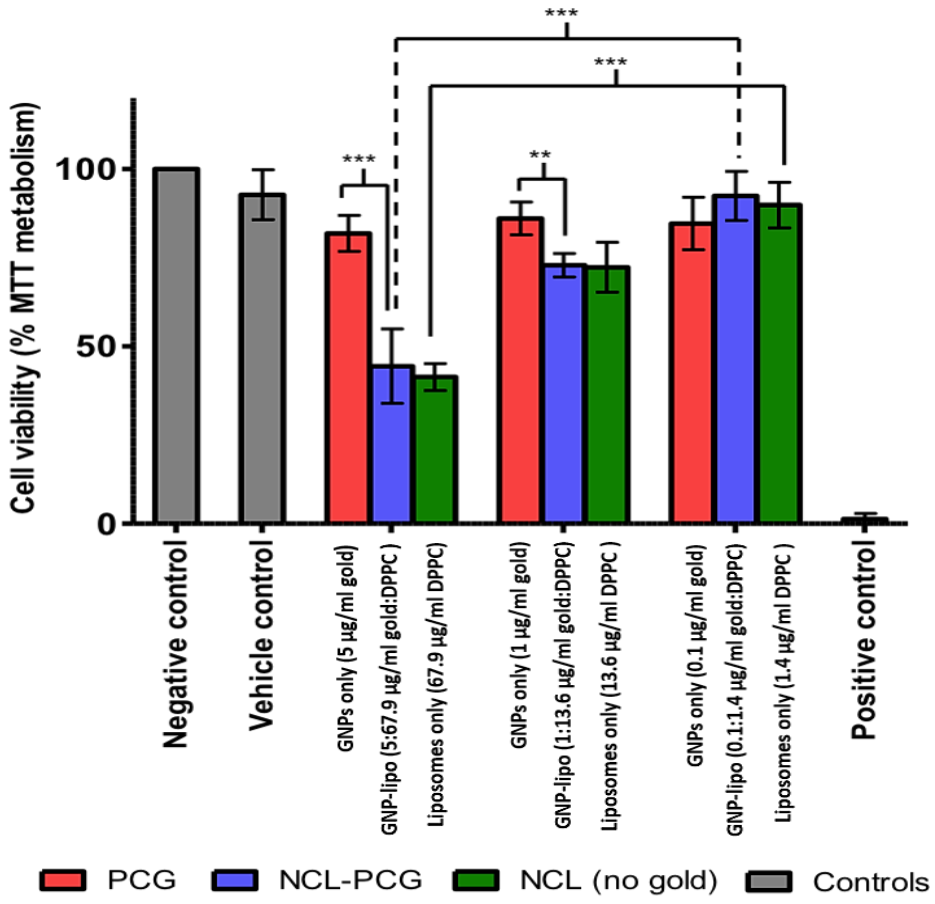

Figure 5.1: Viability of male Chinese hamster lung fibroblast cells (V79) after 24 hours of treatment with test materials. Concentrations range from 5 to 0.1 µg/ml of gold (PCG and NCL-PCG) with corresponding DPPC lipid concentrations of 67.9, 13.6 and 1.4 µg/ml (NCL and NCL-PCG), (n=6, r=6, Mean ± SD). Data was compared using two-way ANOVA and analysed using Bonferroni post-hoc test. Level of significance between data sets is indicated by ** = $p<0.01$ and *** = $p<0.001$.

Figure 5.1 shows the viability of male Chinese hamster lung fibroblast cells (V79) after 24 hours of treatment with positively charged building blocks (PCG) the corresponding lipo-GNP system (NCL-PCG) and negatively charged liposomes without gold (NCL). Statistical comparisons were made using two-way ANOVA and Bonferroni post-hoc analysis. TC^{50} criteria, where a test material concentration reduces assay activity by >50% relative to the negative control, was used to determine whether treatments were representative of a cytotoxic condition. Validating the assay sensitivity, cells treated with the positive control material (1% Triton X100™) produced a cytotoxic response, representative of total cell death. Additionally, no significant difference was revealed between the negative control and vehicle control ($p> 0.05$) confirming that the observed differences in cell viability arise as a result of cellular exposure to test materials.

Treatment with PCG was revealed to be non-cytotoxic at all concentrations investigated, with cell viability measured to be above the TC_{50} threshold. Treatment with NCL-PCG and NCL however, produced a cytotoxic response at the highest concentration investigated (5 µg/ml gold) with cell viability measured to be below the TC_{50} threshold. Comparison to the negative control (healthy cells) for all treatments shows that exposure to NCL-PCG at ≥1 µg/ml gold and the equivalent concentrations of NCL significantly reduce cell viability ($p< 0.05$). No significant difference was revealed between the negative control and cells exposed to GNP building blocks (PCG) at all concentrations ($p>0.05$). Treatment with the positive control material (1% Triton X100™) was also revealed to significantly reduce cell viability compared to each test materials at all concentrations investigated.

To evaluate potential dose-dependent cytotoxicity, statistical analysis was used to compare treatments at the highest and lowest concentration for each test material. Whilst no significant difference was observed between treatment concentrations for PCG ($p> 0.05$), NCL-PCG and NCL displayed significant dose-dependent cytotoxicity trends ($p< 0.001$). Analysis between test materials also shows that cellular response post treatment with NCL-PCG is statistically comparable to NCL at all concentrations ($p>0.05$). In

contrast, treatment with NCG results in significantly higher cell viability than NCL-PCG at 5 µg/ml (*p< 0.001*) and 1 µg/ml gold (*p< 0.01*).

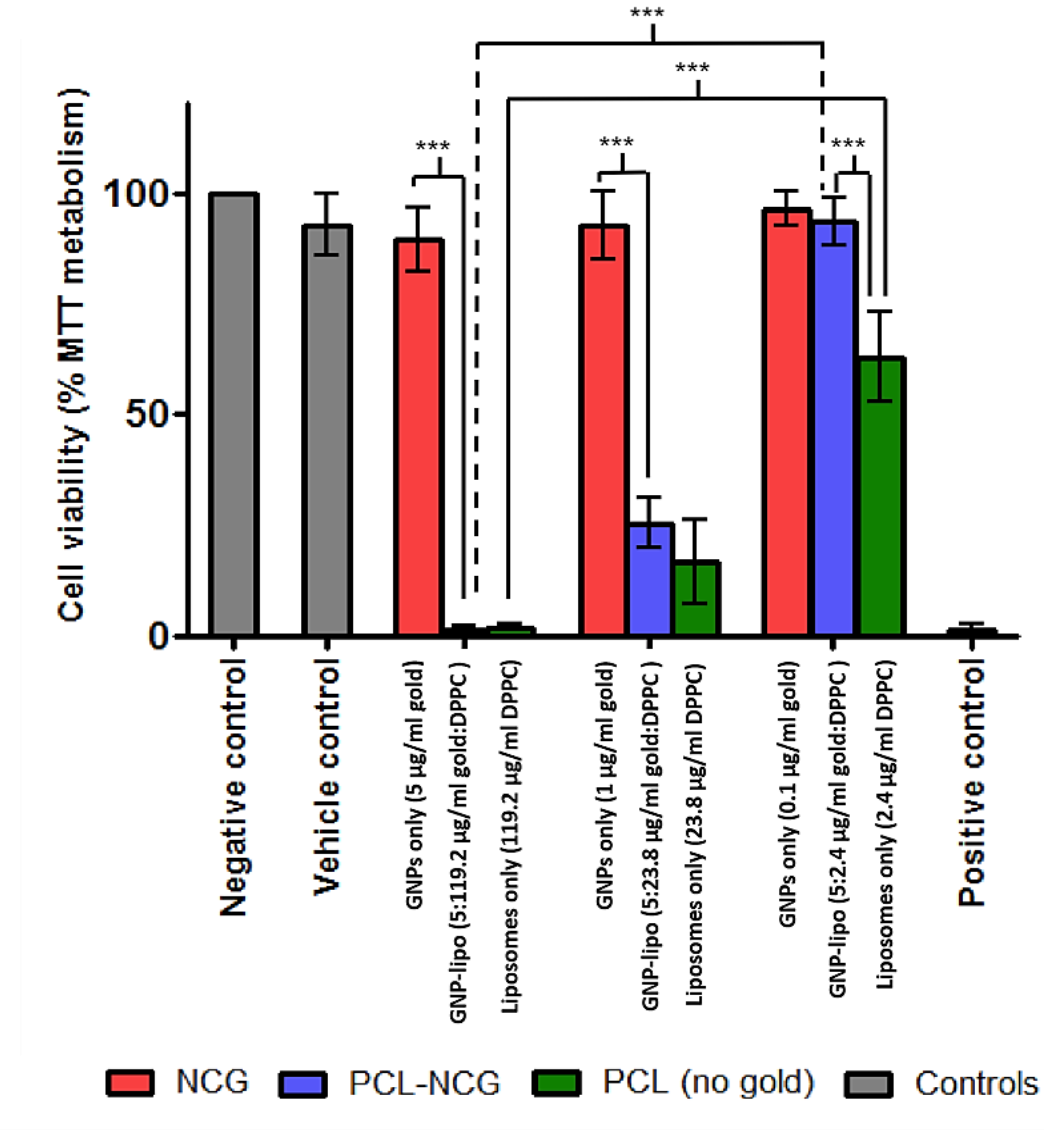

Figure 5.2: Viability of male Chinese hamster lung fibroblast cells (V79) after 24 hours of treatment with test materials. Concentrations range from 5 to 0.1 µg/ml of gold (NCG and PCL-NCG) with corresponding DPPC lipid concentrations of 119.2, 23.8 and 2.4 µg/ml (NCL and NCL-PCG), (n=6, r=6, mean ± SD). Data was compared using two-way ANOVA and analysed using Bonferroni post-hoc test. Level of significance between data sets is indicated by ** = p<0.01 and *** = p<0.001.

Figure 5.2 shows the viability of male Chinese hamster lung fibroblast cells (V79) after 24 hours of treatment with negatively charged building blocks (NCG) the corresponding lipo-GNP system (PCL-NCG) and positively charged liposomes without gold (PCL). As before, statistical comparisons were made using two-way ANOVA and Bonferroni post-hoc analysis with

TC_{50} criteria used to determine whether treatments were representative of a cytotoxic condition (>50% reduction in assay activity compared to negative control). Validating the assay sensitivity, cells treated with the positive control material (1% Triton X100™) produced a cytotoxic response, representative of total cell death. No significant difference was revealed between the negative control and vehicle control (*p> 0.05*) confirming that any observed differences in cell viability arise as a result of cellular exposure to test materials.

Comparable to results post treatment with PCG, cellular exposure to NCG did not produce a cytotoxic response at all concentrations investigated, with cell viability above the TC_{50} threshold. PCL-NCG at a concentration ≥1 µg/ml gold and the equivalent concentrations of PCL were observed to produce a cytotoxic response according to TC_{50}. Furthermore, treatment with the highest concentrations of PCL-NCG (5 µg/ml gold) and PCL resulted in cell viability that was statistically equivalent (*p>0.05*) to the positive control (Triton-X100 1%). Comparison to the negative control also revealed a significant reduction in cell viability after treatment with PCL-NCG at ≥1 µg/ml gold (*p<0.001*) and PCL at all concentrations (*p<0.001*). However, a significant difference was not observed between the negative control and after cells had been exposed to NCG at all concentrations (*p>0.05*).

To evaluate potential dose-dependent cytotoxicity, statistical analysis was used again to compare treatments at the highest and lowest concentrations for each test material. No significant difference was observed between treatment concentrations for NCG (*p> 0.05*), revealing that these GNP building blocks did not display a dose-dependent cytotoxicity trend. A significant dose-dependent response (*p< 0.001*) was exhibited by PCL-NCG and PCL however. Additionally, comparison between test materials at equivalent concentrations showed that cell viability post treatment with PCL-NCG was statistically comparable to PCL at ≥1 µg/ml gold (*p>0.05*). In contrast, treatment with NCG resulted in significantly higher cell viability than PCL-NCG at ≥1 µg/ml gold (*p<0.001*).

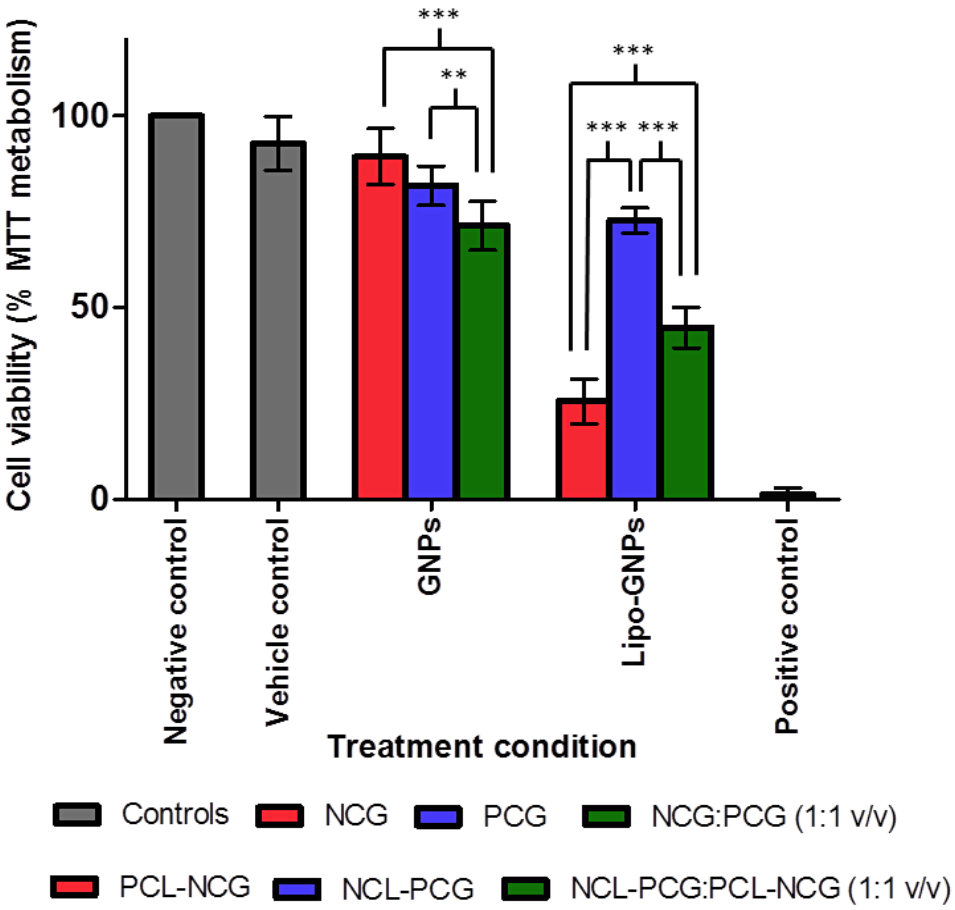

Figure 5.3 Viability of male Chinese hamster lung fibroblast cells (V79) after 24 hours of treatment with NCG, PCG and co-treatment with NCG:PCG (1:1 v/v) each at a concentration of 5 µg/ml gold and NCL-PCG, PCL-NCG and co-treatment with NCL-PCG:PCL-NCG (1:1 v/v) each at a concentration of 1 µg/ml gold, (n=6, r=6, mean ± SD). Data was compared using two-way ANOVA and analysed using Bonferroni post-hoc test. Level of significance between data sets is indicated by ** = $p<0.01$ and *** = $p<0.001$.

Figure 5.3 compares the viability of male Chinese hamster lung fibroblast cells (V79) after 24 hours of individual and co-treatments (1:1 v/v) with NCG and PCG (5 µg/ml total gold) or NCL-PCG and PCL-NCG (1 µg/ml total gold). Co-treatment with NCG and PCG represents *in situ* self-assembly of SANs into suprastructures. Using the same approach of analysis as previously, statistical comparisons were made using two-way ANOVA and Bonferroni post-hoc analysis with TC^{50} criteria used to determine whether treatments were representative of a cytotoxic condition (>50% reduction in assay activity compared to negative control). Validating the assay sensitivity, cells treated with the positive control material (1% Triton X100™) produced a cytotoxic response, representative of total cell death. No significant difference was

revealed between the negative control and vehicle control ($p > 0.05$) confirming that any observed differences in cell viability arise as a result of cellular exposure to test materials.

From the figure it can be seen that co-treatment with NCG and PCG did not induce a cytotoxic response according to the TC_{50} criteria, with cell viability remaining above 50%. Comparison to the negative control however revealed a significant reduction in cell viability ($p < 0.01$), which was not observed after treatment with individual GNP building blocks (NCG or PCG). Co-treatment with NCG and PCG (*in situ* self-assembly) also significantly reduced cell viability compared to treatment with either NCG ($p < 0.001$) or PCG ($p < 0.01$) individually. Additionally, no significance difference was seen in cell viability post treatment with NCG or PCG separately ($p > 0.05$).

For lipo-GNP systems, co-treatment with NCL-PCG and PCL-NCG was seen to induce a cytotoxic response with cell viability below the TC_{50} threshold. A significant reduction in cell viability was also revealed compared to the negative control ($p < 0.001$), analogous to treatment with NCL-PCG and PCL-NCG individually. Comparing between treatments, exposure to NCL-PCG and PCL-NCG simultaneously (co-treatment) was seen to result in cell viability that was significantly higher than PCL-NCG ($p < 0.001$) but lower than NCL-PCG ($p < 0.001$). A comparable difference in cell viability was also observed between treatments with NCL-PCG and PCL-NCG separately ($p < 0.001$).

5.2 LDH release assay results

LDH assay results displayed in Figure 5.4 to Figure 5.6 show the LDH release from the same populations (used for MTT assay) of male Chinese hamster lung fibroblast (V79) after 24 hours of exposure to a range of test material concentrations (5, 1 and 0.1 µg/ml total gold). Values are reported as a % of LDH released relative to a lysed cell population (positive control), by treating with Triton X-100™ (1%), with >50% LDH release indicating a toxic treatment condition as defined by the TC_{50} criteria[313]. A negative control was obtained by providing no treatment (healthy cells), with PBS (pH 7.4) used as a vehicle control.

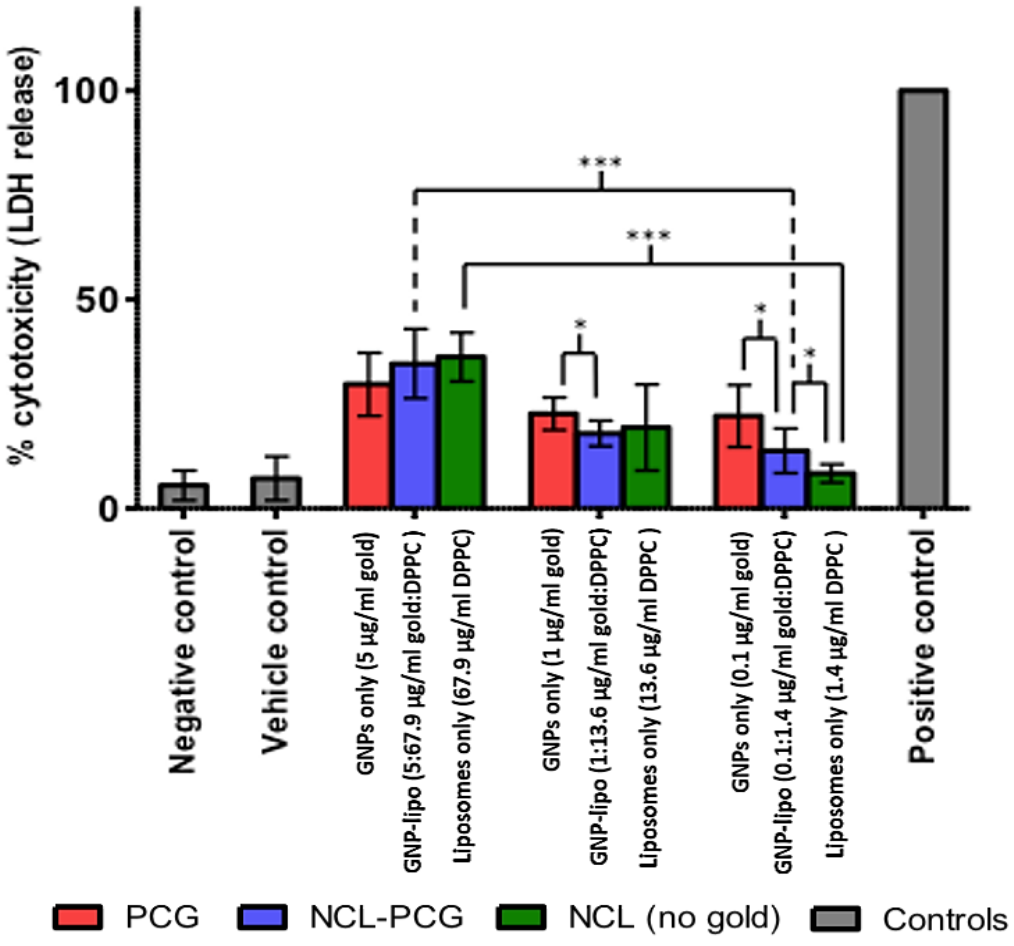

Figure 5.4 LDH release (%) from male Chinese hamster lung fibroblast cells (V79) after 24 hours of treatment with test materials. Concentrations range from 5 to 0.1 µg/ml of gold (PCG and NCL-PCG) with corresponding DPPC lipid concentrations of 67.9, 13.6 and 1.4 µg/ml (NCL and NCL-PCG), (n=6, r=6, mean ± SD). Data was compared using two-way ANOVA and analysed using Bonferroni post-hoc test. Level of significance between data sets is indicated by * = $p<0.05$ and *** = $p<0.001$.

Figure 5.4 shows the LDH release from male Chinese hamster lung fibroblast cells (V79) after 24 hours of treatment with positively charged building blocks (PCG) the corresponding lipo-GNP system (NCL-PCG) and negatively charged liposomes without gold (NCL). Statistical comparisons were made using two-way ANOVA and Bonferroni post-hoc analysis. TC^{50} criteria, where a test material concentration produces assay activity >50% relative to the positive control, was used to determine whether treatments were representative of a cytotoxic condition. Validating the assay sensitivity, the negative control (untreated cells) did not produce a cytotoxic response, representative of background LDH release from healthy cells. Additionally, no significant difference was observed between the negative control and vehicle control ($p> 0.05$) confirming that the differences observed in LDH release arise as a result of cellular exposure to test materials.

From the figure, it can be seen that exposure to each test material at all concentrations investigated resulted in non-cytotoxic treatment conditions, with LDH release below the TC_{50} threshold. In comparison to the negative control (healthy cells), a significant increase in LDH release was revealed after treatment with all concentrations of PCG ($P< 0.001$) and NCL-PCG (0.1 µg/ml gold, $p< 0.01$ and ≥1 µg/ml gold, $p< 0.001$). A significant increase in LDH release was also observed for NCL (no gold) but only at concentrations equivalent to 5 µg/ml gold ($p< 0.001$) and 1 µg/ml gold ($p<0.05$).

To evaluate potential dose-dependent cytotoxicity, statistical analysis was used to compare treatments at the highest and lowest concentrations for each test material. Significant dose-dependent LDH release was observed between treatment concentrations for NCL-PCG and NCL ($p< 0.001$) but a trend was not observed for the PCG building blocks ($p>0.05$), in agreement with the MTT assay. Comparison between test materials also revealed that the release of LDH after exposure to NCL-PCG was statistically comparable to NCL at ≥1 µg/ml gold but differed at the lowest concentration ($p<0.05$). In contrast, the opposite was seen between treatment with NCG and PCL-NCG, where LDH release was seen to be significantly different at ≥1 µg/ml gold ($p<0.05$).

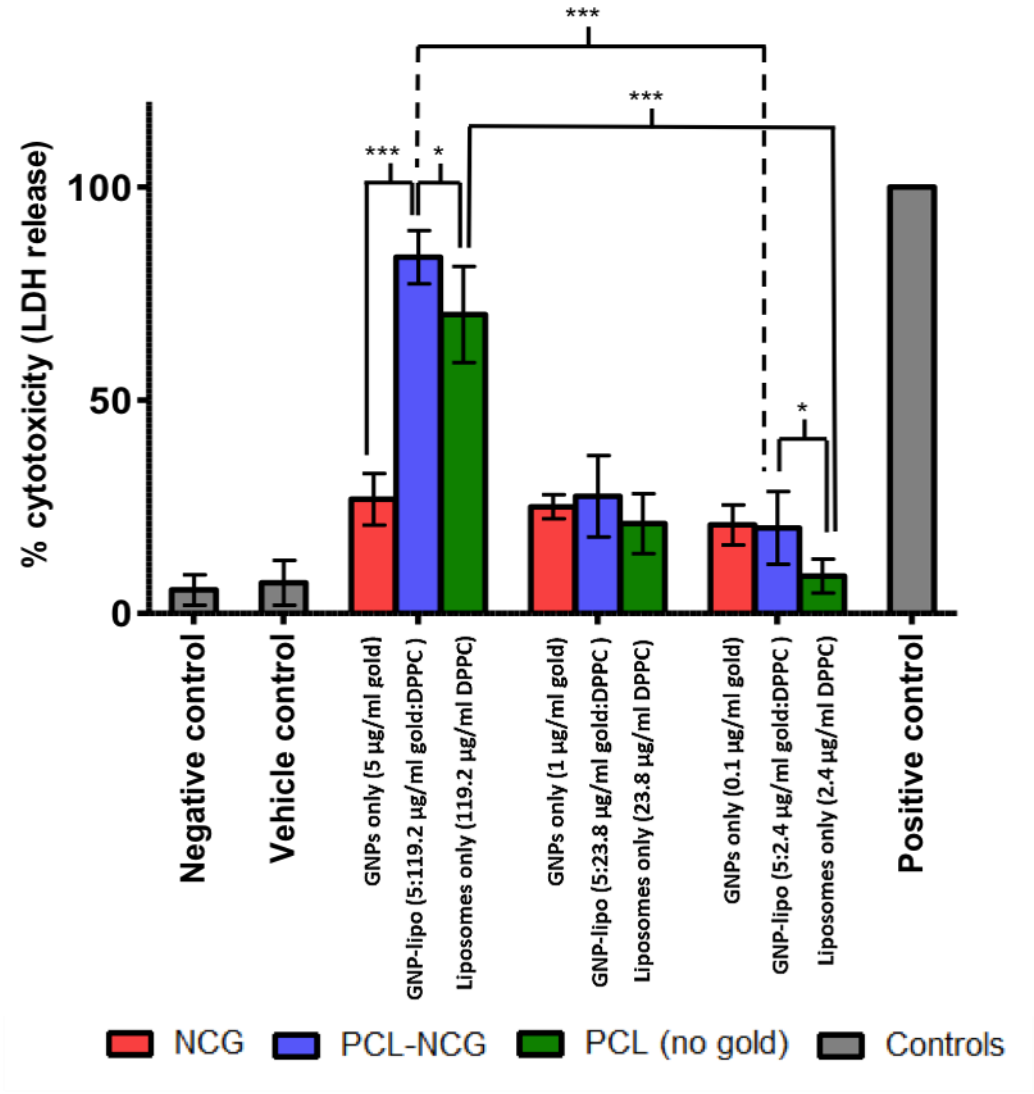

Figure 5.5 LDH release (%) from male Chinese hamster lung fibroblast cells (V79) after 24 hours of treatment with test materials. Concentrations range from 5 to 0.1 µg/ml of gold (NCG and PCL-NCG) with corresponding DPPC lipid concentrations of 119.2, 23.8 and 2.4 µg/ml (NCL and NCL-PCG), (n=6,r=6, mean ± SD) Data was compared using two-way ANOVA and analysed using Bonferroni post-hoc test. Level of significance between data sets is indicated by * = $p<0.05$ and *** = $p<0.001$.

Figure 5.5 shows the LDH release from male Chinese hamster lung fibroblast cells (V79) after 24 hours of treatment with negatively charged building blocks (NCG), the corresponding lipo-GNP system (PCL-NCG) and positively charged liposomes without gold (PCL). As before, statistical comparisons were made using two-way ANOVA and Bonferroni post-hoc analysis with TC_{50} criteria used to determine whether treatments were representative of a cytotoxic condition (>50% assay activity relative to the positive control).

Validating the assay sensitivity, the negative control (untreated cells) did not produce a cytotoxic response, representative of background LDH release from healthy cells. Additionally, no significant difference was observed between the negative control and vehicle control ($p > 0.05$) confirming that the differences observed in LDH release arise as a result of cellular exposure to test materials.

From the figure it can be seen that each test material resulted in LDH release that was not representative of a cytotoxic condition, according to TC_{50} criteria; excluding the highest concentration of PCL-NCG and PCL (5 µg/ml gold), where LDH release was above 50% relative to the positive control. In comparison to the negative control however, a significant increase in LDH release was observed for all treatments ($p<0.001$) apart from PCL (no gold) at the corresponding concentration of 0.1 µg/ml gold.

To evaluate potential dose-dependent cytotoxicity, statistical analysis was used again to compare treatments at the highest and lowest concentrations for each test material. A dose-dependent trend was observed for PCL-NCG and PCL ($p<0.001$), with a correlation between higher concentrations and an increase in LDH release. In Agreement with the MTT assay, a dose-dependent toxicity trend was not observed after treatment with the NCG building blocks. Comparison between test materials showed that post treatment to PCL-NCG, LDH release was significantly higher compared to the LDH release with NCG at 5 µg/ml gold ($p<0.001$), but it was comparable at lower concentrations. In contrast, treatment with PCL resulted in significantly less LDH release compared to PCL-NCG at concentrations of 0.1 µg/ml gold ($p<0.001$) and 5 µg/ml gold ($p<0.05$).

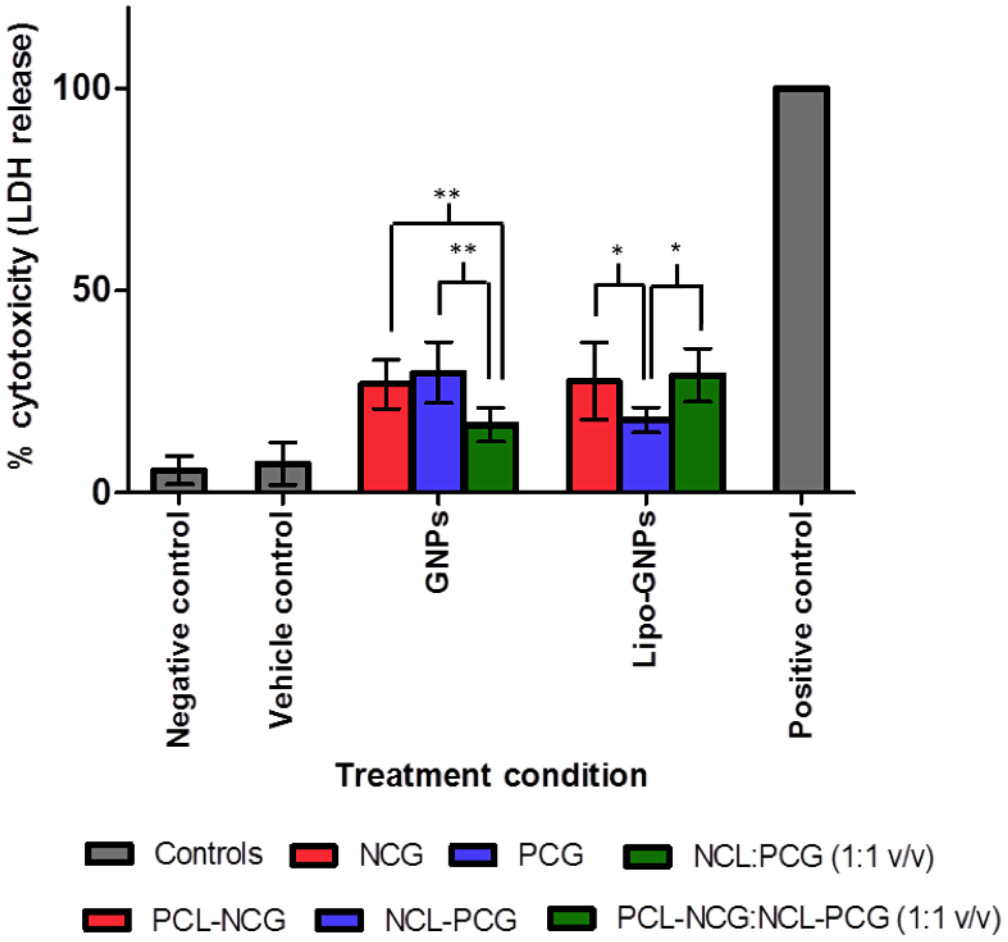

Figure 5.6 Comparison of LDH (%) release from male Chinese hamster lung fibroblast cells (V79) after 24 hours of treatment with NCG, PCG and co-treatment with NCG:PCG (1:1 v/v) at a concentration of 5 µg/ml gold and NCL-PCG, PCL-NCG and co-treatment with NCL-PCG:PCL-NCG (1:1 v/v) at a concentration of 1 µg/ml gold, (n=6, r=6 mean ± SD). Data was compared using two-way ANOVA and analysed using Bonferroni post-hoc test. Level of significance between data sets is indicated by * = $p<0.05$, and ** = $p<0.01$.

Figure 5.6 compares the LDH release from male Chinese hamster lung fibroblast cells (V79) after 24 hours of individual and co-treatments (1:1 v/v) with NCG and PCG (5 µg/ml total gold) or NCL-PCG and PCL-NCG (1 µg/ml total gold). Co-treatment with NCG and PCG represents *in situ* self-assembly of SANs into suprastructures. Using the same approach of analysis as previously, statistical comparisons were made using two-way ANOVA and Bonferroni post-hoc analysis with TC^{50} criteria used to determine whether treatments were representative of a cytotoxic condition (>50% assay activity relative to the positive control). Validating the assay sensitivity, the negative control (untreated cells) did not produce a cytotoxic response, representative of background LDH release from healthy cells. Additionally, no significant

difference was observed between the negative control and vehicle control (*p> 0.05*) confirming that the differences observed in LDH release arise as a result of cellular exposure to test materials.

In agreement with MTT assay, it can be seen from the figure that co-treatment with NCG and PCG did not induce a cytotoxic response according to the TC_{50} criteria, with LDH release <50% relative to the positive control (lysed cells). When comparing against the negative control, a significant increase in LDH release was observed after co-treatment (*p<0.001*), which is analogous to LDH release after treatment with individual building blocks (NCG and PCG). Co-treatment with NCG and PCG (*in situ* self-assembly) however, showed LDH release was significantly lower than for either NCG or PCG individually (*p<0.01*). Interestingly, the decrease in LDH release observed after *in situ* self-assembly of GNP building blocks does not correlate with a reduction in cell viability revealed by the MTT assay. Additionally, no significant difference in LDH release was seen after treatment with NCG or PCG separately (*p>0.05*).

For GNP-lipo systems, LDH release after co-treatment with NCL-PCG and PCL-NCG was below the TC_{50} threshold and was not representative of a cytotoxic condition. Comparison to the negative control revealed a significant increase in LDH release, which is analogous to LDH release after treatment with NCL-PCG and PCL-NCG individually. Comparing between treatments revealed that co-treatment with NCL-PCG and PCL-NCG resulted in LDH release that was significantly higher than that observed for NCL-PCG (*p<0.05*) but comparable to PCL-NCG (*p>0.05)*. Correspondingly, a significant difference in LDH release was also seen after treatment with PCL-NCG and NCL-PCG separately (*p<0.05*).

5.3 Microscopy analysis of V79 cells after treatment

Optical microscopy images presented in Figures 5.7 to 5.9 show the corresponding (used for assays) male Chinese hamster lung fibroblast cells (V79) after 24 hours of individual treatment with test materials. The low magnification images depict the general health, morphology and density of cells that could be associated with cytotoxicity observed from biochemical assays.

Figure 5.7 Optical microscope images (×250 magnification) of male Chinese hamster lung fibroblast cells (V79) exposed to control conditions for 24 hours, incubated at 37°C and 5% CO_2 in DMEM high glucose (4.5 µg/ml) supplemented with 10% FBS. (A) Negative control (no treatment), cells appear uniform and clustered displaying clear membrane structures. (B) Vehicle control treated with medium and PBS pH 7.4 (1:1 v/v), with no notable difference in morphology from negative control. (C) Positive control treated with 1% Triton-X100™, where cells appearing to be non-adherent with a complete absence of cell structure.

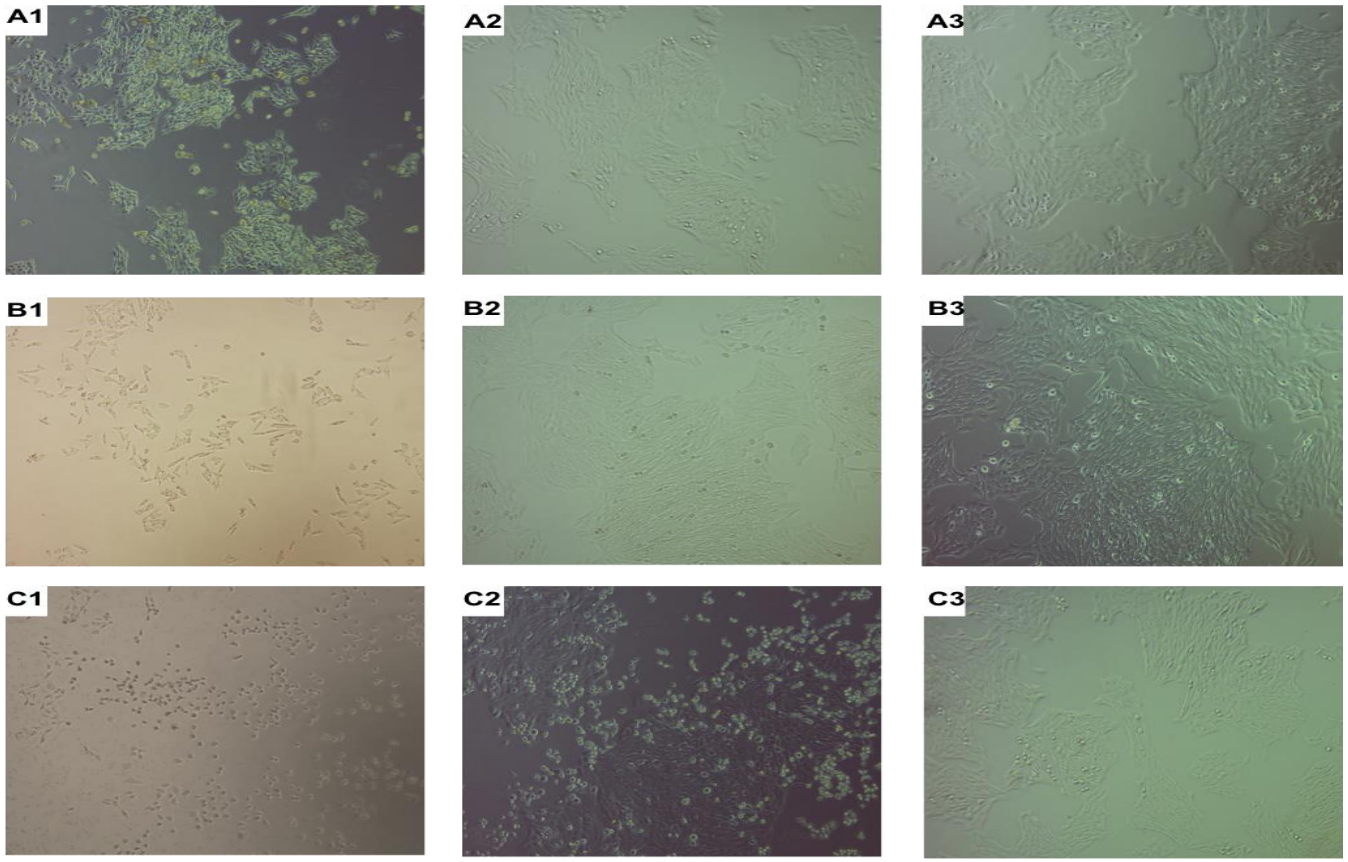

Figure 5.8 Optical microscope images (×250 magnification) of male Chinese hamster lung fibroblast cells (V79) cells after exposure to (A) PCG building blocks, (B) NCL-PCG and (C) NCL (without gold) for 24 hours, incubated at 37°C and 5% CO_2 in DMEM high glucose (4.5 µg/ml) supplemented with 10% FBS. Concentrations of each test material are (left) 5, 1 and 0.1 µg/ml gold. (A) Cell morphology is comparable to the negative control for A2 and A3 but irregular clustering was seen at the highest concentration, A1. (B) No notable difference in morphology was observed compared to negative control for B2 and B3 but cell density appeared to be lower and with an absence of cell clustering exhibited for B3. (C) Cells were seen to lack basic membrane structures, which noticeably increased with concentration, appearing increasingly comparable to the positive control.

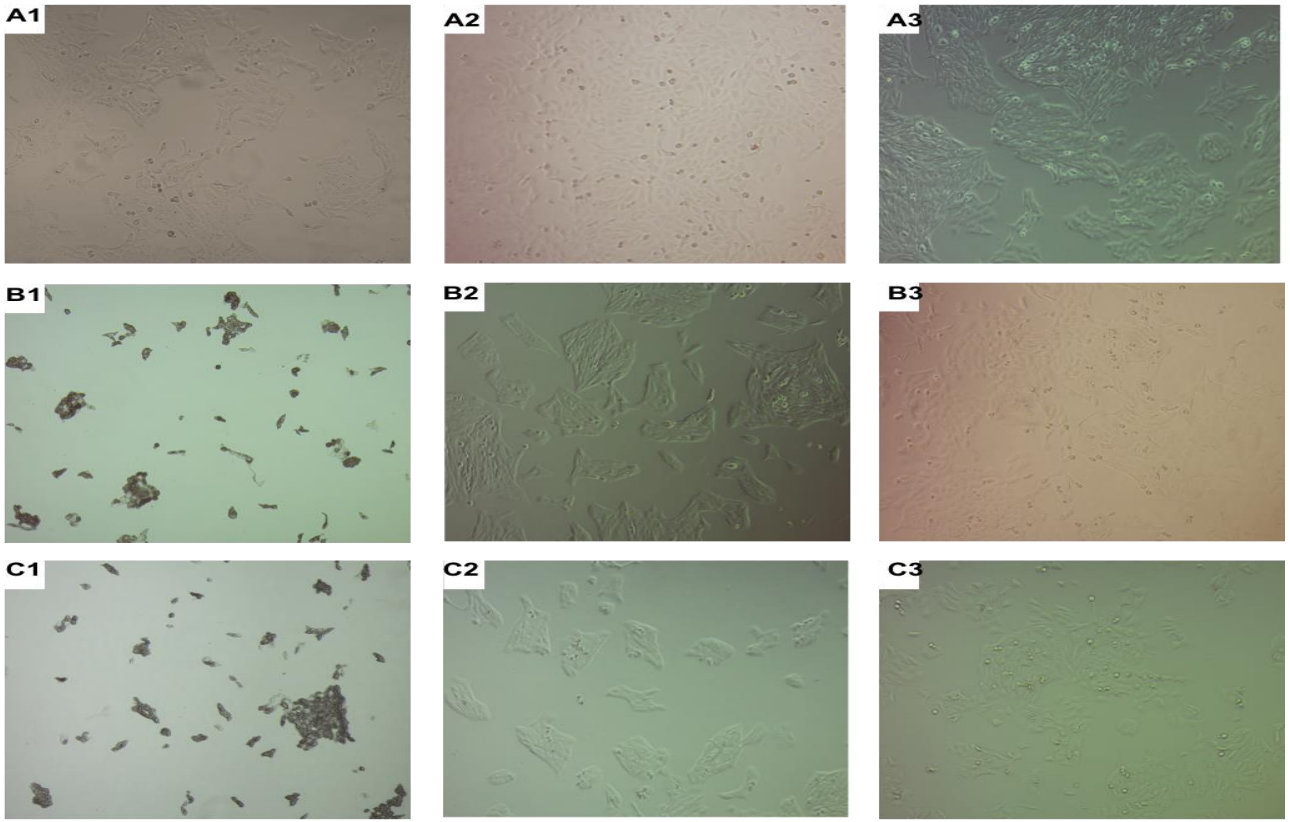

Figure 5.9 Optical microscope images (×250 magnification) of male Chinese hamster lung fibroblast cells (V79) cells after exposure to (A) NCG building blocks, (B) PCL-NCG (C) PCL (without gold) for 24 hours, incubated at 37°C and 5% CO2 in DMEM high glucose (4.5 µg/ml) supplemented with 10% FBS. Concentrations of each test material are (left) 5, 1 and 0.1 µg/ml gold. (A) No notable difference was seen in cell morphology compared to the negative control at all concentrations investigated. (B, C) At the highest concentrations (B1 and C1), no obvious membrane structures were seen with cells appearing as non-uniform, densely aggregated clusters, dissimilar from both the negative and positive control. For B2 and C2 cell morphology was comparable to the negative control, but cell clusters appeared smaller in size. No difference was seen between the lowest concentration B3 and C3 and the negative control.

Micrographs of male Chinese hamster lung fibroblast cells (V79) cells exposed to negative (no treatment) and positive control (1% Triton-X100™) treatments (Figure 5.7) provides a reference to healthy and fully lysed cell populations. It can be seen that the negative control and vehicle control cells (Figure 5.7 A, B), display a consistent morphology that is characteristic of a fibroblasts monolayer with elongated cell structures. In contrast, the positive control cells (Figure 5.7 C) appear to be non-adherent and spherical in shape with an absence of cell clustering and monolayer formation.

Micrographs of cells treated with positively charged building blocks (PCG) the corresponding lipo-GNP system (NCL-PCG) and negatively charged liposomes without gold (NCL). at each concentration are displayed in Figure 5.8. No distinction was observed between treatments with test materials at the lowest concentration (A3-C3) with cell morphology appearing characteristic of fibroblasts with monolayer formation comparable to the negative control. Cells densities after treatment with PCG building blocks were seen to be comparable to the negative control at all concentrations. A minor change in cell morphology was noticed however at 5 µg/ml gold (A1), with cells appearing as tightly packed clusters that display raised surfaces. In contrast, after treatment with NCL-PCG at the same concentration (B1), cells displayed a normal morphology but overall numbers were noticeably lower with an absence of cell-cell adhesion and intact monolayer formation. Treatment with NCL (no gold) (C1, C2) resulted in cells that appeared to be non-adherent and lacking a fibroblastic structure. These cells resembled the positive control, with an increasing number of non-adherent cells correlating with increasing concentration. A clear disparity between cellular health for treatment with the highest and lowest concentrations of NCL-PCG and NCL supports the results of MTT and LDH assays in sections 5.1 and 5.2, which identified dose-dependent cytotoxicity for these test materials.

Figure 5.9 depicts cells after treatment with negatively charged building blocks (NCG) the corresponding lipo-GNP system (PCL-NCG) and positively charged liposomes without gold (PCL). Akin to treatment with PCG, NCL-PCG and NCL (Figure 5.8) there was no difference in cell morphology and

density when compared to the negative control after exposure to each test material at the lowest concentrations (A3-C3). In agreement with assay results, treatment with PCL-NCG and PCL was seen to produce a comparable cellular response. At 1 µg/ml gold concentration (B2, C2) the formation of isolated clusters was revealed rather than characteristic monolayers, with significantly lower overall cell numbers. At the highest concentrations of PCL-NCG and PCL (B1, C1), cells appeared as densely aggregated three-dimensional clusters after treatment with no obvious features that could be compared to either the negative or positive control. Noticeable differences in cell numbers and general cellular health after treatment with the highest and lowest concentrations of PCL-NCG and PCL correlate with the results of MTT and LDH assays, indicating a significant dose-dependent cytotoxic trend for these test materials. In contrast, there was no difference in cell morphology and density after exposure to NCG at each concentration. Accordingly, cellular response to NCG was considered to be analogous to PCG and in agreement with results of the MTT assay, which revealed viability to be above 80% for treatments with GNP building blocks at all concentrations.

5.4 Discussion

Pre-clinical toxicity testing is essential for the development and design of new nanomaterials, which can display unique and complex physicochemical properties that could generate hazardous biological consequences[314]. Initial testing of the nanomaterials developed in this current study was achieved by observing toxicity *in vitro* on an established cell line, reflecting potential cell interactions that could arise from the intended applications for these materials. Tetrazolium-based assays such as MTT used in this study (section 5.1), provide a broad-spectrum analysis of cell viability by measuring mitochondrial function and are routinely applied to evaluate nanomaterial cytotoxicity[315]. Combined with the measurement of LDH (section 5.2), a biomarker that is released from cells which experience membrane disruption (cytolysis), it was possible to identify whether material-induced necrosis was

responsible for observed cytotoxicity[316]. Differences between controls and treated cells seen from cell imaging were then used to compliment biochemical assays results and hypothesise the mechanism of cytotoxicity.

Results were initially compared between GNP building blocks (NCG and PCG, prepared in chapter 3) the corresponding developed GNP-lipo systems (PCL-NCG and NCL-PCG, prepared in chapter 4) and liposomes without gold (PCL and NCL) to elucidate any specific cytotoxicity responses. Assay results after co-treatment with GNP building blocks (*in situ* self-assembly) were then evaluated against individual SANs to determine whether the process of self-assembly and the formation of larger suprastructures (Evidenced in Chapter 3) influenced cytotoxicity. The same approach was also applied to GNP-lipos, to investigate whether comparable effects were observed when a liposomal coating was provided to GNPs, which could potentially inhibit self-assembly.

5.4.1 Evaluation of GNP cytotoxicity

Assessment of cellular viability post treatment with PCG and NCG using the MTT assay revealed that these individual GNP building blocks are not cytotoxic and are well tolerated by the V79 cell line (section 5.1). There was no evidence of a dose-dependent response with cell viability above 80% relative to the negative control at all concentrations investigated. The release of LDH measured after treatments also inversely correlated with results of the MTT assay (section 5.2), with the extent of material-induced cytolysis not characteristic of a cytotoxic response. Microscopy images seen in Figure 5.8 and Figure 5.9 support these observations, with no notable difference in cell numbers when comparing to the negative control and between treatment concentrations (section 5.3). These findings agree with multiple studies that have shown dispersed GNPs of various sizes and surface functionalities to be non-toxic towards a range of cell lines at concentrations up to 1 mg/ml, a magnitude 200× higher than in the present study[315,317,318]. There are however numerous conflicting studies, for example 2 nm GNPs with cationic SAMs

have been revealed to be cytotoxic when tested on fibroblastic kidney cells *in vitro*, but their equivalent anionic counterparts were not at the same concentration[319]. It was hypothesised that the difference in displayed cytotoxicity was as a result of the cationic GNPs interacting and disrupting negatively charged cellular membranes[319]. This concept could explain the irregular cell morphology observed for the highest concentration of PCG investigated. However, measured LDH release after treatment with PCG and NCG revealed no significant difference in cytolysis. Conversely, it has been demonstrated that plasma proteins from culture media can spontaneously absorb onto nanoparticle surfaces, resulting in a negative surface charge that reflects their physiochemical properties[320,321]. It has been further proposed that the absorption of such proteins can increase nanomaterial biocompatibility and either increase or decrease their cellular uptake[322-324]. Furthermore, protein adsorption has also been suggested as an artificial mechanism of cytotoxicity specific to *in vitro* studies, triggered when a depletion of available nutrients results in cell starvation[325]. Whilst nanomaterial-protein interactions were not evaluated in the current work, a lack of dose-dependent cytotoxicity displayed by the investigated GNPs suggests that cell starvation did not occur in these experiments.

To determine if *in situ* self-assembly influences the toxicity displayed by SANs, the same cell model was used to investigate co-treatment with PCG and NCG (1:1 v/v) at a concentration of 5 µg/ml gold. As revealed by both the MTT and LDH assay, co-treatment with complementary building blocks, where they are expected to self-assemble into suprastructures, was also well tolerated by the V79 fibroblastic cells and did not produce a cellular response which could be considered cytotoxic (sections 5.1 and 5.2). Cell viability however was significantly lower compared to treatment with either PCG or NCG alone, indicating that the process of *in situ* self-assembly or resultant suprastructures induced cell death. Surprisingly, the release of LDH was also seen to significantly decrease for co-treatment compared to individual treatments, which does not inversely correlate with findings of the MTT assay as expected for necrotic cell death. Disparity between assay results indicates that *in situ* self-assembly of the investigated GNPs had a significant effect on

their displayed toxicity and additionally the potential underpinning mechanisms responsible. Whilst currently there are no studies elucidating the performance or toxicity of *in situ* self-assembling nanomaterials within biological systems, aggregation of nanomaterials which can occur under physiological conditions[326], could potentially result in similar outcomes. With numerous studies identifying that physical properties of nanomaterials affect their cellular uptake, intracellular transport and subsequent cell functions, including cell death[327,328], it has been suggested by Oberdörster *et al* that assessment of *in situ* aggregation should be an essential component of toxicity testing strategies[329]. Crucially, it has also been highlighted that the size of formed aggregates can determine the cellular uptake pathway[330], with endocytosis and pinocytosis proposed as the primary mechanisms of cell entry for nanomaterials with dimensions up to 200 nm[331,332] and phagocytosis for larger structures[333,334]. Although the route of GNP uptake was not investigated in the current study, it is possible that the same hypothesis could explain the observed differences in cell viability and material-induced membrane disruption seen between individual and co-treatments. Additionally relevant to this study, it has been suggested that aggregation and thus potentially also the assembly of nanoparticles could influence the "*effective dose.*" To put this into context, the exposed and often reactive particle surface area of individual GNPs could be effectively reduced as self-assembly occurs, although at present a standardised approach for assessment has yet to be developed to evidence such affects[335].

5.4.2 Evaluation of GNP-lipo toxicity

Cellular viability as determined by the MTT assay after individual treatment with NCL-PCG and PCL-NCG and the equivalent liposomes without gold (NCL and PCL) showed that these test materials display significant dose-dependent cytotoxicity (section 5.1). Representative of material induced necrosis, the release of LDH also increased with a reduction in cell viability in a dose-dependent trend (section 5.2). Whilst conventional liposomes prepared from natural phospholipids are often considered to exhibit minimal

toxic effects[336], the current findings are supported by studies that have demonstrated liposomes which incorporate cationic or anionic lipids can display dose-dependent toxicity[337,338] PCL-NCG and PCL were revealed to be the least tolerated test materials producing a cytotoxic response at 1 µg/ml gold and above, whereas treatment with NCL-PCG and NCL was only cytotoxic at the highest concentration investigated. Increased toxicity displayed by these cationic formulations was also in agreement with other studies, where cellular tolerance was found to be dependent on the lipid structure with those possessing tertiary amine functional groups, such as DPTAP used in this study, displaying significant cytotoxicity[339]. Additionally, correlation between assay results after treatment with GNP-lipos and the equivalent liposomes without gold, but not GNP building blocks, revealed the lipid compositions utilised are primarily responsible for observed cytotoxic responses on the V79 cell line. This is further highlighted by the MTT assay when comparing against the negative control, where significant reductions in cell viability occurred after treatment at a concentration of 1 µg/ml gold and above for GNP-lipos and the equivalent liposomes but not for treatments with GNPs alone. Cell images shown in Figure 5.7 and Figure 5.8 also support this hypothesis (section 5.3), with comparable variations in cell density and changes to cell morphology seen between treatments with GNP-lipos and liposomes without gold. Considerable changes to cell morphology identified after exposure to PCL-NCG and PCL at the highest concentration investigated are also consistent with earlier reports that liposomes prepared from cationic lipids cause cell shrinkage, increased cluster density and reduce cell replication[339]. Owing to the considerable cytotoxicity displayed by the lipid compositions utilised, elucidation of the effects of GNP encapsulation within liposomes on their displayed cytotoxicity is limited in this investigation. Previous reports however have shown that liposomes can increases the cellular uptake of GNPs with a similar size to those used in this study, up to 1000-fold[340]. This significant increase in cellular internalisation occurs as a result of increasing the overall size of the nanomaterials, which favours the thermodynamically driven process of membrane engulfment that underpins endocytotic uptake[341]. Experimental data indicates nanomaterials with dimensions of approximately 50 nm to be optimal for cell uptake, which

decreases 18-fold at 6 nm and was predicted to be effectively zero for the size of GNPs used in the present study[342,343,340]

To determine whether the encapsulation of complementary GNP building blocks in separate liposome formulations influences cytotoxicity displayed towards the V79 cell line, NCL-PCG and PCL-NCG were administered simultaneously (1:1 v/v). Results of the MTT and LDH assays showed that co-treatment with both GNP-lipo systems did not produce a unique cytotoxic cellular response, with cell viability significantly lower than individual treatment with NCL-PCG but higher than the effects of PCL-NCG (sections 5.1 and 5.2). These results are however clearly different in comparison to co-treatment with PCG and NCG (*in situ* self-assembly), where there was a unanimous decrease in cell viability compared to the individual treatments. Additionally, the release of LDH was inversely proportional to cell viability for combined treatment with GNP-lipos, indicating that observed cell death occurs via necrosis. This is comparable to individual treatment with GNP-lipos but again differs from co-treatment with NCG and PCG building blocks. Disparity between cellular response towards co-treatment with SANs and GNP-lipos indicates that the use of therapeutic delivery could be an effective method of controlling self-assembly activity within biological environments. In turn, this could potentially alter the pharmacokinetics, toxicity and subsequent biodistribution of SANs, although further study is required to elucidate this hypothesis. Encapsulating nanomaterials within therapeutic delivery vehicles including liposomes is a method that has been utilised before, to protect, preserve and isolate functionality under biological conditions[344], although no previous attempts appear to have been made to apply this to SANs. Additionally, with stimuli-responsive delivery systems now established[345], it could be possible to target and trigger the self-assembly process when desired. This could then provide spatial and temporal control, offering scope for future development of nanosystems that could eventually enable targeted or responsive *in situ* self-assembly.

5.5 Conclusion

Cytotoxicity displayed by GNP building blocks and the underpinning mechanisms responsible appear to be dependent upon the state of particle dispersion. *In situ* self-assembly and the formation of suprastructures resultantly influences cell viability and cytolysis compared to the original NCG and PCG counterparts in this investigation. Encapsulation of GNPs within therapeutic delivery systems offers a potential strategy to further control the self-assembly process and the resultant properties displayed by these nanomaterials, although careful consideration should be given to the selection of suitable, non-toxic excipients. Results in this chapter offer preliminary insight into potential approaches towards achieving predictable *in situ* self-assembly, the affects likely to be encountered and suitable experimental designs towards evaluation. Owing to inconsistent toxicology data generated for nanomaterials at present, as a result of using variable cell models, toxicity assays, culture media composition and materials with considerably different properties[346-348], it is recommended that preliminary findings are replicated independently by multiple laboratories, expanding to encompass a range of relevant cell lines and biochemical assays[349]. Whilst *in vitro* modelling does not appropriately mimic complex biological environments that reflect real-life applications, an obvious limitation to the current approach[350], testing is standardised and has provided initial identification of toxicity and a fundamental understanding of cellular response in this study. The approach undertaken, to assess a range of nanomaterial concentrations using widely reported biochemical assays forms the basis for further robust biological screening and follows current experimental trends for new entities that precede *in vivo* and pre-clinical investigations.

6 Self-assembly within Biological Environments

The self-assembly of complementary GNP building blocks facilitated by electrostatic attraction and intermolecular bonding (chapter 3) was studied under biological conditions. Initial investigations were carried out within a biologically relevant medium under representative physiological conditions, simulating potential exposure environments (section 2.2.5). After identifying the formation of assembled nanostructures via the electrostatic approach, further *in vitro* assessment was performed on the adherent, monolayer forming male Chinese hamster lung fibroblast cell line (V79) (section 2.2.6.4). Replicating the experimental design used for cytotoxicity studies, cells were treated separately with GNPs and as they undergo *in situ* self-assembly. Tissue specimens were preserved, imbedded in resin and thin-sectioned after 24 hours of exposure according to protocols described in section 2.2.6.7. Resultant cellular uptake, intracellular distribution and self-assembly activity of GNPs was then evaluated using high-resolution TEM (section 2.2.3.1) and elemental analysis (section 2.2.3.3).

6.1 Interactions of GNPs within cell culture medium

Nanoparticle interactions and extent of bio-complex formation was evaluated for NCG, PCG and oligo-GNPs within DMEM-CCM containing 10% foetal bovine serum. Investigations were carried out under physiological conditions (37°C / 5% CO_2) with analysis performed after one hour of incubation. Resultant complexes were studied using TEM to determine their general size and morphology and evidence interactions between GNPs and components of the utilised cell culture media (CCM). Hydrodynamic size distribution profiles of complexes in suspension were resolved following procedures described in section 2.2.3.4 for DLS analysis, to supplement microscopy observations.

6.1.1 Characterisation of a biologically relevant medium

Results obtained from the analysis of DMEM supplemented with 10% FBS alone (CCM control) are presented in Figure 6.1. Micrographs reveal the presence of densely contrasted structures that appear dispersed and globular in shape, ranging in size from approximately 10 nm and not exceeding 200 nm (Figure 6.1 A-C). The corresponding size distribution curve (Figure 6.1 D) correlates with these findings, with multiple definitive peaks observed below 300 nm, a Z-average particle size of 100.9 nm and a dispersity value of 0.631, indicating structure sizes to be heterogeneous.

6.1.2 Ionic-ligand functionalised GNPs in CCM

Micrographs and size distribution profiles resolved for NCG and PCG after incubation in CCM are displayed in Figure 6.2 and Figure 6.3, respectively. The lowest magnification images provide an overview of CCM-GNP interaction with higher magnification providing detailed resolution of nanoparticle distribution within complexes. After incubation of NCG, large structures were revealed to have formed relative to the CCM-control,

displaying a diverse size distribution spanning the nanometre range and in excess of several microns. Morphology of complexes was seen to be consistent, with features ascribed to GNPs frequently clustered within globular-like structures that appear to have agglomerated, such as those displayed in Figure 6.2 (B). DLS analysis presented in Figure 6.2 (D) supports these observations, revealing a broad size distribution curve comprising multiple peaks that range from several nanometres and greater than 5 μm. A corresponding Z-average hydrodynamic particle size of 70.4 nm was revealed with a dispersity value of 0.750, indicating complex sizes to be further heterogeneous compared to the CCM-control. In contrast, structures formed after incubation of PCG were noticeably smaller in micrographs, typically ranging in size from a few nanometres and not more than 500 nm. From Figure 6.3 (C) it appeared that GNPs had again clustered within formed complexes that had subsequently agglomerated, although overall morphology appeared less consistent, lacking a globular appearance, as observed for NCG-CCM and the CCM-control. Comparing size distribution curves further supports the perceived difference in formed complex size, with all peaks observed to be within a narrower range below 1 μm for PCG-CCM (Figure 6.3 D). A corresponding Z-average hydrodynamic particle size of 118.1 nm was revealed with a dispersity value of 0.456, indicating that structure sizes were more uniform compared to either NCG-CCM or the CCM-control. Interactions between both NCG and PCG with components of CCM showed a consistent behaviour, resulting in GNP-bio complex formation, with no evidence of GNP-GNP aggregation observed.

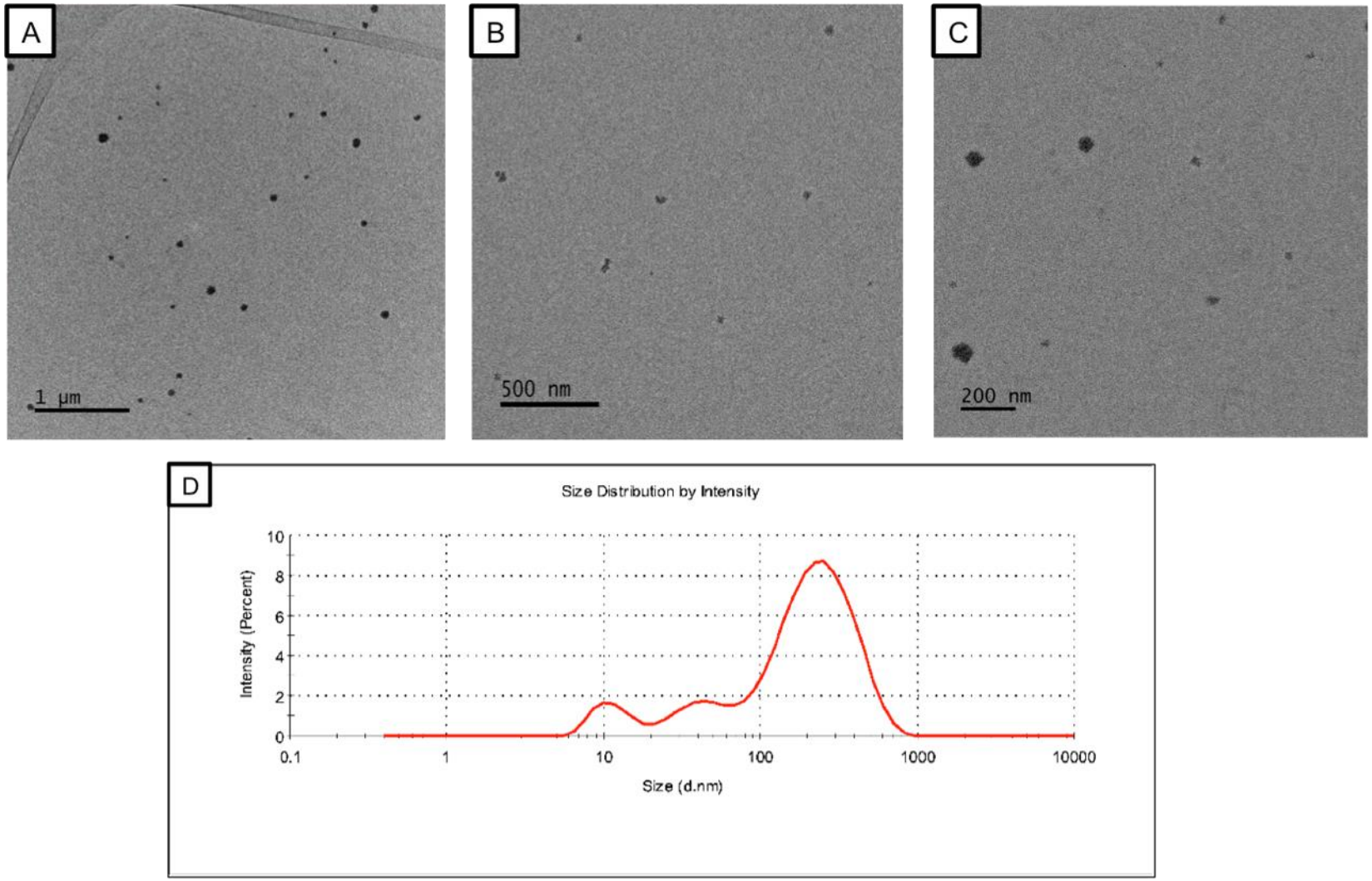

Figure 6.1 (A-C): Bright-field TEM micrographs of structures revealed from DMEM high glucose (4.5 µg/ml) culture media supplemented with 10% FBS after one hour of incubation at 37°C and 5% CO_2, (magnification left to right) 10,000, 20,000 and 30,000. (D): Corresponding mean average (n=3) size distribution curve of complexes in suspension, determined by DLS analysis.

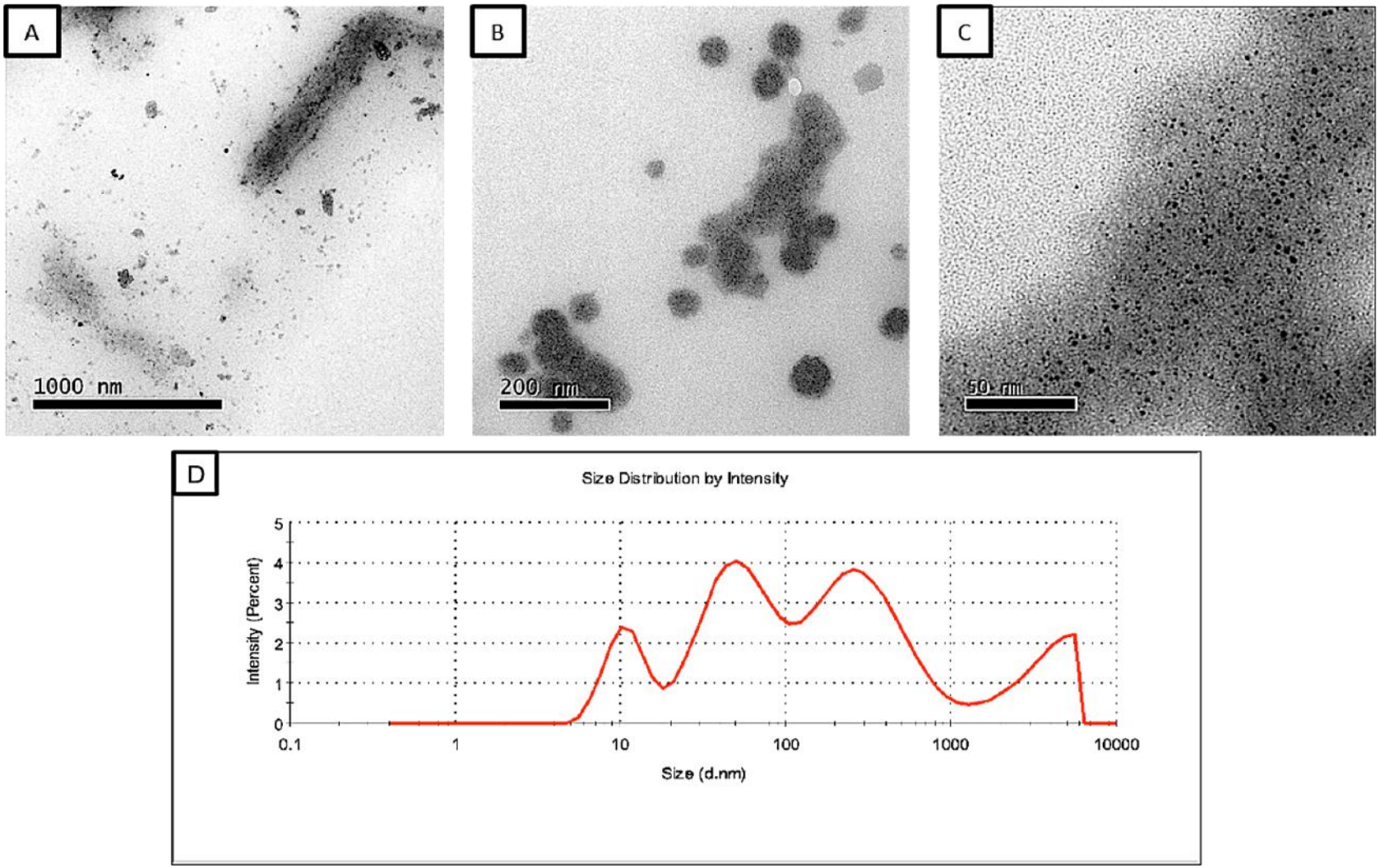

Figure 6.2 (A-C): Bright-field TEM micrographs of structures formed from incubation of NCG in DMEM high glucose (4.5 µg/ml) culture media supplemented with 10% FBS after one hour at 37°C and 5% CO_2, (magnification left to right) 20,000, 50,000 and 200,000. (D): Corresponding mean average (n=3) size distribution curve of suspended complexes in DMEM, determined by DLS analysis.

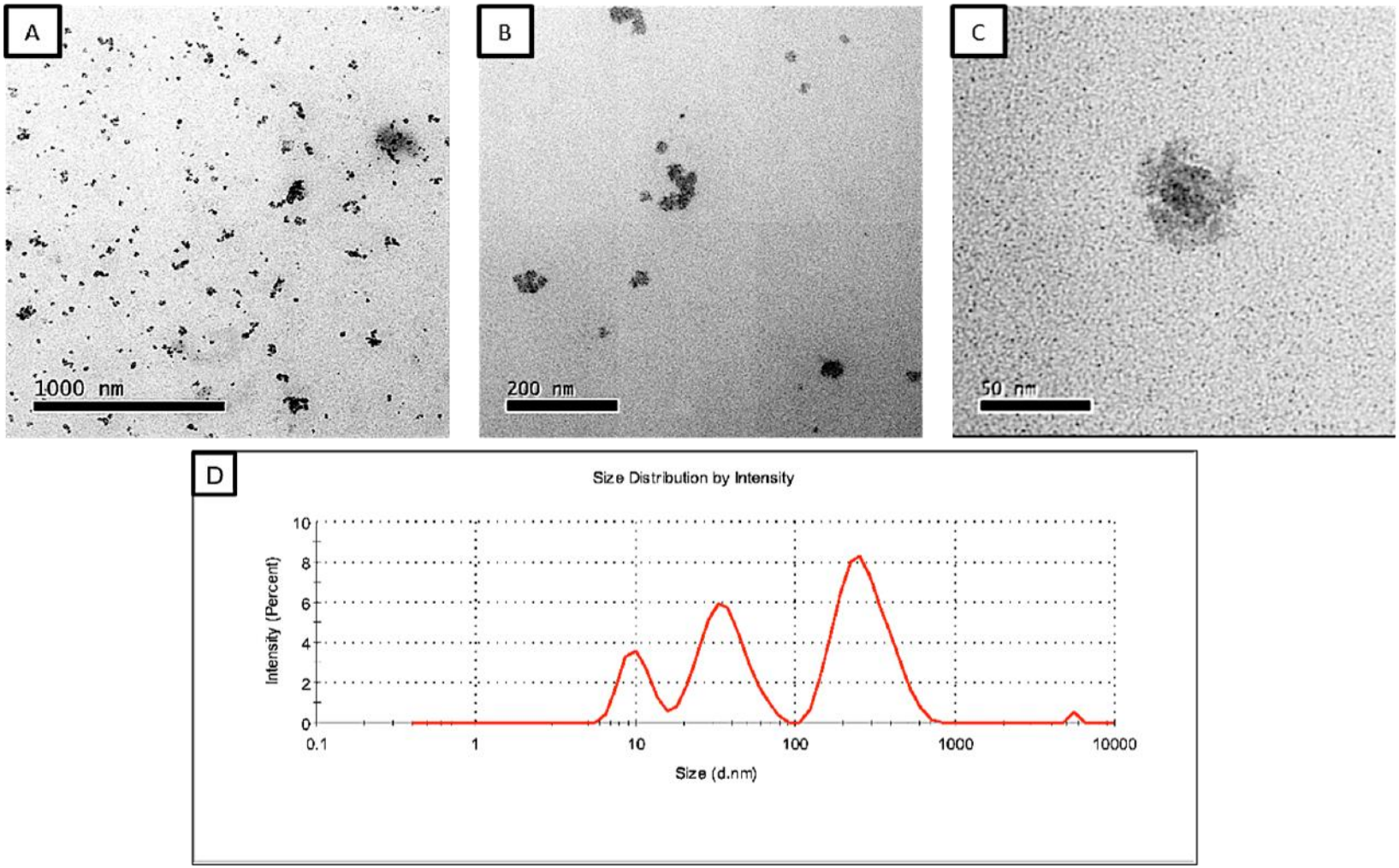

Figure 6.3 (A-C): Bright-field TEM micrographs of structures formed from incubation of PCG in DMEM high glucose (4.5 µg/ml) culture media supplemented with 10% FBS after one hour at 37°C and 5% CO_2, (magnification left to right) 20,000, 50,000 and 200,000. (D): Corresponding mean average (n=3) size distribution curve of suspended complexes in DMEM, determined by DLS analysis.

6.1.3 Oligonucleotide functionalised GNPs in CCM

Micrographs and size distribution profiles resolved after incubation of 5 nm oligo-GNPs in CCM are displayed in Figure 6.4**.** The same approach was taken using lower magnification images to provide an overview of GNP-CCM interactions with higher magnification providing the required resolution to determine the distribution of nanoparticles within complexes. Uniform globular-like complexes were revealed to have formed between oligo-GNPs and components of CCM, with structure sizes spanning the low nanometre range and typically not in excess of 200 nm. Compared to formed complexes of NCG and PCG in CCM respectively, resulting structures of oligo-GNP in CCM were further dispersed with less observed complex-complex agglomeration. GNPs again appeared to be associated with densely contrasted regions of micrographs (Figure 6.4 C), although a clear difference was seen compared to either NCG or PCG in CCM, with oligo-GNPs appearing sparsely distributed rather than clustered predominantly within complexes. Results of DLS analysis presented in Figure 6.4 (D) correlate with these observations, revealing a narrow size distribution curve that displays definitive peaks below 100 nm, with a Z-average of 49.65 nm. A corresponding dispersity value of 0.412 was also determined, indicating that complex sizes were further homogenous compared to the CCM-control. Similarly to NCG and PCG, interactions between oligo-GNPs and components of CCM appear to result in GNP-bio complex formation, with no evidence of GNP-GNP aggregation observed.

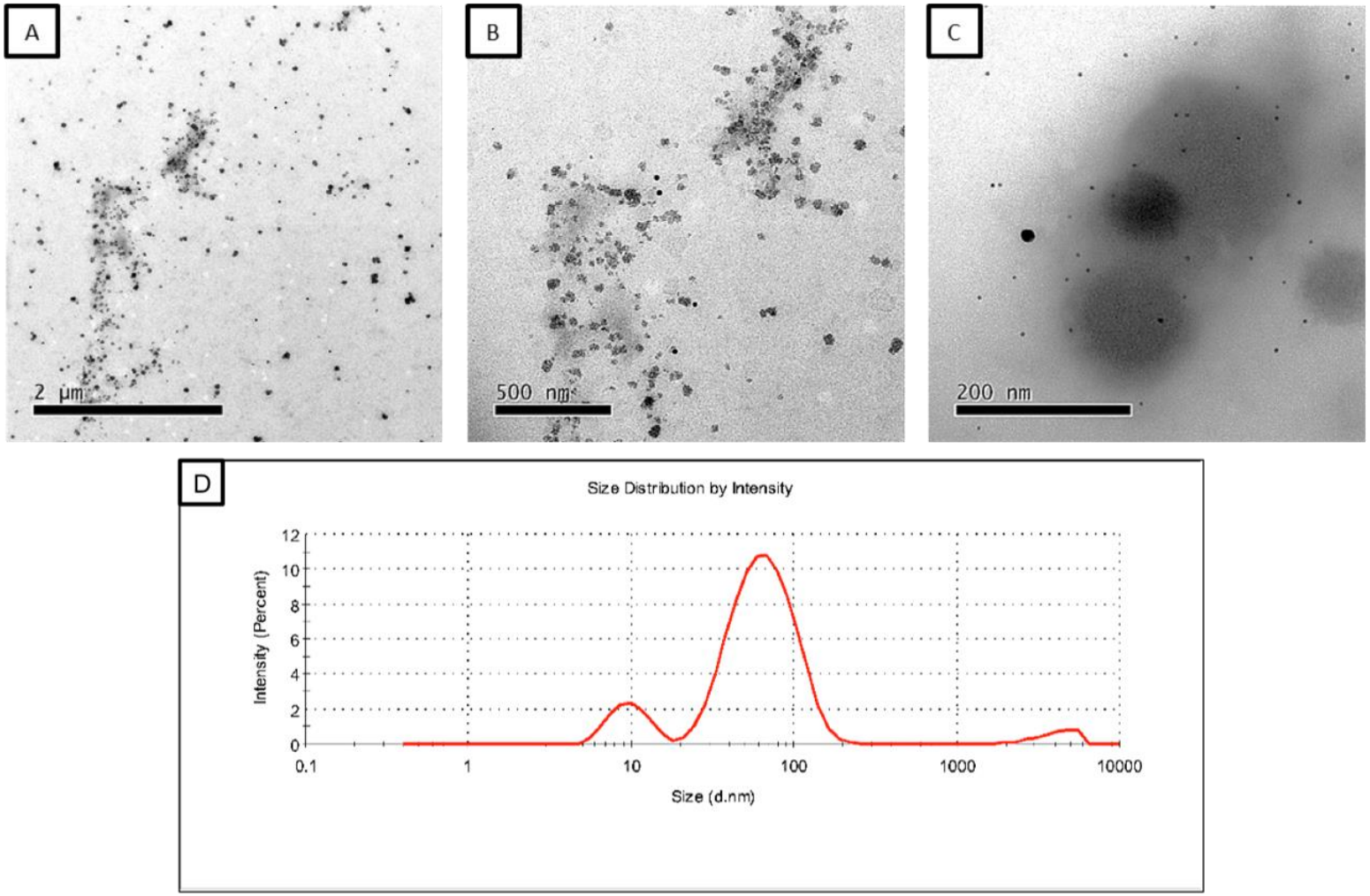

Figure 6.4 (A-C): Bright-field TEM micrographs of structures formed from incubation of 5 nm oligo-GNP in DMEM high glucose (4.5 µg/ml) culture media supplemented with 10% FBS after one hour at 37°C and 5% CO_2, (magnification left to right) 10,000, 20,000 and 80,000. (D): Corresponding mean average (n=3) size distribution curve of suspended complexes in DMEM, determined by DLS analysis

6.1.4 Self-assembly of GNPs in a biologically relevant medium

Self-assembly activity of GNPs under simulated biological conditions, facilitated by either electrostatic interaction or intermolecular bonding was studied. Micrographs revealing structures formed after incubation of complementary nanoparticles, NCG and PCG (1:1 v/v) or 5 nm oligo-GNP (1:1 v/v) in CCM are presented in Figure 6.5 and Figure 6.6 respectively. Hydrodynamic size distribution profiles determined by DLS are also displayed and were compared to results after self-assembly of identical GNPs in PBS. Investigating the electrostatic approach, the formation of irregular GNP clusters was seen (Figure 6.5 A-C), which was not observed after incubation of NCG or PCG individually in CCM (Figure 6.2 and Figure 6.3). These assembled GNP structures were measured to display size dimensions spanning the sub-micron range and were consistently associated with further contrasted features of micrographs. Contrasted regions displayed globular-like appearances, similar to those observed after incubation of NCG in CCM (Figure 6.2). Additionally, densely contrasted structures that appeared roughly spherical and range in size between 5 and 20 nm were identified. These features were detected exclusively amongst GNP clusters and were not observed after incubation of either NCG or PCG individually. Results of DLS analysis (Figure 6.5 D) agree with these findings, revealing suspended structures displaying a broad size distribution, a Z-average size of 73.2 nm and a dispersity value of 0.629. In contrast, incubation of NCG and PCG in PBS resulted in structure sizes of several orders of magnitude higher, with a voluminous Z-average hydrodynamic size of 3.3 μm and a high dispersity value of 0.988. This was considered indicative that self-assembly between NCG and PCG within CCM had been reduced compared to a simple aqueous environment. Investigating the intermolecular bonding approach, TEM analysis revealed an absence of nanoparticle clustering in CCM that could be associated with self-assembly activity (Figure 6.6 A-C). Observations were considered analogous to those after incubation of non-complimentary oligo-GNPs (Figure 6.4), with large globular-like complexes appearing as densely contrasted regions frequented with localised GNPs.

Results of DLS analysis further highlight these similarities, with an equivalent Z-average hydrodynamic size of 37.2 nm, a dispersity value of 0.498 and a size distribution curve of comparable appearance (Figure 6.6 D and Figure 6.4 D). In comparison, incubation of complementary oligo-GNPs in distilled water resulted in the formation of structures that were twenty times larger, with a Z-average hydrodynamic size of 802.8 nm and a dispersity value of 0.902. In summary, it was concluded that self-assembly activity of GNPs facilitated by electrostatic interactions was persistent within the utilised biological medium, although overall nanoparticle cluster sizes are smaller and appear increasingly heterogeneous. Self-assembly activity *via* the intermolecular bonding approach however appears to be entirely obstructed within the biological environment investigated, with no evidence of nanoparticle clustering or assemblage observed.

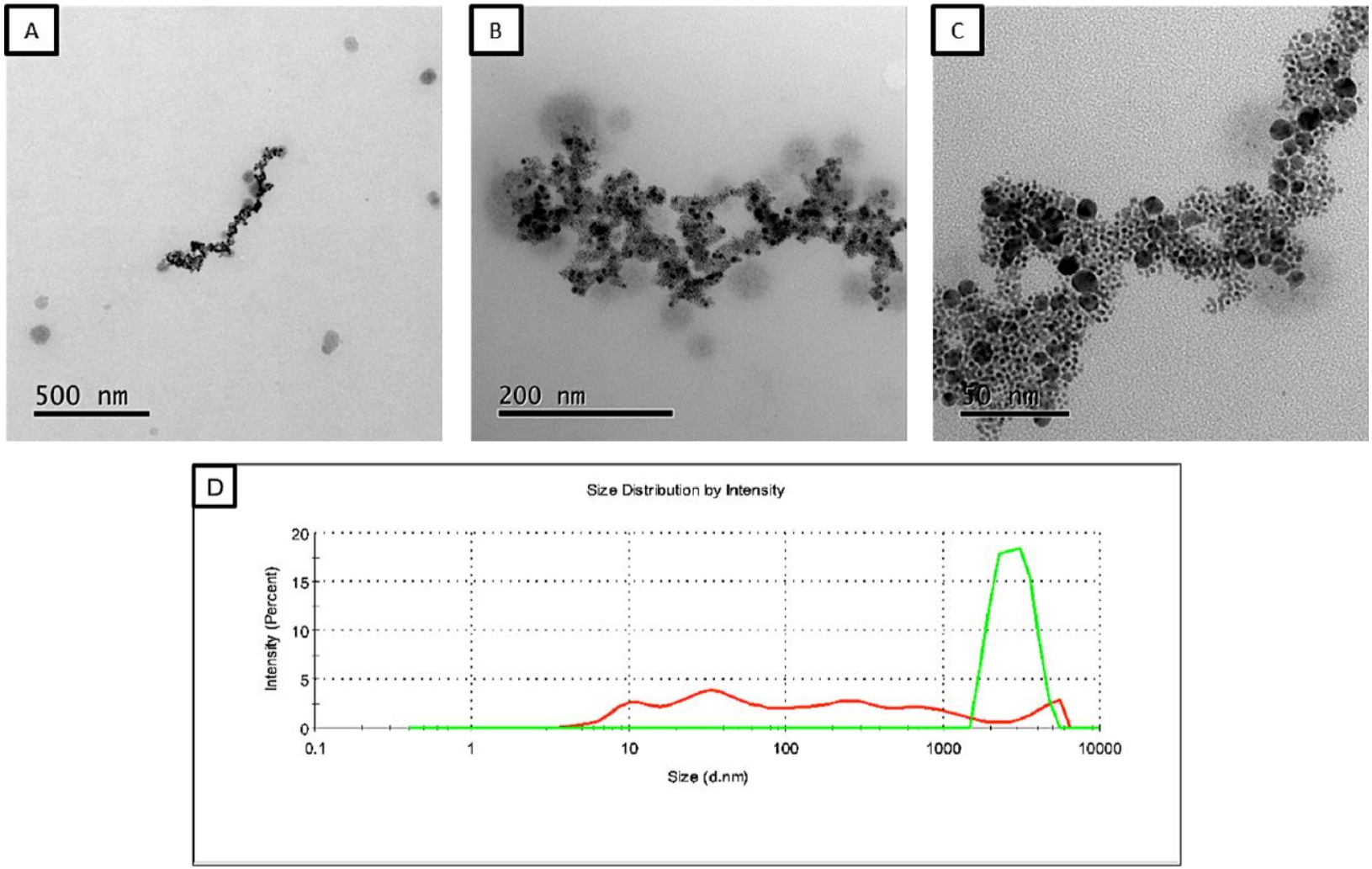

Figure 6.5 (A-C): Bright-field TEM micrographs of structures formed between complementary PCG and NCG in DMEM high glucose (4.5 µg/ml) culture media supplemented with 10% FBS after one hour at 37°C and 5% CO_2, (magnification left to right) 25,000, 80,000 and 200,000. (D): Corresponding mean average (n=3) size distribution curve of suspended complexes in DMEM (red) and distilled water (green), determined by DLS analysis.

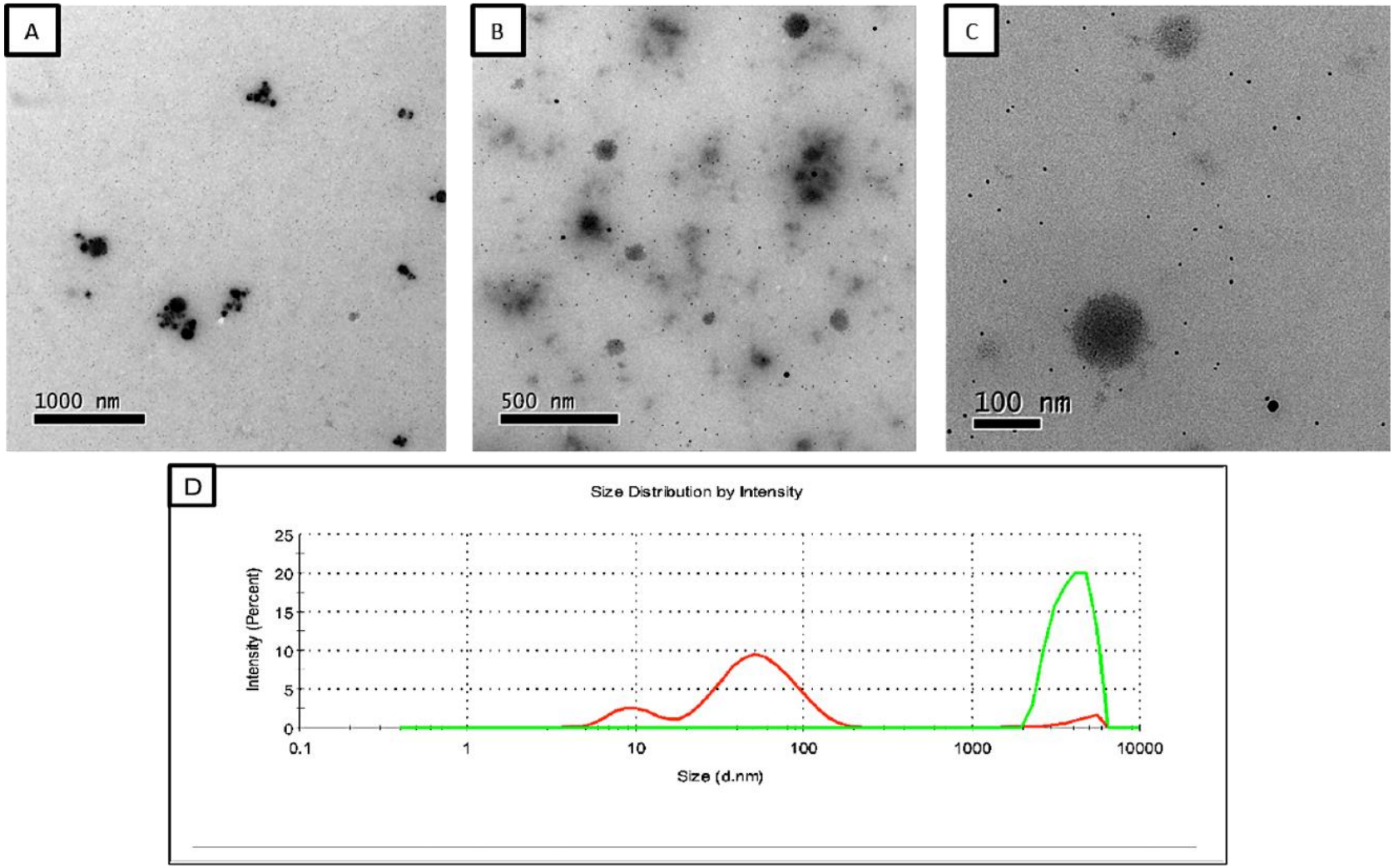

Figure 6.6 A-C: Bright-field TEM micrographs of structures formed between complementary 5 nm oligo-GNPs in DMEM high glucose (4.5 µg/ml) culture media supplemented with 10% FBS after one hour at 37°C and 5% CO_2, (magnification left to right) 12,000, 25,000 and 60,000. (D): Corresponding mean average (n=3) size distribution curve of suspended complexes in DMEM (red) and distilled water (green), determined by DLS analysis.

6.2 Cellular studies and evaluation of *in situ* self-assembly activity of GNPs

Electron microscopy and elemental analysis was used to study the intracellular uptake and distribution of NCG and PCG when administered individually (monodispersed) and simultaneously (*in situ* self-assembly). After 24 hours of treatment, V79 hamster lung fibroblast cells were isolated and prepared for evaluation. Results were compared to determine whether *in situ* self-assembly of GNPs facilitated *via* electrostatic interactions had influenced their intracellular fate. A control specimen consisting of an untreated tissue sample was examined to provide a reference to healthy cell populations, optimise microscope parameters and confirm the validity of analytical approaches.

6.2.1 Morphological evaluation of thin-sectioned cell specimens

Tissue samples were initially studied using bright-field imaging *via* STEM to determine general ultrastructure morphology of cells and confirm the suitability of applied sample preparation techniques. Micrographs of an untreated specimen (control) are presented in Figure 6.8 (A-C) with cells treated either simultaneously or individually with NCG and PCG displayed respectively in Figure 6.8 (D-F) and Figure 6.9 (A-F). For each specimen, a series of images were acquired at increasing magnification to identify features of interest for further analytical study. Intact cellular cross-sections were observed for each specimen with distinguishable extracellular and intracellular features, evidencing effective preservation and processing. Specimen-sections were also revealed to display appropriate electron transparency and contrast, enabling detailed identification of nanoscale structures and cellular organelles. At lower magnification, untreated cells and those treated with GNPs were seen to display definitive cell membranes, intracellular cytoplasmic domains, nuclei and mitochondria. A noticeable increase was observed in the extent of filament-like structures on the surface of cells exposed to GNPs, relative to untreated cells. These features, clearly

seen in Figure 6.8 (D) protruding into the interstitial space were identified as *filopodia*. This observed difference was also shown to correlate with increased interstitial space between cells. Furthermore, cells treated with GNPs appeared to be spherical in shape rather than tightly packed and elongated as observed for untreated cells (Figure 6.8 A). At higher magnification, intracellular vacuoles were revealed within each specimen, such as those highlighted in Figure 6.8 (E, F) and Figure 6.9 (B, C). The general size and shape of vacuoles appeared to be highly variable with no definitive difference observed between cells treated with GNPs and the untreated control. Moreover, vacuoles were frequently observed to contain a multitude of densely contrasted features that had predominantly amassed at their peripheries. These internalised deposits, which can be seen to range in size from approximately 200 to 500 nm, appear to be decorated with darkly contrasted features, comprised of what was assumed to be high atomic mass elements. In addition to these reoccurring sites of interest, structures displaying nanoscale dimensions were also widely revealed within the cell cytoplasm and extracellular matrix of the untreated control and specimens treated with GNPs. Considering that features characteristic of the GNPs under investigation were revealed in both the untreated control specimen and those treated both individual and simultaneously with NCG and PCG, no definitive conclusion was reached at this stage. Consequently, it was decided that further elemental analysis was warranted to elucidate whether features of interest were GNPs, biological matter or potential artefacts produced from sample preparation.

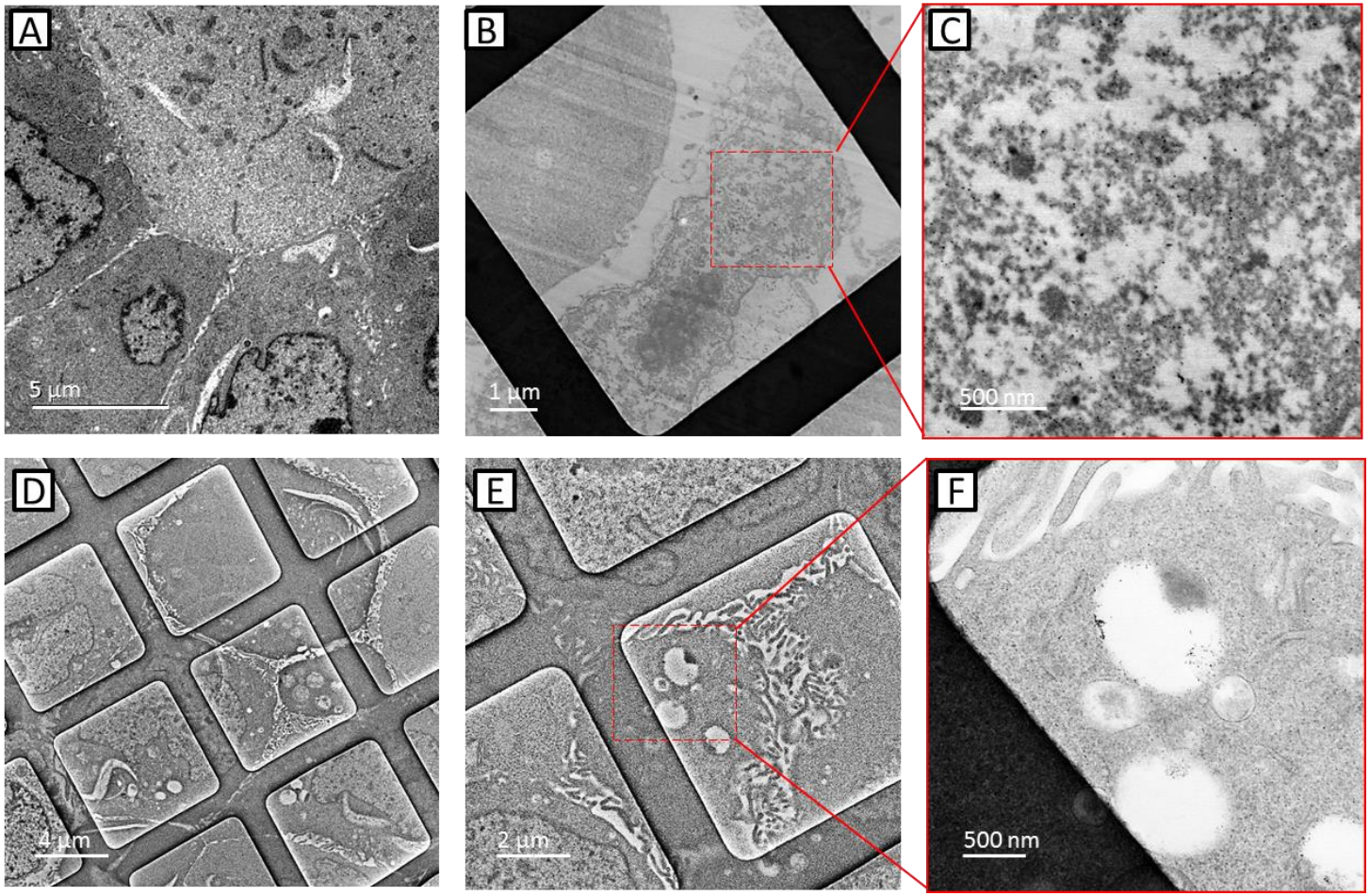

Figure 6.7: Bright-field TEM micrographs displaying an overview of thin-sectioned (60 nm) male Chinese hamster lung fibroblast (V79) cells after 24 hours of treatment. (A-C): (control) cell culture medium only, (magnification left to right) 3,000, 10,000, and 40,000. (D-F): simultaneous exposure to NCG and PCG (1:1 v/v) at a total concentration of 5 µg/ml (gold). Dashed red boxes indicate areas of interest with corresponding micrograph at higher magnification highlighted with red boarders.

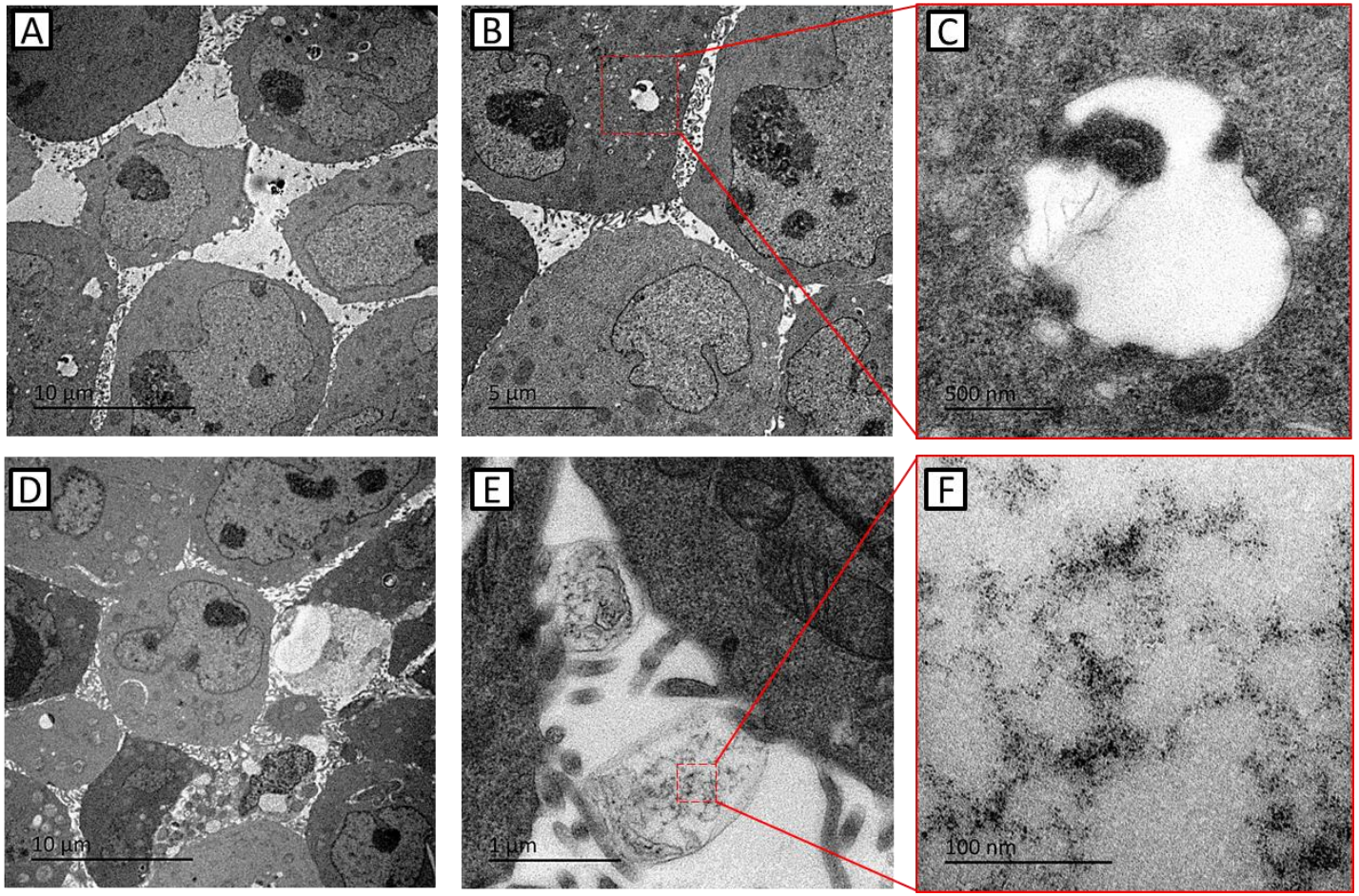

Figure 6.8: Bright-field TEM micrographs displaying an overview of thin-sectioned (60 nm) male Chinese hamster lung fibroblast (V79) cells after 24 hours of treatment. (A-C): exposure to NCG at a concentration of 5 µg/ml (gold). (D-F): exposure to PCG at a concentration of 5 µg/ml (gold), (magnification left to right) 1,200, 30,000 and 320,000. Dashed red boxes indicate areas of interest with corresponding micrograph at higher magnification highlighted with red boarders

6.2.2 STEM-EDS analysis of untreated cellular specimens

An untreated tissue specimen (control) was evaluated using high-resolution STEM and EDS, providing a reference for comparison against cells treated with GNPs. A representative intracellular vacuole was initially identified from HAADF micrographs and a series of increasing magnification images were then acquired to reveal internalised features, presented in Figure 6.10 (A-C). Subsequent EDS analysis was then employed to reveal the identify and distribution of elements within the defined region of the specimen, with elemental maps of gold and osmium displayed alongside their corresponding HAADF micrograph in Figure 6.10 (D-F). From the acquired maps, a definitive correlation was seen between structures of interest (Figure 6.10 B) and the detection and distribution of osmium (Figure 6.10 C). As expected, no observable detection of gold was seen throughout the studied region (Figure 6.10 A). To further confirm these observations, two comprehensive EDS spectra were attained (Figure 6.11), Initially the whole region of interest was analysed, subsequently focusing specifically on structures displaying nanoscale dimensions contained within the intracellular vacuole (see highlighted areas in Figure 6.11 A). Interpretation of spectra (Figure 6.11 B) revealed the presence of osmium, which was used for sample preparation, copper which was present in the sample grid used for analysis and oxygen, lead and chlorine. Notably, the intensity of osmium detection increased when the analysis focused specifically on structures of interest within the vacuolic space. Crucially, no gold was detected from either EDS attempt (circled in Figure 6.11 C), confirming that structures identified within cellular vacuoles did not contain GNPs.

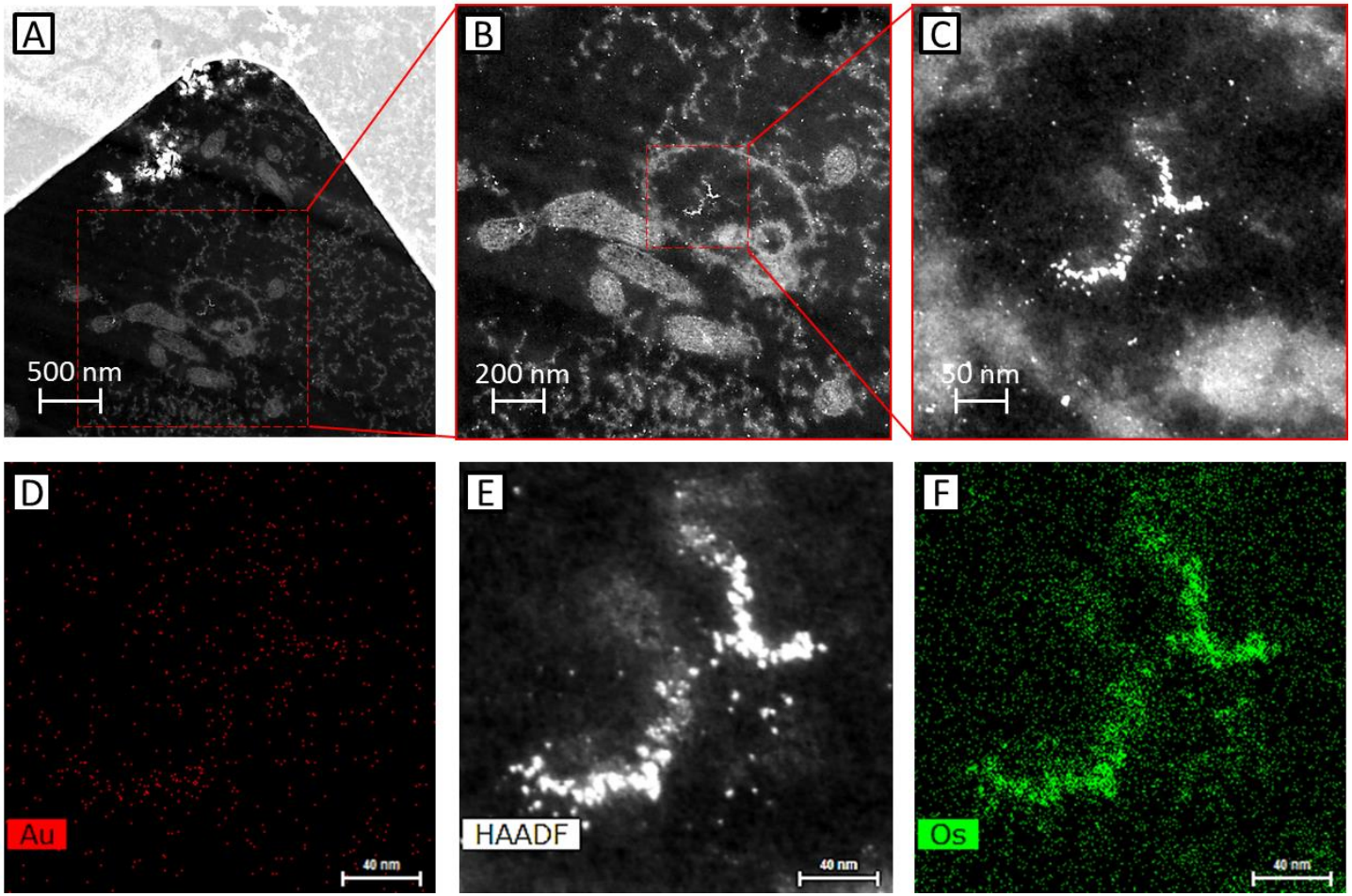

Figure 6.9: Micrographs of an untreated cellular specimen (control) after 24 hours of incubation (A-C): Successive series of STEM-HAADF images of an identified intracellular site of interest containing features displaying nanoscale dimensions, (D-F): EDS maps revealing the distribution of elemental gold and osmium with the corresponding HAADF image. Dashed red boxes indicate areas where successive images were acquired at higher magnification with corresponding micrographs highlighted with red boarders.

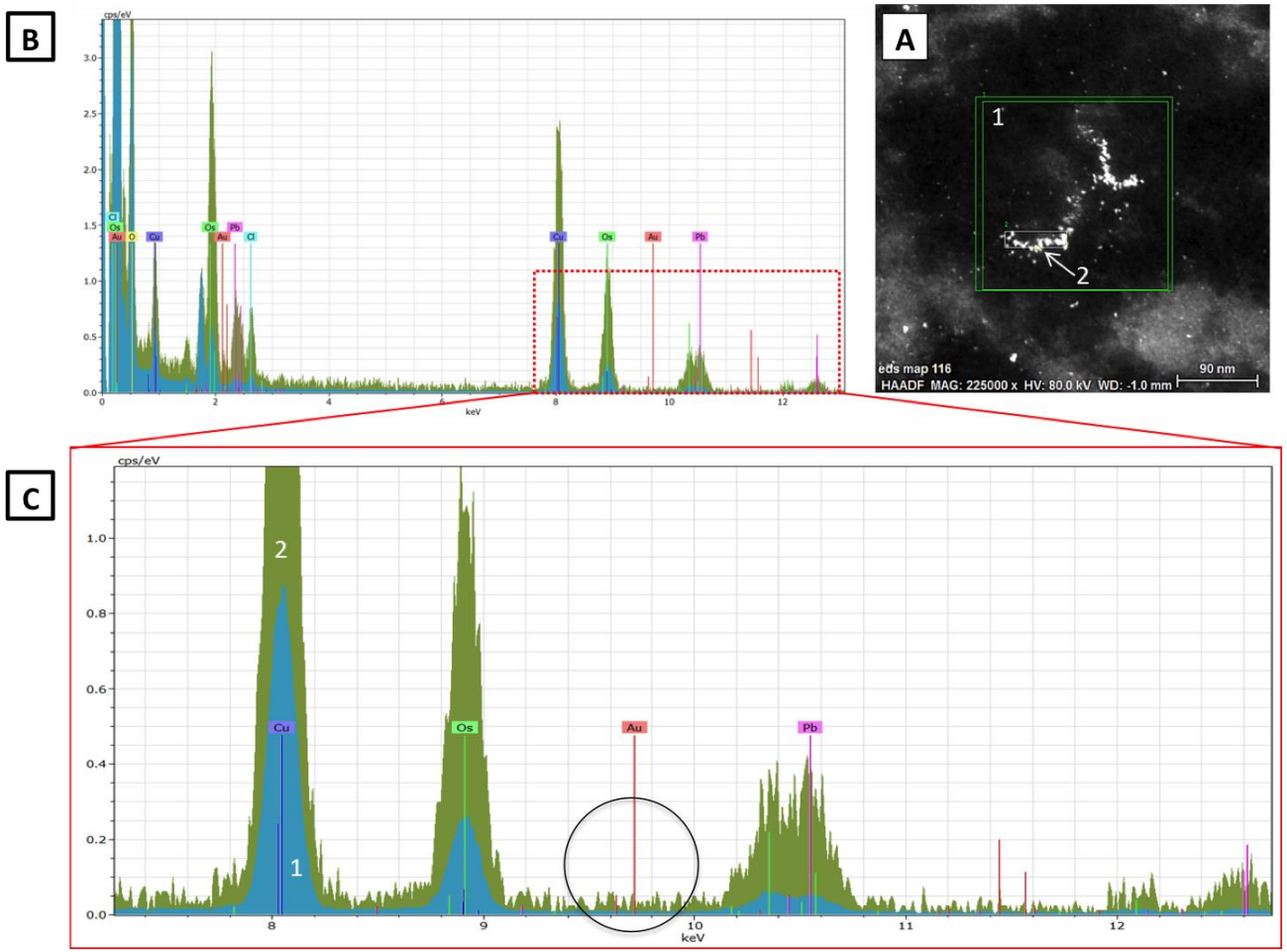

Figure 6.10: EDS spectra obtained from the analysis of an untreated cellular specimen (A): HAADF image of an identified intracellular site of interest displaying the areas selected for evaluation, (B): corresponding interpreted comprehensive EDS spectra with (C): highlight the peaks for gold and osmium. From HAADF image, EDS spectra for area (1) is displayed in blue and area (2) is displayed in green for comparison.

6.2.3 Microscopy optimisation

Optimal image acquisition was attained experimentally using a range of STEM electron-beam accelerating voltages on un-coated specimens. Resultant micrographs were compared to reveal operating parameters that provided sufficient sample-stability, image contrast and resolution. As seen in Figure 6.7 (A-C), resolution and contrast were sufficient to identify cellular organelles and features with nanoscale dimensions at each accelerating voltage investigated. An increase in artificial image contrast, a product of radiation damage, was noticeable at higher accelerating voltages (highlighted with white arrows in Figure 6.7 A-C). This was considered indicative of increasing excessive energy deposition into the specimen[351]. Attempting to further improve specimen stability, a STEM sample grid was coated with carbon on the reverse-side (underneath the specimen) and reanalysed at 80 keV (Figure 6.7 D). Image acquisition after applying this technique appeared superior with less occurrences of radiation damage in micrographs and retention of sufficient resolution. Based on these preliminary findings it was concluded that subsequent analysis would be performed whilst operating at an accelerating voltage of 80 keV on specimens with a carbon coating on the reverse-side of specimen grids.

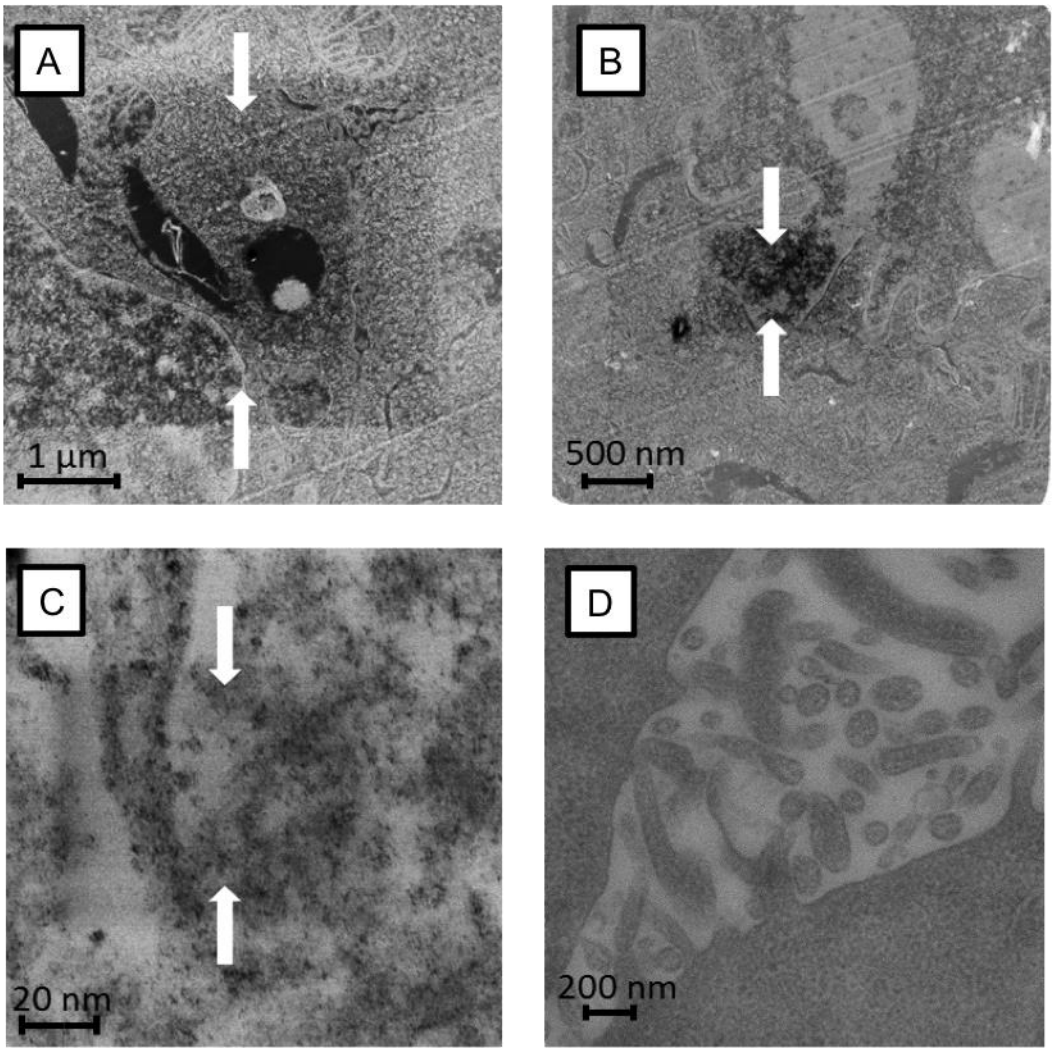

Figure 6.11: Bright-field micrographs of untreated thin-sectioned (60 nm) male Chinese hamster lung fibroblast cells (V79) demonstrating the process of image acquisition optimisation. Micrographs of specimens (Un-coated) were examined operating at accelerating voltages of (A): 200 keV, (B): 120 keV, (C): 80 keV and (D): a specimen sputter-coated with carbon on the reverse side at 80 keV. White arrows highlight areas of radiation damage identified in micrographs.

6.2.4 STEM-EDS analysis of cellular specimens treated with NCG

A tissue specimen was evaluated after treatment with NCG employing the same approach for untreated cells (control). A series of HAADF images were initially acquired *via* STEM to reveal sites of interest with subsequent EDS analysis used to determine identity and distribution of elements. Resultant micrographs presented in Figure 6.12 (A-C) depict an individual representative cellular vacuole identified to contain brightly contrasted material. Structures characteristic of endocytic vesicles were frequently seen

to be “budding” from the periphery of vacuoles into the intravacuolic space (Figure 6.12 B), indicative of the formation and maturation of late-endosomes[352,353]. At higher magnification (Figure 6.12 C), individual structures characteristic of the GNPs under investigation were noticeable amongst larger accumulations of internalised matter. It was noted however that the general appearance of these features was not distinctively different from observations derived from analysis of the untreated (control) tissue specimen. Elucidating further, elemental maps of gold and osmium are presented alongside their equivalent HAADF micrograph in Figure 6.12 (D-F). Similarly to the untreated specimen, internalised structures clearly correlated with the detection of osmium against the background void of the vacuolic domain (Figure 6.12 F). Significantly, gold was also detected within the analysed region, with a positive correlation observed between both structures of interest and distribution of osmium (Figure 6.12 D). Brightly contrasted structures that appeared to have amassed towards the centre of the vacuole displayed the greatest intensity of gold. Further gold detection was noticeable within the identified endocytotic vesicle near the perimeter. Supplementing these findings, EDS spectra obtained from analysing the whole region of interest and subsequently focusing on structures identified to contain gold were compared (see highlighted areas in Figure 6.13 A). As expected, osmium and copper were identified within the analysed specimen regions, as were elements previously detected from analysis of untreated specimen (control); oxygen, chlorine and lead (Figure 6.13 B). Additionally, sulphur and gold were detected, with a 3-fold increase in the observed intensity for gold (circled in Figure 6.13 C) when focusing on structures characteristic of GNPs. It was concluded from these findings that administration of NCG in a monodispersed state had resulted in GNP accumulation within vacuolic compartments of V79 lung fibroblastic cells, within the 24-hour period investigated.

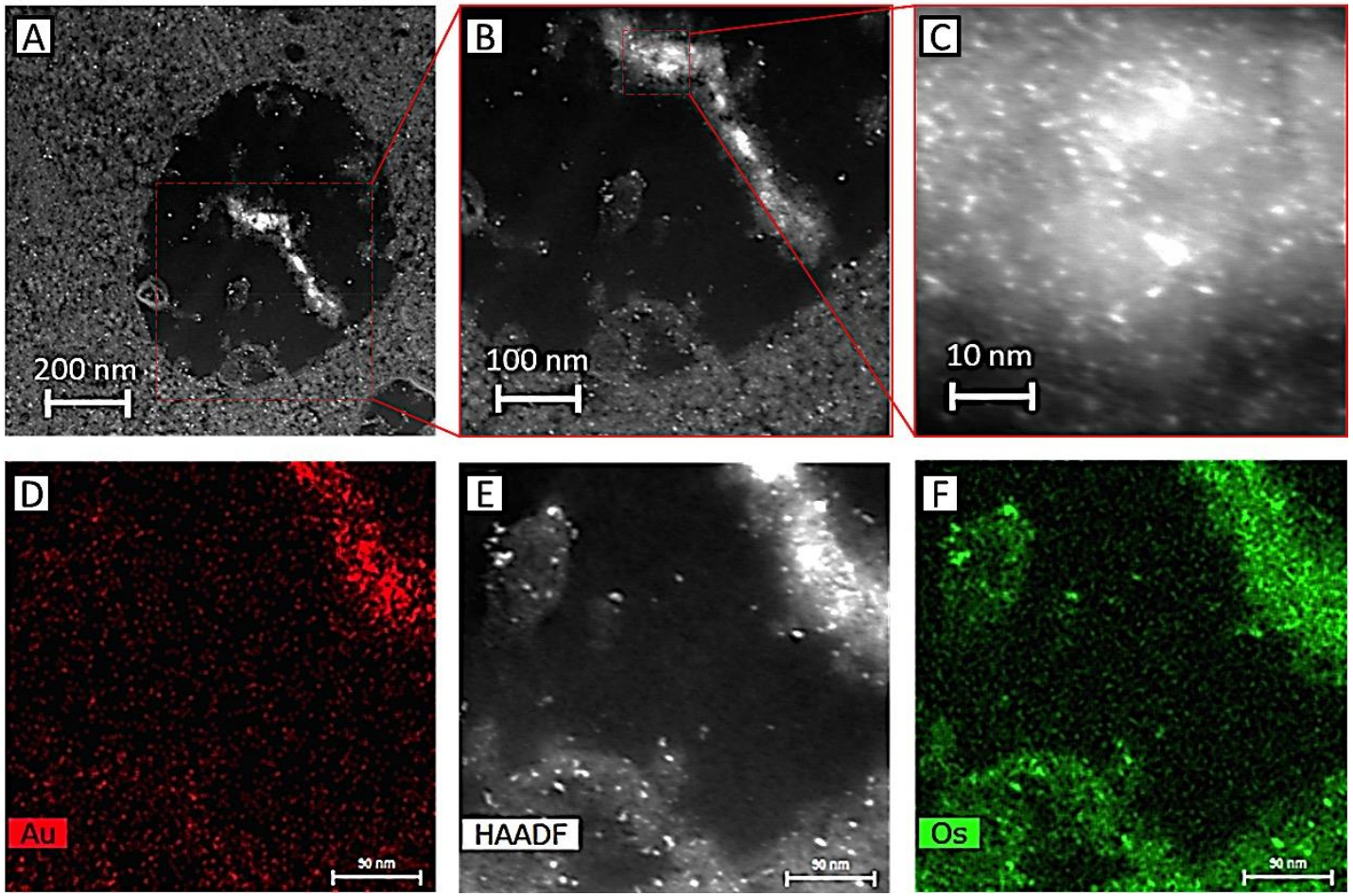

Figure 6.12 Micrographs of a cellular specimen after 24 hours of treatment with NCG (5 µg / ml total gold concentration). (A-C): Successive series of STEM-HAADF images of an intracellular vacuole containing features of interest, (D-F): EDS maps revealing the distribution of elemental gold and osmium with the corresponding HAADF image. Dashed red boxes indicate areas where successive images were acquired at higher magnification with corresponding micrographs highlighted with red boarders.

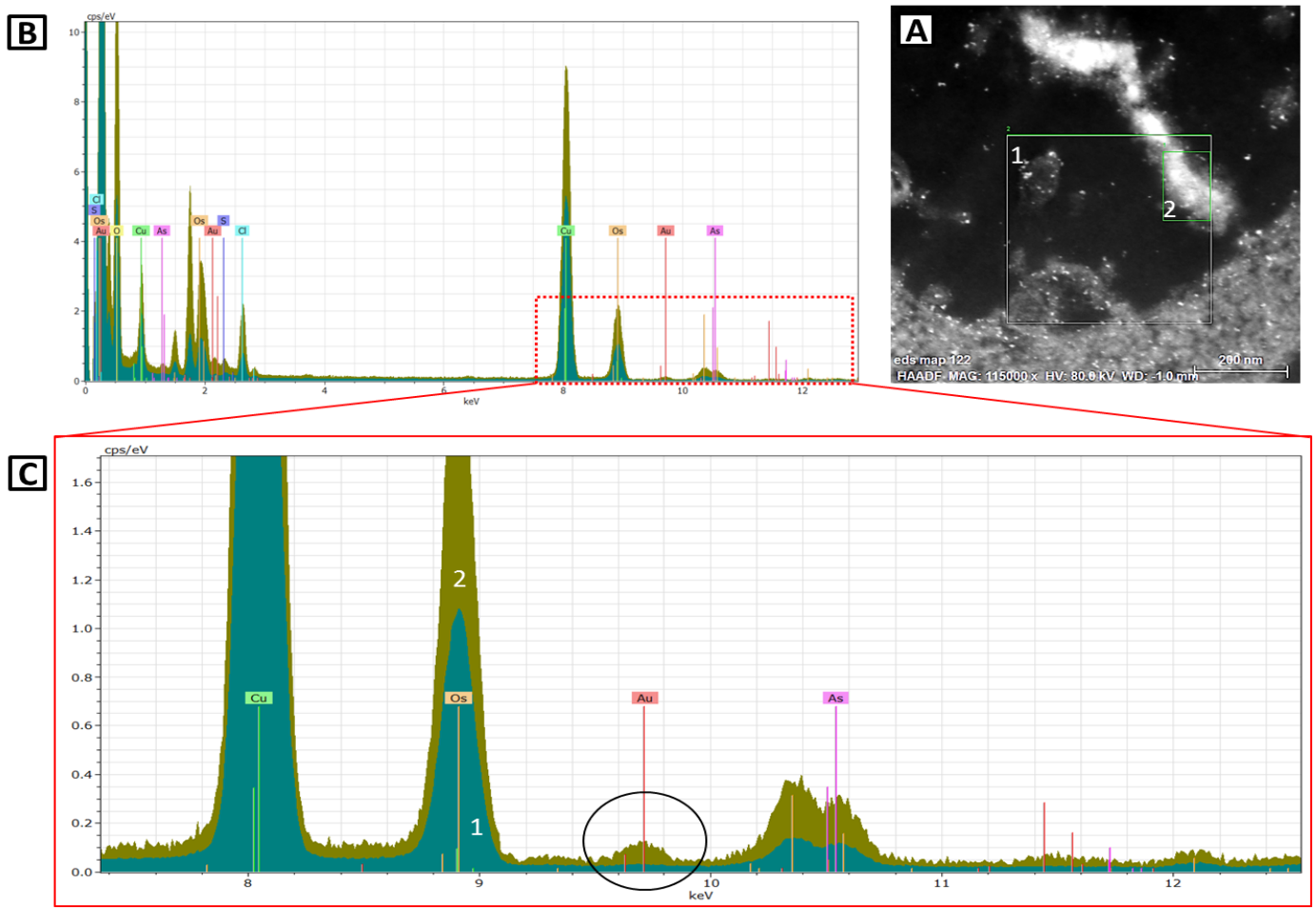

Figure 6.13: EDS spectra obtained from the analysis of a cellular specimen after 24 hours of treatment with NCG (5 µg / ml total gold concentration). (A): HAADF image of an identified intracellular site of interest displaying the areas selected for evaluation, (B): corresponding interpreted comprehensive EDS spectra with (C): highlighting the peaks for gold and osmium. From HAADF image, EDS spectra for area (1) is displayed in blue and area (2) is displayed in green for comparison.

6.2.5 STEM-EDS analysis of cellular specimens treated with PCG

Applying the same approach of evaluation, tissue specimens were studied after treatment with positively charged GNP building blocks (PCG) at 5 µg/ml total gold concentration, which was previously revealed to be a non-cytotoxic treatment (Chapter 5). Presented in Figure 6.14 (A-C), a representative cellular vacuole was identified from micrographs to contain internalised features, appearing similar to observations from untreated specimens (control) and those exposed to NCG. Accumulations of matter were regularly observed at the peripheries of vacuoles, with structures characteristic of endocytic vesicles protruding within the vacuolic space (Figure 6.14 A). Irregular isolated clusters of brightly contrasted features, ranging in size from 20 nm to 400 nm and decorated with structures characteristic of the GNPs under investigation were selected for further analysis (Figure 6.14 B, C). Acquired maps of gold and osmium are presented alongside their equivalent HAADF micrograph in Figure 6.14. (D-F). Surprisingly, no detection of gold (Figure 6.14 D) was revealed for structures initially thought to be GNPs (Figure 6.14 C). A considerable accumulation of gold was however detected elsewhere within the intravacuolic space, correlating with features observed in the HAADF micrograph (Figure 6.14 E). Furthermore, a noticeable detection of gold was revealed at the cytoplasm-vacuole interface, relative to vacant regions of the vacuolic domain. Detection of osmium appeared analogous to results obtained in sections 6.2.3 and 6.2.4, with a positive correlation seen for cytoplasm surrounding the vacuole and internalised matter (Figure 6.14 F). Comprehensive EDS spectra obtained by initially analysing the whole region of interest and subsequently focusing on structures identified to contain gold from elemental maps are displayed in Figure 6.15. Comparable to evaluation of untreated cells (control), elements detected included copper from the sample grid used in the analysis, osmium used for sample preparation and oxygen, chlorine and arsenic (Figure 6.15 B). Furthermore, in agreement with previous results gold and sulphur were identified from the spectra, indicative of the GNPs under investigation with their thiol (SH) containing functional groups. Comparison of spectra obtained

from the two regions (see highlighted areas in Figure 6.15 A) indicate that the distribution of gold is limited to isolated regions within the selected vacuole; no definitive peak for gold was observed when initially analysing the region of interest, with a 4-fold increase when the analysis was focused on features of the micrograph previously identified to contain gold (circled in Figure 6.15 C). Comparable to conclusions derived from analysis of cells treated with NCG, administration of PCG in a monodispersed state had resulted in GNP accumulation within vacuolic compartments of V79 lung fibroblastic cells within the 24-hour period investigated.

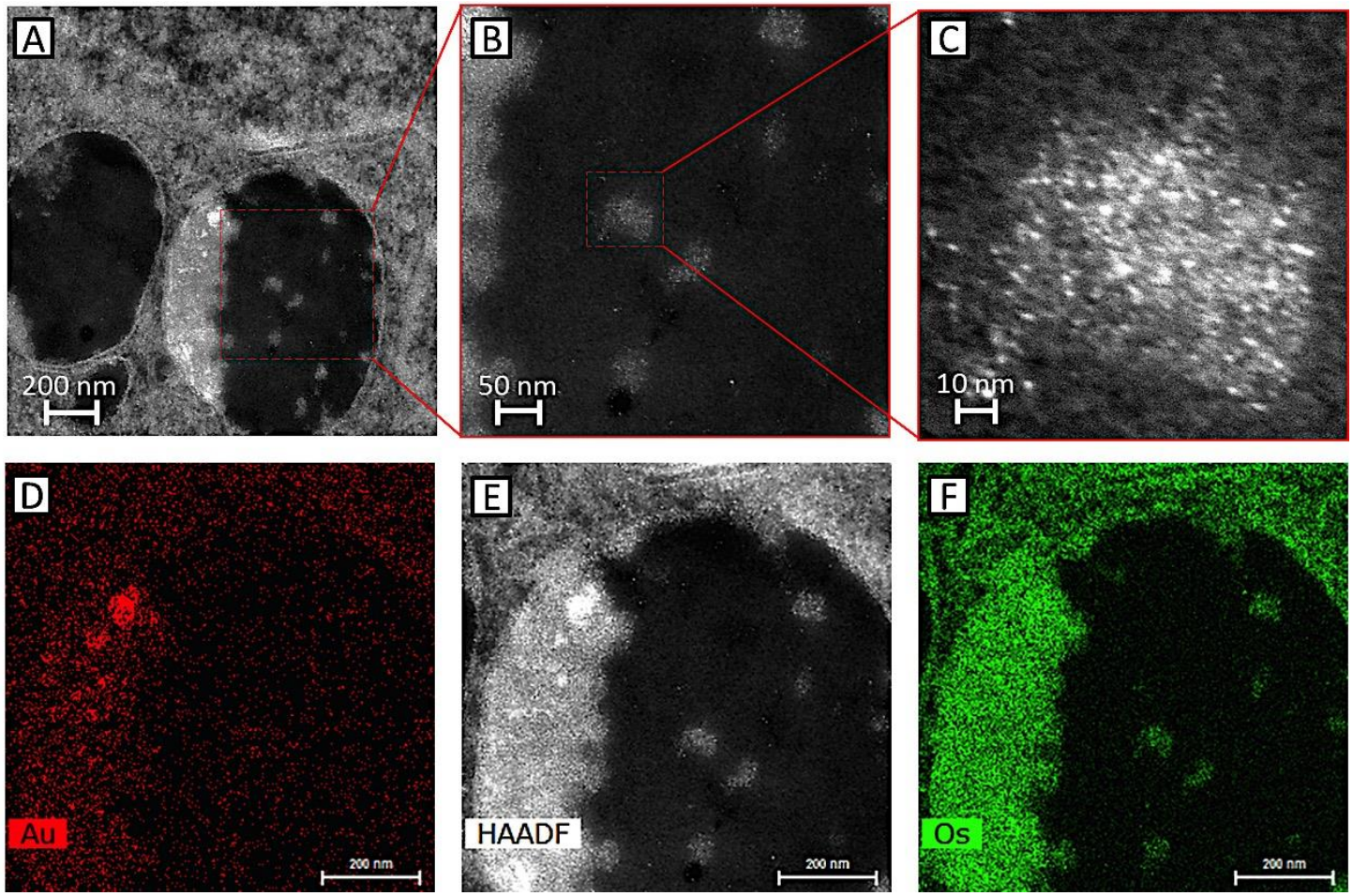

Figure 6.14. Micrographs of a cellular specimen after 24 hours of treatment with PCG (5 µg / ml total gold concentration). (A-C): Successive series of STEM-HAADF images of an intracellular vacuole containing features of interest, (D-F): EDS maps revealing the distribution of elemental gold and osmium with the corresponding HAADF image. Dashed red boxes indicate areas where successive images were acquired at higher magnification with corresponding micrographs highlighted with red boarders.

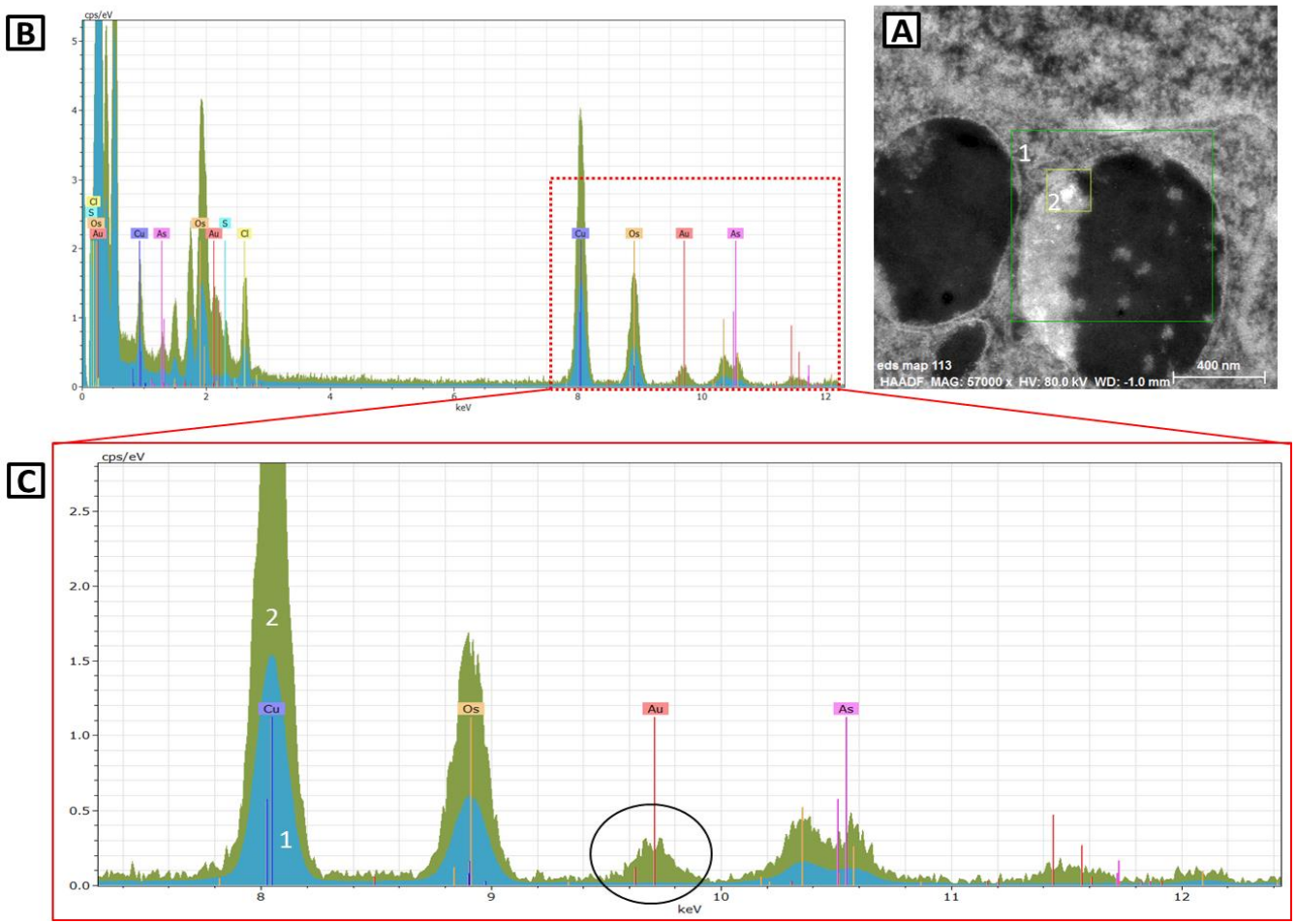

Figure 6.15 EDS spectra obtained from the analysis of a cellular specimen after 24 hours of treatment with PCG (5 µg / ml total gold concentration). (A): HAADF image of an identified intracellular site of interest displaying the areas selected for evaluation, (B): corresponding interpreted comprehensive EDS spectra with (C): highlighting the peaks for gold and osmium. From HAADF image, EDS spectra for area (1) is displayed in blue and area (2) is displayed in green for comparison.

6.2.6 STEM-EDS analysis of cellular specimens co-treated with NCG and PCG

Tissue specimens were evaluated after simultaneous treatment with NCG and PCG (1:1) to determine if intracellular self-assembly had occurred. Additionally, the intracellular fate of these GNPs relative to their monodispersed counterparts was compared to elucidate any effects of *in situ* self-assembly activity as evidenced in section 6.1.3. Utilising the same approach as previously, a series of HAADF images were studied to identify sites of interest with subsequent EDS analysis revealing the identity and distribution of elements. Representative cellular vacuoles were identified from micrographs (Figure 6.16 A-C) containing a multitude of internalised features, varying in size below 500 nm. Amongst intravacuolic material, brightly contrasted structures characteristic of the GNPs under investigation were consistently observed. It was concluded that the distribution and morphology of structures within the studied vacuoles were analogous to those evaluated from specimens treated with either NCG or PCG individually. Additionally, well-defined structures characteristic of endocytic vesicles were regularly identified protruding within the intravacuolic space (Figure 6.16 B), further comparable to observations after exposure to monodispersed NCG and PCG in sections 6.2.4 and 6.2.5. Crucially, it was determined that there was no definitive evidence from current results to suggest that *in situ* self-assembly activity had influenced the intracellular fate of the GNPs under investigation. To clarify further, a vacuole containing structures characteristic of the GNPs under investigation was selected for EDS analysis. Acquired elemental maps for gold and osmium are presented alongside their equivalent HAADF micrograph in Figure 6.16. (D-F). Comparable to individual treatments, distribution of gold (Figure 6.16 D) appeared to correlate with structures expected to be GNPs (Figure 6.16 E). Detection of gold however was noticeably lower and appeared further spread out within the selected specimen region compared to those studied after treatment with NCG and PCG individually. A definitive correlation was also seen between the detection and distribution of osmium (Figure 6.16 F) and features of the HAADF micrograph, comparable to results obtained from analysis of

untreated cells (control) and individual treatments. Unfortunately, owing to inadequate specimen stability an alternative cellular vacuole had to be selected for further elemental analysis, with resultant spectra presented in Figure 6.17. Utilising the same approach as previously, a region of interest was initially evaluated with analysis subsequently focusing on structures appearing characteristic of GNPs (see highlighted areas in Figure 6.17 A). As expected, interpretation of EDS spectra (Figure 6.17 B) revealed the presence of copper from the sample grid used in the analysis and osmium from sample preparation. Additional elements detected within the specimen region included oxygen, chlorine, arsenic and lead, consistent with prior results. Crucially, gold and sulphur were not detected in the analysed region (circled in Figure 6.17 C), even when focusing on features of the micrograph that appeared representative of GNPs. Although results of elemental maps appear to contradict with an absence of gold detection in EDS spectra, it was considered conceivable that the distribution of gold was variable between the two intravacuolic sites studied for this specimen. Taking into consideration the difficulty in detecting gold in this instance, no further evidence was obtained supporting the notion that *in situ* self-assembly activity had influenced the intracellular fate of GNPs. Furthermore, the internalisation, distribution and morphology of structures that did appear to correlate with the detection of gold provided no assertive evidence for intracellular self-assembly.

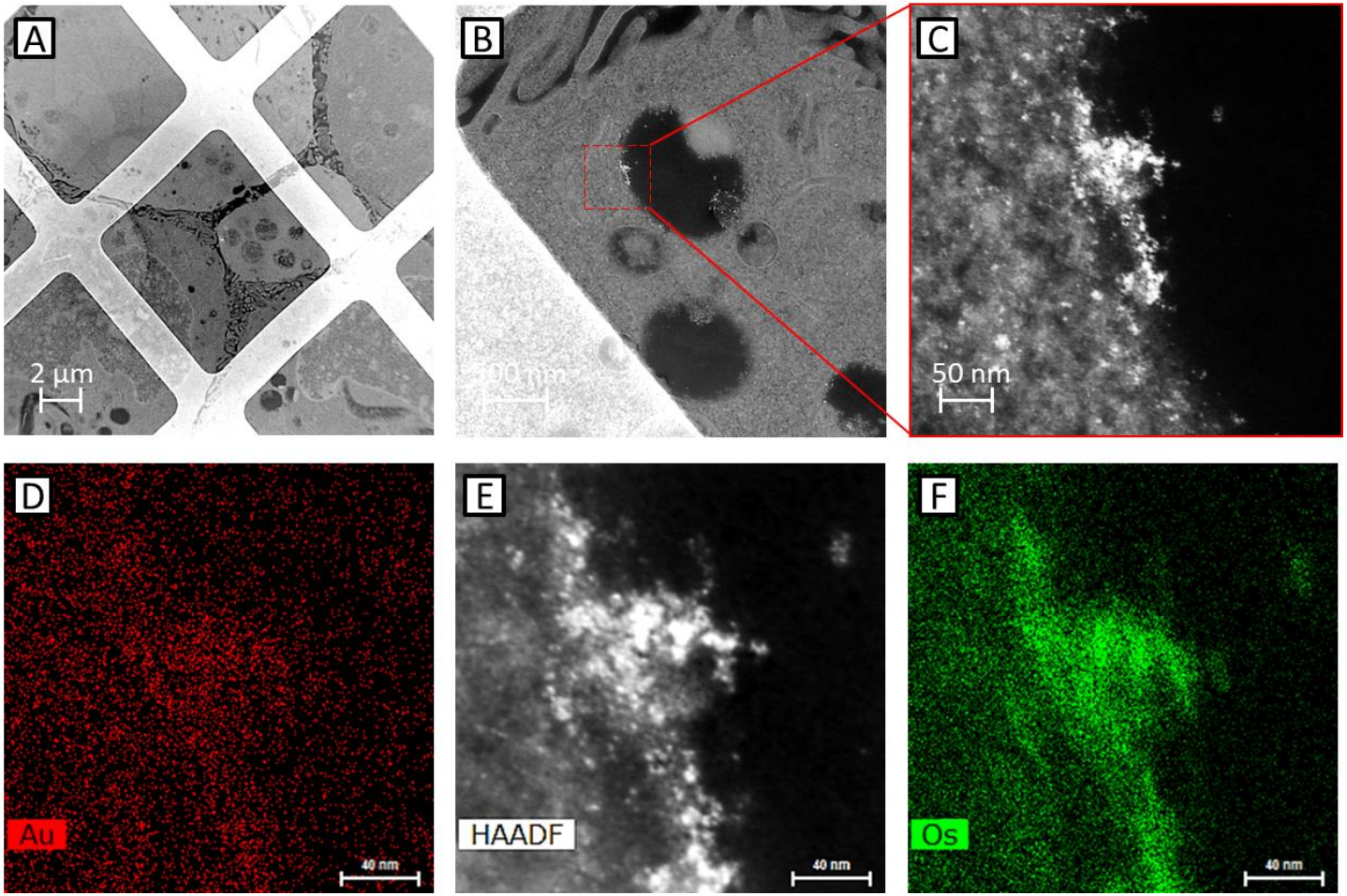

Figure 6.16: Micrographs of a cellular specimen after 24 hours of treatment with NCG and PCG simultaneously (1:1, 5 µg / ml total gold concentration). (A-C): Successive series of STEM-HAADF images of an intracellular vacuole containing features of interest, (D-F): EDS maps revealing the distribution of elemental gold and osmium with the corresponding HAADF image. Dashed red boxes indicate areas where successive images were acquired at higher magnification with corresponding micrographs highlighted with red boarders.

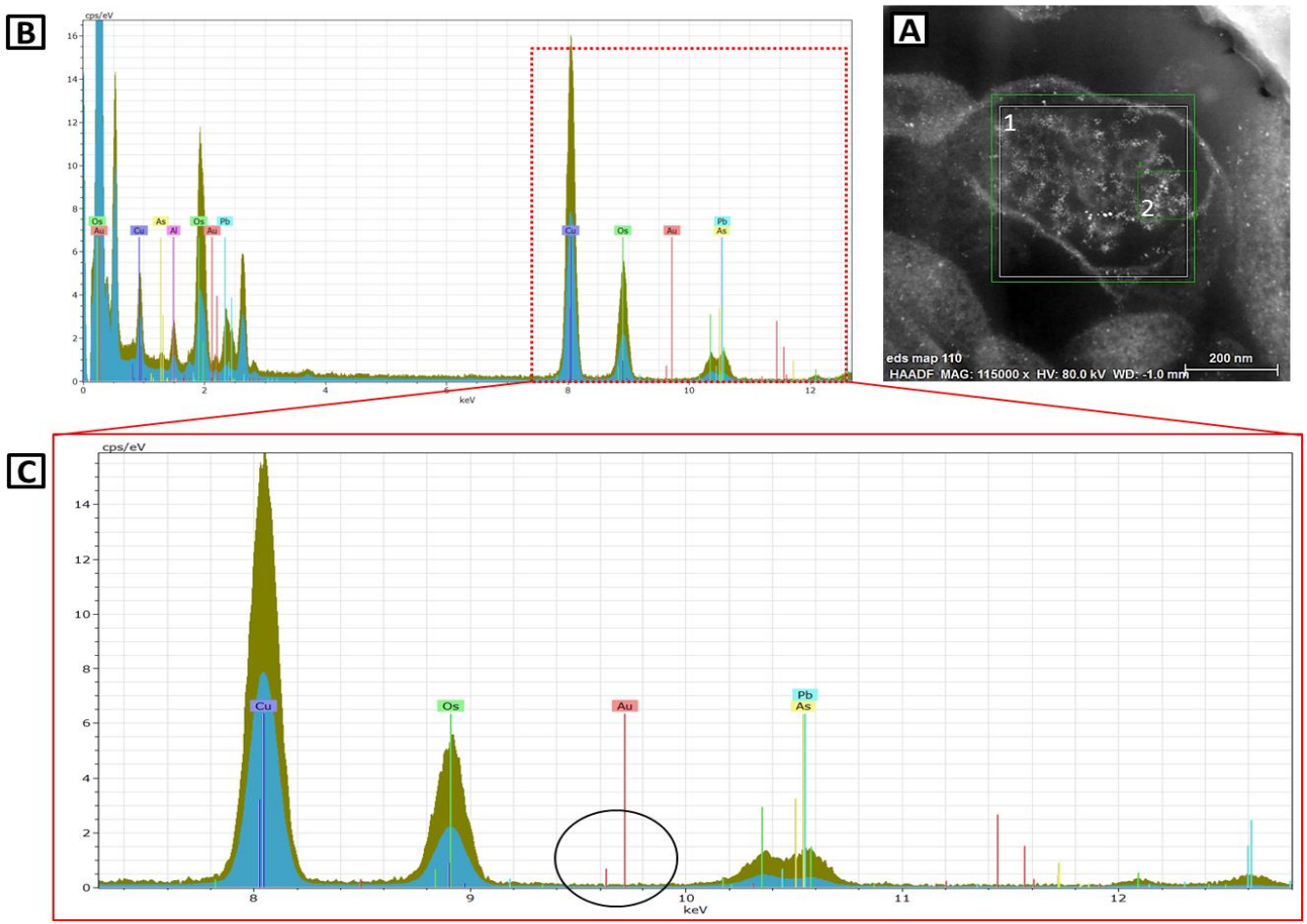

Figure 6.17: EDS spectra obtained from the analysis of a cellular specimen after 24 hours of treatment with NCG and PCG simultaneously (5 µg / ml total gold concentration). (A): HAADF image of an identified intracellular site of interest displaying the areas selected for evaluation, (B): corresponding interpreted comprehensive EDS spectra with (C): highlighting the peaks for gold and osmium. From HAADF image, EDS spectra for area (1) is displayed in blue and area (2) is displayed in green for comparison.

6.3 Discussion

Physicochemical properties of nanomaterials are known to influence their biological interaction and responses which can ultimately determine their behaviour in such environments[354]. However, at present numerous studies concerning the fate of nanomaterials *in vitro* and *in vivo* lack emphasis with respect to the properties of these materials after they have been introduced into a biological system. One aspect of nanoparticle behaviour identified in particular that has been overlooked, is the state of particle dispersion, whether as a result of uncontrolled aggregation or intentional self-assembly[355]. Consequently, understanding the *in situ* behaviour of the GNPs under investigation in this project was considered crucial to the interpretation of results obtained from toxicological assays and cellular evaluation.

Characterisation of GNPs within a biologically relevant medium as attained in this study are considered to provide a general overview of nanomaterial-biological interactions. Analysis in this study is used to compare the behaviour of GNPs when administered individually (monodispersed) and simultaneously as a complementary pair (*in situ* self-assembly). Resultant uptake and distribution of GNPs by V79 lung fibroblast cells is discussed and compared to recent literature to determine the feasibility of utilising electrostatic interactions for *in situ* self-assembly under biological conditions. Utilised methodology is reviewed, encompassing findings of this work with current literature to suggest approaches to overcome current limitations.

6.3.1 Evaluation of a biologically relevant medium

Dulbecco's modified eagle medium (DMEM) supplemented with 10 % fetal bovine serum (FBS) was selected as a biological medium to simulate potential exposure conditions. This decision to use this medium was based on the necessity to retain consistency between toxicity studies in Chapter 5 and appropriately mimic the complex aqueous environment presented *in*

vivo. Displayed in Table 6.1, the main components of the utilised medium and human plasma were compared. Notably, pH of the utilised medium and the electrolyte composition and concentration are comparable to that of human plasma, two fundamental parameters that influence nanoparticle stability and behaviour[355]. Equally important, protein composition of the utilised medium is comprised of bovine serum albumins (BSA), which are typically analogous in terms of size, shape and functionality to human serum albumins (HSA) that constitute the major components of human plasma[355,356]. Micrographs and the corresponding size distribution curve from the analysis of CCM revealed globular-shaped structures with an average hydrodynamic diameter of 100.9 nm. According to previous reports, individual globulin and albumin proteins that constitute the utilised medium display a similar globular domain but are typically sized between 5 -10 nm[357,358]. The observed difference in size correlates with the higher than expected dispersity value obtained (section 6.1.1) indicating that proteins are not exclusively in free form. Furthermore, protein configuration is retained as a result of a balance of hydrodynamic and hydrophobic forces, which were not maintained during microscopy analysis. Nevertheless, experimental conditions remained identical for subsequent analysis and micrographs of CCM were considered as a suitable control reference for comparison.

Table 6.1. Main components of utilised medium compared to human blood plasma

Classification	Component details		DMEM + 10% FBS	Human plasma
Amino acids	Total	(mM)	10.65	2.32 – 4.05
Vitamins	Total……	(mM)	0.15	< 0.07
Cations	Sodium, Na^+	(mM)	155.31	142.00
	Potassium, K^+	(mM)	5.33	4.00
	Calcium, Ca^{2+}	(mM)	1.80	2.50
	Magnesium, Mg^{2+}	(mM)	0.81	1.50
	Iron, Fe^{3+}	(mM)	0.25	10.00 – 27.00
Anions	Chloride, Cl^-	(mM)	117.47	103.00
	Bicarbonate, HCO_3^-	(mM)	44.05	27.00
	Sulphate, SO_4^-	(mM)	0.81	0.50
	Nitrate, NO_3^-	(mM)	0.74	20.00
	Phosphate, PO_4^{3-}	(mM)	0.92	1.00
Proteins	Total	($g\ L^{-1}$)	3.00 – 4.50	65.00 - 80.00
pH	(pH range)		7.00 – 7.40	7.34 – 7.42
Osmolality	($mOsm\ kg^{-1}$)		320 -360	276 -

* Tabulated data obtained from Moore, T. L. *et al* 2015[355].

6.3.2 Evidencing interactions between GNPs and biological constituents

Nanomaterials are well documented interacting with a range of biomolecules when introduced into a physiological environment[359]. Whilst numerous studies have focused on the properties of nanoparticles and how their interfaces with biological constituents influence cellular responses *in vitro*[360,361], consideration is not always given to the colloidal state of materials suspended in biological fluids[355]. Consequently, it was decided that the dispersion of GNPs in CCM when administered in a monodispersed state should be investigated. Incubation of NCG, PCG (section 6.1.2) and oligo-GNPs (section 6.1.3) individually (monodispersed) in CCM were found to result in extensive complex formation. In agreement, numerous studies have demonstrated the adsorption of proteins including BSA onto the surface of nanoparticles, resulting in the formation of a "*protein corona*"[362,363]. There are two main hypotheses proposed that explain GNP-protein corona formation; "*hard corona*" arising from high affinity protein binding directly to the GNP surfaces by displacing surface-ligands, and "*soft corona*" where proteins interact with GNPs and their surface-bound ligands *via* a range of interactions, undergoing dynamic exchange overtime[364,365]. The process of nanoparticle-biomolecule structure formation is evidently complex and a combination of coordination, hydrogen bonding, van der Waals forces, electrostatic and hydrophobic interactions between proteins, electrolytes, nanoparticle surfaces and their bound-ligands and considered to contribute[364-367]. Furthermore, as a consequence of these interactions, conformational changes can occur in the protein structures, resulting in unfolding, aggregation and nanoparticle-protein assemblies[368], as observed in the present study. Typically, the overall sum of these attractive and repulsive forces will dictate the extent and type of nanoparticle-protein complexation, which could explain observed differences seen for NCG, PCG and oligo-GNPs. For example, cationic amine-functionalised nanoparticles were previously demonstrated to adsorb fewer proteins than their anionic carboxylate-functionalised counterparts[369]. Additionally, studies have revealed that plasma proteins bind more efficiently to larger nanoparticles as

a result of nanoparticle-curvature dependant binding constants[370]. This was not observed however for 5 nm oligo-GNPs compared to either 2 nm NCG or PCG in this study, possibly due to a predominant influence arising from differing surface properties for these nanoparticles. It was concluded that interactions between the GNPs under investigation and biological constituents of the utilised CCM had ensued. Resultantly, nanoparticle-biomolecule complexes formed, with their variable morphology thought to be dependent on the types of interactions taking place. Furthermore, no occurrences of GNP-GNP aggregation were observed, suggesting the functionalised GNPs were stable under the physiological conditions investigated.

6.3.3 Evaluation of GNP self-assembly within a biological medium

Investigations regarding the self-assembly of nanomaterial building blocks into complex nanostructures for diagnostic and therapeutic purposes have progressively increased. However, at present the majority of studies have assembled structures before their introduction into biological systems[11,12]. Accordingly, the aims of the current project were directed towards demonstrating a proof-of-concept, evidencing *in situ* assembly of GNPs under physiological conditions. Two different strategies of self-assembly demonstrated in Chapter 3 were investigated within CCM, revealing whether nanoparticle-biomolecule interactions discussed in section 6.3.2 influenced their activity.

6.3.3.1 Utilising electrostatic interactions

Exploiting electrostatic attractions between NCG and PCG, effective self-assembly was evidenced by the formation of GNP clusters after their simultaneous incubation in CCM (section 6.1.4). Morphology of the assembled GNPs appeared to correspond with results of self-assembly in Chapter 3, which was not observed after incubation of either NCG or PCG individually (sections 6.1.2 and 6.1.3). Bio-complex formation was further

revealed with assembled nanoparticles consistently distributed amongst globular-like structures comparable to protein structures identified in section 6.1.1**.** DLS analysis showed that resultant structures were similar in size to nanoparticle-biomolecule complexes formed after incubation of NCG individually, but larger than observed for PCG. It was noted however that these observations reflected the overall hydrodynamic dimensions of nanoparticle-biomolecule complexes and could not be related directly to the assembled GNP clusters. Interestingly, previous studies have also shown that regardless of the original particle size, GNPs form nanoparticle-biomolecule complexes of comparable magnitude in DMEM culture media[371]. Comparing the hydrodynamic size of structures arising from incubation of NCG and PCG in PBS however, revealed at least a 46-fold decrease in the size of assembled GNP constructs within CCM (Figure 6.5 D). This suggested that whilst self-assembly facilitated *via* electrostatic attraction had occurred; interactions between GNPs and constituents of the biological medium discussed in section 6.3.2 had noticeably reduced this activity. To elucidate, there are several key factors considered likely to be influencing overall self-assembly activity; firstly, electrolytes, proteins and other charged species in the utilised CCM could be contributing towards long-range interactions, whereby the sum of cohesive and depletion forces would dictate the overall attraction between NCG and PCG[372] and secondly, protein adsorption onto GNP surfaces could induce steric hindrance preventing interparticle contact, a mechanism previously demonstrated to enhance nanoparticle colloidal stability under certain conditions[371]. Lastly, when proteins form coronas on nanoparticles they are believed to act like “complex surfactants”, ultimately sheltering intrinsic nanoparticle surface properties and providing altered characteristics[373]. In regard to the surface charge of GNPs, this effect could be considered analogous to the PEGylation of liposomes in Chapter 4; where an additional PEG coating induces charge-shielding and provides altered surface properties that reflect the PEG structure itself. If an equivalent process was to result in NCG and PCG displaying similar surface charges, electrostatic induced self-assembly would be reduced or entirely averted[374]. Since self-assembly activity appears to have been diminished but not prevented in this investigation, it is proposed

that the opposite surface charge displayed by NCG and PCG could promote interactions with oppositely charged counter-ions and functional groups expressed on proteins[375]. Consequently, a range of complex interactions between neighbouring GNPs and surface-bound components of varying iconicity could have prompted the observed self-assembly,[372,374,376] as portrayed in the schematic presented in Figure 6.18.

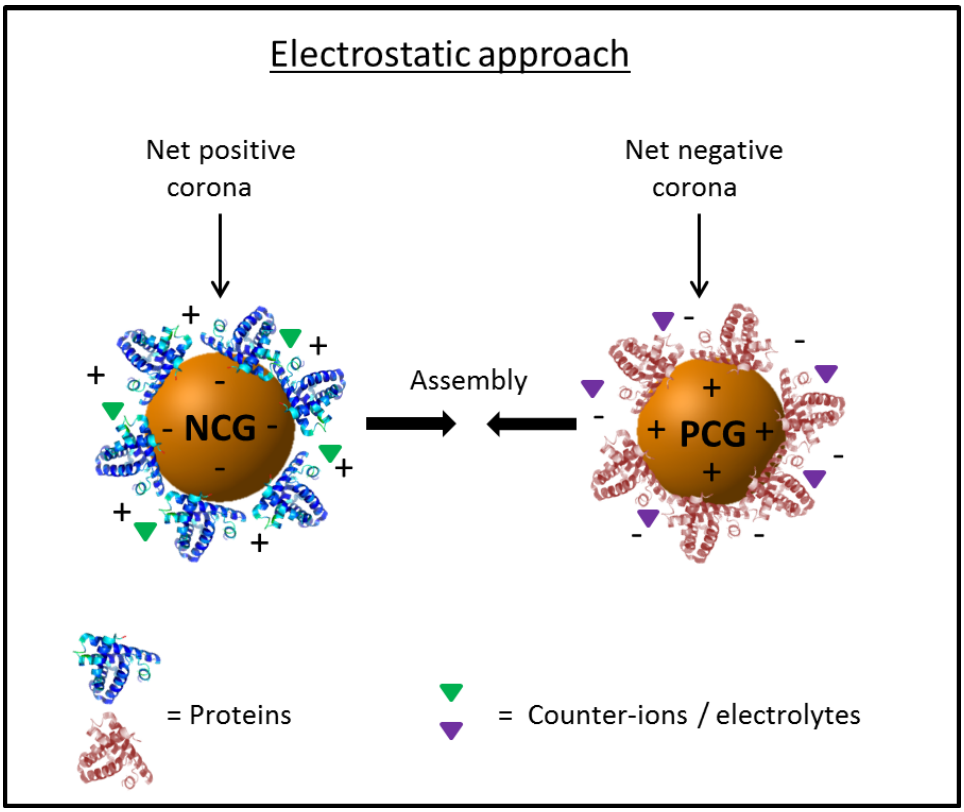

Figure 6.18 Schematic displaying NCG and PCG with adsorbed protein-electrolyte coronas and their subsequent attraction, a proposed mechanism for the self-assembly of oppositely charged GNPs under physiological conditions. (*Original image.*)

6.3.3.2 Utilising intermolecular bonding

Utilising the intermolecular bonding approach *via* oligonucleotide hybridisation, characteristic assemblage of GNPs as seen in Chapter 3 was not evidenced under physiological conditions investigated (section 6.1.4). Resultantly, structures after incubation of complementary oligo-GNPs in CCM appeared analogous to those after incubation of their monodispersed counterparts in section 6.1.3. Accordingly, oligo-GNPs were observed to be

sparsely distributed and interacting with globular-like biomolecules, characteristic of protein structures identified from the CCM control in section 6.1.1. These findings were further supported by DLS studies, where comparable values were derived for the average hydrodynamic size and dispersity of structures arising from incubation of individual and complementary oligo-GNPs. As previously, average hydrodynamic dimensions obtained after incubation of GNPs in CCM were considered representative of the overall size of nanoparticle-biomolecule complexes. Accordingly, incubation of complimentary oligo-GNPs in PBS resulted in GNP cluster formation displaying a 22-fold increase in size relative to those formed in CCM (Figure 6.6 D). It was therefore concluded that within the utilised CCM, complementary oligonucleotides on the surface of GNPs had not hybridised and intermolecular bonding was not an effective approach in the present study for the self-assembly of GNPs under biological conditions. Owing to the formation of irregular oligo-GNP biomolecular complexes revealed (section 6.1.3) it is suggested that influential factors discussed for electrostatic self-assembly (section 6.3.3.1) could inhibit hydrogen bonding required for Watson-Crick nucleobase-pairing (hybridisation). In agreement, short-chain oligonucleotides have previously been shown to rapidly interact with biological constituents including albumin-proteins and electrolytes[377,378], which can hinder subsequent hybridisation with intended targets. Whilst oligonucleotides have widely been applied as probes for detecting complementary DNA-sequences *ex vivo*[379], they often only effectively hybridise with a substrate if base-pair sequences entirely match[380]. In addition to this concept, the equivalent surface properties and molecular structures of complementary oligonucleotides on discrete GNPs were also considered. At physiological pH (7.4) the phosphodiester bond of oligonucleotides that covalently links the deoxyribose-backbone of individual nucleotides exists as an anion, with the overall molecule negatively charged. Under *in vitro* conditions this plays an important role in the formation of three-dimensional DNA structures and their packing within protein complexes[381]. In this investigation however, oligonucleotides are in free molecular form, providing each of the complementary GNPs with an equivalent negatively charged surface[382]. Consequently, complementary oligo-GNPs are

suggested to form bio-complexes that also display similar properties, contrary to NCG and PCG, as represented in Figure 6.19. Resultantly, the sum of attractive and repulsive forces between these particles may not favour their assembly[372]. Interestingly however, whilst oligonucleotide-functionalised nanoparticles have not previously been demonstrated to self-assemble under biological conditions, their pre-assembled nanostructures have been shown to remain intact within CCM after 8 hours[383]. Whilst oligonucleotide hybridisation was not able to demonstrate the feasibility of intermolecular bonding for self-assembly of nanoparticles under biological conditions, a range of alternative methods utilising the same principle could be investigated in future. In particular, "click-chemistry" and "host-guest" approaches appear to be fields with heightened interest and progress[384-386], with the potential to develop specific intermolecular bonding approaches that may prove resilient under physiological conditions.

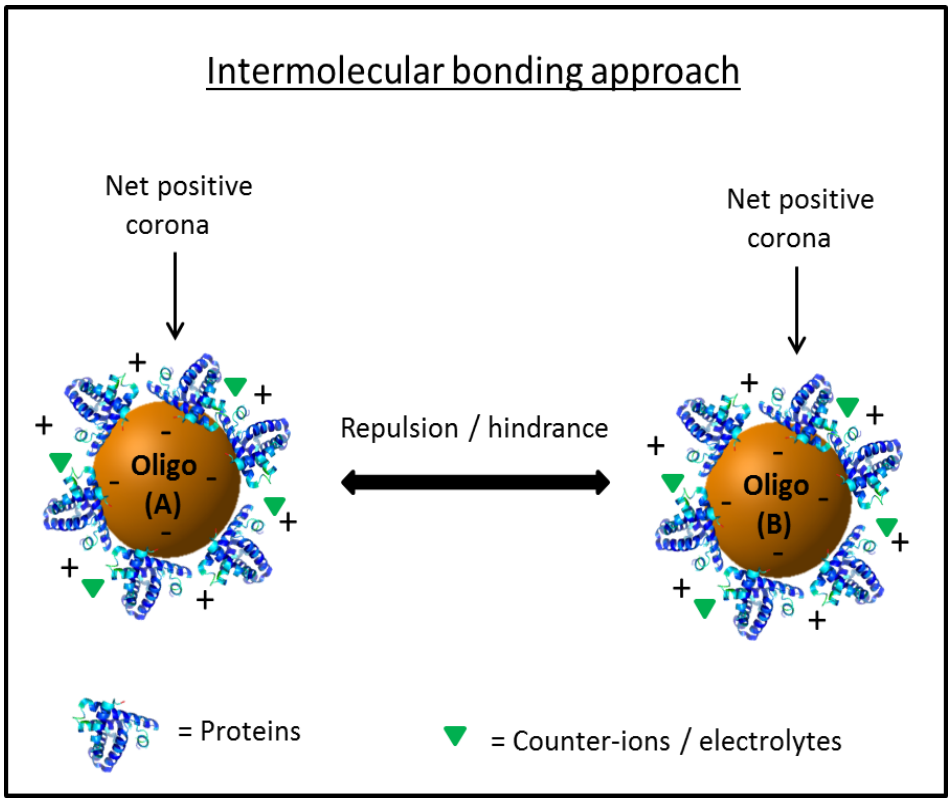

Figure 6.19 Schematic displaying adsorbed protein-electrolyte coronas on complementary oligo-GNPs (A and B) and their subsequent repulsion, a proposed mechanism of hindrance for the self-assembly of GNPs using oligonucleotide hybridisation under physiological conditions. (*Original image.*)

6.3.3.3 Investigating intracellular fate of GNPs and *in situ* self-assembly activity

Despite increasing interest and recent progress in nanotechnology, understanding the effects and behaviour of nanomaterials within living tissues and organisms remains incredibly challenging. Development of *in vitro* approaches and analytical techniques has only further highlighted the significance of understanding the complex responses involved, including uptake, localisation and subsequent interactions and consequences both at a cellular and sub-cellular level[387]. In this study the intracellular fate of NCG and PCG when administered individually (monodispersed) and simultaneously (*in situ* self-assembly) are evaluated (section 6.2). Results are compared to determine whether self-assembly activity *via* electrostatic interactions evidenced under simulated physiological conditions (section 6.3.3.1) occur intracellularly within culturing V79 lung fibroblasts. Current literature was utilised to explain findings of this study with a review of techniques and current approaches providing scope for future investigations and development that could advance the work in the current project.

6.3.3.4 Techniques for the intracellular evaluation of nanomaterials

Well-established imaging techniques are available that provide the resolution required for the visualisation of materials with nanoscale dimensions, each with their merits and limitations[387]. At present, there is a clear lack of standardised or accepted protocols for the characterisation or detection of nanomaterials intended for biomedical applications, reflecting the challenging nature of this field[388]. In the current work, a combination of bright field (BF) and high-angle annular dark field (HAADF) imaging was acquired by operating a TEM instrument, as detailed in section 2.2.3. According to available literature, TEM is the most frequently used technique for the study of nanomaterials owing to its superior spatial resolution compared to other electron microscopy techniques, providing enhanced structural and morphological analysis[388]. The decision to use this technique in combination with STEM in the current work reflected the size of GNPs (~ 2 nm) under

investigation (section 3.1.2) and the desire to couple microscopy work with elemental techniques, which have known limitations when integrated with other approaches such as SEM[389,390]. However, there are certain drawbacks associated with TEM, namely high vacuum conditions of the microscope and ultra-thin specimen sections required for electron-beam penetration[390]. Owing to the risk of damaging samples and generating artificial artefacts during the extensive specimen preparation process, well-established protocols that have been traditionally utilised to study biological specimens were employed[214] (section 2.2.6.7) This approach was found to sufficiently preserve samples, providing sections of the desired thickness, electron transparency and exceptional image contrast (section 6.2.1). Further optimisation of sample stability and microscope parameters were determined experimentally, with observations resulting in the decision to carbon-coat the reverse side of specimen grids and utilise a lower operating voltage of 80 KeV (section 6.2.1). Interestingly, reverse coating of specimens does not appear to be a widely used method but there are earlier reports which suggest that its application for samples containing inorganic materials can reduce temperature induced damage and electrostatic-charging[391]. In agreement, intensified radiation damage was observed in this study at higher accelerating voltages on un-coated specimens, possibly owing to excessive energy deposition into the specimen. This was markedly reduced by the application of the conductive carbon coating, with the suggested mechanism portrayed in Figure 6.20. Furthermore, this strategy avoids directly coating the specimens, which would limit the optical resolution required for the GNPs under investigation and make subsequent elemental analysis difficult owing to excessive carbon content.

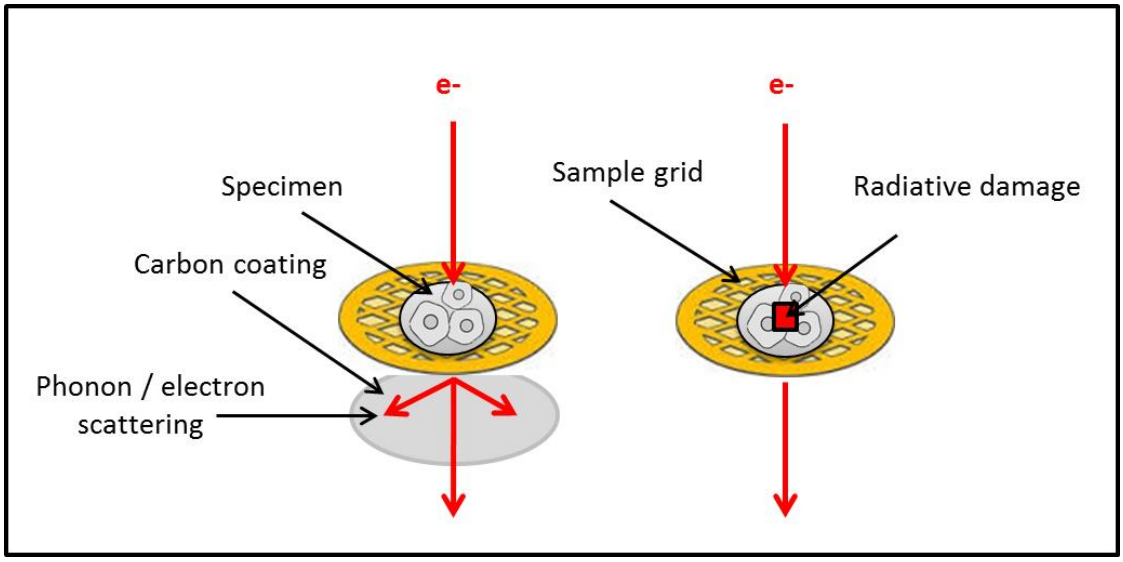

Figure 6.20 A representation showing the deposition of excess electrons and phonons onto a conductive carbon coating on the reverse side of a sample grid (left) reducing the radiative damage otherwise caused to specimens (right). (*Original image.*)

6.3.3.5 Cellular internalisation and distribution of GNPs

Cellular uptake of nanoparticles has been demonstrated to be variable owing to the diversity of physicochemical properties displayed by these materials and various functions of different cell types[392,393]. In the current study a lung fibroblast cell line derived from hamster (V79) undergoing exponential growth was treated for 24 hours with NCG and PCG in a monodispersed state and as they underwent *in situ* self-assembly (section 6.2). Analysis revealed features characteristic of the GNPs under investigation within intracellular vacuoles characteristic of endosomes after exposure to both NCG (section 6.2.4) and PCG (section 6.2.5) individually and simultaneously (section 6.2.6). Cluster-like structures observed from microscopy studies were subsequently confirmed by EDS to be comprised of gold, surrounded by material that had been labelled with osmium as a consequence of sample preparation (Figures 6.12 to 6.17). These findings agree with numerous other studies, where nanoparticles of a similar size have been internalised by cells and localised within cytoplasmic vesicles[393-395]. Owing to the small size of nanoparticles it is understood that they interact with cells in a similar way to endogenous macromolecules, actively incorporated into cells *via* a vesicular

transport system broadly defined as endocytosis[396]. Two key pathways have been shown to be responsible for the uptake of nanoparticles with dimensions below several hundred nanometres; *pinocytosis,* which is a non-specific fluid phase mechanism and *clathrin-mediated endocytosis,* which occurs when proteins adsorbed onto the surface of nanoparticles activate receptors on cell membranes[397]. In each case, these mechanisms follow a general progression of material-cell binding, invagination (membrane wrapping), vesicle formation and subsequent fusion of vesicles to form vacuolic endosomes, as portrayed in Figure 6.21 At this stage endosomes are either trafficked back to the cell surface for exocytosis or undergo further fusion events eventually proceeding to lysosomes, where a diverse range of proteins and enzymes attempt to degrade the nanoparticles[398]. Whilst the specific pathways responsible for the internalisation and intracellular trafficking of NCG and PCG were not studied in the current work, definitive structures characteristic of vesicle and endosome formation were observed (sections 6.2.4 and 6.2.5). Consequently, it was concluded that cellular uptake of NCG and PCG had occurred when administered individually, with their intracellular fate likely to be consistent with the processes explained above. When NCG and PCG were administered simultaneously (section 6.2.6), no conclusive detection of gold was revealed intracellularly from EDS analysis. Structures appearing similar to clusters of GNPs seen for individual treatments were still observed within cellular vacuoles, with elemental mapping revealing a correlation with gold and osmium detection. It was further noted that these structures were similar to features seen in the analysis of the untreated control specimen (section 6.2.3), which were also confirmed to be osmium deposits. Although not evidenced in the current work, based on previous studies it was considered conceivable that the increased size of assembled GNP clusters evidenced within CCM could have limited cellular uptake and altered subsequent intracellular trafficking[400,401]. It must be emphasised however that attempts to detect gold in all specimens was both challenging and time consuming, which limited overall analysis. An absence of gold detection from EDS spectra was consequently considered as inconclusive evidence to suggest the uptake of gold had been limited. Further highlighting the inherent sensitivity of this work, EDS spectra

obtained after treatment with NCG (Figure 6.9) and PCG (Figure 6.11) individually only display definitive peaks for gold detection when the analysis focused specifically on structures previously confirmed to be GNPs. Accordingly, GNPs could have been present in other nearby regions of the specimen after simultaneous treatment, but not successfully detected. It is suggested that further examination is required to assert these findings and confirm whether *in situ* self-assembly of GNPs *via* electrostatic interactions as discussed in section 6.3.3.1 inhibits particle internalisation within the lung fibroblast cell line investigated.

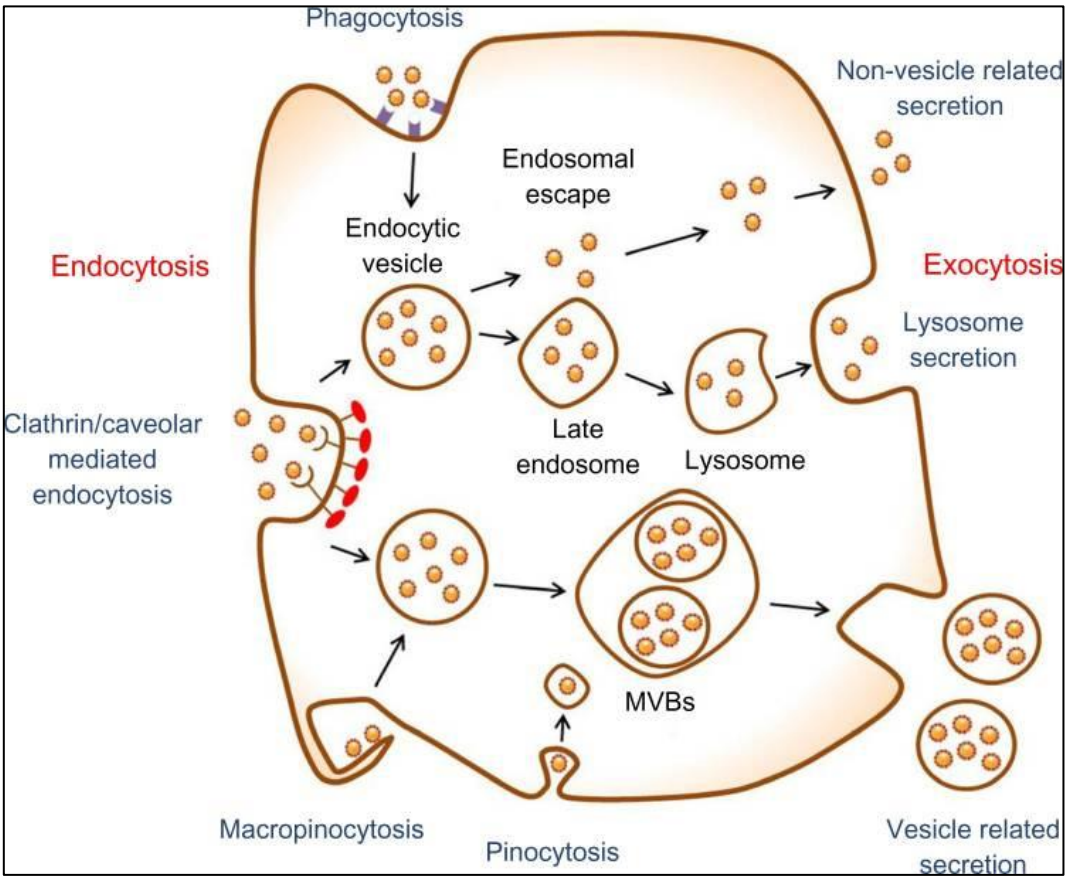

Figure 6.21: Schematic of major endocytosis and exocytosis pathways of nanoparticles within cells, including *pinocytosis* and *clathrin-mediated endocytosis*, two proposed entry-mechanisms for the GNPs investigated in the present study. (Image obtained from N. Oh Ji. Park, 2014)[402]

6.3.3.6 Electrostatic interactions towards self-assembly of GNPs under biological conditions

Whilst electrostatic attraction provides a relatively straightforward and rapid approach towards the self-assembly of nanoparticles, a lack of control with respect to the timing of this activity and the overall structure formation are clear drawbacks that will need to be overcome. Whilst no definitive evidence of intracellular self-assembly was obtained in the current study, Yang *et al* recently reported the formation of GNP clusters within a human breast cancer cell line when exposed to cationic and anionic particles sequentially[403]. Their method of exposing cells to complementary GNPs consecutively rather than simultaneously as in the current study appears to be an interesting strategy that could potentially limit the extent of GNP self-assembly before the particles are internalised. Indeed, the basis for

undertaking this approach was founded on their reasoning that intracellular assembly of GNPs would avoid the necessity for cells to internalise larger nanostructures, which can be limited[403]. However, no attempt was made to characterise the GNPs within the utilised biological media, making it difficult to conclude whether their experimental design prevented uncontrolled aggregation of particles within CCM and whether this influenced their subsequent internalisation and intracellular assembly. It was also noted that their approach to detecting GNP internalisation relied exclusively on dark-field imaging *via* TEM whilst self-assembly was indirectly measured by detecting differences in the production of reactive oxygen species (ROS) and cell viability[403]. An alternative approach investigated by Nam *et al* functionalised GNPs with pH responsive surface ligands, providing particles with complementary electrostatic charges only under acidic environments[404]. Interestingly, they further confirmed the ability to "trigger" the pH induced self-assembly within CCM, concluding that their electrostatic approach would prevail under biological conditions and resist interference from biomolecules[404]. A marked increase in the detection of these GNPs was then confirmed intracellularly relative to a control GNP that was not designed to assemble using bright-filed imaging *via* TEM. Furthermore, the formation of intracellular GNP clusters was found to increase with longer exposure times, leading to the hypothesis that intracellular self-assembly of nanoparticles prevented their subsequent exocytosis within the range of fibroblastic cell lines investigated[404]. Limiting this study however, the detection of gold relied exclusively on the differing ability of individual and assembled GNPs to interact with electrons within TEM analysis, providing varying image contrast within micrographs from which their conclusions were founded. If this approach had be utilised in the present study, structures comprised of osmium could have been mistaken as internalised GNPs. In the present study, EDS analysis was found to be the only technique able to differentiate between similarly appearing nano-scale features and confirm the presence or absence of gold with confidence.

In principle, the fundamentals of utilising electrostatic interactions for the self-assembly of nanomaterials within biological environments have recently been

established. Ongoing research in this area appears to already be attempting to overcome identified limitations. However, whilst this area of nanotechnology holds great promise, care must be taken to fully understand the mechanisms involved both before and after cellular internalisation of nanomaterials and guarantee the validity of experimental interpretation. It is suggested that whilst self-assembly was not definitively evidenced in this project, development of analytical approaches and further understanding of the inherent sensitivity involved will support future efforts in this field. In hindsight of the work undertaken, utilising different sized and shaped nanoparticles may assist the identification of intracellular self-assembly and provide a viable route towards further architectural control. Furthermore, whilst microscopy and elemental analysis has provided an outstanding qualitative approach towards determining the localisation of GNPs, quantification methods would be beneficial to understanding the influence of *in situ* self-assembly. This could be achieved by blocking specific endocytotic pathways with known inhibitors and quantitatively evaluating the resultant uptake of particles using established methods such as flow cytometry, mass spectrometry or emission spectrometry[393,397,399].

6.4 Conclusion

Utilising intermolecular bonding *via* oligonucleotide hybridisation was not an effective approach towards the *in situ* self-assembly of GNPs under physiological conditions in the current study. By contrast, self-assembly facilitated by electrostatic attraction appears to prevail under the same conditions, although overall sizes of assembled structures are reduced compared to within a simple aqueous environment. It is hypothesised that this persistent self-assembly activity arises from differing biological identities adsorbed onto the surface of the oppositely charged particles, NCG and PCG, which indirectly maintains the attractive forces between them. These results highlight the importance of understanding nanoparticle-biomolecule interactions that appear to interfere with the process of *in situ* self-assembly under biological conditions. Whilst cellular uptake and localisation of NCG and PCG within cytoplasmic vacuoles was confirmed when administered individually, no evidence was obtained to suggest that intracellular self-assembly activity had occurred *via* the electrostatic approach when the same GNPs were administered simultaneously. Utilised microscopy and elemental analysis approaches have provided further understanding of the complex nanomaterial-biological interactions that occur and the importance of interpreting results confidently by application of supplementary techniques. It is concluded that whilst self-assembly was not evidenced in the current study, further control of the processes involved and the development of specific complementary chemistry will provide promising avenues for future research.

7 General Discussion and Conclusions

The current work set out to evaluate the feasibility, associated risk and current limitations of utilising SANs for *in situ* activity within biological environments. Ascertaining how self-assembly of individual SANs translates from pre-defined conditions to within biological environments was considered fundamental to addressing current gaps in knowledge regarding the behaviour of these functional nanomaterials[355,405,406]. For this reason and considering an absence of standardised protocols to assess nanomaterial bio-performance[406,407], a step-wise approach towards evaluating nanomaterial self-assembly was undertaken in the present study. Initially in chapter 3, individual building blocks and resultant self-assembled suprastructures were characterised within simple aqueous conditions. Demonstrating how conventional therapeutic delivery methods could be applied to isolate and potentially deliver functional SANs, chapter 4 focused on encapsulating individual building blocks within liposomes, a well-established lipid-based technology, using a newly developed synthesis strategy. Potential toxicity was then assessed in chapter 5 for SANs individually and as they underwent self-assembly *in vitro*, using a lung fibroblast cell model. Subsequent studies in chapter 6 focused on evidencing self-assembly using different mechanisms within a relevant biological fluid and *in vitro* cell model. This experimental design was adopted to provide a facile route of evaluation that would identify potential risks and limitations at a preliminary stage. It was envisaged that this approach would enable future efforts to routinely assess critical design parameters, permitting optimisation and further understanding of nanomaterial-biological interactions that could potentially influence self-assembly activity. With ongoing progress in the field of self-assembling nanosystems, it appears inevitable that this technology will develop in tandem to the continuous demand for innovation regarding effective and non-invasive medical procedures. It is anticipated that the research and conclusions presented in this project will contribute and facilitate future development of associated *in situ* self-assembling nanotechnologies and their application in healthcare.

7.1 Investigative conclusions

Conclusions of this study are derived from the outcomes of experimental work, having considered available literature and current research directives. The study can be described as having been successful in fulfilling research objectives and contributing towards knowledge concerning the key research questions stated in the aims. The main conclusions from investigations are summarised below:

I. As established in chapter 3, electrostatic interactions and intermolecular recognition are effective mechanisms in the current study that facilitate self-assembly of individual GNPs into three-dimensional suprastructures. Characterisation showed that suprastructures were representative of structural agglomerates, which were multiple orders of magnitude larger than the original individual building blocks. Reversible self-assembly was achieved by thermally triggering dissociation of complementary hybridised oligonucleotides between assembled GNPs, demonstrating how external parameters could be used to implement further control and functionality.

II. Chapter 4 evidenced how individual SANs could be incorporated into PEGylated multilamellar liposomes, using a novel strategy that exploits electrostatic interactions between oppositely charged GNPs and lipids. Elemental analysis revealed a regular distribution of GNPs between adjacent bilayers, which appears to be different to previous reports of encapsulating hydrophobic particles directly within bilayers or hydrophilic particles within the central aqueous core of liposomes. Additionally, ensuing attractions between GNPs and lipids when using this approach were shown to significantly influence the loading content (ratio of gold to lipid) of the final formulations and could be exploited for further optimisation.

III. *In vitro* assessments applied in chapter 5 revealed that *in situ* self-assembly of GNPs significantly influenced cell viability and cytolysis relative to treatment with individual building blocks. It was hypothesised that the formation of self-assembled suprastructures with larger size dimensions could have altered the underpinning mechanisms of cytotoxicity, which resulted in a different biological response. Significant dose-dependent toxicity was also seen for GNP-liposome formulations, highlighting the importance of assessing all aspects of novel nanosystems in addition to the primary functional components.

IV. Nanoparticle-biomolecule aggregation seen in chapter 6 revealed that individual building blocks undergo extensive interactions with a range of biomolecules under the simulated physiological conditions investigated. Subsequent *in situ* self-assembly of complementary GNPs was evidenced to prevail via the electrostatic approach but intermolecular bonding was revealed to be an ineffective mechanism in the current study. It was hypothesised that the difference in self-assembly activity displayed by the two approaches was dependent on the biological identities adsorbed onto the surface of individual building blocks. Furthermore, definitive evidence of intracellular self-assembly of GNPs was not obtained in the current study, although internalisation and subsequent accumulation of GNPs within cytoplasmic vesicles was clearly revealed. It was concluded that intracellular evaluation and interpretation was challenging because differentiating between individual building blocks and self-assembled suprastructures relied on visual elucidation alone.

Investigations of the current project have contributed towards further understanding of how the activity of *in situ* self-assembling nanomaterials translates from simple aqueous conditions to within complex biological environments. The developed step-wise approach towards evaluation is proposed as an appropriate strategy that will enable assessment of bio-performance for alternative self-assembling nanosystems in the future.

Results highlight the importance of designing suitable building blocks, which ideally should retain their complementary functionality and resist biological interactions. Insight into the differing potential for toxicity between individual building blocks and their assembled counterparts raises an important consideration. Consequently, suitable assessment should be included in the experimental design of future studies to ascertain associated toxic effects. Whilst definitive evidence of intracellular self-assembly was not obtained in the current study, there are no obvious limitations at present that should inhibit future attempts given that experimental designs are well considered and optimised accordingly.

7.2 Experimental limitations

Despite careful consideration and planning, difficulties related to some aspects of applied research were encountered in the project. Limitations identified throughout that could be overcome in future are discussed with supporting literature.

7.2.1 Characterisation of Nanomaterials and Tissue Specimens

Nanomaterials are well known for their size-dependent properties and physicochemical attributes that contribute to their displayed behaviour. These phenomena collectively make characterisation vitally important, often requiring unequalled levels of structural analysis. Similarly, their meticulous evaluation within biological samples and tissue specimens is crucial towards understanding nanomaterial-biological interactions, associated toxicity and performance of functional materials. Paralleling this challenge, there have been numerous advances in techniques available to researchers, including electron microscopy. Notably, resolution acquired by TEM can now reach atomic levels and integrated spectroscopic techniques that enable elemental and chemical analysis have become widely available[408,409]. However, there are well-documented drawbacks when using electron microscopy, relating to the analysis of small data sets compared to other techniques and the extensive sample preparation and requirements to make specimens suitable for analysis[410]. Relating to the current work, cellular specimens were fixed and dehydrated – and therefore deceased – according to a well-established protocol that utilises osmium tetroxide. Whilst osmium application can be advantageous in comparison to alternative reagents, acting as a contrast enhancing fixative towards membrane lipids and proteins, numerous mechanisms of specimen distortion and artefact formation have been catalogued[410,411]. Alternatively, cryogenic sample preparation techniques are being increasingly developed and applied, whereby samples are rapidly frozen under high-pressure, effectively stopping biological processes whilst

retaining their viability. This can often enable a better reflection of their native-sate compared to chemical fixation methods, additionally avoiding subsequent embedding of samples in resin or plastics to acquire thin-section specimens for analysis[412,413]. Although cryo-techniques have been demonstrated in certain circumstances to enhance microscopy analysis of sub-cellular structures and intracellular features, unique challenges and limitations persist[412,414]. Therefore, selection from available methods for a particular investigation should ultimately be decided through optimisation studies, similar to those carried out in the present study.

Furthermore, considering the focus of the current work towards *in situ* self-assembly of nanomaterials, an inability to provide “real-time” analysis is considered a significant drawback. Since interactions between nanomaterials, biological components and subsequent self-assembly activity is a dynamic process, an understanding of how and when these processes occur would be highly advantageous. At present, there is significant motivation to develop *in situ* electron microscopy approaches, to meet novel scientific challenges, particularly regarding nanomaterial characterisation and activity[415]. Foremost, suitable specimen-holders must be designed and specialised to particular investigations, such as the liquid-cell utilised by Liu *et al* to evaluate self-assembly of oppositely charged GNPs within an aqueous suspension[416]. Coupled with ongoing development of other aspects of electron microscopy, such as variable vacuum conditions[417], improved time-resolution acquired from new camera technology and data collection capabilities[418,419], *in situ* microscopy will become an increasingly powerful and available tool that will eventually progress from specific custom-designs to commercial availability.

7.2.2 *In vitro* models and toxicity studies

Equally important to the characterisation of novel SANs, predictive toxicity and hazard capabilities should be assessed at a preliminary stage. This requirement reflects the unpredictable outcomes that could arise from potential human exposure to new nanomaterials and ethical issues

surrounding *in vivo* testing[420]. Accordingly, a comprehensive set of standardised tests designed to characterise risks and underpinning mechanisms should be applied similar to traditional toxicology approaches[421]. This would enable any specific biological responses to be identified and evaluation of potential dose-dependent toxicity. By using various levels of physiological modelling (molecular, cellular, tissue and organ)[421] experimental framework could be designed to reflect and predict any subsequent *in vivo* studies, which could provide justification and alleviate ethical issues.

Owing to the extensive array of physicochemical properties displayed by nanomaterials, biological responses and impact are highly variable. Consequently, nanomaterials must be evaluated individually on a case-by-case basis and testing should encompass a range of tests and cell lines that reflect potential exposure and application[422]. Recently, comprehensive "intelligent testing strategies" have been developed, with appropriate validation, standardisation and inclusion of nanomaterial controls[422,423]. These approaches for example, include as many as 10 biochemical assays to evaluate cytotoxicity through changes in cell viability and metabolism (MTT, WST-8, Reazurin and neutral red assays), membrane integrity (LDH assay) and oxidative stress (dichlorofluorescein assay)[423,424]. Tests are performed on multiple cell models, representing major systems and organs including immune, respiratory, gastrointestinal, heart, lung, kidney, liver and spleen[422,424]. In the present study however, only a single lung fibroblast cell model was utilised (V79) in conjunction with biochemical assays MTT and LDH. Whilst the V79 model is well established in toxicology studies and has been applied to broadly identify biological responses and general toxicity in a dose-dependent manner[425], collected data is known to be highly variable between cell-types[426,347]. Accordingly, use of a single cell model is considered a significant limitation and cannot be considered representative of overall toxicity. Similarly, whilst the coupling of MTT and LDH assays enables a reliable measure of material-induced necrosis, this wide-spectrum assessment of cytotoxicity will not differentiate between contributing, underpinning mechanism. Although these limitations are relatively broad, they were foreseen, with experimental designs purposely excluded further robust

toxicity testing, to enable a focus on the key aims of the current project. Instead, the rudimentary toxicity studies applied affords a predictive basis for future studies, providing general insight into the potential for variable toxicity between building blocks and their self-assembled suprastructures, which will inevitably be different for each developed nanosystem.

7.2.3 Three-dimensional *in vitro* experiments

Three-dimensional *in vitro* models are increasingly being utilised of recent because they provide unique opportunities to study specific biological microenvironments, which often cannot be replicated using traditional two-dimensional models[427]. It is well-understood that extracellular matrix plays a significant role in cell behaviour and nanomaterial-cell interactions, consequently, three-dimensional models more appropriately represent *in vivo* environments[428]. Considering the current study focused on evidencing intracellular self-assembly, three-dimensional cellular models would have been further advantageous in determining whether self-assembly occurred before cellular internalisation (chapter 6). Furthermore, with a suitable three-dimensional experimental cell model it could be possible to study mechanisms towards optimising *in situ* extracellular or intracellular self-assembly activity and how these different approaches influence resultant toxicity (chapter 4).

7.3 Future perspectives

Reflecting on experimental conclusions, identified limitations and further understanding acquired regarding the *in situ* self-assembly of nanomaterials within biological systems, residual and original questions are considered. These questions can be utilised to formulate research aims, directing future research.

- What approaches towards the self-assembly of nanomaterials will enable further control and implement programmability, and how will this be demonstrated through applied research?

The current project focused on two fundamental approaches, electrostatic interactions and molecular recognition. Whilst only the former approach was successful in facilitating the assembly of GNPs under biological conditions in the present work, it has become apparent that with careful designing and rational chemistry the latter approach could offer the greatest potential for further manipulation and control. From a basic perspective, electrostatic interactions as a mechanism of facilitating self-assembly are restricted because fundamentally there are only two possible charges, positive and negative. As a result, the number of “encoded” building blocks is also limited, although sequential deliver of SANs and layer-by-layer assembly approaches could potentially be applied to overcome this.

As evidenced in this work, nanomaterials displaying ionic surfaces also interact extensively with biological entities, yet exposure of their complementary charged surfaces is required to facilitate self-assembly. By contrast, molecular recognition provides endless opportunities. Complex nanoscale “DNA origami” macromolecular designs are a key example of how further programmability can be achieved if similar chemistry was applied to nanomaterials[429]. As revealed in the current project, however, effective bio-performance will not be readily achieved by functionalising nanomaterials with existing analogues of DNA. Alternatively, synthetic macromolecules, including

arrangements utilised for “click chemistry”[430] and those inspired by DNA itself, such as peptide nucleic acid[431] appear as promising candidates. They offer high levels of specificity and could be precision-engineered to encode multiple building blocks whilst avoiding unintended biological interactions that may otherwise hinder their functionality. To demonstrate this, a proof-of-concept could be achieved by introducing complementary surfaces to nanoparticles with different shapes, sizes and composition, which would assist characterisation and evaluation. This has become an increasingly attractive opportunity as these nanoparticles have become commercially available and cheaper in recent years.

- How can *in situ* self-assembling nanomaterials function for applications in healthcare?

Similar to nanomaterials in general, properties of self-assembled structures are governed by the size, shape, chemistry and other parameters native to the original building blocks. Similarly, the composition, arrangement and proportions of these individual building blocks within an assembled structure as a whole will provide endless means to modify resultant characteristics. This in turn provides broad opportunities to enhance existing technologies and discover unique functionalities that can be utilised. Interestingly, known properties and applications of discrete nanomaterials appear to be retained and even enhanced in some circumstances by their assembled counterparts, which has already been demonstrated for assembled GNPs and photothermal therapy[432]. Therefore, it would be highly advantageous if nanomaterials could be delivered to a site of interest, assembled for effective treatment and then subsequently dissociated for clearance from the body. A proof-of-concept could be achieved using simplified *in vitro* models, applying similar techniques and a step-wise approach towards evaluation as demonstrated in the current work. Furthermore, sequential administration of building blocks for defined “stages” of self-assembly may facilitate multifunctional approaches to treatment, where a medical condition is first identified, diagnosed, treated and later monitored; these concepts are already being investigated and realised[433,434].

7.4 Contribution to knowledge

At present there is a clear gap in knowledge concerning the behaviour and performance of SANs within biological systems and suitable experimental framework for evaluation. Specifically, this relates to the effectiveness of different mechanism towards achieving predictable self-assembly, potential toxicity arising from the process of *in situ* self-assembly and methods of assessing *in vitro* outcomes. The current work has contributed towards further understanding of how the activity of self-assembling nanomaterials translates from predefined laboratory settings to within complex biological environments. In particular, several aspects of this project can be described as novel and having made a contribution towards knowledge.

I. A synthetic strategy was developed for the preparation of PEGylated liposomes containing encapsulated metallic nanoparticles that display ionic surfaces. Additionally, demonstrating how complementary building blocks for self-assembly can be isolated within traditional drug delivery technologies.

II. Preliminary toxicity studies have identified that there could be differences in the associated toxicity of individual building blocks compared to their self-assembled suprastructures, a phenomenon that is supported by toxicity studies regarding the state of dispersion of nanomaterials and their aggregates.

III. A comparison between two discrete mechanisms towards self-assembly of nanomaterials under biological conditions reveals that extensive bio-complex formation can impair activity; electrostatic interactions appear to prevail whilst molecular recognition using oligonucleotides was ineffective.

IV. Evaluation of intracellular self-assembly and the ability to differentiate between individual building blocks and assembled structures is

inherently difficult when elucidating from visual interpretation alone. However, based on the findings of the current study it appears that considerate experimental planning and optimisation of microscopy and further supplementary techniques will expedite further research efforts.

8 References:

1.Eric, D. K. (1986). Engines of Creation. The Coming Era of Nanotechnology. Anchor Book.
2.Mansoori, G. A., & Soelaiman, T. F. (2005). Nanotechnology - an introduction for the standards. Community.Journal of ASTM International, 2(6), 1-22.
3.Mendes, P. M. (2013). Cellular nanotechnology: making biological interfaces smarter. Chemical Society Reviews,42(24), 9207-9218.
4.Lehner, R., Wang, X., Marsch, S., & Hunziker, P. (2013). Intelligent nanomaterials for medicine: carrier platforms and targeting strategies in the context of clinical application. Nanomedicine: Nanotechnology, Biology and Medicine, 9(6), 742-757.
5.Michalet, X., Pinaud, F. F., Bentolila, L. A., Tsay, J. M., Doose, S. J. J. L., Li, J. J., & Weiss, S. (2005). Quantum dots for live cells, in vivo imaging, and diagnostics. Science, 307(5709), 538-544.
6.Petros, R. A., & desimone, J. M. (2010). Strategies in the design of nanoparticles for therapeutic applications. Nature reviews. Drug discovery, 9(8), 615.
7.Cha, C., Shin, S. R., Annabi, N., Dokmeci, M. R., & Khademhosseini, A. (2013). Carbon-based nanomaterials: multifunctional materials for biomedical engineering. ACS nano, 7(4), 2891-2897.
8.Freitas, R. A. (2005). Current status of nanomedicine and medical nanorobotics. Journal of Computational and Theoretical Nanoscience, 2(1), 1-25.
9.Cui, W., Li, J., & Decher, G. (2016). Self-Assembled Smart Nanocarriers for Targeted Drug Delivery. Advanced Materials, 28(6), 1302-1311.
10.Son, S., Kim, N., You, D. G., Yoon, H. Y., Yhee, J. Y., Kim, K., & Kim, S. H. (2017). Antitumor therapeutic application of self-assembled RNAi-AuNP nanoconstructs: Combination of VEGF-rnai and photothermal ablation. Theranostics, 7(1), 9.
11.Sun, L., Zheng, C., & Webster, T. J. (2017). Self-assembled peptide nanomaterials for biomedical applications: promises and pitfalls. International journal of nanomedicine, 12, 73.
12.Lin, R., & Cui, H. (2015). Supramolecular nanostructures as drug carriers. Current Opinion in Chemical Engineering, 7, 75-83.
13.ISO. (2015). Terminology and definitions for nano-objects. ISO/TS, 80004-2.
14.Erickson, H. P. (2009). Size and shape of protein molecules at the nanometer level determined by sedimentation, gel filtration, and electron microscopy. Biological procedures online, 11(1), 32.
15.Behabtu, N, Young, CC, Tsentalovich, DE, et al. (2013) Strong, Light, Multifunctional Fibers of Carbon Nanotubes with Ultrahigh Conductivity. Science, 339(6116), 182-6
16.Jain, P. K., Huang, X., El-Sayed, I. H., & El-Sayed, M. A. (2007). Review of some interesting surface plasmon resonance-enhanced properties of noble metal nanoparticles and their applications to biosystems. Plasmonics, 2(3), 107-118.
17.Lou, X. W. D., Archer, L. A., & Yang, Z. (2008). Hollow micro-/nanostructures: Synthesis and applications. Advanced Materials, 20(21), 3987-4019.
18.Wang, J. T. W., Ball, J. M., Barea, E. M., Abate, A., Alexander-Webber, J. A., Huang, J., & Nicholas, R. J. (2013). Low-temperature processed electron collection layers of graphene/tio2 nanocomposites in thin film perovskite solar cells. Nano letters, 14(2), 724-730.

19.Aitken, R., Chaudhry, M. Q., Boxall, A. B. A., & Hull, M. (2006). Manufacture and use of nanomaterials: current status in the UK and global trends. Occupational medicine, 56(5), 300-306.
20.Grassian, V. H. (2008). When size really matters: size-dependent properties and surface chemistry of metal and metal oxide nanoparticles in gas and liquid phase environments. The Journal of Physical Chemistry C, 112(47), 18303-18313.
21.Savolainen, K., Alenius, H., Norppa, H., Pylkkänen, L., Tuomi, T., & Kasper, G. (2010). Risk assessment of engineered nanomaterials and nanotechnologies - a review. Toxicology, 269(2), 92-104.
22.Jha, R. K., Jha, P. K., Chaudhury, K., Rana, S. V., & Guha, S. K. (2014). An emerging interface between life science and nanotechnology: present status and prospects of reproductive healthcare aided by nano-biotechnology. Nano reviews, 5(1), 22762.
23.Bleeker, E. A., de Jong, W. H., Geertsma, R. E., Groenewold, M., Heugens, E. H., Koers-Jacquemijns, M., & Cassee, F. R. (2013). Considerations on the EU definition of a nanomaterial: science to support policy making. Regulatory toxicology and pharmacology, 65(1), 119-125.
24.Chakraborty, S. (Ed.). (2012). Microfluidics and microscale transport processes. CRC Press, 268.
25.Tan, Y., Dai, X., Li, Y., & Zhu, D. (2003). Preparation of gold, platinum, palladium and silver nanoparticles by the reduction of their salts with a weak reductant–potassium bitartrate. Journal of Materials Chemistry, 13(5), 1069-1075.
26.Drbohlavova, J., Adam, V., Kizek, R., & Hubalek, J. (2009). Quantum dots—characterization, preparation and usage in biological systems. International journal of molecular sciences, 10(2), 656-673.
27.Jun, Y. W., Choi, J. S., & Cheon, J. (2007). Heterostructured magnetic nanoparticles: their versatility and high performance capabilities. Chemical Communications, (12), 1203-1214.
28.Dykman, L., & Khlebtsov, N. (2012). Gold nanoparticles in biomedical applications: recent advances and perspectives. Chemical Society Reviews, 41(6), 2256-2282.
29.Gao, J., Huang, X., Liu, H., Zan, F., & Ren, J. (2012). Colloidal stability of gold nanoparticles modified with thiol compounds: bioconjugation and application in cancer cell imaging. Langmuir, 28(9), 4464-4471.
30.Pfeiffer, C., Rehbock, C., Hühn, D., Carrillo-Carrion, C., de Aberasturi, D. J., Merk, V., & Parak, W. J. (2014). Interaction of colloidal nanoparticles with their local environment: the (ionic) nanoenvironment around nanoparticles is different from bulk and determines the physico-chemical properties of the nanoparticles. Journal of The Royal Society Interface, 11(96), 20130931.
31.Kraynov, A., & Müller, T. E. (2011). Concepts for the stabilization of metal nanoparticles in ionic liquids. In Applications of Ionic Liquids in Science and Technology. Intech.
32.Hierrezuelo, J., Sadeghpour, A., Szilagyi, I., Vaccaro, A., & Borkovec, M. (2010). Electrostatic stabilization of charged colloidal particles with adsorbed polyelectrolytes of opposite charge. Langmuir, 26(19), 15109-15111.
33.Heller, W., & Pugh, T. L. (1960). “Steric” stabilization of colloidal solutions by adsorption of flexible macromolecules. Journal of Polymer Science Part A: Polymer Chemistry, 47(149), 203-217.
34.Nuopponen, M., & Tenhu, H. (2007). Gold nanoparticles protected with ph and temperature-sensitive diblock copolymers. Langmuir, 23(10), 5352-5357.
35.Thanh, N. T., & Green, L. A. (2010). Functionalisation of nanoparticles for biomedical applications. Nano Today, 5(3), 213-230.

36.Perrault, S. D., & Chan, W. C. (2009). Synthesis and surface modification of highly monodispersed, spherical gold nanoparticles of 50− 200 nm. Journal of the American Chemical Society, 131(47), 17042-17043.
37.Grzelczak, M., Pérez-Juste, J., Mulvaney, P., & Liz-Marzán, L. M. (2008). Shape control in gold nanoparticle synthesis. Chemical Society Reviews, 37(9), 1783-1791.
38.Link, S., & El-Sayed, M. A. (2000). Shape and size dependence of radiative, non-radiative and photothermal properties of gold nanocrystals. International reviews in physical chemistry, 19(3), 409-453.
39.Dykman, L. A., & Khlebtsov, N. G. (2011). Gold nanoparticles in biology and medicine: recent advances and prospects. Acta Naturae, 3(2 (9)).
40.Ferrari, M. (2005). Cancer nanotechnology: opportunities and challenges. Nature reviews. Cancer, 5(3), 161.
41.Ding, Y., Jiang, Z., Saha, K., Kim, C. S., Kim, S. T., Landis, R. F., & Rotello, V. M. (2014). Gold nanoparticles for nucleic acid delivery. Molecular Therapy, 22(6), 1075-1083.
42.Arvizo, R., Bhattacharya, R., & Mukherjee, P. (2010). Gold nanoparticles: opportunities and challenges in nanomedicine. Expert opinion on drug delivery, 7(6), 753-763.
43.Wiley, D. T., Webster, P., Gale, A., & Davis, M. E. (2013). Transcytosis and brain uptake of transferrin-containing nanoparticles by tuning avidity to transferrin receptor. Proceedings of the National Academy of Sciences, 110(21), 8662-8667.
44.Mahon, E., Salvati, A., Bombelli, F. B., Lynch, I., & Dawson, K. A. (2012). Designing the nanoparticle–biomolecule interface for “targeting and therapeutic delivery”. Journal of Controlled Release, 161(2), 164-174.
45.Mie, G. (1908). Beiträge zur Optik trüber Medien, speziell kolloidaler Metallösungen. Annalen der physik, 330(3), 377-445.
46.Jain, P. K., Huang, X., El-Sayed, I. H., & El-Sayed, M. A. (2008). Noble metals on the nanoscale: optical and photothermal properties and some applications in imaging, sensing, biology, and medicine. Accounts of chemical research, 41(12), 1578-1586.
47.Cordeiro, M., Ferreira Carlos, F., Pedrosa, P., Lopez, A., & Baptista, P. V. (2016). Gold Nanoparticles for Diagnostics: Advances towards Points of Care. Diagnostics, 6(4), 43.
48.Huang, X., & El-Sayed, M. A. (2010). Gold nanoparticles: optical properties and implementations in cancer diagnosis and photothermal therapy. Journal of advanced research, 1(1), 13-28.
49.Kreibig, U., & Vollmer, M. (2013). Optical properties of metal clusters (Vol. 25). Springer Science & Business Media.
50.Jain, P. K., Lee, K. S., El-Sayed, I. H., & El-Sayed, M. A. (2006). Calculated absorption and scattering properties of gold nanoparticles of different size, shape, and composition: applications in biological imaging and biomedicine. J. Phys. Chem. B, 110(14), 7238-7248.
51.El-Sayed, I. H., Huang, X., & El-Sayed, M. A. (2005). Surface plasmon resonance scattering and absorption of anti-EGFR antibody conjugated gold nanoparticles in cancer diagnostics: applications in oral cancer. Nano letters, 5(5), 829-834.
52.Mayer, K. M., & Hafner, J. H. (2011). Localized surface plasmon resonance sensors. Chemical reviews, 111(6), 3828-3857.
53.Fabris, L. (2015). Gold-based SERS tags for biomedical imaging. Journal of Optics, 17(11), 114002.
54.Webb, J. A., & Bardhan, R. (2014). Emerging advances in nanomedicine with engineered gold nanostructures. Nanoscale, 6(5), 2502-2530.

55.Weissleder, R. (2001). A clearer vision for in vivo imaging. Nature biotechnology, 19(4), 316-316.
56.Kennedy, L. C., Bickford, L. R., Lewinski, N. A., Coughlin, A. J., Hu, Y., Day, E. S., & Drezek, R. A. (2011). A New Era for Cancer Treatment: Gold-Nanoparticle-Mediated Thermal Therapies. Small, 7(2), 169-183.
57.Steger, A. C., Lees, W. R., Walmsley, K., & Bown, S. G. (1989). Interstitial laser hyperthermia: a new approach to local destruction of tumours. Bmj, 299(6695), 362-365.
58.Park, J. H., von Maltzahn, G., Ong, L. L., Centrone, A., Hatton, T. A., Ruoslahti, E., & Sailor, M. J. (2010). Cooperative nanoparticles for tumor detection and photothermally triggered drug delivery. Advanced Materials, 22(8), 880-885.
59.Park, H., Yang, J., Seo, S., Kim, K., Suh, J., Kim, D., & Yoo, K. H. (2008). Multifunctional nanoparticles for photothermally controlled drug delivery and magnetic resonance imaging enhancement. Small, 4(2), 192-196.
60.Xing, P., & Zhao, Y. (2016). Multifunctional Nanoparticles Self-Assembled from Small Organic Building Blocks for Biomedicine. Advanced Materials, 28(34), 7304-7339.
61.Whitesides, G. M., & Grzybowski, B. (2002). Self-assembly at all scales. Science, 295(5564), 2418-2421.
62.Cho, J. H., & Gracias, D. H. (2009). Self-assembly of lithographically patterned nanoparticles. Nano letters, 9(12), 4049-4052.
63.Giner-Casares, J. J., & Reguera, J. (2016). Directed self-assembly of inorganic nanoparticles at air/liquid interfaces. Nanoscale, 8(37), 16589-16595.
64.Nie, Z., Petukhova, A., & Kumacheva, E. (2010). Properties and emerging applications of self-assembled structures made from inorganic nanoparticles. Nature nanotechnology, 5(1), 15-25.
65.Zhou, W., Gao, X., Liu, D., & Chen, X. (2015). Gold nanoparticles for in vitro diagnostics. Chem. Rev, 115(19), 10575-10636.
66.Ou, Y. Y., & Huang, M. H. (2006). High-density assembly of gold nanoparticles on multiwalled carbon nanotubes using 1-pyrenemethylamine as interlinker. The Journal of Physical Chemistry B, 110(5), 2031-2036.
67.Nykypanchuk, D., Maye, M. M., Van Der Lelie, D., & Gang, O. (2008). DNA-guided crystallization of colloidal nanoparticles. Nature, 451(7178), 549.
68.Park, S. Y., Lytton-Jean, A. K., Lee, B., Weigand, S., Schatz, G. C., & Mirkin, C. A. (2008). DNA-programmable nanoparticle crystallization. Nature, 451(7178), 553.
69.Cheng, Y. H., Tang, H., & Jiang, J. H. (2017). Enzymatic Mediated Assembly of Gold Nanoparticles for Ultrasensitive Colorimetric Detection of Hepatitis C Virus Antibody. Analytical Methods, 25(9), 3777-3781.
70.Hu, X., Yang, P., He, J., Liang, R., Niu, D., Wang, H., & Li, Y. (2017). In vivo self-assembly induced retention of gold nanoparticles for enhanced photothermal tumor treatment. Journal of Materials Chemistry B, 5(30), 5931-5936.
71.Walter, D. (2013). Primary particles–agglomerates–aggregates. Nanomaterials, 9-24.
72.Shim, J. Y., & Gupta, V. K. (2007). Reversible aggregation of gold nanoparticles induced by pH dependent conformational transitions of a self-assembled polypeptide. Journal of colloid and interface science, 316(2), 977-983.
73.Wen, D., Liu, W., Haubold, D., Zhu, C., Oschatz, M., Holzschuh, M., & Eychmüller, A. (2016). Gold aerogels: three-dimensional assembly of nanoparticles and their use as electrocatalytic interfaces. ACS nano, 10(2), 2559-2567.
74.Ghosh, S. K., & Pal, T. (2007). Interparticle coupling effect on the surface plasmon resonance of gold nanoparticles: from theory to applications. Chemical Reviews, 107(11), 4797-4862.

75.Koole, R., Liljeroth, P., de Mello Donegá, C., Vanmaekelbergh, D., & Meijerink, A. (2006). Electronic coupling and exciton energy transfer in cdte quantum-dot molecules. Journal of the American Chemical Society, 128(32), 10436-10441.
76.Zeng, H., Li, J., Liu, J. P., Wang, Z. L., & Sun, S. (2002). Exchange-coupled nanocomposite magnets by nanoparticle self-assembly. Nature, 420(6914), 395.
77.Guo, L., Jackman, J. A., Yang, H. H., Chen, P., Cho, N. J., & Kim, D. H. (2015). Strategies for enhancing the sensitivity of plasmonic nanosensors. Nano Today, 10(2), 213-239.
78.Lee, J., Hernandez, P., Lee, J., Govorov, A. O., & Kotov, N. A. (2007). Exciton-plasmon interactions in molecular spring assemblies of nanowires and wavelength-based protein detection. Nature materials, 6(4), 291.
79.Pileni, M. P. (2007). Self-assembly of inorganic nanocrystals: fabrication and collective intrinsic properties. Accounts of chemical research, 40(8), 685-693.
80.Lu, Y., & Liu, J. (2007). Smart nanomaterials inspired by biology: dynamic assembly of error-free nanomaterials in response to multiple chemical and biological stimuli. Accounts of chemical research, 40(5), 315-323.
81.Schopf, C., Noonan, E., Quinn, A. J., & Iacopino, D. (2016). Self-Assembly of Gold Nanocrystals into Discrete Coupled Plasmonic Structures. Crystals, 6(9), 117.
82.Paterson, S., Thompson, S. A., Wark, A. W., & de la Rica, R. (2017). Gold Suprashells: Enhanced Photothermal Nanoheaters with Multiple Localized Surface Plasmon Resonances for Broadband Surface-Enhanced Raman Scattering. The Journal of Physical Chemistry C, 121(13), 7404-7411.
83.Gong, J., Newman, R. S., Engel, M., Zhao, M., Bian, F., Glotzer, S. C., & Tang, Z. (2017). Shape-dependent ordering of gold nanocrystals into large-scale superlattices. Nature communications, 8, 14038.
84.Whitesides, G. M., & Grzybowski, B. (2002). Self-assembly at all scales. Science, 295(5564), 2418-2421.
85.Whitesides, G. M., & Boncheva, M. (2002). Beyond molecules: Self-assembly of mesoscopic and macroscopic components. Proceedings of the National Academy of Sciences, 99(8), 4769-4774.
86.Leekumjorn, S., & Wong, M. S. (2010). 5.07-Self-Assembly of Nanoparticle Building Blocks. Elsivier.
87.Sahoo, Y., Cheon, M., Wang, S., Luo, H., Furlani, E. P., & Prasad, P. N. (2004). Field-directed self-assembly of magnetic nanoparticles. The Journal of Physical Chemistry B, 108(11), 3380-3383.
88.Hsiao, A. P., & Heller, M. J. (2012). Electric-field-directed self-assembly of active enzyme-nanoparticle structures. Biomed Research International, 2012.
89.Grzybowski, B. A., Wilmer, C. E., Kim, J., Browne, K. P., & Bishop, K. J. (2009). Self-assembly: from crystals to cells. Soft Matter, 5(6), 1110-1128.
90.Moulton, B., & Zaworotko, M. J. (2001). From molecules to crystal engineering: supramolecular isomerism and polymorphism in network solids. Chemical Reviews, 101(6), 1629-1658.
91.Aizenberg, J., Muller, D. A., Grazul, J. L., & Hamann, D. R. (2003). Direct fabrication of large micropatterned single crystals. Science, 299(5610), 1205-1208.
92.Park, C., Yoon, J., & Thomas, E. L. (2003). Enabling nanotechnology with self assembled block copolymer patterns. Polymer, 44(22), 6725-6760.
93.Antonietti, M., & Förster, S. (2003). Vesicles and liposomes: a self-assembly principle beyond lipids. Advanced Materials, 15(16), 1323-1333.
94.Holliday, B. J., & Mirkin, C. A. (2001). Strategies for the construction of supramolecular compounds through coordination chemistry. Angewandte Chemie International Edition, 40(11), 2022-2043.

95.Tao, F. (2008). Nanoscale surface chemistry in self-and directed-assembly of organic molecules on solid surfaces and synthesis of nanostructured organic architectures. Pure and Applied Chemistry, 80(1), 45-57.
96.Carroll, J. B., Frankamp, B. L., Srivastava, S., & Rotello, V. M. (2004). Electrostatic self-assembly of structured gold nanoparticle/polyhedral oligomeric silsesquioxane (POSS) nanocomposites. Journal of Materials Chemistry, 14(4), 690-694.
97.Ofir, Y., Samanta, B., & Rotello, V. M. (2008). Polymer and biopolymer mediated self-assembly of gold nanoparticles. Chemical Society Reviews, 37(9), 1814-1825.
98.Monti, S., Barcaro, G., Sementa, L., Carravetta, V., & Ågren, H. Dynamics and self-assembly of bio-functionalized gold nanoparticles in solution: Reactive molecular dynamics simulations. Nano Research, 1-11.
99.Ozin, G. A., Hou, K., Lotsch, B. V., Cademartiri, L., Puzzo, D. P., Scotognella, F., & Thomson, J. (2009). Nanofabrication by self-assembly. Materials Today, 12(5), 12-23.
100.Zhang, J., Li, Y., Zhang, X., & Yang, B. (2010). Colloidal self-assembly meets nanofabrication: From two-dimensional colloidal crystals to nanostructure arrays. Advanced materials, 22(38), 4249-4269.
101.Walker, D. A., Kowalczyk, B., de La Cruz, M. O., & Grzybowski, B. A. (2011). Electrostatics at the nanoscale. Nanoscale, 3(4), 1316-1344.
102.Witt, D., Klajn, R., Barski, P., & Grzybowski, B. A. (2004). Applications, properties and synthesis of ω-functionalized n-alkanethiols and disulfides-the building blocks of self-assembled monolayers. Current Organic Chemistry,8(18), 1763-1797.
103.Luo, D., Yan, C., & Wang, T. (2015). Interparticle Forces Underlying Nanoparticle Self-Assemblies. Small, 11(45), 5984-6008.
104.Whitelam, S. (2014). A Recipe for Error-Free Self-Assembly. Physics, 7, 62.
105.Haensch, C., Hoeppener, S., & Schubert, U. S. (2010). Chemical modification of self-assembled silane based monolayers by surface reactions. Chemical Society Reviews, 39(6), 2323-2334.
106.Kalsin, A. M., Kowalczyk, B., Smoukov, S. K., Klajn, R., & Grzybowski, B. A. (2006). Ionic-like behavior of oppositely charged nanoparticles. Journal of the American Chemical Society, 128(47), 15046-15047.
107.Gschneidtner, T. A., Fernandez, Y. A. D., Syrenova, S., Westerlund, F., Langhammer, C., & Moth-Poulsen, K. (2014). A versatile self-assembly strategy for the synthesis of shape-selected colloidal noble metal nanoparticle heterodimers. Langmuir, 30(11), 3041.
108.Nam, J., Won, N., Jin, H., Chung, H., & Kim, S. (2009). Ph-induced aggregation of gold nanoparticles for photothermal cancer therapy. Journal of the American Chemical Society, 131(38), 13639-13645.
109.Yang, Y., Hu, Y., Du, H., & Wang, H. (2014). Intracellular gold nanoparticle aggregation and their potential applications in photodynamic therapy. Chemical Communications, 50(55), 7287-7290.
110.Kim, J. W., & Deaton, R. (2013). Molecular Self-Assembly of Multifunctional Nanoparticle Composites with Arbitrary Shapes and Functions: Challenges and Strategies. Particle & Particle Systems Characterization, 30(2), 117-132.
111.Li, H., Carter, J. D., & labean, T. H. (2009). Nanofabrication by DNA self-assembly. Materials Today, 12(5), 24-32.
112.Thorkelsson, K., Bai, P., & Xu, T. (2015). Self-assembly and applications of anisotropic nanomaterials: A review. Nano Today, 10(1), 48-66.
113.Sun, Y., & Kiang, C. H. (2005). DNA-based artificial nanostructures: Fabrication, properties, and applications. Arxiv preprint physics/0503114.
114.Taton, T. A. (2002). Preparation of gold nanoparticle–DNA conjugates. Current Protocols in Nucleic Acid Chemistry, 12-2.

115.Claridge, S. A., Goh, S. L., Fréchet, J. M., Williams, S. C., Micheel, C. M., & Alivisatos, A. P. (2005). Directed assembly of discrete gold nanoparticle groupings using branched DNA scaffolds. Chemistry of materials, 17(7), 1628-1635.
116.Zhang, Y., Lu, F., Yager, K. G., Van Der Lelie, D., & Gang, O. (2013). A general strategy for the DNA-mediated self-assembly of functional nanoparticles into heterogeneous systems. Nature nanotechnology, 8(11), 865-872.
117.Mirkin, C. A., Letsinger, R. L., Mucic, R. C., & Storhoff, J. J. (1996). A DNA-based method for rationally assembling nanoparticles into macroscopic materials. Nature, 382(6592), 607-609.
118.Tan, S. J., Campolongo, M. J., Luo, D., & Cheng, W. (2011). Building plasmonic nanostructures with DNA. Nature nanotechnology, 6(5), 268-276.
119.Yan, Y., Chen, J. I., & Ginger, D. S. (2012). Photoswitchable oligonucleotide-modified gold nanoparticles: controlling hybridization stringency with photon dose. Nano letters, 12(5), 2530-2536.
120.Seela, F., & Budow, S. (2006). Ph-Dependent Assembly of DNA–Gold Nanoparticles Based on the i-Motif: A Switchable Device with the Potential of a Nanomachine. Helvetica chimica acta, 89(9), 1978-1985.
121.Rankin, S., Reszka, A. P., Huppert, J., Zloh, M., Parkinson, G. N., Todd, A. K., & Neidle, S. (2005). Putative DNA quadruplex formation within the human c-kit oncogene. Journal of the American Chemical Society, 127(30), 10584.
122.Tang, L., Yu, G., Tan, L., Li, M., Deng, X., Liu, J., & Hu, J. (2017). Highly Stabilized Core-Satellite Gold Nanoassemblies in Vivo: DNA-Directed Self-Assembly, PEG Modification and Cell Imaging. Scientific Reports, 7.
123.Donaldson, K., & Poland, C. A. (2013). Nanotoxicity: challenging the myth of nano-specific toxicity. Current opinion in biotechnology, 24(4), 724-734.
124.Dekkers, S., Oomen, A. G., Bleeker, E. A., Vandebriel, R. J., Micheletti, C., Cabellos, J., & Silva, M. J. (2016). Towards a nanospecific approach for risk assessment. Regulatory Toxicology and Pharmacology, 80, 46-59.
125.Auffan, M., Rose, J., Bottero, J. Y., Lowry, G. V., Jolivet, J. P., & Wiesner, M. R. (2009). Towards a definition of inorganic nanoparticles from an environmental, health and safety perspective. Nature nanotechnology, 4(10), 634-641.
126.Boverhof, D. R., Bramante, C. M., Butala, J. H., Clancy, S. F., Lafranconi, M., West, J., & Gordon, S. C. (2015). Comparative assessment of nanomaterial definitions and safety evaluation considerations. Regulatory Toxicology and Pharmacology, 73(1), 137-150.
127.Vert, M., Doi, Y., Hellwich, K. H., Hess, M., Hodge, P., Kubisa, P., ... & Schué, F. (2012). Terminology for biorelated polymers and applications (IUPAC Recommendations 2012). Pure and Applied Chemistry, 84(2), 377-410.
128.Sohaebuddin, S. K., Thevenot, P. T., Baker, D., Eaton, J. W., & Tang, L. (2010). Nanomaterial cytotoxicity is composition, size, and cell type dependent. Particle and fibre toxicology, 7(1), 22.
129.Li, X., Wang, L., Fan, Y., Feng, Q., & Cui, F. Z. (2012). Biocompatibility and toxicity of nanoparticles and nanotubes. Journal of Nanomaterials, 2012, 6.
130.Chen, L., Mccrate, J. M., Lee, J. C., & Li, H. (2011). The role of surface charge on the uptake and biocompatibility of hydroxyapatite nanoparticles with osteoblast cells. Nanotechnology, 22(10), 105708.
131.Aggarwal, P., Hall, J. B., mcleland, C. B., Dobrovolskaia, M. A., & mcneil, S. E. (2009). Nanoparticle interaction with plasma proteins as it relates to particle biodistribution, biocompatibility and therapeutic efficacy. Advanced drug delivery reviews, 61(6), 428-437.
132.Zhang, X. D., Wu, D., Shen, X., Liu, P. X., Yang, N., Zhao, B., ... & Fan, F. Y. (2011). Size-dependent in vivo toxicity of PEG-coated gold nanoparticles. International journal of nanomedicine, 6, 2071.

133.Lin, W., Huang, Y. W., Zhou, X. D., & Ma, Y. (2006). In vitro toxicity of silica nanoparticles in human lung cancer cells. Toxicology and applied pharmacology, 217(3), 252-259.
134.Mcmillan, J., Batrakova, E., & Gendelman, H. E. (2011). Cell delivery of therapeutic nanoparticles. Progress in molecular biology and translational science, 104, 563.
135.Jones, C. F., & Grainger, D. W. (2009). In vitro assessments of nanomaterial toxicity. Advanced drug delivery reviews, 61(6), 438-456.
136.Thrivikraman, G., Madras, G., & Basu, B. (2014). In vitro/In vivo assessment and mechanisms of toxicity of bioceramic materials and its wear particulates. RSC Advances, 4(25), 12763-12781.
137.Naahidi, S., Jafari, M., Edalat, F., Raymond, K., Khademhosseini, A., & Chen, P. (2013). Biocompatibility of engineered nanoparticles for drug delivery. Journal of controlled release, 166(2), 182-194.
138.Khanna, P., Ong, C., Bay, B. H., & Baeg, G. H. (2015). Nanotoxicity: an interplay of oxidative stress, inflammation and cell death. Nanomaterials, 5(3), 1163-1180.
139.Yildirimer, L., Thanh, N. T., Loizidou, M., & Seifalian, A. M. (2011). Toxicology and clinical potential of nanoparticles. Nano today, 6(6), 585-607.
140.Oberdörster, G. (2010). Safety assessment for nanotechnology and nanomedicine: concepts of nanotoxicology. Journal of internal medicine, 267(1), 89-105.
141.Kettiger, H., Schipanski, A., Wick, P., & Huwyler, J. (2013). Engineered nanomaterial uptake and tissue distribution: from cell to organism. International journal of nanomedicine, 8, 3255.
142.Manke, A., Wang, L., & Rojanasakul, Y. (2013). Mechanisms of nanoparticle-induced oxidative stress and toxicity. Biomed research international, 2013.
143.Holgate, S. T. (2010). Exposure, uptake, distribution and toxicity of nanomaterials in humans. Journal of biomedical nanotechnology, 6(1), 1-19.
144.Limbach, L. K., Wick, P., Manser, P., Grass, R. N., Bruinink, A., & Stark, W. J. (2007). Exposure of engineered nanoparticles to human lung epithelial cells: influence of chemical composition and catalytic activity on oxidative stress. Environmental science & technology, 41(11), 4158-4163.
145.Liu, X., Jin, Q., Ji, Y., & Ji, J. (2012). Minimizing nonspecific phagocytic uptake of biocompatible gold nanoparticles with mixed charged zwitterionic surface modification. Journal of Materials Chemistry, 22(5), 1916-1927.
146.Sun, I. C., Na, J. H., Jeong, S. Y., Kim, D. E., Kwon, I. C., Choi, K., & Kim, K. (2014). Biocompatible glycol chitosan-coated gold nanoparticles for tumor-targeting CT imaging. Pharmaceutical research, 31(6), 1418-1425.
147.Zhang, Y., Xu, D., Li, W., Yu, J., & Chen, Y. (2012). Effect of size, shape, and surface modification on cytotoxicity of gold nanoparticles to human hep-2 and canine MDCK cells. Journal of Nanomaterials, 2012, 7.
148.Yildirimer, L., Thanh, N. T., Loizidou, M., & Seifalian, A. M. (2011). Toxicology and clinical potential of nanoparticles. Nano today, 6(6), 585-607.
149.Schachter, D. (2013). The source of toxicity in CTAB and CTAB-stabilized gold nanorods. Rutgers The State University of New Jersey-New Brunswick and University of Medicine and Dentistry of New Jersey.
150.Alkilany, A. M., & Murphy, C. J. (2010). Toxicity and cellular uptake of gold nanoparticles: what we have learned so far?. Journal of nanoparticle research, 12(7), 2313-2333.
151.Bozich, J. S., Lohse, S. E., Torelli, M. D., Murphy, C. J., Hamers, R. J., & Klaper, R. D. (2014). Surface chemistry, charge and ligand type impact the toxicity of gold nanoparticles to Daphnia magna. Environmental Science: Nano, 1(3), 260-270.

152.Harper, S. L., Carriere, J. L., Miller, J. M., Hutchison, J. E., Maddux, B. L., & Tanguay, R. L. (2011). Systematic evaluation of nanomaterial toxicity: utility of standardized materials and rapid assays. ACS nano, 5(6), 4688-4697.
153.Gatoo, M. A., Naseem, S., Arfat, M. Y., Mahmood Dar, A., Qasim, K., & Zubair, S. (2014). Physicochemical properties of nanomaterials: implication in associated toxic manifestations. Biomed research international, 2014.
154.Wolfram, J., Yang, Y., Shen, J., Moten, A., Chen, C., Shen, H., & Zhao, Y. (2014). The nano-plasma interface: implications of the protein corona. Colloids and Surfaces B: Biointerfaces, 124, 17-24.
155.Hou, W. C., Westerhoff, P., & Posner, J. D. (2013). Biological accumulation of engineered nanomaterials: a review of current knowledge. Environmental Science: Processes & Impacts, 15(1), 103-122.
156.Lesniak, A., Fenaroli, F., Monopoli, M. P., Åberg, C., Dawson, K. A., & Salvati, A. (2012). Effects of the presence or absence of a protein corona on silica nanoparticle uptake and impact on cells. ACS nano, 6(7), 5845-5857.
157.Albanese, A., & Chan, W. C. (2011). Effect of gold nanoparticle aggregation on cell uptake and toxicity. ACS nano, 5(7), 5478-5489.
158.Gosens, I., Post, J. A., de la Fonteyne, L. J., Jansen, E. H., Geus, J. W., Cassee, F. R., & de Jong, W. H. (2010). Impact of agglomeration state of nano- and submicron sized gold particles on pulmonary inflammation. Particle and fibre toxicology, 7(1), 37.
159.De Jong, W. H., & Borm, P. J. (2008). Drug delivery and nanoparticles: applications and hazards. International journal of nanomedicine, 3(2), 133.
160.Singh, R., & Lillard, J. W. (2009). Nanoparticle-based targeted drug delivery. Experimental and molecular pathology, 86(3), 215-223.
161.Malam, Y., Loizidou, M., & Seifalian, A. M. (2009). Liposomes and nanoparticles: nanosized vehicles for drug delivery in cancer. Trends in pharmacological sciences, 30(11), 592-599.
162.Sanna, V., Pala, N., & Sechi, M. (2014). Targeted therapy using nanotechnology: focus on cancer. International journal of nanomedicine, 9, 467.
163.Torchilin, V. P. (2014). Multifunctional, stimuli-sensitive nanoparticulate systems for drug delivery. Nature reviews Drug discovery, 13(11), 813-827.
164.Abeylath, S. C., Ganta, S., Iyer, A. K., & Amiji, M. (2011). Combinatorial-designed multifunctional polymeric nanosystems for tumor-targeted therapeutic delivery. Accounts of chemical research, 44(10), 1009-1017
165.Dichello, G. A., Fukuda, T., Maekawa, T., Whitby, R. L., Mikhalovsky, S. V., Alavijeh, M., & Sarker, D. K. (2017). Preparation of liposomes containing small gold nanoparticles using electrostatic interactions. European Journal of Pharmaceutical Sciences, 105, 55-63.
166.Lee, J. S., & Feijen, J. (2012). Polymersomes for drug delivery: design, formation and characterization. Journal of controlled release, 161(2), 473-483.
167.Liu, Z., Robinson, J. T., Tabakman, S. M., Yang, K., & Dai, H. (2011). Carbon materials for drug delivery & cancer therapy. Materials today, 14(7), 316-323.
168.Safari, J., & Zarnegar, Z. (2014). Advanced drug delivery systems: Nanotechnology of health design A review. Journal of Saudi Chemical Society, 18(2), 85-99.
169.Bulbake, U., Doppalapudi, S., Kommineni, N., & Khan, W. (2017). Liposomal Formulations in Clinical Use: An Updated Review. Pharmaceutics, 9(2), 12.
170.Bangham, A. D., & Horne, R. W. (1964). Negative staining of phospholipids and their structural modification by surface-active agents as observed in the electron microscope. Journal of molecular biology, 8(5).
171.Barenholz, Y. C. (2012). Doxil®—the first FDA-approved nano-drug: lessons learned. Journal of controlled release, 160(2), 117-134.
172.Gregoriadis, G., & Perrie, Y. (2010). Liposomes. eLS.

173.Immordino, M. L., Dosio, F., & Cattel, L. (2006). Stealth liposomes: review of the basic science, rationale, and clinical applications, existing and potential. International journal of nanomedicine, 1(3), 297.
174.Bibi, S., Lattmann, E., Mohammed, A. R., & Perrie, Y. (2012). Trigger release liposome systems: local and remote controlled delivery? Journal of microencapsulation, 29(3), 262-276.
175.Wu, G., Mikhailovsky, A., Khant, H. A., Fu, C., Chiu, W., & Zasadzinski, J. A. (2008). Remotely triggered liposome release by near-infrared light absorption via hollow gold nanoshells. Journal of the American Chemical Society, 130(26), 8175-8177.
176.Rengan, A. K., Jagtap, M., De, A., Banerjee, R., & Srivastava, R. (2014). Multifunctional gold coated thermo-sensitive liposomes for multimodal imaging and photo-thermal therapy of breast cancer cells. Nanoscale, 6(2), 916-923.
177.Chen, T., Wang, X., Alizadeh, M. H., & Reinhard, B. M. (2017). Monitoring transient nanoparticle interactions with liposome-confined plasmonic transducers. Microsystems & Nanoengineering, 3, 16086.
178.Feynman, R. P. (1960). There's plenty of room at the bottom. Engineering and science, 23(5), 22-36.
179.Turkevich, J., Stevenson, P. C., & Hillier, J. (1951). A study of the nucleation and growth processes in the synthesis of colloidal gold. Discussions of the Faraday Society,11, 55-75.
180.Brust, M., Fink, J., Bethell, D., Schiffrin, D. J., & Kiely, C. (1995). Synthesis and reactions of functionalised gold nanoparticles. Journal of the Chemical Society, Chemical Communications, (16), 1655-1656.
181.Warner, M. G., Reed, S. M., & Hutchison, J. E. (2000). Small, water-soluble, ligand-stabilized gold nanoparticles synthesized by interfacial ligand exchange reactions. Chemistry of materials, 12(11), 3316-3320.
182.Taton, T. A. (2002). Preparation of gold nanoparticle–DNA conjugates. Current Protocols in Nucleic Acid Chemistry, 12-2.
183.Jana, N. R., Gearheart, L., & Murphy, C. J. (2001). Wet chemical synthesis of high aspect ratio cylindrical gold nanorods. The Journal of Physical Chemistry B, 105(19), 4065-4067.
184.Shankar, S. S., Bhargava, S., & Sastry, M. (2005). Synthesis of gold nanospheres and nanotriangles by the Turkevich approach. Journal of nanoscience and nanotechnology, 5(10), 1721-1727.
185.Cheng, L. C., Huang, J. H., Chen, H. M., Lai, T. C., Yang, K. Y., Liu, R. S., & Tsai, D. P. (2012). Seedless, silver-induced synthesis of star-shaped gold/silver bimetallic nanoparticles as high efficiency photothermal therapy reagent. Journal of Materials Chemistry, 22(5), 2244-2253.
186.Weare, W. W., Reed, S. M., Warner, M. G., & Hutchison, J. E. (2000). Improved synthesis of small (d core≈ 1.5 nm) phosphine-stabilized gold nanoparticles. Journal of the American Chemical Society, 122(51), 12890-12891.
187.Kimling, J., Maier, M., Okenve, B., Kotaidis, V., Ballot, H., & Plech, A. (2006). Turkevich method for gold nanoparticle synthesis revisited. The Journal of Physical Chemistry B, 110(32), 15700-15707.
188.Demers, L. M., Mirkin, C. A., Mucic, R. C., Reynolds, R. A., Letsinger, R. L., Elghanian, R., & Viswanadham, G. (2000). A fluorescence-based method for determining the surface coverage and hybridization efficiency of thiol-capped oligonucleotides bound to gold thin films and nanoparticles. Analytical chemistry, 72(22), 5535-5541.
189.Szoka, F., & Papahadjopoulos, D. (1978). Procedure for preparation of liposomes with large internal aqueous space and high capture by reverse-phase evaporation. Proceedings of the National Academy of Sciences, 75(9), 4194-4198.

190.Olson, F., Hunt, C. A., Szoka, F. C., Vail, W. J., & Papahadjopoulos, D. (1979). Preparation of liposomes of defined size distribution by extrusion through polycarbonate membranes. Biochimica et Biophysica Acta (BBA)-Biomembranes, 557(1), 9-23.
191.Awasthi, V. D., Garcia, D., Klipper, R., Goins, B. A., & Phillips, W. T. (2004). Neutral and anionic liposome-encapsulated hemoglobin: effect of postinserted poly (ethylene glycol)-distearoylphosphatidylethanolamine on distribution and circulation kinetics. Journal of Pharmacology and Experimental Therapeutics, 309(1), 241-248.
192.Chen, C. S., Yao, J., & Durst, R. A. (2006). Liposome encapsulation of fluorescent nanoparticles: Quantum dots and silica nanoparticles. Journal of Nanoparticle Research, 8(6), 1033-1038.
193.Ruozi, B., Belletti, D., Tombesi, A., Tosi, G., Bondioli, L., Forni, F., & Vandelli, M. A. (2011). AFM, ESEM, TEM, and CLSM in liposomal characterization: a comparative study. International journal of nanomedicine, 6, 557.
194.Egerton, R. F. (2016). TEM specimens and images. In Physical principles of electron microscopy (pp. 89-120). Springer International Publishing
195.Flegler, S. L., Heckman Jr, J. W., & Klomparens, K. L. (1993). Scanning and transmission electron microscopy: an introduction. Oxford University Press(UK), 1993, 225.
196.Winey, M., Meehl, J. B., O'Toole, E. T., & Giddings, T. H. (2014). Conventional transmission electron microscopy. Molecular biology of the cell, 25(3), 319-323.
197.Nagashima, K., Zheng, J., Parmiter, D., & Patri, A. K. (2011). Biological tissue and cell culture specimen preparation for TEM nanoparticle characterization. Characterization of Nanoparticles Intended for Drug Delivery, 83-91.
198.Yao, N., & Wang, Z. L. (2005). Handbook of microscopy for nanotechnology. 2005. Price, 189, 146.
199.Pennycook, S. J., David, B., & Williams, C. B. (2010). Transmission electron microscopy: a textbook for materials science. Microscopy and Microanalysis, 16(1), 111.
200.Bozzola, J. J., & Russell, L. D. (1999). Electron microscopy: principles and techniques for biologists. Jones & Bartlett Learning.
201.Lee, S. K., Lee, J. H., & Choi, Y. W. (2007). Characterization and evaluation of freeze-dried liposomes loaded with ascorbyl palmitate enabling anti-aging therapy of the skin. Bulletin of the Korean Chemical Society, 28(1), 99-102.
202.Goldstein, J. Et al, Scanning electron microscopy and X-ray microanalysis: a text for biologists, materials scientists, and geologists. Springer Science & Business Media, 2012.
203.Schmitz, K. S., & Phillies, G. D. (1991). An introduction to dynamic light scattering by macromolecules. Physics Today, 44, 66.
204.Hunter, R. J. (1993). Introduction to modern colloid science Oxford University Press.
205.Derjaguin, B. V., & Landau, L. (1941). Theory of the stability of strongly charged lyophobic sols and of the adhesion of strongly charged particles in solutions of electrolytes. Acta physicochim. URSS, 14(6), 633-662.
206.Delgado, Á. V., González-Caballero, F., Hunter, R. J., Koopal, L. K., & Lyklema, J. (2007). Measurement and interpretation of electrokinetic phenomena. Journal of colloid and interface science, 309(2), 194-224.
207.Das, S. K., Choi, S. U., Yu, W., & Pradeep, T. (2007). Nanofluids: science and technology. John Wiley & Sons.
208.Kaszuba, M., Corbett, J., Watson, F. M., & Jones, A. (2010). High-concentration zeta potential measurements using light-scattering techniques. Philosophical Transactions of the Royal Society of London A: Mathematical, Physical and Engineering Sciences, 368(1927), 4439-4451.

209. Storhoff, J. J., Elghanian, R., Mucic, R. C., Mirkin, C. A., & Letsinger, R. L. (1998). One-pot colorimetric differentiation of polynucleotides with single base imperfections using gold nanoparticle probes. Journal of the American Chemical Society, 120(9), 1959-1964.
210. Chithrani, B. D., Ghazani, A. A., & Chan, W. C. (2006). Determining the size and shape dependence of gold nanoparticle uptake into mammalian cells. Nano letters, 6(4), 662-668.
211. Stewart, J. C. M. (1980). Colorimetric determination of phospholipids with ammonium ferrothiocyanate. Analytical biochemistry, 104(1), 10-14.
212. Bradley, M. O., Bhuyan, B., Francis, M. C., Langenbach, R., Peterson, A., & Huberman, E. (1981). Mutagenesis by chemical agents in V79 Chinese hamster cells: A review and analysis of the literature: A report of the gene-tox program. Mutation Research/Reviews in Genetic Toxicology, 87(2), 81-142.
213. Lundholt, B. K., Scudder, K. M., & Pagliaro, L. (2003). A simple technique for reducing edge effect in cell-based assays. Journal of biomolecular screening, 8(5), 566-570.
214. Davies, H.A., General preparation of materials and staining of sections, Electron microscopy: methods and protocols. Springer Science and Business Media, 1999. P. 1-11.
215. Mosmann, T., Rapid colorimetric assay for cellular growth and survival: application to proliferation and cytotoxicity assays. Jorunal of Immunological methods, 1983. 65(1-2): p.55-63.
216. Lanone, S., Rogerieux, F., Geys, J., Dupont, A., Maillot-Marechal, E., Boczkowski, J., & Hoet, P. (2009). Comparative toxicity of 24 manufactured nanoparticles in human alveolar epithelial and macrophage cell lines. Particle and fibre toxicology, 6(1), 14.
217. Stellamn, J.M., Encyclopaedia of occupational health and safety: The body, healthcare, management and policy, tools and approaches, International Labour Organisation, 1998. Toxicology, pp. 33.45-33.47
218. Wacker, W.E.C. et al, Metalloenzymes and Myocardial Infarction. New England Journal of Medicine, 1956. 255(10): p. 449-456
219. Miller, J.N. et al, Calibration methods in instrumental analysis: regression and correlation, Statistics and chemometrics for analytical chemistry, Pearson Hall, 2010. P.110-153
220. Murthy, S.K., Nanoparticles in modern medicine: state of the art and future challenges. International Journal of Nanomedicine, 2007. 2(2) p.129.
221. Lee, Y. J., Schade, N. B., Sun, L., Fan, J. A., Bae, D. R., Mariscal, M. M., & Yi, G. R. (2013). Ultrasmooth, highly spherical monocrystalline gold particles for precision plasmonics. ACS nano, 7(12), 11064-11070.
222. Alvarez, M. M., Khoury, J. T., Schaaff, T. G., Shafigullin, M. N., Vezmar, I., & Whetten, R. L. (1997). Optical absorption spectra of nanocrystal gold molecules. The Journal of Physical Chemistry B, 101(19), 3706-3712.
223. Haiss, W., Thanh, N. T., Aveyard, J., & Fernig, D. G. (2007). Determination of size and concentration of gold nanoparticles from UV− Vis spectra. Analytical chemistry, 79(11), 4215-4221.
224. Mirkin, C. A., Letsinger, R. L., Mucic, R. C., & Storhoff, J. J. (1996). A DNA-based method for rationally assembling nanoparticles into macroscopic materials. Nature, 382(6592), 607-609.
225. Breslauer, K. J., Frank, R., Blöcker, H., & Marky, L. A. (1986). Predicting DNA duplex stability from the base sequence. Proceedings of the National Academy of Sciences, 83(11), 3746-3750
226. Grzelczak, M., Vermant, J., Furst, E. M., & Liz-Marzán, L. M. (2010). Directed self-assembly of nanoparticles. ACS nano, 4(7), 3591-3605.
227. Ulman, A. (1996). Formation and structure of self-assembled monolayers. Chemical reviews, 96(4), 1533-1554.

228. Higashi, N., Takagi, T., & Koga, T. (2010). Layer-by-layer fabrication of well-packed gold nanoparticle assemblies guided by a [beta]-sheet peptide network. Polymer journal, 42(1), 95.
229. Yan, S., Wang, T., Feng, L., Zhu, J., Zhang, K., Chen, X., & Yin, J. (2014). Injectable in situ self-cross-linking hydrogels based on poly (L-glutamic acid) and alginate for cartilage tissue engineering. Biomacromolecules, 15(12), 4495-4508.
230. Lin, Y. X., Qiao, S. L., Wang, Y., Zhang, R. X., An, H. W., Ma, Y., & Wang, H. (2017). An in Situ Intracellular Self-Assembly Strategy for Quantitatively and Temporally Monitoring Autophagy. ACS nano, 11(2), 1826-1839.
231. Yang, Y., Hu, Y., Du, H., & Wang, H. (2014). Intracellular gold nanoparticle aggregation and their potential applications in photodynamic therapy. Chemical Communications, 50(55), 7287-7290.
232. Warner, M. G., Reed, S. M., & Hutchison, J. E. (2000). Small, water-soluble, ligand-stabilized gold nanoparticles synthesized by interfacial ligand exchange reactions. Chemistry of materials, 12(11), 3316-3320.
233. Gao, J., Huang, X., Liu, H., Zan, F., & Ren, J. (2012). Colloidal stability of gold nanoparticles modified with thiol compounds: bioconjugation and application in cancer cell imaging. Langmuir, 28(9), 4464-4471.
234. Chen, H., Paholak, H., Ito, M., Sansanaphongpricha, K., Qian, W., Che, Y., & Sun, D. (2013). 'Living' PEGylation on gold nanoparticles to optimize cancer cell uptake by controlling targeting ligand and charge densities. Nanotechnology, 24(35), 355101.
235. Opdahl, A., Petrovykh, D. Y., Kimura-Suda, H., Tarlov, M. J., & Whitman, L. J. (2007). Independent control of grafting density and conformation of single-stranded DNA brushes. Proceedings of the National Academy of Sciences, 104(1), 9-14.
236. Park, J. S., Vo, A. N., Barriet, D., Shon, Y. S., & Lee, T. R. (2005). Systematic control of the packing density of self-assembled monolayers using bidentate and tridentate chelating alkanethiols. Langmuir, 21(7), 2902-2911.
237. Hanauer, M., Pierrat, S., Zins, I., Lotz, A., & Sönnichsen, C. (2007). Separation of nanoparticles by gel electrophoresis according to size and shape. Nano letters, 7(9), 2881-2885.
238. Zhu, X., & Mason, T. G. (2016). Separating nanoparticles by surface charge group using pH-controlled passivated gel electrophoresis. Soft Materials, 14(3), 204-209.
239. Hinterwirth, H., Kappel, S., Waitz, T., Prohaska, T., Lindner, W., & Lämmerhofer, M. (2013). Quantifying thiol ligand density of self-assembled monolayers on gold nanoparticles by inductively coupled plasma–mass spectrometry. ACS nano, 7(2), 1129-1136.
240. Liu, R. S., Cheng, L. C., Huang, J. H., Chen, H. M., Lai, T. C., Hsiao, M., & Her, L. J. (2013). Highly efficient urchin-like bimetallic nanoparticles for photothermal cancer therapy.SPIE Newsroom, 2-4.
241. Dewi, M. R., Laufersky, G., & Nann, T. (2014). A highly efficient ligand exchange reaction on gold nanoparticles: preserving their size, shape and colloidal stability. RSC Advances, 4(64), 34217-34220.
242. Grzelczak, M., Pérez-Juste, J., Mulvaney, P., & Liz-Marzán, L. M. (2008). Shape control in gold nanoparticle synthesis. Chemical Society Reviews, 37(9), 1783-1791.
243. Chapel, J. P., & Berret, J. F. (2012). Versatile electrostatic assembly of nanoparticles and polyelectrolytes: Coating, clustering and layer-by-layer processes. Current opinion in colloid & interface science, 17(2), 97-105.
244. Kalsin, A. M., Kowalczyk, B., Smoukov, S. K., Klajn, R., & Grzybowski, B. A. (2006). Ionic-like behavior of oppositely charged nanoparticles. Journal of the American Chemical Society,128(47), 15046-15047.

245. Pinchuk, A. O., Kalsin, A. M., Kowalczyk, B., Schatz, G. C., & Grzybowski, B. A. (2007). Modeling of electrodynamic interactions between metal nanoparticles aggregated by electrostatic interactions into closely-packed clusters. The Journal of Physical Chemistry C,111(32), 11816-11822.
246. Kostiainen, M. A., Hiekkataipale, P., Laiho, A., Lemieux, V., Seitsonen, J., Ruokolainen, J., & Ceci, P. (2013). Electrostatic assembly of binary nanoparticle superlattices using protein cages. Nature nanotechnology, 8(1), 52-56.
247. Busseron, E., Ruff, Y., Moulin, E., & Giuseppone, N. (2013). Supramolecular self-assemblies as functional nanomaterials. Nanoscale, 5(16), 7098-7140.
248. Liu, Y., Lin, X. M., Sun, Y., & Rajh, T. (2013). In situ visualization of self-assembly of charged gold nanoparticles. Journal of the American Chemical Society, 135(10), 3764-3767.
249. Gellner, M., Steinigeweg, D., Ichilmann, S., Salehi, M., Schütz, M., Kömpe, K., & Schlücker, S. (2011). 3D Self-Assembled Plasmonic Superstructures of Gold Nanospheres: Synthesis and Characterization at the Single-Particle Level. Small, 7(24), 3445-3451.
250. Zhou, C., Yu, J., Qin, Y., & Zheng, J. (2012). Grain size effects in polycrystalline gold nanoparticles. Nanoscale, 4(14), 4228-4233.
251. Kreibig, U., & Vollmer, M. (2013). Optical properties of metal clusters. Springer Science & Business Media (25).
252. Gellman, S. H. (1997). Introduction: molecular recognition. Chemical Reviews 5(97), 1231.
253. Li, H., Carter, J. D., & labean, T. H. (2009). Nanofabrication by DNA self-assembly. Materials Today, 12(5), 24-32.
254. Garnett, J. M. (1906). Colours in metal glasses, in metallic films, and in metallic solutions. II. Philosophical Transactions of the Royal Society of London. Series A, Containing Papers of a Mathematical or Physical Character, 237-288.
255. Toma, H. E., Zamarion, V. M., Toma, S. H., & Araki, K. (2010). The coordination chemistry at gold nanoparticles. Journal of the Brazilian Chemical Society, 21(7), 1158-1176.
256. Willets, K. A., & Van Duyne, R. P. (2007). Localized surface plasmon resonance spectroscopy and sensing. Annual Review of Physical Chemistry., 58, 267-297.
257. Radziuk, D., & Moehwald, H. (2015). Prospects for plasmonic hot spots in single molecule SERS towards the chemical imaging of live cells. Physical Chemistry Chemical Physics, 17(33), 21072-21093.
258. Zheng, Y. B., Kiraly, B., Weiss, P. S., & Huang, T. J. (2012). Molecular plasmonics for biology and nanomedicine. Nanomedicine, 7(5), 751-770.
259. Deng, H., Zhong, Y., Du, M., Liu, Q., Fan, Z., Dai, F., & Zhang, X. (2014). Theranostic self-assembly structure of gold nanoparticles for NIR photothermal therapy and X-Ray computed tomography imaging. Theranostics, 4(9), 904.
260. Paterson, S., Thompson, S. A., Wark, A. W., & de la Rica, R. (2017). Gold Suprashells: Enhanced Photothermal Nanoheaters with Multiple Localized Surface Plasmon Resonances for Broadband Surface-Enhanced Raman Scattering. The Journal of Physical Chemistry C, 121(13), 7404-7411.
261. Yang, Z., Song, J., Dai, Y., Chen, J., Wang, F., Lin, L., & Fan, W. (2017). Self-Assembly of Semiconducting-Plasmonic Gold Nanoparticles with Enhanced Optical Property for Photoacoustic Imaging and Photothermal Therapy. Theranostics, 7(8), 2177.
262. Hurst, S. J., Lytton-Jean, A. K., & Mirkin, C. A. (2006). Maximizing DNA loading on a range of gold nanoparticle sizes. Analytical Chemistry, 78(24), 8313-8318.
263. Demers, L. M., Mirkin, C. A., Mucic, R. C., Reynolds, R. A., Letsinger, R. L., Elghanian, R., & Viswanadham, G. (2000). A fluorescence-based method for determining the surface coverage and hybridization efficiency of thiol-capped

oligonucleotides bound to gold thin films and nanoparticles. Analytical chemistry, 72(22), 5535-5541.
264. Demers, L. M., Östblom, M., Zhang, H., Jang, N. H., Liedberg, B., & Mirkin, C. A. (2002). Thermal desorption behavior and binding properties of DNA bases and nucleosides on gold. Journal of the American Chemical Society, 124(38), 11248-11249.
265. Chen, Y., & Mao, C. (2008). Ph-Induced Reversible Expansion/Contraction of Gold Nanoparticle Aggregates.Small,4(12), 2191-2194.
266. Manna, D., Udayabhaskararao, T., Zhao, H., & Klajn, R. (2015). Orthogonal Light-Induced Self-Assembly of Nanoparticles using Differently Substituted Azobenzenes. Angewandte Chemie International Edition, 54(42), 12394-12397.
267. Gupta, V., Sengupta, M., Prakash, J., & Tripathy, B. C. (2017). Fundamentals of Recombinant DNA Technology. In Basic and Applied Aspects of Biotechnology (pp. 23-58). Springer Singapore.
268. Balazs, D. A., & Godbey, W. T. (2010). Liposomes for use in gene delivery. Journal of drug delivery, 2011.
269. Nakamura, K., Yamashita, K., Itoh, Y., Yoshino, K., Nozawa, S., & Kasukawa, H. (2012). Comparative studies of polyethylene glycol-modified liposomes prepared using different PEG-modification methods. Biochimica et Biophysica Acta (BBA)-Biomembranes, 1818(11), 2801-2807.
270. Park, S. H., Oh, S. G., Mun, J. Y., & Han, S. S. (2006). Loading of gold nanoparticles inside the DPPC bilayers of liposome and their effects on membrane fluidities. Colloids and Surfaces B: Biointerfaces, 48(2), 112-118.
271. Hong, K., Friend, D. S., Glabe, C. G., & Papahadjopoulos, D. (1983). Liposomes containing colloidal gold are a useful probe of liposome-cell interactions. Biochimica et Biophysica Acta (BBA)-Biomembranes, 732(1), 320-323.
272. Chen, C. S., Yao, J., & Durst, R. A. (2006). Liposome encapsulation of fluorescent nanoparticles: Quantum dots and silica nanoparticles. Journal of Nanoparticle Research, 8(6), 1033-1038
273. Pornpattananangkul, D., Olson, S., Aryal, S., Sartor, M., Huang, C. M., Vecchio, K., & Zhang, L. (2010). Stimuli-responsive liposome fusion mediated by gold nanoparticles. ACS nano, 4(4), 1935-1942.
274. Szoka, F., & Papahadjopoulos, D. (1978). Procedure for preparation of liposomes with large internal aqueous space and high capture by reverse-phase evaporation. Proceedings of the National Academy of Sciences, 75(9), 4194-4198.
275. Shailesh, S., Neelam, S., & Sandeep, K. (2009). Liposomes: a review. Journal of Pharmacy Research Vol, 2(7).
276. Olson, F., Hunt, C. A., Szoka, F. C., Vail, W. J., & Papahadjopoulos, D. (1979). Preparation of liposomes of defined size distribution by extrusion through polycarbonate membranes. Biochimica et Biophysica Acta (BBA)-Biomembranes, 557(1), 9-23.
277. Neutral and anionic liposome-encapsulated hemoglobin: effect of postinserted poly(ethylene glycol)-distearoylphosphatidylethanolamine on distribution and circulation kinetics
278. Nakamura, K., Yamashita, K., Itoh, Y., Yoshino, K., Nozawa, S., & Kasukawa, H. (2012). Comparative studies of polyethylene glycol-modified liposomes prepared using different PEG-modification methods. Biochimica et Biophysica Acta (BBA)-Biomembranes, 1818(11), 2801-2807.
279. Bozzuto, G., & Molinari, A. (2015). Liposomes as nanomedical devices. International journal of nanomedicine, 10, 975.
280. Dhawan, A., & Sharma, V. (2010). Toxicity assessment of nanomaterials: methods and challenges. Analytical and bioanalytical chemistry, 398(2), 589-605.

281.Wang, B., Zhang, L., Bae, S. C., & Granick, S. (2008). Nanoparticle-induced surface reconstruction of phospholipid membranes. Proceedings of the National Academy of Sciences, 105(47), 18171-18175.
282.Somerharju, P., Virtanen, J. A., & Cheng, K. H. (1999). Lateral organisation of membrane lipids: the superlattice view. Biochimica et Biophysica Acta (BBA)-Molecular and Cell Biology of Lipids, 1440(1), 32-48.
283.Cevc, G., & Marsh, D. (1987). Phospholipid bilayers: physical principles and models. Wiley.
284.Woodle, M. C., Newman, M. S., & Cohen, J. A. (1994). Sterically stabilized liposomes: physical and biological properties. Journal of drug targeting, 2(5), 397-403.
285.Michel, R., Plostica, T., Abezgauz, L., Danino, D., & Gradzielski, M. (2013). Control of the stability and structure of liposomes by means of nanoparticles. Soft Matter, 9(16), 4167-4177.
286.Gregoriadis, G. (Ed.). (2006). Liposome technology: interactions of liposomes with the biological milieu (3). CRC press
287.Nag, O. K., & Awasthi, V. (2013). Surface engineering of liposomes for stealth behavior. Pharmaceutics, 5(4), 542-569.
288.Dan, N. (2002). Effect of liposome charge and PEG polymer layer thickness on cell–liposome electrostatic interactions. Biochimica et Biophysica Acta (BBA)-Biomembranes, 1564(2), 343-348.
289.Bibi, S., Kaur, R., Henriksen-Lacey, M., mcneil, S. E., Wilkhu, J., Lattmann, E.,& Perrie, Y. (2011). Microscopy imaging of liposomes: from coverslips to environmental SEM. International journal of pharmaceutics, 417(1), 138-150.
290.Edwards, K. A., & Baeumner, A. J. (2006). Analysis of liposomes. Talanta, 68(5), 1432-1441.
291.Thompson, R. F., Walker, M., Siebert, C. A., Muench, S. P., & Ranson, N. A. (2016). An introduction to sample preparation and imaging by cryo-electron microscopy for structural biology. Methods, 100, 3-15.
292.Zhang, L., Song, J., Cavigiolio, G., Ishida, B. Y., Zhang, S., Kane, J. P., & Ren, G. (2011). Morphology and structure of lipoproteins revealed by an optimized negative-staining protocol of electron microscopy. Journal of lipid research, 52(1), 175-184.
293.Ruozi, B., Belletti, D., Tombesi, A., Tosi, G., Bondioli, L., Forni, F., & Vandelli, M. A. (2011). AFM, ESEM, TEM, and CLSM in liposomal characterization: a comparative study. International journal of nanomedicine, 6, 557.
294.Yang, S., Liu, C., Liu, W., Yu, H., Zheng, H., Zhou, W., & Hu, Y. (2013). Preparation and characterization of nanoliposomes entrapping medium-chain fatty acids and vitamin C by lyophilization. International journal of molecular sciences, 14(10), 19763-19773.
295.Ola, H., Yahiya, S. A., & El-Gazayerly, O. N. (2010). Effect of formulation design and freeze-drying on properties of fluconazole multilamellar liposomes. Saudi pharmaceutical journal, 18(4), 217-224.
296.De Carlo, S., & Harris, J. R. (2011). Negative staining and cryo-negative staining of macromolecules and viruses for TEM. Micron, 42(2), 117-131.
297.Shaheen, S. M., Shakil Ahmed, F. R., Hossen, M. N., Ahmed, M., Amran, M. S., & Ul-Islam, M. A. (2006). Liposome as a carrier for advanced drug delivery. Pak The Journal of Biological Sciences 9(6), 1181-1191.
298.Mady, M. M., Fathy, M. M., Youssef, T., & Khalil, W. M. (2012). Biophysical characterization of gold nanoparticles-loaded liposomes. Physica Medica, 28(4), 288-295.
299.Adhikari, C., Das, A., & Chakraborty, A. (2015). Controlled Release of a Sparingly Water-Soluble Anticancer Drug through ph-Responsive Functionalized Gold-Nanoparticle-Decorated Liposomes. Chemphyschem, 16(4), 866-871.

300.Chithrani, B. D., Ghazani, A. A., & Chan, W. C. (2006). Determining the size and shape dependence of gold nanoparticle uptake into mammalian cells. Nano letters, 6(4), 662-668.
301.Stewart, J. C. M. (1980). Colorimetric determination of phospholipids with ammonium ferrothiocyanate. Analytical biochemistry. 104(1), 10-14.
302.Hein, R., Uzundal, C. B., & Hennig, A. (2016). Simple and rapid quantification of phospholipids for supramolecular membrane transport assays. Organic & biomolecular chemistry, 14(7), 2182-2185.
303.Roces, C. B., Kastner, E., Stone, P., Lowry, D., & Perrie, Y. (2016). Rapid quantification and validation of lipid concentrations within liposomes. Pharmaceutics, 8(3), 29.
304.Papadimitriou, S., & Bikiaris, D. (2009). Novel self-assembled core–shell nanoparticles based on crystalline amorphous moieties of aliphatic copolyesters for efficient controlled drug release. Journal of Controlled Release, 138(2), 177-184.
305.Xing, F., Cheng, G., Yang, B., & Ma, L. (2004). Microencapsulation of capsaicin by the complex coacervation of gelatin, acacia and tannins. Journal of Applied Polymer Science, 91(4), 2669-2675.
306.Laaksonen, T., Ahonen, P., Johans, C., & Kontturi, K. (2006). Stability and Electrostatics of Mercaptoundecanoic Acid-Capped Gold Nanoparticles with Varying Counterion Size. Chemphyschem, 7(10), 2143-2149.
307.Langner, M., & Kubica, K. (1999). The electrostatics of lipid surfaces. Chemistry and physics of lipids, 101(1), 3-35.
308.Colletier, J. P., Chaize, B., Winterhalter, M., & Fournier, D. (2002). Protein encapsulation in liposomes: efficiency depends on interactions between protein and phospholipid bilayer. BMC biotechnology, 2(1), 9.
309.Ma, B., Zhang, S., Jiang, H., Zhao, B., & Lv, H. (2007). Lipoplex morphologies and their influences on transfection efficiency in gene delivery. Journal of Controlled Release, 123(3), 184-194.
310.Hwang, S. Y., Kim, H. K., Choo, J., Seong, G. H., Hien, T. B. D., & Lee, E. K. (2012). Effects of operating parameters on the efficiency of liposomal encapsulation of enzymes. Colloids and Surfaces B: Biointerfaces, 94, 296-303.
311.Shariat, S., Badiee, A., Jaafari, M. R., & Mortazavi, S. A. (2014). Optimization of a method to prepare liposomes containing HER2/Neu-derived peptide as a vaccine delivery system for breast cancer. Iranian Journal of Pharmaceutical Research, 13, 15-25.
312.Coradegini, R. Et al, Size-dependant toxicity and cell interaction mehcnisms of gold nanoparticles on mouse fibroblasts. Toxicology Letters, 2013. 217(3), p. 205-216
313.Lanone, S., Rogerieux, F., Geys, J., Dupont, A., Maillot-Marechal, E., Boczkowski, J., & Hoet, P. (2009). Comparative toxicity of 24 manufactured nanoparticles in human alveolar epithelial and macrophage cell lines. Particle and fibre toxicology, 6(1), 14.
314.Nel, A. Et al, nanomaterial toxicity testing in the 21st ceuntury: use of a predictive toxicological approach and high-throughput screening. Accounts of Chemical Research, 2012. 46(3) p. 607-621
315.Connor, E. E., Mwamuka, J., Gole, A., Murphy, C. J., & Wyatt, M. D. (2005). Gold nanoparticles are taken up by human cells but do not cause acute cytotoxicity. Small, 1(3), 325-327.
316.Chan, F. K. M., Moriwaki, K., & De Rosa, M. J. (2013). Detection of necrosis by release of lactate dehydrogenase activity. Immune Homeostasis: Methods and Protocols, 65-70.
317.Shukla, R., Bansal, V., Chaudhary, M., Basu, A., Bhonde, R. R., & Sastry, M. (2005). Biocompatibility of gold nanoparticles and their endocytotic fate inside

the cellular compartment: a microscopic overview. Langmuir, 21(23), 10644-10654.
318. Xu, Z. P., Zeng, Q. H., Lu, G. Q., & Yu, A. B. (2006). Inorganic nanoparticles as carriers for efficient cellular delivery. Chemical Engineering Science, 61(3), 1027-1040.
319. Goodman, C. M., mccusker, C. D., Yilmaz, T., & Rotello, V. M. (2004). Toxicity of gold nanoparticles functionalized with cationic and anionic side chains. Bioconjugate chemistry, 15(4), 897-900.
320. Cedervall, T., Lynch, I., Foy, M., Berggård, T., Donnelly, S. C., Cagney, G., & Dawson, K. A. (2007). Detailed identification of plasma proteins adsorbed on copolymer nanoparticles. Angewandte Chemie International Edition, 46(30), 5754-5756.
321. Alkilany, A. M., Nagaria, P. K., Hexel, C. R., Shaw, T. J., Murphy, C. J., & Wyatt, M. D. (2009). Cellular uptake and cytotoxicity of gold nanorods: molecular origin of cytotoxicity and surface effects. Small, 5(6), 701-708.
322. Wolfram, J., Yang, Y., Shen, J., Moten, A., Chen, C., Shen, H., & Zhao, Y. (2014). The nano-plasma interface: implications of the protein corona. Colloids and Surfaces B: Biointerfaces, 124, 17-24.
323. Lesniak, A., Fenaroli, F., Monopoli, M. P., Åberg, C., Dawson, K. A., & Salvati, A. (2012). Effects of the presence or absence of a protein corona on silica nanoparticle uptake and impact on cells. ACS nano, 6(7), 5845-5857.
324. Tenzer, S., Docter, D., Kuharev, J., Musyanovych, A., Fetz, V., Hecht, R., & Landfester, K. (2013). Rapid formation of plasma protein corona critically affects nanoparticle pathophysiology. Nature nanotechnology, 8(10), 772-781.
325. Horie, M., & Iwahashi, H. (2014). The Impact of the Physiochemical Properties of Manufactured Nanoparticles on In vitro and In vivo Evaluation of Particle Toxicity. Journal of Physical Chemistry & Biophysics, 2014.
326. Rausch, K., Reuter, A., Fischer, K., & Schmidt, M. (2010). Evaluation of nanoparticle aggregation in human blood serum. Biomacromolecules, 11(11), 2836-2839.
327. Jiang, W., Kim, B. Y., Rutka, J. T., & Chan, W. C. (2008). Nanoparticle-mediated cellular response is size-dependent. Nature nanotechnology, 3(3), 145-150.
328. Chithrani, B. D., Ghazani, A. A., & Chan, W. C. (2006). Determining the size and shape dependence of gold nanoparticle uptake into mammalian cells. Nano letters, 6(4), 662-668.
329. Oberdörster, G., Maynard, A., Donaldson, K., Castranova, V., Fitzpatrick, J., Ausman, K., & Olin, S. (2005). Principles for characterizing the potential human health effects from exposure to nanomaterials: elements of a screening strategy. Particle and fibre toxicology, 2(1), 8.
330. Albanese, A., & Chan, W. C. (2011). Effect of gold nanoparticle aggregation on cell uptake and toxicity. ACS nano, 5(7), 5478-5489.
331. Chithrani, B. D., & Chan, W. C. (2007). Elucidating the mechanism of cellular uptake and removal of protein-coated gold nanoparticles of different sizes and shapes. Nano letters, 7(6), 1542-1550.
332. Kettiger, H., Schipanski, A., Wick, P., & Huwyler, J. (2013). Engineered nanomaterial uptake and tissue distribution: from cell to organism. International Journal of Nanomedicine, 8, 3255-3269.
333. Alkilany, A. M., & Murphy, C. J. (2010). Toxicity and cellular uptake of gold nanoparticles: what we have learned so far?. Journal of nanoparticle research, 12(7), 2313-2333.
334. Hess, H., & Tseng, Y. (2007). Active intracellular transport of nanoparticles: opportunity or threat?. ACS nano, 1(5), 390-392.

335.Love, S. A., Maurer-Jones, M. A., Thompson, J. W., Lin, Y. S., & Haynes, C. L. (2012). Assessing nanoparticle toxicity. Annual review of analytical chemistry, 5, 181-205.
336.Sercombe, L., Veerati, T., Moheimani, F., Wu, S. Y., Sood, A. K., & Hua, S. (2015). Advances and challenges of liposome assisted drug delivery. Frontiers in pharmacology, 6, 286
337.Campbell, P. I. (1982). Toxicity of some charged lipids used in liposome preparations. Cytobios, 37(145), 21-26
338.Gregoriadis, G. (Ed.). (2006). Liposome technology: interactions of liposomes with the biological milieu (3). CRC press.
339.Lv, H., Zhang, S., Wang, B., Cui, S., & Yan, J. (2006). Toxicity of cationic lipids and cationic polymers in gene delivery. Journal of Controlled Release, 114(1), 100-109
340.Chithrani, D. B., Dunne, M., Stewart, J., Allen, C., & Jaffray, D. A. (2010). Cellular uptake and transport of gold nanoparticles incorporated in a liposomal carrier. Nanomedicine: Nanotechnology, Biology and Medicine, 6(1), 161-169.
341.Paasonen, L., Laaksonen, T., Johans, C., Yliperttula, M., Kontturi, K., & Urtti, A. (2007). Gold nanoparticles enable selective light-induced contents release from liposomes. Journal of Controlled Release, 122(1), 86-93.
342.Chithrani, B. D., Ghazani, A. A., & Chan, W. C. (2006). Determining the size and shape dependence of gold nanoparticle uptake into mammalian cells. Nano letters, 6(4), 662-668.
343.Zhang, S., Li, J., Lykotrafitis, G., Bao, G., & Suresh, S. (2009). Size-dependent endocytosis of nanoparticles. Advanced materials, 21(4), 419-424.
344.Nam, J., Ha, Y. S., Hwang, S., Lee, W., Song, J., Yoo, J., & Kim, S. (2013). Ph-responsive gold nanoparticles-in-liposome hybrid nanostructures for enhanced systemic tumor delivery. Nanoscale, 5(21), 10175-10178.
345.Mura, S., Nicolas, J., & Couvreur, P. (2013). Stimuli-responsive nanocarriers for drug delivery. Nature materials, 12(11), 991-1003
346.Kroll, A., Pillukat, M. H., Hahn, D., & Schnekenburger, J. (2009). Current in vitro methods in nanoparticle risk assessment: limitations and challenges. European journal of Pharmaceutics and Biopharmaceutics, 72(2), 370-377.
347.Patra, H. K., Banerjee, S., Chaudhuri, U., Lahiri, P., & Dasgupta, A. K. (2007). Cell selective response to gold nanoparticles. Nanomedicine: Nanotechnology, Biology and Medicine, 3(2), 111-119.
348.Maiorano, G., Sabella, S., Sorce, B., Brunetti, V., Malvindi, M. A., Cingolani, R., & Pompa, P. P. (2010). Effects of cell culture media on the dynamic formation of protein− nanoparticle complexes and influence on the cellular response. ACS nano, 4(12), 7481-7491.
349.Farcal, L., Andón, F. T., Di Cristo, L., Rotoli, B. M., Bussolati, O., Bergamaschi, E., & Ponti, J. (2015). Comprehensive in vitro toxicity testing of a panel of representative oxide nanomaterials: first steps towards an intelligent testing strategy. Plos One, 10(5), e0127174.
350.Han, X., Corson, N., Wade-Mercer, P., Gelein, R., Jiang, J., Sahu, M., & Oberdörster, G. (2012). Assessing the relevance of in vitro studies in nanotoxicology by examining correlations between in vitro and in vivo data. Toxicology, 297(1), 1-9
351.Egerton, R. F., Li, P., & Malac, M. (2004). Radiation damage in the TEM and SEM. Micron, 35(6), 399-409.
352.Huotari, J., & Helenius, A. (2011). Endosome maturation. The EMBO journal, 30(17), p. 3481-3500.
353.Stoorvogel, W., Strous, G. J., Geuze, H. J., Oorschot, V., & Schwartzt, A. L. (1991). Late endosomes derive from early endosomes by maturation. Cell, 65(3), 417-427.

354.Zhang, X. Q., Xu, X., Bertrand, N., Pridgen, E., Swami, A., & Farokhzad, O. C. (2012). Interactions of nanomaterials and biological systems: Implications to personalized nanomedicine. Advanced drug delivery reviews, 64(13), 1363-1384.
355.Moore, T. L., Rodriguez-Lorenzo, L., Hirsch, V., Balog, S., Urban, D., Jud, C., & Petri-Fink, A. (2015). Nanoparticle colloidal stability in cell culture media and impact on cellular interactions. Chemical Society Reviews, 44(17), 6287-6305.
356.Carter, D. C., & Ho, J. X. (1994). Structure of serum albumin. Advances in protein chemistry, 45, 153-203.
357.Izak-Nau, E., Voetz, M., Eiden, S., Duschl, A., & Puntes, V. F. (2013). Altered characteristics of silica nanoparticles in bovine and human serum: the importance of nanomaterial characterization prior to its toxicological evaluation. Particle and fibre toxicology, 10(1), 56.
358.Erickson, H. P. (2009). Size and shape of protein molecules at the nanometer level determined by sedimentation, gel filtration, and electron microscopy. Biological procedures online, 11(1), 32.
359.Nel, A. E., Mädler, L., Velegol, D., Xia, T., Hoek, E. M., Somasundaran, P., & Thompson, M. (2009). Understanding biophysicochemical interactions at the nano–bio interface. Nature materials, 8(7), 543-557.
360.Mahon, E., Salvati, A., Bombelli, F. B., Lynch, I., & Dawson, K. A. (2012). Designing the nanoparticle–biomolecule interface for “targeting and therapeutic delivery”. Journal of Controlled Release, 161(2), 164-174.
361.Lee, Y. K., Choi, E. J., Webster, T. J., Kim, S. H., & Khang, D. (2015). Effect of the protein corona on nanoparticles for modulating cytotoxicity and immunotoxicity. International journal of nanomedicine, 10, 97.
362.Nel, A. E., Mädler, L., Velegol, D., Xia, T., Hoek, E. M., Somasundaran, P., & Thompson, M. (2009). Understanding biophysicochemical interactions at the nano–bio interface. Nature materials, 8(7), 543-557.
363.Cedervall, T., Lynch, I., Lindman, S., Berggård, T., Thulin, E., Nilsson, H., & Linse, S. (2007). Understanding the nanoparticle–protein corona using methods to quantify exchange rates and affinities of proteins for nanoparticles. Proceedings of the National Academy of Sciences, 104(7), 2050-2055.
364.Wang, P., Wang, X., Wang, L., Hou, X., Liu, W., & Chen, C. (2015). Interaction of gold nanoparticles with proteins and cells. Science and technology of advanced materials, 16(3), 034610.
365.Brewer, S. H., Glomm, W. R., Johnson, M. C., Knag, M. K., & Franzen, S. (2005). Probing BSA binding to citrate-coated gold nanoparticles and surfaces. Langmuir, 21(20), 9303-9307.
366.Wang, L., Li, J., Pan, J., Jiang, X., Ji, Y., Li, Y., & Chen, C. (2013). Revealing the binding structure of the protein corona on gold nanorods using synchrotron radiation-based techniques: understanding the reduced damage in cell membranes. Journal of the American Chemical Society, 135(46), 17359-17368.
367.Brancolini, G., Kokh, D. B., Calzolai, L., Wade, R. C., & Corni, S. (2012). Docking of ubiquitin to gold nanoparticles. ACS nano, 6(11), 9863-9878.
368.Zhang, D., Neumann, O., Wang, H., Yuwono, V. M., Barhoumi, A., Perham, M., & Halas, N. J. (2009). Gold nanoparticles can induce the formation of protein-based aggregates at physiological pH. Nano letters, 9(2), 666-671.
369.Fleischer, C. C., & Payne, C. K. (2014). Secondary structure of corona proteins determines the cell surface receptors used by nanoparticles. The Journal of Physical Chemistry B, 118(49), 14017-14026.
370.Lacerda, S. H. D. P., Park, J. J., Meuse, C., Pristinski, D., Becker, M. L., Karim, A., & Douglas, J. F. (2009). Interaction of gold nanoparticles with common human blood proteins. ACS nano, 4(1), 365-379.

371.Sabuncu, A. C., Grubbs, J., Qian, S., Abdel-Fattah, T. M., Stacey, M. W., & Beskok, A. (2012). Probing nanoparticle interactions in cell culture media. Colloids and Surfaces B: Biointerfaces, 95, 96-102.
372.Kewalramani, S., Guerrero-García, G. I., Moreau, L. M., Zwanikken, J. W., Mirkin, C. A., Olvera de la Cruz, M., & Bedzyk, M. J. (2016). Electrolyte-Mediated Assembly of Charged Nanoparticles. ACS central science, 2(4), 219-224.
373.Piella, J., Bastús, N. G., & Puntes, V. (2016). Size-dependent protein–nanoparticle interactions in citrate-stabilized gold nanoparticles: the emergence of the protein corona. Bioconjugate chemistry, 28(1), 88-97.
374.Pinchuk, A. O., Kalsin, A. M., Kowalczyk, B., Schatz, G. C., & Grzybowski, B. A. (2007). Modeling of electrodynamic interactions between metal nanoparticles aggregated by electrostatic interactions into closely-packed clusters. The Journal of Physical Chemistry C, 111(32), 11816-11822.
375.Meissner, J., Prause, A., Bharti, B., & Findenegg, G. H. (2015). Characterization of protein adsorption onto silica nanoparticles: influence of pH and ionic strength. Colloid and polymer science, 293(11), 3381.
376.Kalsin, A. M., Pinchuk, A. O., Smoukov, S. K., Paszewski, M., Schatz, G. C., & Grzybowski, B. A. (2006). Electrostatic Aggregation and Formation of Core− Shell Suprastructures in Binary Mixtures of Charged Metal Nanoparticles. Nano letters, 6(9), 1896-1903.
377.Wang, J., & Zhao, H. (2013). Drug–Drug Interactions for Nucleic Acid-Based Derivatives. Pharmaceutical Sciences Encyclopedia.
378.Evtugyn, G. (2014). Biochemical Components Used in Biosensor Assemblies. In Biosensors: Springer Berlin Heidelberg.
379.Trevino, V., Falciani, F., & Barrera-Saldaña, H. A. (2007). DNA microarrays: a powerful genomic tool for biomedical and clinical research. Molecular Medicine, 13(9-10), 527.
380.Saiki, R. K., Walsh, P. S., Levenson, C. H., & Erlich, H. A. (1989). Genetic analysis of amplified DNA with immobilized sequence-specific oligonucleotide probes. Proceedings of the National Academy of Sciences, 86(16), 6230-6234.
381.Clark, D. J., & Kimura, T. (1990). Electrostatic mechanism of chromatin folding. Journal of molecular biology, 211(4), 883-896.
382.Zhang, Z., Liu, Y., Jarreau, C., Welch, M. J., & Taylor, J. S. A. (2013). Nucleic acid-directed self-assembly of multifunctional gold nanoparticle imaging agents. Biomaterials science, 1(10), 1055-1064.
383.Chou, L. Y., Zagorovsky, K., & Chan, W. C. (2014). DNA assembly of nanoparticle superstructures for controlled biological delivery and elimination. Nature nanotechnology, 9(2), 148-155.
384.Locatelli, E., Ori, G., Fournelle, M., Lemor, R., Montorsi, M., & Comes Franchini, M. (2011). Click chemistry for the assembly of gold nanorods and silver nanoparticles. Chemistry-A European Journal, 17(33), 9052-9056.
385.Zeng, Q., Marthi, R., McNally, A., Dickinson, C., Keyes, T. E., & Forster, R. J. (2009). Host− Guest Directed Assembly of Gold Nanoparticle Arrays. Langmuir, 26(2), 1325-1333.
386.Wang, Y., Li, H., Jin, Q., & Ji, J. (2015). Intracellular host–guest assembly of gold nanoparticles triggered by glutathione. Chemical Communications, 52(3), 582-585.
387.Ostrowski, A., Nordmeyer, D., Boreham, A., Holzhausen, C., Mundhenk, L., Graf, C., & Rühl, E. (2015). Overview about the localization of nanoparticles in tissue and cellular context by different imaging techniques. Beilstein journal of nanotechnology, 6, 263.
388.Lin, P. C., Lin, S., Wang, P. C., & Sridhar, R. (2014). Techniques for physicochemical characterization of nanomaterials. Biotechnology advances, 32(4), 711-726.

389.Patri, A. K., Dobrovolskaia, M. A., Stern, S. T., McNeil, S. E., & Amiji, M. (2007). Preclinical characterization of engineered nanoparticles intended for cancer therapeutics. Nanotechnology for cancer therapy, 105-138.
390.Hall, J. B., Dobrovolskaia, M. A., Patri, A. K., & McNeil, S. E. (2007). Characterization of nanoparticles for therapeutics. Future Medicine, 789-903.
391.Salih, S. M., & Cosslett, V. E. (1974). Reduction in electron irradiation damage to organic compounds by conducting coatings. Philosophical Magazine, 30(1), 225-228.
392.Kettler, K., Veltman, K., van de Meent, D., van Wezel, A., & Hendriks, A. J. (2014). Cellular uptake of nanoparticles as determined by particle properties, experimental conditions, and cell type. Environmental toxicology and chemistry, 33(3), 481-492.
393.Coulter, J. A., Jain, S., Butterworth, K. T., Taggart, L. E., Dickson, G. R., McMahon, S. J., & O'Sullivan, J. M. (2012). Cell type-dependent uptake, localization, and cytotoxicity of 1.9 nm gold nanoparticles. International journal of nanomedicine, 7, 2673.
394.Hao, X., Wu, J., Shan, Y., Cai, M., Shang, X., Jiang, J., & Wang, H. (2012). Caveolae-mediated endocytosis of biocompatible gold nanoparticles in living Hela cells. Journal of Physics: Condensed Matter, 24(16), 164207.
395.Ng, C. T., Tang, F. M. A., Li, J. J. E., Ong, C., Yung, L. L. Y., & Bay, B. H. (2015). Clathrin-Mediated Endocytosis of Gold Nanoparticles In Vitro. The Anatomical Record, 298(2), 418-427.
396.Kumari, S., Mg, S., & Mayor, S. (2010). Endocytosis unplugged: multiple ways to enter the cell. Cell research, 20(3), 256.
397.Kettiger, H., Schipanski, A., Wick, P., & Huwyler, J. (2013). Engineered nanomaterial uptake and tissue distribution: from cell to organism. International journal of nanomedicine, 8, 3255.
398.Saftig, P., & Klumperman, J. (2009). Lysosome biogenesis and lysosomal membrane proteins: trafficking meets function. Nature reviews. Molecular cell biology, 10(9), 623.
399.Ivanov, A. I. (2008). Pharmacological inhibition of endocytic pathways: is it specific enough to be useful?. Exocytosis and Endocytosis, 15-33.
400.Wang, S. H., Lee, C. W., Chiou, A., & Wei, P. K. (2010). Size-dependent endocytosis of gold nanoparticles studied by three-dimensional mapping of plasmonic scattering images. Journal of nanobiotechnology, 8(1), 33.
401.Chithrani, B. D., Ghazani, A. A., & Chan, W. C. (2006). Determining the size and shape dependence of gold nanoparticle uptake into mammalian cells.Nano letters, 6(4), 662-668.
402.Oh, N., & Park, J. H. (2014). Endocytosis and exocytosis of nanoparticles in mammalian cells. International journal of nanomedicine, 9, 51.
403.Intracellular gold nanoparticle aggregation and their potential applications in photodynamic therapy
404.Nam, J., Won, N., Jin, H., Chung, H., & Kim, S. (2009). pH-induced aggregation of gold nanoparticles for photothermal cancer therapy. Journal of the American Chemical Society, 131(38), 13639-13645.
405.Mu, Q., Jiang, G., Chen, L., Zhou, H., Fourches, D., Tropsha, A., & Yan, B. (2014). Chemical basis of interactions between engineered nanoparticles and biological systems. Chem. Rev, 114(15), 7740-7781.
406.Stark, W. J. (2011). Nanoparticles in biological systems. Angewandte Chemie International Edition, 50(6), 1242-1258.
407.Pelaz, B., Charron, G., Pfeiffer, C., Zhao, Y., De La Fuente, J. M., Liang, X. J., & Del Pino, P. (2013). Interfacing engineered nanoparticles with biological systems: anticipating adverse nano–bio interactions. Small, 9(9-10), 1573-1584.

408.Lu, P., Zhou, L., Kramer, M. J., & Smith, D. J. (2014). Atomic-scale chemical imaging and quantification of metallic alloy structures by energy-dispersive X-ray spectroscopy. Scientific reports, 4.
409.Su, D. (2017). Advanced electron microscopy characterization of nanomaterials for catalysis. Green Energy & Environment.
410.Winey, M., Meehl, J. B., O'Toole, E. T., & Giddings, T. H. (2014). Conventional transmission electron microscopy. Molecular biology of the cell, 25(3), 319-323.
411.Bozzola, J. J., & Russell, L. D. (1999). Electron microscopy: principles and techniques for biologists. Jones & Bartlett Learning.
412.Pierson, J., Vos, M., McIntosh, J. R., & Peters, P. J. (2011). Perspectives on electron cryo-tomography of vitreous cryo-sections. Journal of electron microscopy, 60, S93-S100.
413.Thompson, R. F., Walker, M., Siebert, C. A., Muench, S. P., & Ranson, N. A. (2016). An introduction to sample preparation and imaging by cryo-electron microscopy for structural biology. Methods, 100, 3-15.
414.Sartori Blanc, N., Studer, D., Ruhl, K., & Dubochet, J. (1998). Electron beam-induced changes in vitreous sections of biological samples. Journal of microscopy, 192(2), 194-201.
415.Taheri, M. L., Stach, E. A., Arslan, I., Crozier, P. A., Kabius, B. C., LaGrange, T., & Sharma, R. (2016). Current status and future directions for in situ transmission electron microscopy. Ultramicroscopy, 170, 86-95.
416.Liu, Y., Lin, X. M., Sun, Y., & Rajh, T. (2013). In situ visualization of self-assembly of charged gold nanoparticles. J. Am. Chem. Soc, 135(10), 3764-3767.
417.Gai, P. L., Sharma, R., & Ross, F. M. (2008). Environmental (S) TEM studies of gas–liquid–solid interactions under reaction conditions. MRS bulletin, 33(2), 107-114.
418.Zewail, A. H. (2006). 4D ultrafast electron diffraction, crystallography, and microscopy. Annu. Rev. Phys. Chem., 57, 65-103.
419.McMullan, G., Faruqi, A. R., Clare, D., & Henderson, R. (2014). Comparison of optimal performance at 300keV of three direct electron detectors for use in low dose electron microscopy. Ultramicroscopy, 147, 156-163.
420.Jones, C. F., & Grainger, D. W. (2009). In vitro assessments of nanomaterial toxicity. Advanced drug delivery reviews, 61(6), 438-456.
421.Nel, A., Xia, T., Mädler, L., & Li, N. (2006). Toxic potential of materials at the nanolevel. science, 311(5761), 622-627.
422.Farcal, L., Andón, F. T., Di Cristo, L., Rotoli, B. M., Bussolati, O., Bergamaschi, E., & Ponti, J. (2015). Comprehensive in vitro toxicity testing of a panel of representative oxide nanomaterials: first steps towards an intelligent testing strategy. PLoS One, 10(5), e0127174.
423.Hillegass, J. M., Shukla, A., Lathrop, S. A., MacPherson, M. B., Fukagawa, N. K., & Mossman, B. T. (2010). Assessing nanotoxicity in cells in vitro. Wiley Interdisciplinary Reviews: Nanomedicine and Nanobiotechnology, 2(3), 219-231.
424.Arts, J. H., Hadi, M., Irfan, M. A., Keene, A. M., Kreiling, R., Lyon, D., & Warheit, D. (2015). A decision-making framework for the grouping and testing of nanomaterials (DF4nanoGrouping). Regulatory Toxicology and Pharmacology, 71(2), S1-S27.
425.Ekwall, B., Silano, V., Paganuzzi-Stammati, A., & Zucco, F. (1990). Toxicity tests with mammalian cell cultures. Short-term toxicity tests for non-genotoxic effects, 75-99.
426.Kroll, A., Pillukat, M. H., Hahn, D., & Schnekenburger, J. (2009). Current in vitro methods in nanoparticle risk assessment: limitations and challenges. European journal of Pharmaceutics and Biopharmaceutics, 72(2), 370-377

427.Bray, L. J., & Werner, C. (2017). Evaluation of Three-Dimensional in Vitro Models to Study Tumor Angiogenesis. ACS Biomaterials Science & Engineering, 4(2), pp 337–346
428.Pampaloni, F., Reynaud, E. G., & Stelzer, E. H. (2007). The third dimension bridges the gap between cell culture and live tissue. Nature reviews Molecular cell biology, 8(10), 839.
429.Fu, Y., Chao, J., Liu, H., & Fan, C. (2013). Programmed self-assembly of DNA origami nanoblocks into anisotropic higher-order nanopatterns. Chinese Science Bulletin, 21(58), 2646-2650.
430.Locatelli, E., Ori, G., Fournelle, M., Lemor, R., Montorsi, M., & Comes Franchini, M. (2011). Click chemistry for the assembly of gold nanorods and silver nanoparticles. Chemistry-A European Journal, 17(33), 9052-9056.
431.Anstaett, P., Zheng, Y., Thai, T., Funston, A. M., Bach, U., & Gasser, G. (2013). Synthesis of Stable Peptide Nucleic Acid-Modified Gold Nanoparticles and their Assembly onto Gold Surfaces. Angewandte Chemie International Edition, 52(15), 4217-4220.
432.Hu, X., Yang, P., He, J., Liang, R., Niu, D., Wang, H., & Li, Y. (2017). In vivo self-assembly induced retention of gold nanoparticles for enhanced photothermal tumor treatment. Journal of Materials Chemistry B, 5(30), 5931-5936.
433.Deng, H., Zhong, Y., Du, M., Liu, Q., Fan, Z., Dai, F., & Zhang, X. (2014). Theranostic self-assembly structure of gold nanoparticles for NIR photothermal therapy and X-Ray computed tomography imaging. Theranostics, 4(9), 904.
434.Chen, Q., Wang, X., Wang, C., Feng, L., Li, Y., & Liu, Z. (2015). Drug-induced self-assembly of modified albumins as nano-theranostics for tumor-targeted combination therapy. ACS nano, 9(5), 5223-5233.

9 Appendices

Appendix 1 - Standard addition plots for the recovery and validation of gold using atomic emission spectroscopy.

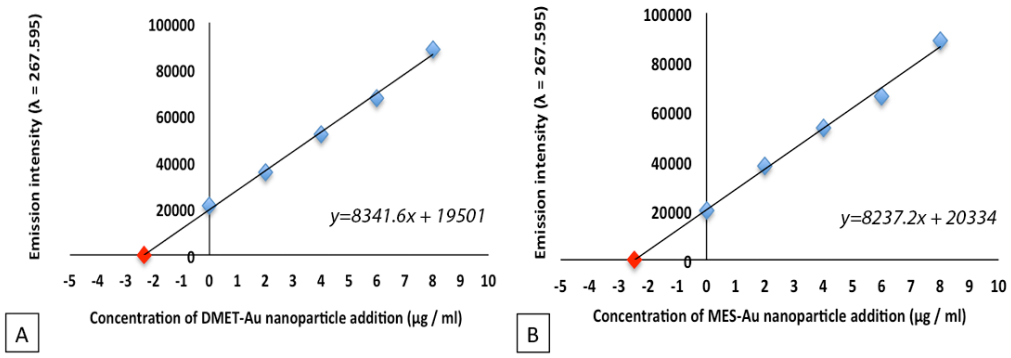

Standard addition plots for the recovery of gold using atomic emission spectroscopy. (A): PCG and (B): NCG. Extrapolated values (red markers) correspond to the original concentration of gold utilised (2.5 µg / ml).

Appendix 2 – Validation of hydrodynamic size analysis

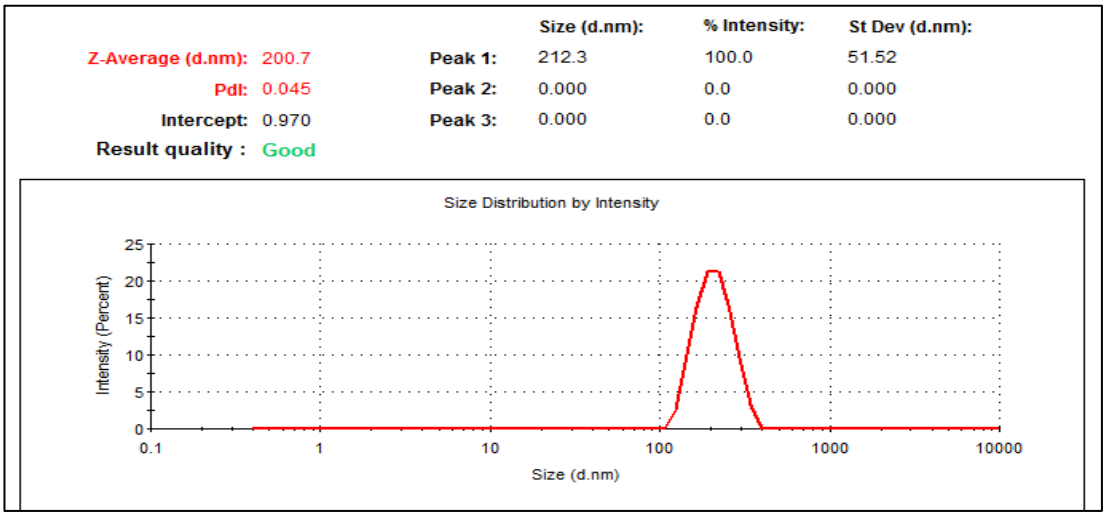

Analysis of polystyrene latex standard reference material with a hydrodynamic diameter of 192 ± 11 nm. A corresponding Z-average size of 200.7 nm was recorded, within the manufacturer's specified limits.

Appendix 3 – Validation of zeta potential analysis

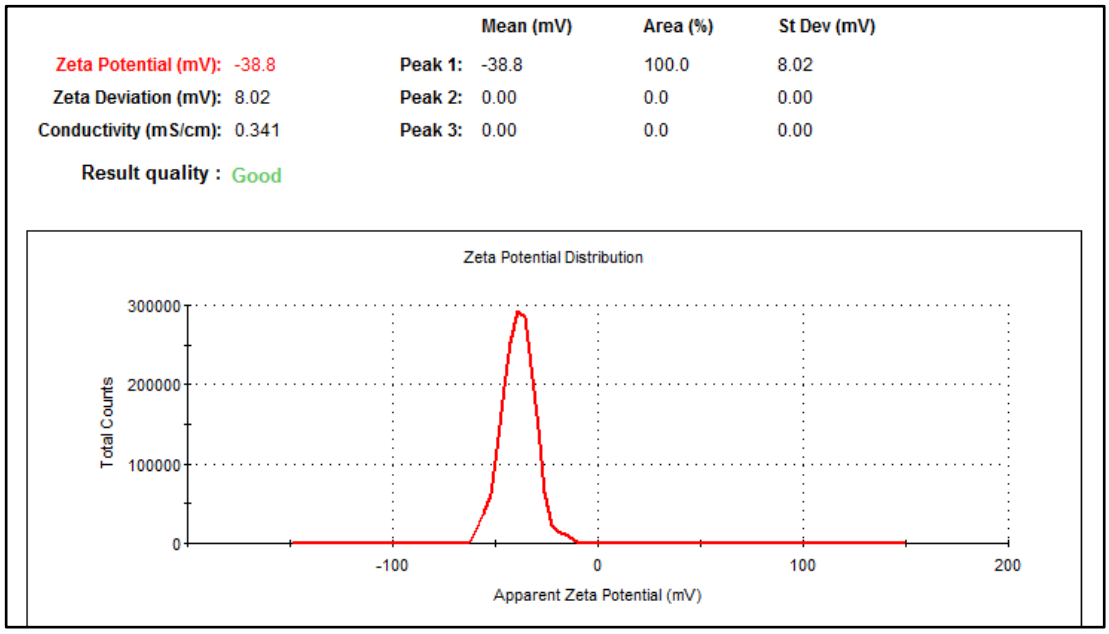

Analysis of a zeta potential transfer standard reference with a value of -42 ± 4.2 mV. A corresponding mean value of -38.8 mV was recorded, within the manufacturer's specified limits.